Complexity at Cobaltite Interfaces: The Interplay between Strain, Stoichiometry, Magnetism and Transport

A DISSERTATION
SUBMITTED TO THE FACULTY OF THE
UNIVERSITY OF MINNESOTA
BY

Shameek Bose

IN PARTIAL FULFILLMENT OF THE REQUIREMENTS
FOR THE DEGREE OF
DOCTOR OF PHILOSOPHY

Advisor: Chris Leighton

Department of Chemical Engineering and Materials Science
University of Minnesota, Twin Cities

December 2014

Acknowledgements

A few years from now, this dissertation will be remembered, if at all, as the fruit of my labor and that of my advisor. However, it is the culmination of more than ten years of education and training, spread over two continents, three institutes, and four departments. Along the way, I have been helped and motivated by numerous people, without whom this dissertation would not have been written. Before their contributions are then lost in the mists of time, I would like to take a moment to acknowledge all those who have helped me cross the finish line.

The biggest thanks goes to my advisor, Chris Leighton. A remarkable and motivated scientist, he leads by example and expects from his students the same exacting standards that he sets for himself. He took me on all those years ago as a green recruit and has patiently guided me through many missteps as I slowly worked my way up the steep learning curve he set before me. It has been a privilege to have been under his tutelage, and to have worked with the millions of dollars' worth of advanced equipment that is part of daily life in the Leighton lab; the scientific training I have received is indeed, if I may say so, priceless.

It has also been my good fortune to have worked with the motley crew of budding scientists that make up the Leighton research group. Mike Manno, Manish Sharma and Mike Erickson were the senior graduate students when I joined the lab and were instrumental in getting me started, not only in learning the ways and joys of scientific research but also in dealing with the frustrations of dead samples and failed experiments. I have also benefitted greatly from the many wonderful discussions I've had with Mike Manno, Danny Phelan, Liam O'Brien, Shun Wang, Srinivas Polisetty, Srinivas Polisetty, Kanwal P. Bhatti, and Maria Torija – all talented postdoctoral scholars who have been my scientific mentors at various stages of my Ph.D. and who have now all moved on to excellent academic and industrial careers. I would like to extend a special thanks to Javier Garcia Barriocanal – a friend, mentor and colleague. An incredibly accomplished yet humble scientist, he, along with Mike Manno, Danny and Liam, has always shown me the light during the dark days when nothing seemed to go right, be it a leaking chamber, a misbehaving plasma or an intransigent mathematical analysis. I have also been fortunate to have worked with a talented bunch of undergraduate and junior graduate students – Jenny Kuplic, Josh Schmitt, Matt Taylor, Dan Mamerow, Michael Braun, Palak Ambwani, Xin Zhang, Jeff Walter and Koustav Ganguly, who have all run experiments for me at odd hours and

at short notice. Amazingly smart and hardworking, they all have bright futures ahead of them and I wish them all the very best.

It is true that scientific discussions and ideas have been the focus of my graduate career, yet none of the science would have been possible without the constant support of the wonderful staff we have in the department. I would especially like to thank Teresa Bredahl, who has always gone out of her way to help me with myriad logistical concerns, be it a last minute credit card order, an urgent sample shipment or a parking pass for cold winter days. A big thanks also to Julie Prince, who has always helped me weave through various administrative hoops, and to Mary Nissen, who always knew which form had to be signed so I could keep getting paid. I would also like to acknowledge the help over the years of Bill Gruhlke, Dave Hultman and Mario Costello, all amazing machinists who have translated my craziest design ideas into working prototypes without batting an eyelid. Thanks also to Kevin Roberts, Mark Fisher, Tony Whipple and Lage von Dissen, the ever helpful staff scientists at the Minnesota Nano Center who have taught me almost everything I know about working in a cleanroom, and to the helpful scientists at the University of Minnesota Characterization Facility.

Outside the University of Minnesota, I would like to thank Ulrich Poppe, the inventor of the high pressure sputtering system that has been at the center of my Ph.D., for being a constant source of technical support over the years. I would also like extend a special thanks to Bob and Beverly Sundahl, whose wonderful benevolence has enabled my graduate fellowship support these past few years.

Going back a few years, I would like to thank the many hardworking professors I've had as an undergraduate student at the Fr. Conceicao Rodrigues College of Engineering, and as a graduate student at the University of Minnesota. The many hours of physics, chemistry, math and engineering lectures, and the numerous laboratory and tutorial sessions have been invaluable in building the foundation of my scientific career. I would like to especially thank Prof. K. V. V. Murthy, my soft-spoken undergraduate thesis advisor, under whose guidance I got my feet wet in scientific research and who has played a pivotal role in my coming to graduate school. I would also like to thank Prof. Rakesh Lal, Prof. Dinesh Sharma, Prof. Richard Pinto and Aniruddh Sarkar, all of whom helped me get started in microelectronics research as a junior research assistant at IIT Bombay.

Finally, I would like to acknowledge my parents, Shankar and Reeta Bose, my sister, Aditi Bose, and my grandmother, Sabita Bose, for all their encouragement and support over the years, and for always being a mere phone call away, no matter the time of day. And a big, big thanks to all the wonderful friends I've made over the years, who have been my family ten thousand miles away from home, and who have made the Minnesota summers more fun and the Minnesota winters more bearable.

To my grandmother,

Sabita Bose,

who has patiently waited for this day.

Abstract

Thin films and heterostructures of the perovskite cobaltites are of great interest, not only from the point of view of fundamental physics and materials science, but also for technological applications such as solid oxide fuel cells and gas membranes. Their properties are, however, severely deteriorated from the bulk, being dominated by the presence of interfacial "dead layers". Working with the prototypical $SrTiO_3$ (001)/$La_{1-x}Sr_xCoO_3$ (LSCO) system, our group recently discovered that this degradation in the magnetism and electronic transport at the interface is caused by nanoscopic magneto-electronic phase separation. This was shown to occur primarily due to accumulation of oxygen vacancies near the interface, driven by the interplay between the strain state and the ordering of oxygen vacancies. In the present work we show how this understanding allows for engineering of the interfacial magnetic and electronic transport properties *via* manipulation of this oxygen vacancy superstructure.

We first demonstrate a synthesis technique that utilizes a unique high pressure oxygen plasma to sputter LSCO thin films over a wide doping range $0.05 \leq x \leq 0.80$. Then, using reciprocal space mapping and transmission electron microscopy, we demonstrate the ability to control, *via* the vacancy ordering, the critical strain relaxation thickness by changing the sign of the strain (from tensile on $SrTiO_3$ to compressive on $LaAlO_3$) and crystallographic orientation ((001) *vs.* (110)). We then provide cross sectional electron energy loss spectroscopy data to show that this strain and orientation control preserves both oxygen and hole carrier concentration at the $LaAlO_3$(001)/LSCO and $SrTiO_3$(110)/LSCO interfaces, strikingly different to the severely depleted $SrTiO_3$(001)/LSCO interface. SQUID magnetometry, polarized neutron reflectometry (PNR) and magneto-transport confirm the concomitant mitigation of the interfacial degradation for LSCO films grown on $LaAlO_3$(001) and $SrTiO_3$(110), as compared to films grown on $SrTiO_3$ (001). Finally, we use scanning tunneling microscopy to provide direct real space images of the magneto-electronic phase separation in ultrathin LSCO on $SrTiO_3$(001).

Our work thus demonstrates the ability to utilize oxygen vacancy ordering as a tunable control parameter to tailor interfacial electronic and magnetic properties, with profound implications for the myriad other systems that exhibit unique properties due to such ordering.

Contents

List of Tables

Chapter 1

Chapter 4

Chapter 5

List of Figures

Chapter 1

Chapter 2

Chapter 3

Chapter 4

Chapter 5

Chapter 6

List of Abbreviations

AC	Alternating Current
ADF	Annular Dark Field
AF	Antiferromagnetic
AFM	Atomic Force Microscope
AMR	Anisotropic Magnetoresistance
BCS	Bardeen – Cooper – Schrieffer
CO	Charge Ordered
DC	Direct Current
DFT	Density Functional Theory
DMFT	Dynamic Mean Field Theory
EELS	Electron Energy Loss Spectroscopy
ESR	Electron Spin Resonance
FM	Ferromagnetic Metal
f.u.	Formula unit
FWHM	Full Width at Half Maximum
GGA	Generalized Gradient Approximation
GI	Glassy Insulator
GIXR	Grazing Incidence X-ray Reflectivity
GMR	Giant Magnetoresistance
GPA	Geometric Phase Analysis
HAADF	High Angle Annular Dark Field
HRTEM	High Resolution Transmission Electron Microscope
HRXRD	High Resolution X-Ray Diffraction
HS	High Spin
IGMR	Intercluster Giant Magnetoresistance
INS	Inelastic Neutron Scattering
IS	Intermediate Spin
LAO	$LaAlO_3$
LDA	Local Density Approximation
LDOS	Local Density of States

LS	Low Spin
LSCO	$La_{1-x}Sr_xCoO_3$
LSCO50	$La_{0.5}Sr_{0.5}CoO_{3-\delta}$
LSCOx28	$La_{0.72}Sr_{0.28}CoO_{3-\delta}$
LSCOx50	$La_{0.5}Sr_{0.5}CoO_{3-\delta}$
MBE	Molecular Beam Epitaxy
MEPS	Magneto-Electronic Phase Separation
MOCVD	Metal-Organic Chemical Vapor Deposition
MR	Magnetoresistance
NMR	Nuclear Magnetic Resonance
OVO	Oxygen Vacancy Ordering
PID	Proportional – Integral – Derivative
PLD	Pulsed Laser Deposition
PLZT	$Pb_{0.9}La_{0.1}(Zr_{0.2}Ti_{0.8})_{0.975}O_3$
PM	Paramagnetic Metal
PNR	Polarized Neutron Reflectivity
PS	Phase Separated
PSD	Position Sensitive Detector
RC	Rocking Curve
RF	Radio Frequency
RMS	Root Mean Square
RRR	Residual Resistivity Ratio
RSM	Reciprocal Space Map
SANS	Small Angle Neutron Scattering
SCO	$SrCoO_{2.5}$
SOFC	Solid Oxide Fuel Cell
SLD	Scattering Length Density
SPM	Scanning Probe Microscopy
SRP	Strain Relaxation Percentage
STEM	Scanning Transmission Electron Microscope
STM	Scanning Tunneling Microscope
STO	$SrTiO_3$
STS	Scanning Tunneling Spectroscopy

SQUID	Superconducting Quantum Interferometry Device
TEM	Transmission Electron Microscope
TM	Transition Metal
TMP	Turbomolecular Pump
UHV	Ultrahigh Vacuum
VSM	Vibrating Sample Magnetometer
WAXRD	Wide Angle X-Ray Diffraction
XRD	X-Ray Diffraction
ZBC	Zero Bias Conductance

"Remember, Red, hope is a good thing, maybe the best of things,
and no good thing ever dies"

Andy Dufresne
The Shawshank Redemption (1994)

Chapter 1

Introduction

1.1 The perovskites

Solid oxides are perhaps some of the most ubiquitous materials on earth and can be found in rocks, sand, clay, rust, pigments, gemstones and ceramics. As the name suggests, they comprise oxygen and at least one other element, and can range from simple binary oxides such as Al_2O_3 to more complex ternary and quaternary formulations containing multiple cations. Although solid oxides are often associated with being insulators, and the majority of them are indeed so, many of them are in fact conductors and possess interesting electronic properties. This has opened up the vast field of oxide electronics and metal oxides form the basis of a wide variety of commercially available products, such as transparent conductive coatings (indium tin oxide) [1], solid oxide fuel cells (yttrium stabilized zirconia electrolytes) [2], piezoelectric and ferroelectric transducers (lead zirconate titanate) [3], and ferroelectric non-volatile memory (strontium bismuth tantalate) [4].

A particular class of complex oxides that have garnered much attention over the past 50 years are the perovskites, so named after the eponymous mineral $CaTiO_3$. All perovskites crystallize in a structure whose unit cell closely resembles a cube with three different atomic sites (Fig. 1.1 (a)) – the body corners, called the *A* site, are usually occupied by an alkaline earth or rare earth element, the body center, referred to as the *B* site usually has a transition metal, and the face

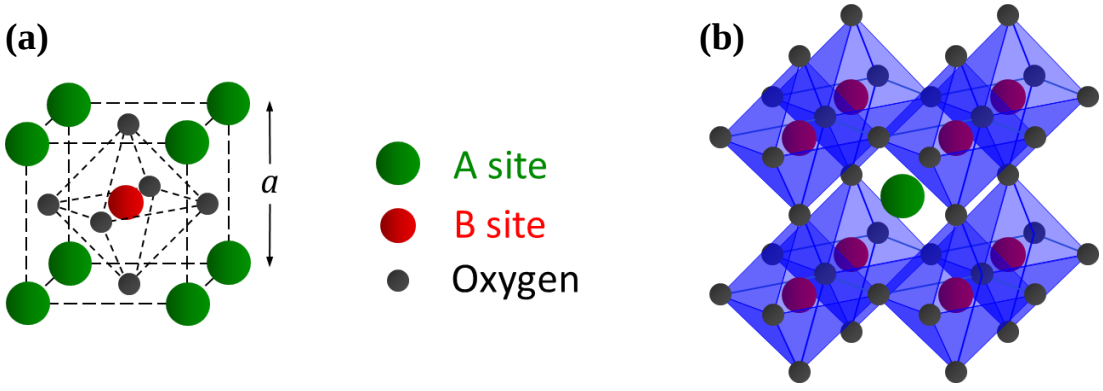

Fig. 1.1: (a) The perovskite unit cell showing the positions of the A site, the B site and oxygen. (b) An alternate and equivalent rendering of the perovskite crystal as a long range network of corner sharing BO_6 octahedra. *a* is the edge length of the cubic unit cell.

centers are occupied by oxygen, thereby yielding a general formula ABO_3. The six oxygen ions thus form an octahedral cage around the *B* site and the crystal structure can be equivalently represented as a long range network of corner sharing BO_6 octahedra (Fig. 1.1 (b)). The edge length a of the cubic unit cell can be related to the size of the *A* site and *B* site ions through simple geometry as:

$$2(r_A + r_O) = \sqrt{2}a$$
$$2(r_B + r_O) = a$$

(1.1.1a)

and therefore

$$(r_A + r_O) = \sqrt{2}(r_B + r_O)$$

(1.1.1b)

where r_A, r_B and r_O are the ionic radii of the *A* site, *B* site and oxygen respectively. The equality however holds true *only* for a perfect cubic unit cell, with all edge lengths equal and all unit cell angles 90º. In general, the ionic radii are related to each other through the Goldschmidt tolerance factor *t*, defined as:

$$t = \frac{r_A + r_O}{\sqrt{2}(r_B + r_O)}$$

(1.1.2)

The value of t is 1 for the ideal cubic cell and is rarely seen in real structures. But the perovskite structure is surprisingly tolerant to variations in the *A* site and *B* site radii, and t is known to achieve values between 0.89 and 1.02 without affecting the stability of the crystal structure. The variation in t is accommodated through tilts of the BO_6 octahedra and displacements of the cations, which distort the octahedra, change the $B - O - B$ bond angle, lower the crystal symmetry to rhombohedral, tetragonal, orthorhombic, monoclinic or triclinic (there are 23 possible tilt systems) and induce non-centrosymmetric properties such as ferroelectricity and antiferroelectricity [5]. The robustness of the perovskite structure is exemplified by Fig. 1.2 which shows the various elements that can go into the *A* and *B* sites.

The perovskite structure is amenable to substitutional alloying or 'doping', both on the *A* and *B* sites and can further tolerate a finite concentration of oxygen vacancies, an example of a doped

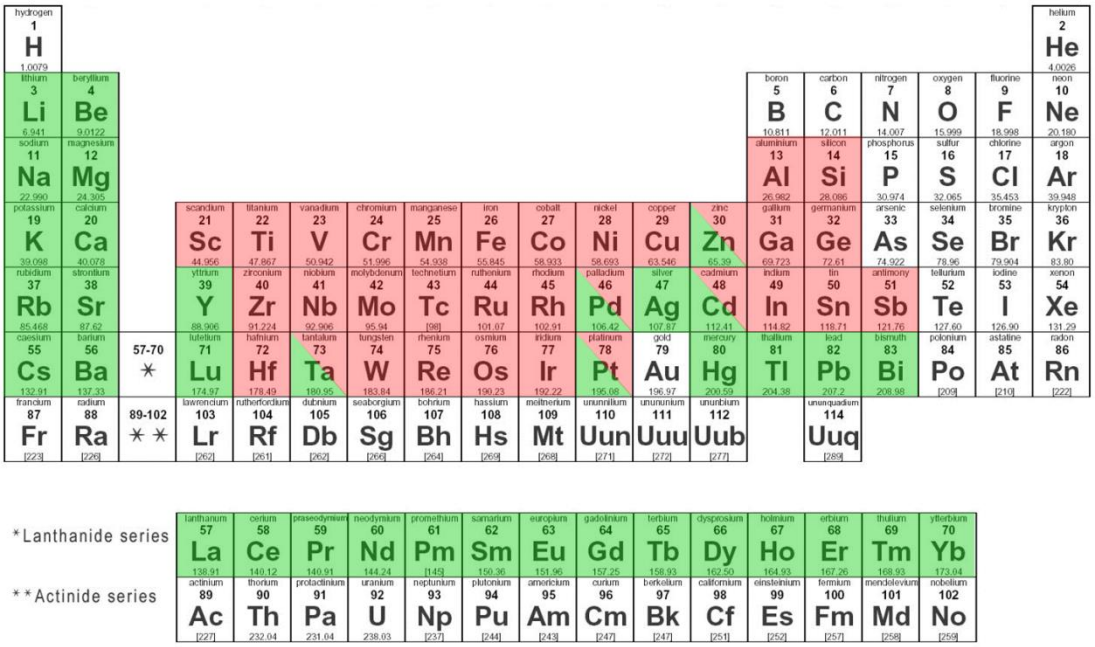

Fig. 1.2: Elements that can be incorporated in the perovskite structure. Elements shaded in green can go into the *A* site while those in red can go into the *B* site. Ta, Pd, Pt, Zn, and Cd can go into both *A* and *B* sites.

perovskite formula being $A_{1-x}A'_xB_{1-y}B'_yO_{3-\delta}$, with δ the oxygen non-stoichiometry. Similar to other oxides like ZnO [6], oxygen vacancies in the perovskites act as electron donors (or compensators in hole rich *p* type materials). The oxygen non-stoichiometry, even when not disrupting the crystal structure, thus has a profound impact on the electronic and magnetic properties of the material.

The flexibility in elemental composition of the perovskites and their derived compounds leads to a fascinatingly diverse range of functionalities, such as ferromagnetism and colossal magnetoresistance in the manganites [7], high T_C superconductivity in the cuprates [8], mixed-ionic conductivity in the cobaltites [9], and ferroelectricity in $BaTiO_3$ [10] (Fig. 1.3). Furthermore, since they all have almost identical crystal structures and similar lattice parameters, they can potentially be seamlessly integrated with each other to give a range of multifunctional materials such as multiferroics [11].

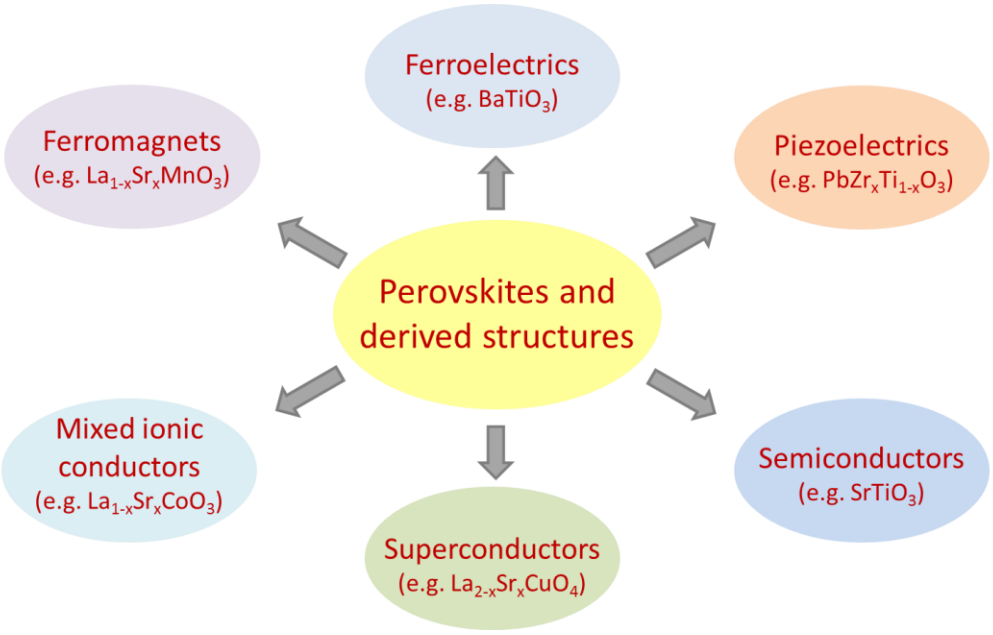

Fig. 1.3: Diverse functionalities of the perovskite oxides and their derived structures.

1.2 Basic physics of transition metal perovskites

Unlike metals and conventional semiconductors, bonding in transition metal (TM) perovskites is dominantly ionic due to the large difference in electronegativities between the cations and oxygen, with a relatively smaller covalent contribution often leading to electron occupancy of hybridized orbitals. The electronic properties of such TM perovskites are primarily due to the *d* shell electrons of the *B* site atom and their hybridization with the neighboring oxygen 2*p* orbitals. Electron transfer between neighboring *B* atoms is acutely dependent on the *B* – *O* – *B* bond angle and the *B* – *O* bond length, with the *A* site atom only indirectly affecting transport through its influence on these bond properties. Therefore, a review of the *d* orbital physics in such materials is a prerequisite to understanding their complex electronic and magnetic behavior.

1.2.1 Crystal field splitting

Transition metals, by definition, possess partially or completely filled *d* orbitals, and despite possessing higher shell *s* electrons (as a result of the Madelung $n + l$ rule of orbital filling) [12], it is the *d* electrons that participate in bonding and transport. In a free atom (or ion), the five *d*

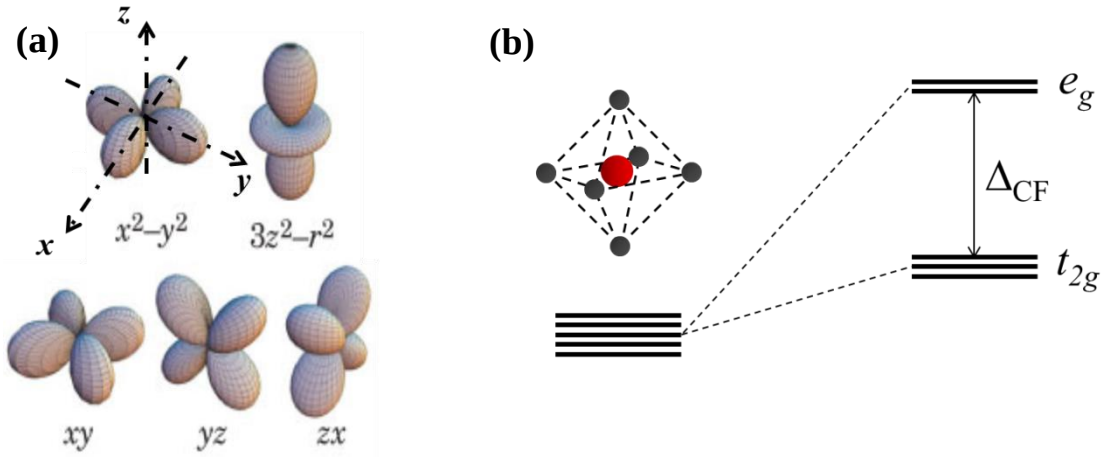

Fig. 1.4: (a) The five-fold degenerate *d* orbitals in an isolated transition metal atom. (b) The crystal field induced energy level split in an octahedral coordination. (Image from [13]

orbitals (*xy*, *yz*, *zx*, $x^2 - y^2$, $3z^2 - r^2$) are degenerate and are only distinguished by their spatial shape. In a Cartesian coordinate system, the $x^2 - y^2$, $3z^2 - r^2$ orbitals point along the axes while the *xy*, *yz*, *zx* orbitals point between the axes (Fig. 1.4 (a)). However, in an ionic crystal or a metal complex, the degeneracy is lifted by the static electric fields of the anionic nearest neighbors (ligands). In a material with octahedral coordination symmetry, the $x^2 - y^2$, $3z^2 - r^2$ orbitals (referred to as the e_g orbitals) point directly towards the ligands; the electrons in these orbitals thus experience increased Coulombic repulsion compared to the *xy*, *yz*, *zx* orbitals (known as the t_{2g} orbitals), which are oriented between the ligands. The t_{2g} orbitals are therefore lower in energy than the e_g orbitals. Due to the octahedral symmetry, the three t_{2g} orbitals are themselves degenerate as are the two e_g. The e_g and t_{2g} orbitals are thus separated by an energy Δ_{CF} given by [14]:

$$\Delta_{CF} = \frac{5}{3} z e^2 \left(\frac{\overline{r^4}}{a^5} \right) \tag{1.2.1}$$

where z is the atomic number of the ligand ions, e he electronic charge, $\overline{r^4}$ the mean fourth power radius of the metal ion and a is the distance between the metal and ligand ions. This phenomenon is known as crystal field splitting (Fig. 1.4 (b)). $\Delta_{CF} \approx 1$ eV for $LaMnO_3$ [15]. It is to be noted that in tetradedrally coordinated systems, the three t_{2g} levels are higher in energy than the e_g levels.

1.2.2 Hund's rules for orbital filling

In the absence of any other interaction, the crystal field induced energy gap alone would determine the orbital occupation of the *d* electrons. However, the Hund's rules for electron occupancy, along with the Pauli exclusion principle (which prohibits two electrons with the same spin from occupying the same orbital), try to maximize the total spin and angular momentum of the atom [16]. This is often quantified as an intra-atomic exchange energy term H_{ex}, which is the energy penalty for violating the occupancy rule. Therefore while the crystal field favors the confinement of all *d* electrons in the lower t_{2g} orbitals, Hund's rules try to have electrons in the maximum number of orbitals. As a result, the ground state of the crystal is a competition between these two opposing interactions – if the energies involved are comparable, small perturbations such as temperature and pressure can drive the system from one ground state to the other. Fig. 1.5 illustrates the two extreme cases of orbital filling for a hypothetical ion with six *d* electrons. When the crystal field splitting greatly exceeds the Hund's energy, all six electrons are confined to the t_{2g} states and the ion has a zero net spin. This is known as the low spin state and the material will show diamagnetic behavior. On the other hand, when Hund's exchange is the dominant energy term, such as in the manganites [15], the spin of the system is maximized through occupation of all orbitals and the ion has a spin of S = 2. This is known as the high spin state and depending on the inter-atomic exchange interaction, the moments could be disordered , resulting in paramagnetic behavior, or form long range order to yield ferromagnetism, antiferromagnetism, ferrimagnetism, or helimagnetism and other non-collinear structures.

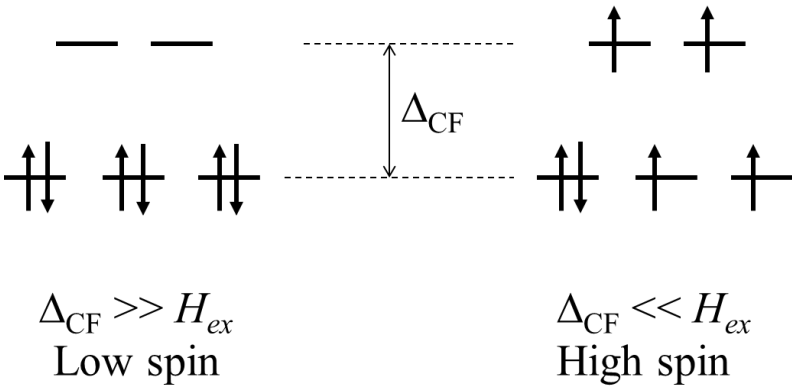

Fig. 1.5: The two limiting cases of electron occupation in a d^6 species depending on the relative strengths of the crystal field splitting and the Hund's coupling energy.

1.2.3 Jahn – Teller effect

The Jahn – Teller effect refers to a particular distortion observed in octahedral and tetrahedral lattices and coordination complexes whereby the system lifts the degeneracy of the t_{2g} and e_g orbitals by lowering its symmetry so as to lower the total energy of the system [17]. This is achieved *via* elongation or compression of the coordination polyhedron. Fig. 1.6 illustrates this effect in a perovskite lattice. Under elongation (of the *z* axis) the orbitals with a *z* component are lowered in energy (due to reduced overlap with the oxygen 2*p* orbitals) while those in the *xy* plane are raised in energy. The distortion affects both the t_{2g} and e_g orbitals; however the energy split is greater for the e_g orbitals. Under compression, the orbitals in the *xy* plane are stabilized over the ones with a *z* component. The Jahn – Teller distorted lattice will be more stable than the undistorted lattice only if the number of electrons are such that they can preferentially occupy the stabilized orbitals. Further, since the energy split is higher in the e_g band, the number of e_g electrons has a dominant effect on the presence of a Jahn – Teller effect. Thus systems with 1 and 3 e_g electrons are strongly Jahn – Teller active while those with 1, 2, 4, and 5 t_{2g} electrons are weakly Jahn – Teller active. The Jahn – Teller effect is a crucial factor in determining the electronic and magnetic properties of the perovskites since its presence tends to localize the e_g electrons which participate in transport and magnetic exchange interactions. Jahn – Teller distortions are typically ~ 0.1 Å, with energy scales ~ 0.25 eV in the manganites [15].

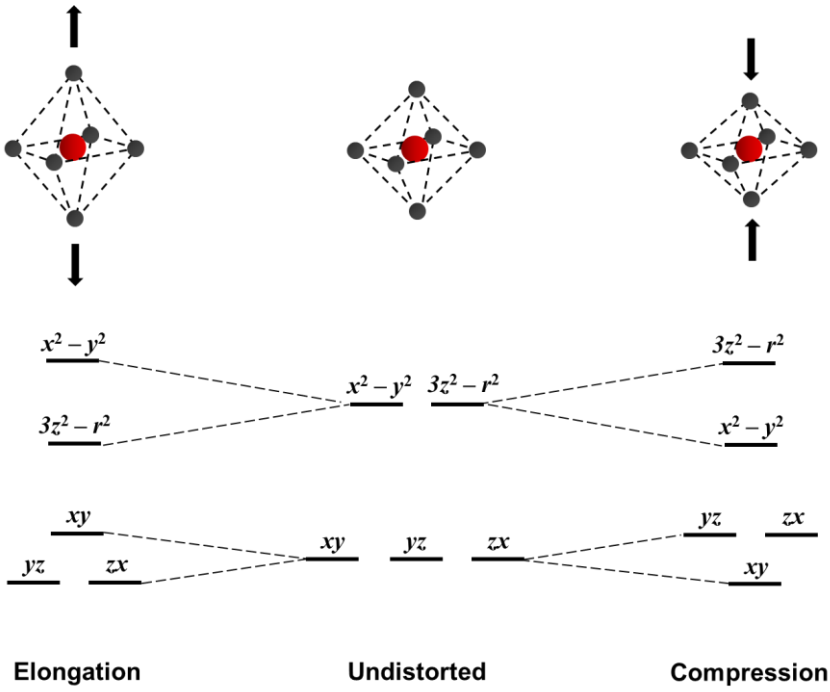

Fig. 1.6: The Jahn – Teller effect as seen in octahedral coordination complexes and perovskite oxides.

1.2.4 Doping and disorder

Doping in semiconductors is a well-established technique of introducing controlled quantities of impurity atoms in the host lattice to precisely adjust the carrier concentration and thereby tune the Fermi level. Since the conduction bands of the perovskite oxides are formed by the hybridization of the *B* site *d* and the oxygen 2*p* orbitals, doping these materials requires the manipulation of the number of 3*d* electrons on the B site. One way to achieve this is by direct substitution of the *B* site atom with a different transition metal *B*'. However, this smears the properties of the *B* – O – *B* hybridized band with those of the *B*' – O - *B*' band. Although this is often desirable, a more common way of doping the perovskite oxides is by aliovalent substitution of the *A* site which alters the oxidation state of the *B* state through charge balance. Since most transition metals that can occupy the *B* site are multivalent, this simply results in alteration of the number of *d* electrons. For instance, $LaMnO_3$ has the Mn ion in the 3+ state while $SrMnO_3$ has it in the 4+ state. Thus the alloyed series $(La,Sr)MnO_3$ would have a distribution of Mn^{3+} and Mn^{4+} that would be commensurate with the La:Sr ratio. Ideally such doping would merely change the electron concentration and leave the band structure unaltered. However since the ionic radii of the host atom and dopant atom are invariably different, substitution changes the local Goldschmidt tolerance factor and results in structural distortions such as octahedral tilts and rotations. This results in alteration of the *B* – O – *B* bond angle and the *B* – O bond length, both of which change the bandwidth. Furthermore, since these crystals are ionic, randomness in the dopant distribution leads to a disordered potential landscape which often results in inhomogeneity in carrier concentration [18] and strong localization and scattering of the electrons [19]. Finally, it is not always possible to synthesize both end members of the alloy series. In such cases, the stability of the structure determines the upper limit to doping. Table 1.1 shows the number of *d* electrons of the 3*d* transition metals in their commonly found perovskite oxidation states.

	Sc	Ti	V	Cr	Mn	Fe	Co	Ni	Cu	Zn
+2	1	2	3	4	5	6	7	8	9	10
+3	0	1	2	3	4	5	6	7	8	-
+4	-	0	1	2	3	4	5	6	7	-

Table 1.1: Number of *d* electrons in the various oxidation states of the 3*d* transition metals

An alternative way to dope electrons and holes into the perovskite oxides is through oxygen vacancies and interstitials respectively. An oxygen vacancy is a charged defect and donates two electrons to the lattice through the reaction:

$$O_O^{\times} \rightarrow V_O^{\bullet\bullet} + 2e' \tag{1.2.2}$$

Oxygen vacancies are commonly used to dope electrons in semiconducting oxides such as $SrTiO_3$ [20]. The enthalpy of formation of oxygen vacancies is strongly dependent on the stability of the formal valence of the transition metal cation in the system and in many materials, like the hole doped cobaltites, vacancies are the predominant oxygen defect. In such hole doped systems, oxygen vacancies behave as hole compensators and lead to degraded electronic and magnetic properties.

1.2.5 Double exchange

Magnetic exchange refers to the quantum mechanical interaction between two particles with spin that tends to align them parallel or antiparallel to each other. When neighboring atoms interact directly with each other, it is referred to as direct exchange and is the basis for the stabilization of ferromagnetism in metals such as iron, cobalt and nickel. On the other hand, ionic crystals such as the perovskite oxides exhibit *indirect* exchange whereby the magnetic interaction between neighboring cations is mediated by the intermediate oxygen anion. One such magnetic exchange is the double exchange interaction that stabilizes ferromagnetism in oxides such as the manganites through the interaction between localized spins and delocalized electrons. It was first proposed by Zener [21] to explain the correlation between ferromagnetism and metallicity first observed by Jonker and van Santen in the manganites [22, 23]. Although the theory of double exchange was developed for mixed-valence manganites and related perovskites, it has also been used to explain the ferromagnetic metallicty of CrO_2 [24]. In mixed valence systems, double exchange occurs between two oxygen sharing *B* cations which have different oxidation states and differ by a single e_g electron, for instance Mn^{3+} – O – Mn^{4+}. In this scenario, an e_g electron is *simultaneously* transferred between the lower valence ion (Mn^{3+}) to the oxygen and from the oxygen to the higher valence ion (Mn^{4+}) (Fig. 1.7 (a)). This is equivalent to the e_g electron hopping between neighboring sites and since the ions are otherwise identical, the process effectively interchanges the position of the two ions. Double exchange thus delocalizes the e_g electrons and thereby stabilizes a metallic ground state.

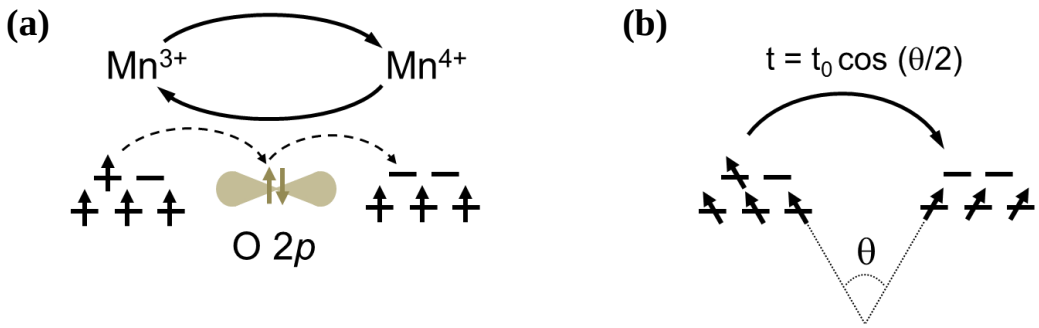

Fig. 1.7: (a) The double exchange process in a Mn^{3+}/Mn^{4+} compound. Electron transfer between the Mn^{3+} and Mn^{4+} ions takes place through the intermediate oxygen. (b) Dependence of the double exchange transfer probability on the angle between the neighboring spins.

As explained in section 1.2.2, Hund's exchange maximizes the spin of an atom or ion by aligning the spins of all the *d* electrons parallel to each other, implying the e_g spins are always aligned parallel to the t_{2g} spins. In a simple model then, treating the t_{2g} spins classically and the e_g electrons as quantum mechanical particles capable of tunneling, an e_g electron hopping between neighboring Mn ions with spins differing by an angle θ, the spin of the e_g electron being transferred must "rotate" by θ to match the t_{2g} spins of the destination ion and not violate Hund's rules (Fig. 1.7 (b)). The transfer probability for such a case was worked out by Anderson and Hasegawa to be [25]:

$$t = t_0 \cos\left(\frac{\theta}{2}\right) \tag{1.2.3}$$

where t_0 is the transfer probability for perfectly aligned spins. Double exchange is thus facilitated by ferromagnetic ordering of the ionic moments (t is maximized when θ is 0) and thereby provides an explicit link between metallic transport and ferromagnetism in such mixed valence compounds.

1.2.6. Charge and orbital ordering

Charge ordering in a mixed valence oxide refers to the static periodic arrangement (as opposed to a random distribution) of the two oxidation states of the *B* site cation. It is often accompanied by orbital ordering wherein the orbital occupancy of the *d* electrons follows a similar periodic arrangement as a sublattice. Such sub-ordering is commonly seen in the manganites and Fig. 1.8 shows one such ordering instance found in $La_{0.5}Ca_{0.5}MnO_3$ [26]. Both charge and orbital

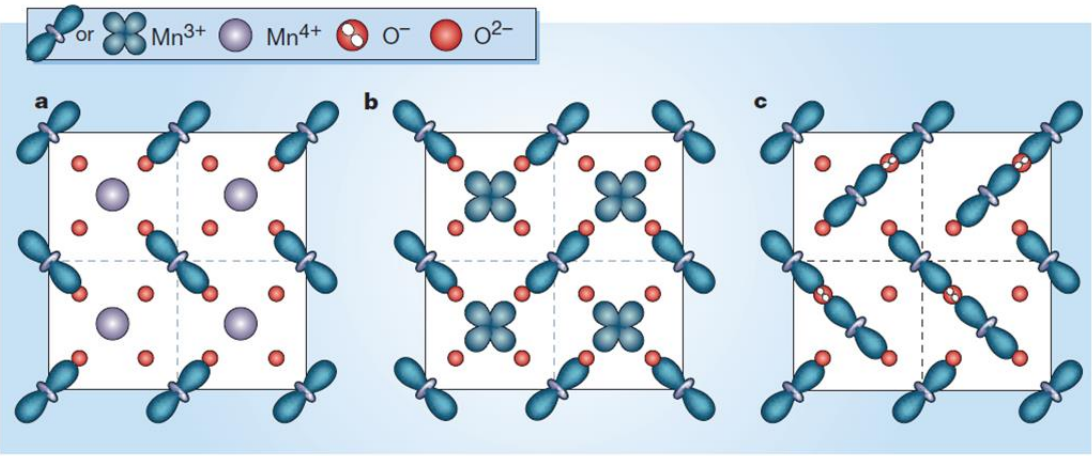

Fig. 1.8: Charge and orbital order of the Mn ions in $La_{0.5}Ca_{0.5}MnO_3$. Figure adapted from [26].

ordering strongly localize the e_g electrons in a commensurate static arrangement and therefore create an insulating ground state. Furthermore, through another indirect exchange mechanism called superexchange [27], both forms of ordering often stabilize an antiferromagnetic order, and thus provide a competing ground state to the double exchange mediated metallic ferromagnetism.

1.3 Phase competition

Section 1.2 outlines only some of the basic physics and interactions found in the perovskites, but it can already be seen that many of these interactions are in direct opposition to each other. A few such instances are the crystal field splitting stabilizing low spin against Hund's exchange favoring high spin, Jahn – Teller distortions that tend to localize e_g electrons working against double exchange that tends to delocalize them, or double exchange promoting a ferromagnetic metallic ground state competing with superexchange and charge/orbital ordering that promote an antiferromagnetic insulating state. In fact, phase competition is a recurring theme commonly found in the perovskites and related oxides and leads to them possessing a multitude of electronic ground states, many of which are separated by extremely small energy differences. As a result, subtle perturbations such as temperature, pressure, magnetic fields, electric fields and biaxial strain are sufficient to drive the system from one state to the other. This manifests itself as the colossal magnetoresistance effect in the manganites [15], spin-state transitions in the cobaltites [28], Mott metal – insulator transitions in the nickelates [29] and superconductor –

insulator transitions in the cuprates [30]. These phenomena make these materials rich playgrounds for physicists and material scientists alike and there is currently tremendous interest in their potential for applications in logic circuits, spintronics and transducers.

A fascinating outcome of the phase competition between localization and delocalization of carriers in the perovskites, abetted in no small part by the quenched potential fluctuations due to disordered dopants, is the phenomenon of magneto – electronic phase separation (MEPS). It refers to the spatial coexistence of multiple magnetic and electronic ground states in materials that otherwise have long range chemical homogeneity. The phenomenon of MEPS has been observed at two different length scales separated by almost three orders of magnitude, and although qualitatively similar, the two have been attributed to different origins [31]. The first kind of MEPS occurs on the nanometer length scale and is the direct outcome of phase competition along with long range Coulomb interactions. The coexisting phases have different electron densities and charge stabilization requirements preclude the formation of larger

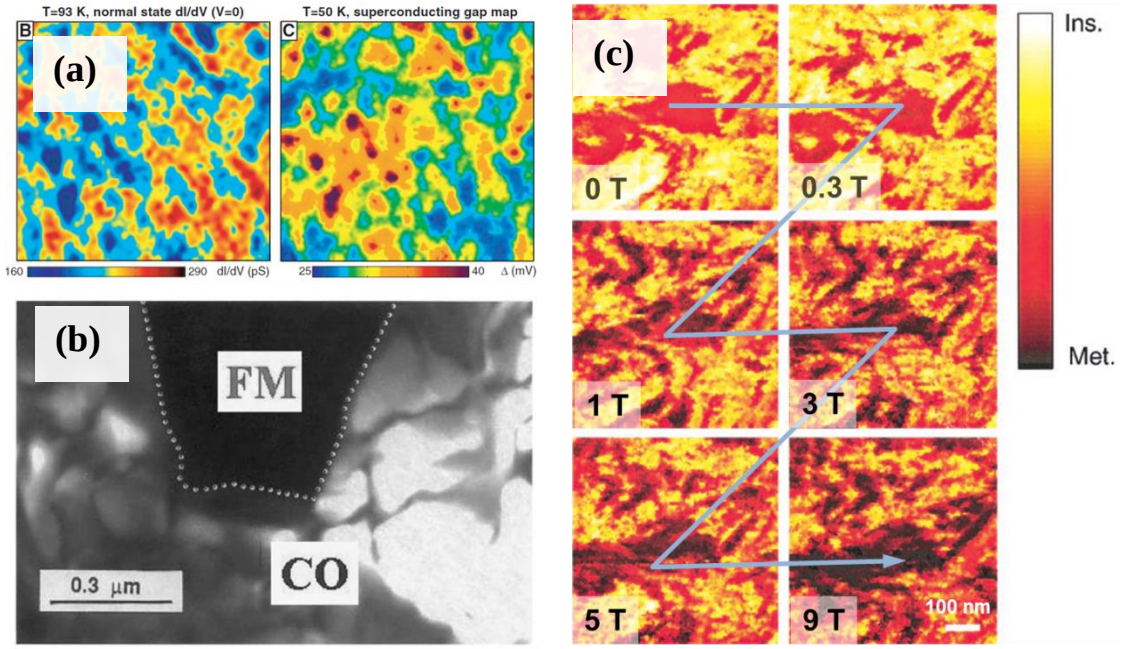

Fig. 1.9: MEPS observed in a variety of oxide materials. (a) Nanoscopic MEPS evident in the patially varying normal state differential conductance and superconducting gap in a $Bi_2Sr_2CaCu_2O_{8+\delta}$ single crystal observed with an STM (scan size 300 Å) [31] (b) Ferromagnetic metallic (FM) and charge ordered insulating (CO) regions observed in $La_{0.25}Pr_{0.375}Ca_{3/8}MnO_3$ observed in dark field TEM. [37] (c) Differential conductance map of a $La_{0.73}Ca_{0.27}MnO_3$ thin film showing MEPS just below the Curie temperature and its subsequent suppression under the influence of a magnetic field. [35]

clusters. Such nanoscopic electronic phase separation has been widely observed in the manganites and the cuprates, an example being Fig. 1.9(a) which shows the electronic inhomogeneity on a 15 – 20 Å length scale in a $Bi_2Sr_2CaCu_2O_{8+\delta}$ single crystal observed with scanning tunneling microscope [32]. The second form of MEPS is on a much longer length scale (submicron to micron) and arises from the presence of quenched chemical disorder. This form of MEPs is most pronounced at first-order phase transitions and can be significantly suppressed by the application of perturbations such as magnetic fields and hydrostatic pressure that drive the system deeper into either of the competing phases – it is the key ingredient behind the colossal magnetoresistance observed in the manganites [15, 31]. A few examples of such disorder driven MEPS is shown in Figs. 1.9(b) and (c). MEPS is the underlying ingredient of many of the fascinating properties of the complex oxides and has been observed in a variety of systems such as the manganites [31], cuprates [33] and cobaltites [34], both in the bulk and in thin films. MEPS in the oxides has been verified experimentally by a number of techniques such as small-angle neutron scattering (SANS) [18], scanning tunneling microscopy (STM) [31, 35], nuclear magnetic resonance (NMR) [36], transmission electron microscopy [37], heat capacity [38] and magneto-transport [39].

1.4 The perovskite cobaltites

The cobaltites are a subset of the perovskites with Co on the *B* site giving the general formula $ACoO_3$. Co (Z = 27) has an electronic configuration [Ar]$4s^2 3d^7$ and belongs to the first row of transition metals. In its bulk metallic form, Co is a ferromagnet with a T_C of 1388 K and a magnetization ~ 1.72 μ_B / Co [40] (The Bohr magneton μ_B is a fundamental unit of magnetic moments and equals the spin magnetic moment of an electron ($1\mu_B = 9.2704 \times 10^{-21}$ emu). In its ionic form Co can take up multiple oxidation states with valences as high as +5, the most stable and commonly occuring states being +2 (CoO, $CoBr_2$, CoS_2) and +3 (Co_2O_3, $LiCoO_2$, $[Co(NH_3)_6]Cl_3$). In the perovskite structure, however, Co is commonly found to be in the 3+ and 4+ states, the latter being highly unstable and difficult to synthesize under atmospheric conditions. One of the most interesting aspects of Co in the perovskite structure is that the crystal field splitting Δ_{CF} and Hund's exchange H_{ex} have very similar magnitudes, with Δ_{CF} being marginally greater. As a result, subtle variations in temperature and pressure are sufficient to trigger spin state transitions in the cobaltites – indeed such transitions are widely observed in

	Low spin	Intermediate spin	High spin
Co^{3+} $[Ar]3d^6$	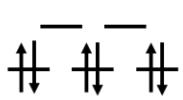 S = 0 $\mu_S = 0$	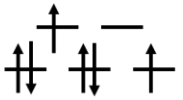 S = 1 $\mu_S = 2\mu_B$	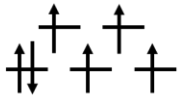 S = 2 $\mu_S = 4\mu_B$
Co^{4+} $[Ar]3d^5$	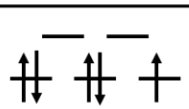 S = 1/2 $\mu_S = 1\mu_B$	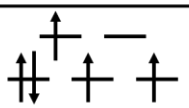 S = 3/2 $\mu_S = 3\mu_B$	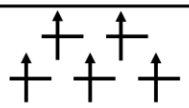 S = 5/2 $\mu_S = 5\mu_B$

Table 1.2: Possible spin states and magnetic moments of Co ions in hole doped perovskites

these materials and are almost considered their signature property. Table 1.2 lists the possible spin states and the associated magnetic moments of Co ions in hole doped perovskites.

As with other perovskites, the electronic and magnetic properties of the cobaltites are predominantly determined by the Co – O – Co network. The *A* site cation however does affect the octahedral tilts and rotations, and since any deviation of the Co – O – Co bond angle from the ideal 180° reduces the e_g electron transfer probability, and thereby the one electron bandwidth of the e_g conduction band. Table 1.3 shows the crystal symmetry and Co – O – Co bond angle for various *A* site cations. It must be noted that Sr is a divalent cation and therefore $SrCoO_3$ has Co in the 4+ valence state whereas the other compounds listed in Table 1.2 have Co^{3+} ions.

	Sr	La	Pr	Nd	Y
Ionic radius	144	136	129	127	119
Symmetry	C	R	O	O	O
Space group	$Pm\bar{3}m$	$R\bar{3}c$	*Pbnm*	*Pbnm*	*Pbnm*
Bond angle	180	163.71(2)	158.3(1)	156.8(3)	148.0(2)

Table 1.3: Room temperature ionic radii (in pm), crystal symmetry, space group and Co – O – Co bond angles (in degrees) for various *A* site cations in the perovskite structure. [6, 41 – 45]

It is evident that a reduction in the *A* site radius distorts the lattice and reduces the symmetry from cubic (C) to rhombohedral (R) to orthorhombic (O), with a commensurate and significant reduction in the Co – O – Co bond angle. Consequently, $SrCoO_3$ is metallic down to the lowest temperatures [41] while the other members of the series are insulating with a metal – insulator transition temperature that scales systematically with cation radius [46]. The focus of the remainder of this dissertation will be the series of large bandwidth cobaltites $(La,Sr)CoO_3$.

1.4.1 $LaCoO_3$

$LaCoO_3$, the parent compound of the $(La,Sr)CoO_3$ series, is the prototypical large bandwidth cobaltite. It has Co in the 3+ state and crystallizes in a distorted perovskite lattice with rhombohedral ($R\bar{3}c$) symmetry at 300K. The rhombohedral distortion is generated *via* cooperative rotation and compression of the CoO_6 octahedra along the [111] axis through displacement of *only* the oxygen ions, and the rhombohedral unit cell is completely described by its edge length a_R (which is related to the undistorted cubic lattice parameter a_C as $a_R = \sqrt{2}a_C$) and its rhombohedral angle α_R (α_R is 60° for a cubic lattice). A rhombohedral cell may also equivalently be represented by a hexagonal cell having parameters a_H and c_H, which are related to the rhombohedral parameters as:

$$a_R = \frac{1}{3}\sqrt{3a_H^2 + c_H^2}$$

$$\alpha_R = 2\sin^{-1}\left(\frac{3}{2\sqrt{3 + (c_H^2/a_H^2)}}\right) \quad (1.4.1)$$

Fig. 1.10 shows the rhombohedral unit cell for $LaCoO_3$ [42] and the variation of the lattice parameters as a function of temperature [47]. It is to be noted that the distortion decreases with increasing temperature and the lattice attains cubic symmetry above 1610 K [48].

The measurement of the bandgap of $LaCoO_3$ has been controversial, with different measurement techniques yielding different results [49]. Nonetheless, $LaCoO_3$ has been reported to have a charge transfer optical gap of ~ 100 – 200 meV and a spin gap (defined as the difference between the crystal field splitting and Hund's exchange) of ~ 10 – 80 meV [49 – 52].

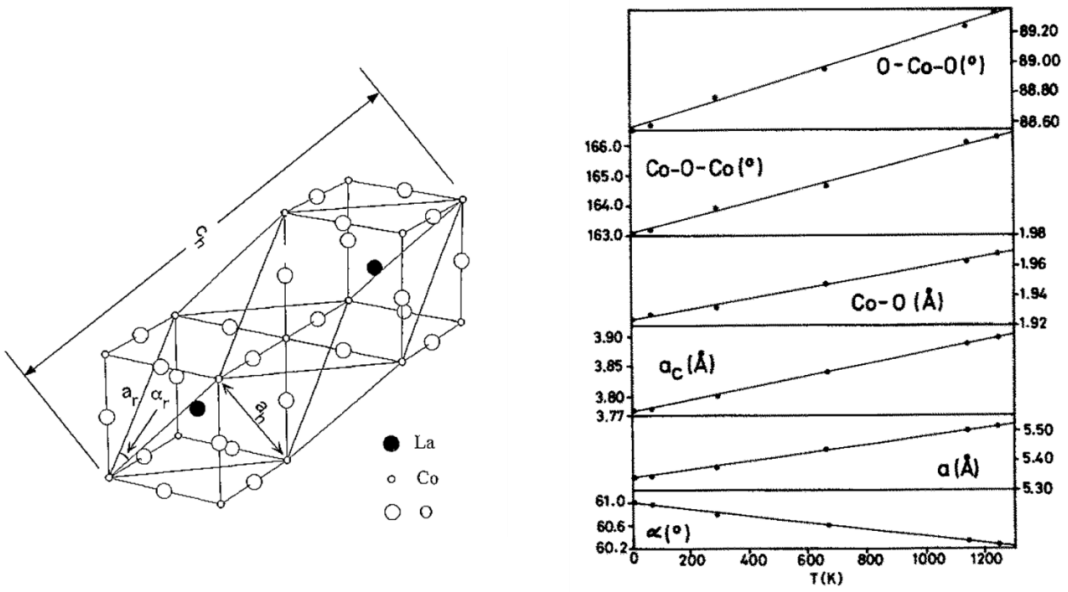

Fig. 1.10: Rhombohedral unit cell and temperature dependent lattice parameters of $LaCoO_3$ [42, 47]

As a result, at 0 K all the Co atoms are in the low spin ($t_{2g}^6 e_g^0$) state and $LaCoO_3$ is a diamagnetic insulator ($\rho > 10^9$ Ωcm) [57]). As the temperature is increased above 30 K, thermal energy promotes some of the t_{2g} electrons to the e_g levels and the Co ions achieve a higher spin state with a magnetic moment. This spin state transition persists over a temperature range between ~ 30 K and 100 K and manifests itself as an increase in the magnetic susceptibility over this temperature range. However, despite the Co ions possessing a magnetic moment above 100 K, there is no long range ordering of the moments and the susceptibility follows a paramagnetic Curie – Weiss behavior with $\theta \sim$ -220 K. Although in the low spin state, $LaCoO_3$ should have a weak diamagnetic response ($\chi < 0$), practical measurements show the presence of a low temperature Curie – Weiss tail. This has been ascribed to local moments from oxygen vacancies [53], surface effects [54] and other impurities that are extrinsic to the sample. Fig. 1.11 shows the temperature dependent magnetic susceptibility of a polycrystalline $LaCoO_3$ sample under a 55 kOe field [53]. Electronically, $LaCoO_3$ behaves as a semiconductor up until 500 K, at which point it undergoes a rather well studied insulator – metal transition (Fig. 1.12 (a)). The high temperature metallic ground state has been attributed to an increase in the number of delocalized carriers and a closing of the charge gap and has been shown to be similar to the case of hole-doping [55]. The insulator – metal transition coincides with a plateau in the magnetic susceptibility while the metallic state once more follows a Curie law, albeit with a different μ_{eff}

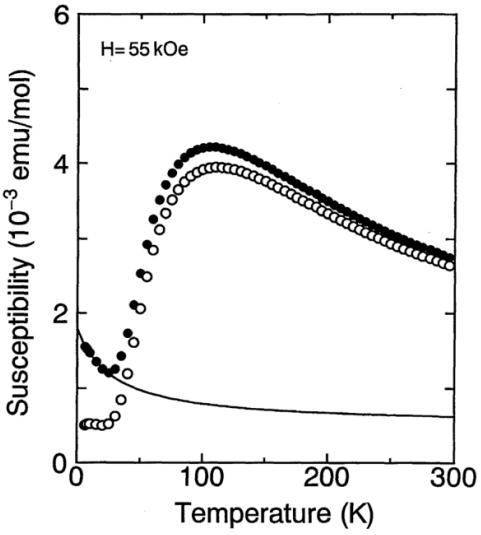

Fig. 1.11: Magnetic susceptibility of polycrystalline $LaCoO_3$ as a function of temperature showing both the raw experimental data (closed circles) and the intrinsic susceptibility after subtracting out the low temperature Curie – Weiss term (open circles). Reproduced from [53]

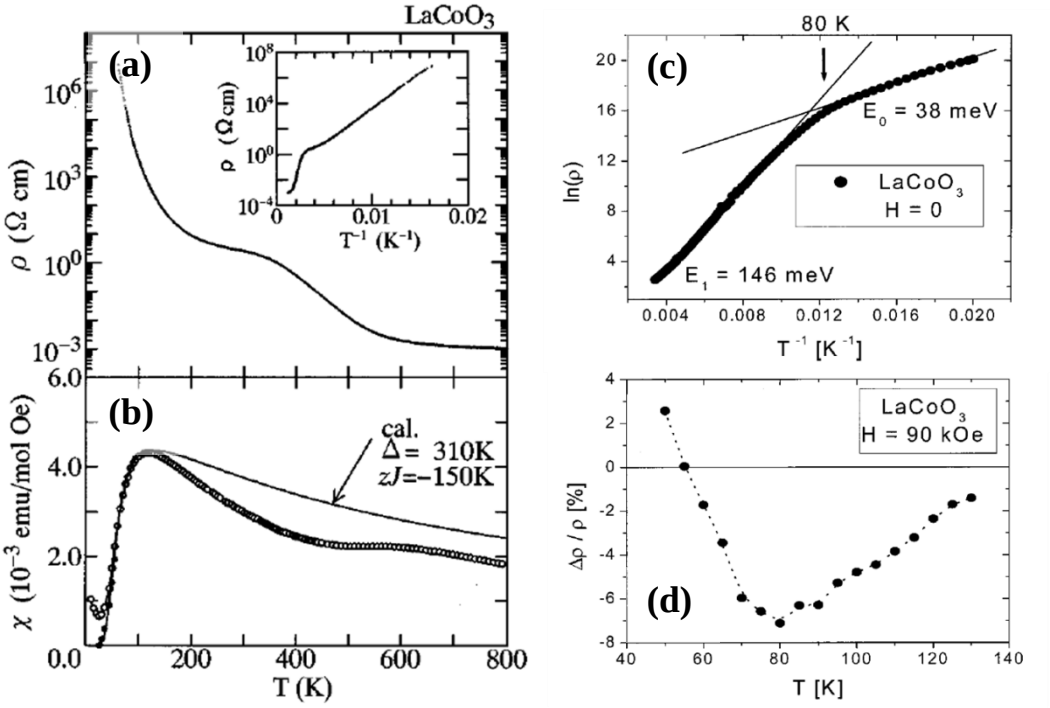

Fig. 1.12: (a) Temperature dependent resistivity of a $LaCoO_3$ single crystal. The inset shows the same data plotted as a function of inverse temperature. (b) Magnetic susceptibility of the same $LaCoO_3$ crystal showing two transitions. Both datasets reproduced from [52] (c) 80 K inflection in a LaCoO3 polycrystalline sample transport data clearly observed when plotted as ln(ρ) vs T^{-1}. (d) Peak at 80 K in 9T magneto-resistance of the same sample. Both datasets reproduced from [56].

(Fig. 1.12 (b)). Although the 30 – 100 K spin state transition, clearly observed in the magnetic susceptibility, is not as pronounced in the resistivity data, it has been correlated with a prominent peak at 80 K in the 9T magnetoresistance and has been attributed to the suppression of the spin disorder scattering by the large field (Fig. 1.12 (b, c)) [56].

Despite such electronic and magnetic behavior being widely observed, there has been much ambiguity about the precise evolution of the Co spin state. It was initially proposed by Raccah and Goodenough that the Co^{3+} ion in $LaCoO_3$ can exist only in two spin states – low spin (LS) and high spin (HS) [58]. The stability of these two spin states over the intermediate spin (IS) state is supported by simple ligand-field analysis. However Asai *et al.* proposed a two spin state transition model on the basis of an anomalous thermal lattice expansion from neutron powder diffraction – an LS to IS transition at 100 K, followed by an IS to HS transition at 500K [57]. However, a number of LDA+*U* and *ab inito* DFT calculations, which better capture the Co e_g – O 2*p* hybridization, then established the stabilization of the IS over the HS and proposed a 100 K crossover from LS to a localized IS, and subsequent delocalization of carriers at 500 K [59, 60]. But now, more recent theoretical work based on the GGA+*U* and LDA+DMFT methods have repostulated the existence of HS Co^{3+} by proposing the coexistence of a mixed LS/HS phase and an IS phase that melts into a metallic phase with IS – like character above 500 K [61 – 63]. A recent experimental study based on infrared and inelastic x-ray spectroscopy too has suggested a complicated spin state disproportionation among LS, IS and HS Co^{3+} [64]. Till date the exact nature of these spin state transitions remains unresolved, although there is increasing consensus that the strong Co – O covalency might invalidate to a certain degree models based on simple atomic states of IS and HS.

1.4.2 $La_{1-x}Sr_xCoO_3$

Introduction of Sr into the $LaCoO_3$ lattice has a profound impact on its properties, both structurally and electronically. The Sr^{2+} being a larger ion than La^{3+} (Table 1.2), it increases the average *A* site radius and thereby the lattice parameter, and simultaneously reduces the rhombohedral distortion. The 300 K rhombohedral $R\bar{3}c$ symmetry changes to a cubic *Pm3m* around $x = 0.5$. This involves the evolution of the rhombohedral angle α_R to 60° and the Co – O – Co bond angle to 180° [42]. Effectively, the Sr doping reduces the rhombohedral – cubic

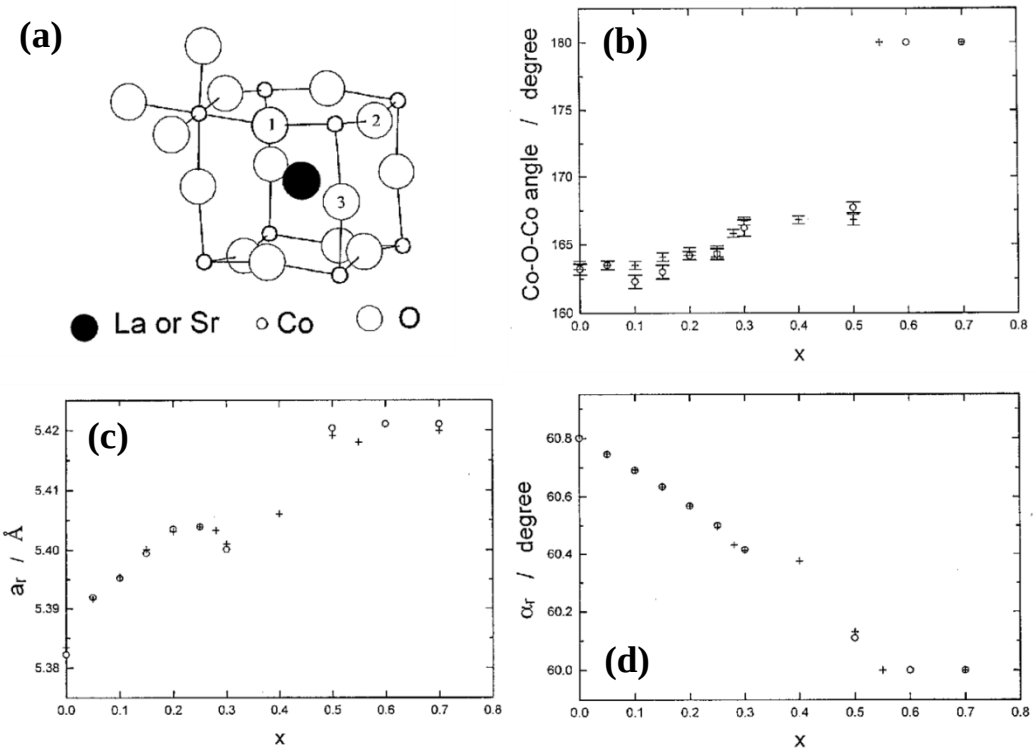

Fig. 1.13: (a) Rhombohedral distortion in $La_{1-x}Sr_xCoO_3$ for $x < 0.5$. (b) Evolution of the structural parameters with doping in $La_{1-x}Sr_xCoO_3$. (O) indicate samples fast cooled at 873 K/hr. while (+) represent samples slow cooled at 42 K/hr. [42].

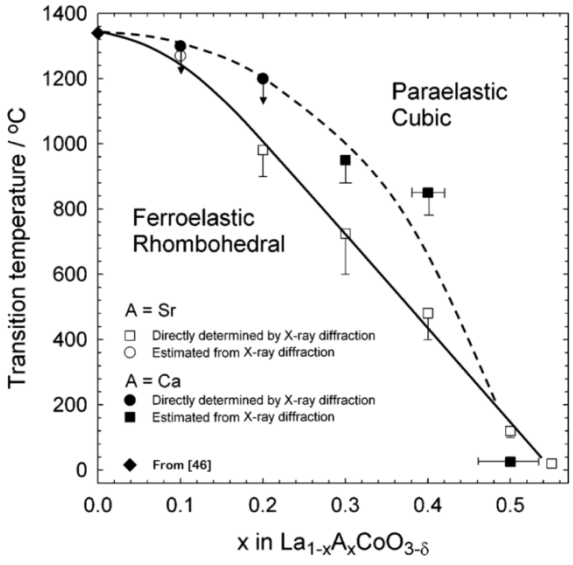

Fig. 1.14: Structural phase diagram of $La_{1-x}Sr_xCoO_3$. The phase diagram of $La_{1-x}Ca_xCoO_3$ is included for comparison [65].

transition temperature from 1610 K in $LaCoO_3$ to far less than 300 K. In the rhombohedral phase, the hexagonal *c* axis lies along the cubic [111] directions, resulting in four equivalent hexagonal domains. This gives rise to a twinned structure and ferroelasticity, both of which disappear in the cubic phase [65]. Fig. 1.13 shows the evolution of the structural parameters of $La_{1-x}Sr_xCoO_3$ (LSCO) with increasing *x* while Fig. 1.14 shows the structural phase diagram. It is to be noted that there is a drastic, almost abrupt change in the structure between $x = 0.2$ and $x = 0.4$ which has been attributed to a change in the band structure as a result of the Sr induced insulator – metal transition [42, 66].

Electronically, the influence of Sr dopants is a bit more complicated. Substitution of trivalent La with divalent Sr oxidizes a commensurate number of Co^{3+} to Co^{4+} and introduces holes into the system. One model that has been postulated is that the Co^{4+}, by virtue of its smaller ionic radius, draws in the neighboring oxygen ions, which in turn closes the spin gap of the neighboring Co^{3+} ions and promotes them to a Jahn – Teller stabilized IS while the Co^{4+} itself remains in LS. Double exchange interactions between IS Co^{3+} and LS Co^{4+} (which only differ by an e_g electron) delocalizes the e_g hole over these seven ions, thereby creating a seven-site magnetic polaron with a large spin quantum number [52, 67 – 70]. In fact Yamaguchi *et al.* have reported numbers as large as S = 10 – 16 for this spin polaron, raising the possibility of a HS ion [52]. It

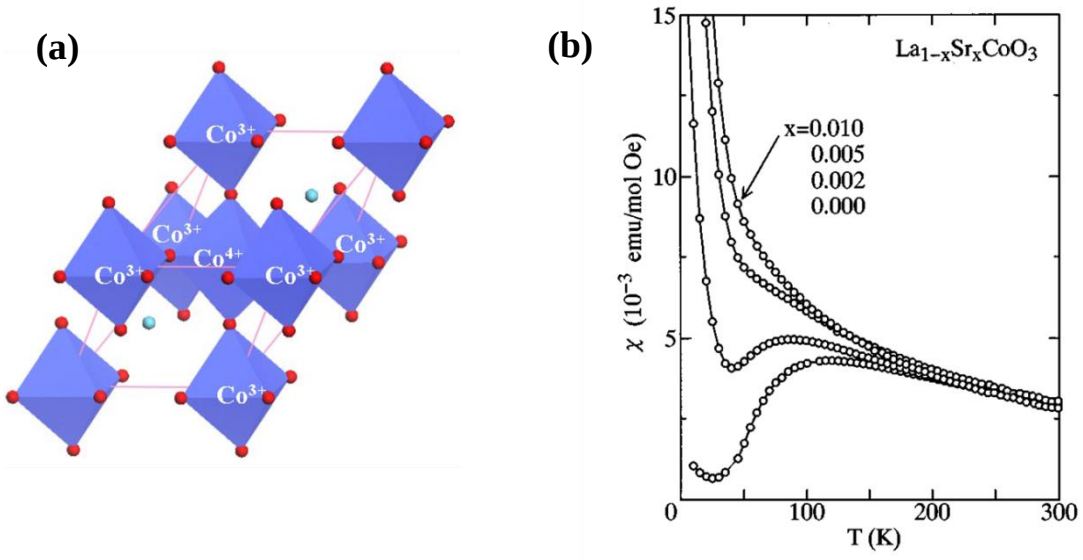

Fig. 1.15: (a) Schematic of the seven site magnetic polaron found in $La_{1-x}Sr_xCoO_3$ under light doping conditions [68] (b) Magnetic susceptibility of lightly doped $La_{1-x}Sr_xCoO_3$ crystals showing the suppression in the low temperature susceptibility drop [52].

is to be noted that due to the large extent of Co – O hybridization the hole exists in a hybridized orbital and has a significant O 2*p* character [129]. Under light doping conditions ($x \lesssim 0.04$) these spin polarons remain isolated and weakly interacting but prominently manifest themselves as a suppression of the low temperature susceptibility drop by the appearance of a paramagnetic contribution below 100 K [52] as well as clear in elastic neutron scattering signatures [69, 70]. It is to be noted that this suppression does *not* imply the complete disappearance of the spin state transition – the LS ions in the unperturbed region still undergo the crossover. Rather their weak magnetic signal is simply swamped by the larger magnetic moments of the IS ions. Fig. 1.15 shows a schematic of this seven-site magnetic polaron [68] and its effect on the susceptibility of lightly doped compounds [52]. An alternative picture forwarded by Nagaev and Podel'shchikov proposes the presence of disordered low frequency magnetoexcitons and the self-trapping of carriers by the hole – exciton complex [71]. Qualitatively similar to the spin polaron model, the magnetoexcitons too separate the material into ferromagnetic metallic and non-ferromagnetic insulating regions, with percolation setting in above a critical dopant density.

As the Sr doping exceeds a critical value of ~ 0.04, the polaron density becomes high enough for neighboring polarons to merge together and form hole-rich short-range ferromagnetic (FM) clusters. These clusters reside in a hole-poor non-FM insulating matrix that still contains isolated spin polarons and a mixture of IS Co^{3+}/LS Co^{4+}. It must be noted that the persistence of an insulating matrix at these doping values, despite the prediction of the onset of percolation by simple density arguments, has been postulated to be due to the fluctuations of the polaron spins on time scales shorter than those of electronic transport [72]. Such magneto-electronic phase separation (MEPS) into FM clusters – non-FM matrix has been verified independently by small angle neutron scattering (SANS) [18, 38], nuclear magnetic resonance (NMR) [36, 73 – 75], inelastic neutron scattering (INS) [68, 76], and electron spin resonance (ESR) [69]. The intercluster interactions are predominantly FM while there are antiferromagnetic (AF) interactions in the matrix (between the isolated HS/IS polarons) [70], with weak and locally frustrated interactions between the clusters and the matrix [77]. Such competing magnetic interactions lead to cluster glass behavior in this MEPS regime, with clear signatures in magnetometry [78], transport [79, 80] and heat capacity [38]. A particular signature of the MEPS in transport is the presence of an intercluster giant magnetoresistance effect (IGMR) [39]. Ordinarily, a long range ordered ferromagnetic metal exhibits anisotropic magnetoresistance (AMR), where the magnetoresistance (MR) changes sign with change in

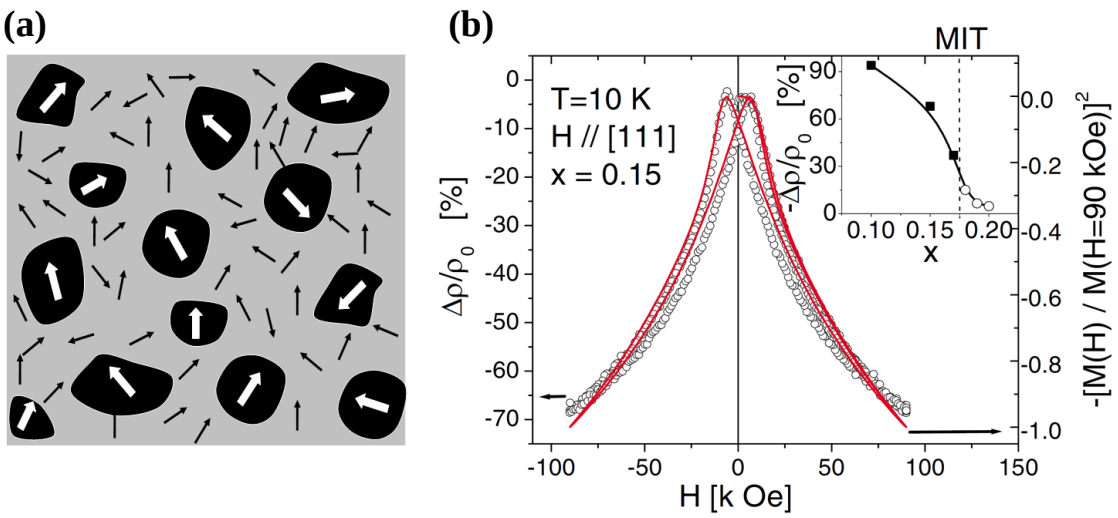

Fig. 1.16: (a) Illustration of the spin disordered clustered state in magneto-electronically phase separated LSCO. (b) Intergranular giant magnetoresistance in an x = 0.15 single crystal showing the large high field negative MR in such materials. The inset shows the evolution of the negative MR with doping [39].

angle between the current flow and the applied field [81]. In phase separated LSCO with isolated FM clusters, however, electron transport is through intercluster hopping and is maximized when the spins of all clusters are aligned parallel to each other and is minimized when the spins are randomized. This results in a large isotropic high field negative magnetoresistance which is similar to the giant magnetoresistance (GMR) effect seen in artificially engineered multilayers and granular metals [82 – 86]. Fig. 1.16 illustrates the spin disordered clustered state of MEPS LSCO and shows an example of the IGMR effect in an x = 0.15 single crystal [39].

With increasing x the clusters show a modest increase in size, from ~ 6 – 8 Å (~ 2 unit cells) at x = 0.05 to ~ 20 – 25 Å (~ 6 unit cells) at x = 0.15 [15]. However, there is a significant increase in their density and at a critical value of x = 0.18, there is sufficient overlap between neighboring clusters for them to form a percolative network throughout the material. At this point, *despite remaining magnetically and electronically phase separated*, LSCO undergoes an insulator – metal transition and starts behaving as a ferromagnetic metal. MEPS in this metallic phase has been independently verified by SANS [15] and NMR [67, 79]. The MEPS persists until $x \cong$ 0.22, at which point the material transforms into a homogenous metallic ferromagnet. Statistical simulations by He *et al.* [18] have established the origin of this MEPS to nanoscale dopant fluctuations arising from a random dopant distribution in the host lattice, and their simulated

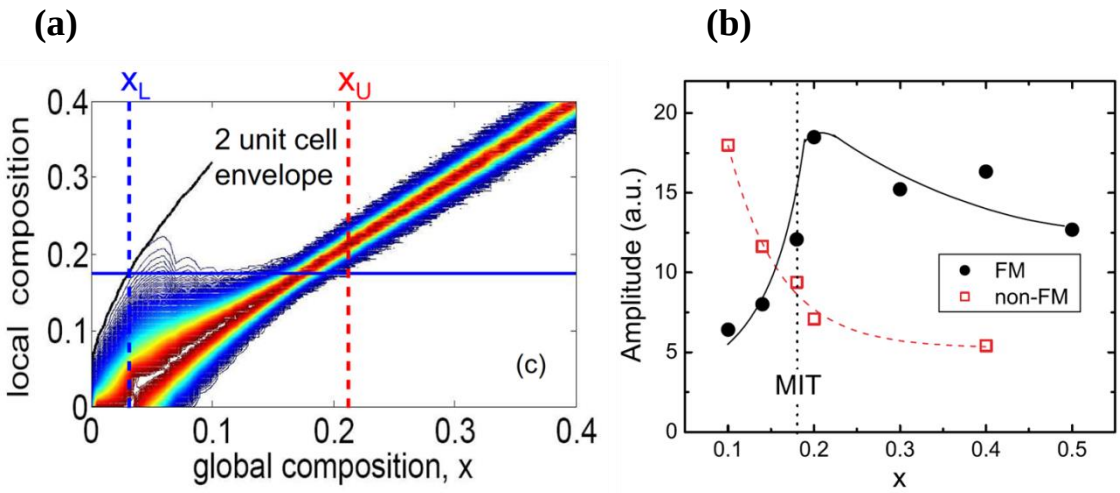

Fig. 1.17: (a) Statistical simulation results showing local composition fluctuations and the upper and lower bounds of MEPS in LSCO [18]. (b) Integrated areas of ^{59}Co NMR spectra showing the evolution of FM and non-FM phase in polycrystalline LSCO with doping [36].

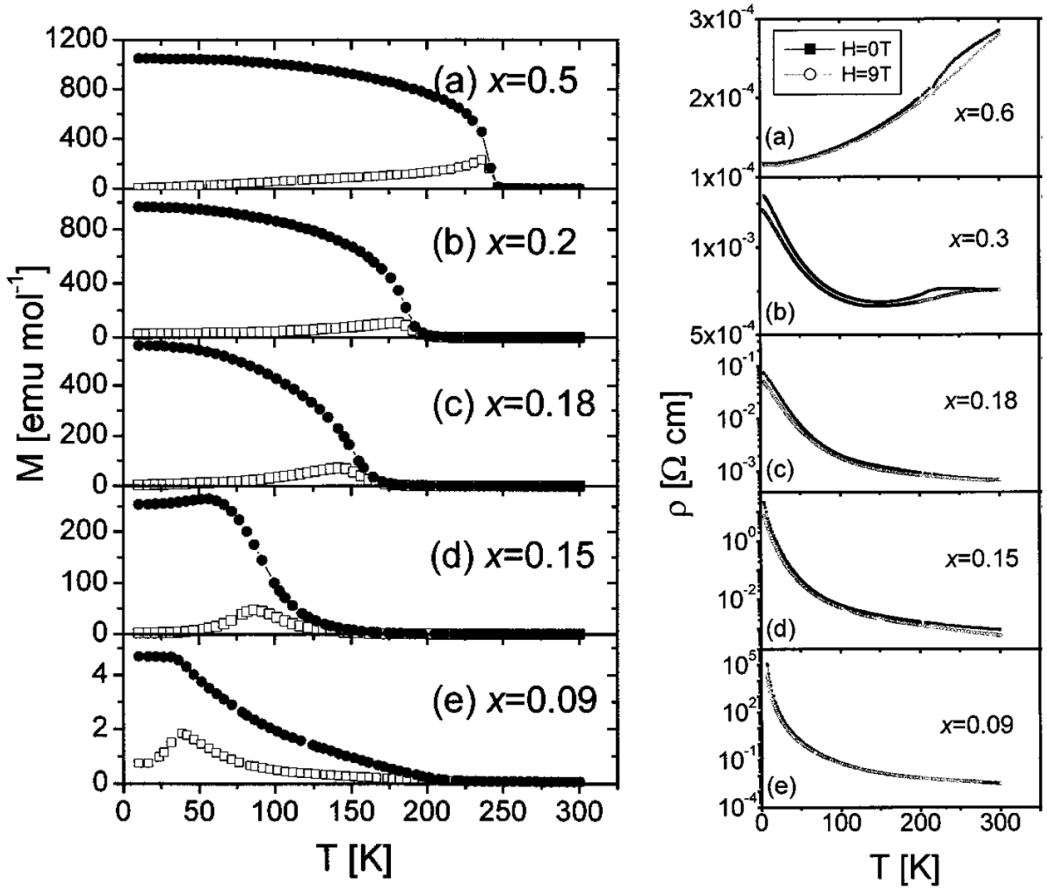

Fig. 1.18: Magnetization and resistivity as a function of temperature for representative doping values of polycrystalline LSCO [78]

upper and lower bounds for the existence of MEPS are in good agreement with experimental values (Fig. 1.17 (a)). Beyond $x \cong 0.22$, the high carrier density overcomes local doping disorder and creates a long range homogenous electronic and magnetic ground state. Although signatures of non-FM insulating regions have been detected at these doping values by ^{59}Co NMR (Fig. 1.17 (b)) [36], it must be stressed that these measurements were on polycrystalline samples and the signals are likely from non-stoichiometry at the grain boundaries. Single crystals do not show this effect. Addition of thermal energy tends to destabilize the low temperature FM ground state described above and the highest T_C for the LSCO system is ~ 250 K at $x = 0.5$ (although a T_C of 305 K has been reported for $SrCoO_3$ single crystals prepared under special oxygenation conditions [41]). With increasing temperature, the long range FM breaks up into short range FM clusters,and finally the material evolves into a homogenous paramagnetic ground state. Fig. 1.18 shows the temperature dependent magnetism and transport behavior at representative doping values of LSCO [78].

Based on the above experimental data, a doping – temperature phase diagram may be constructed that captures the essential features of LSCO behavior. Fig. 1.19 shows a comprehensive phase diagram extending well into the FM doping range and constructed on the basis of magnetometry, transport and SANS measurements [88], while Fig. 1.20 shows a complementary phase diagram constructed independently on the basis of ^{139}La NMR measurements and focusing on the polaronic and phase separated behavior at the low end of the LSCO doping spectrum [87]. It must be mentioned that the reentrant spin glass behavior depicted in Fig. 1.20 is not unequivocally proven by the linear interpolation between two data points. It is likely that the glassy region transitions to a long range ferromagnet at ~ 0.22, consistent with Fig. 1.19. Further, it must also be pointed out that most phase diagrams extend up to $x \sim 0.5$ since beyond this range the Co^{4+} instability results in large oxygen non-stoichiometry and oxygen-sufficient phase-pure compounds with high x may only be synthesized under special oxygenation conditions such as high pressure oxygen annealing [41] or electrochemical oxidation [89].

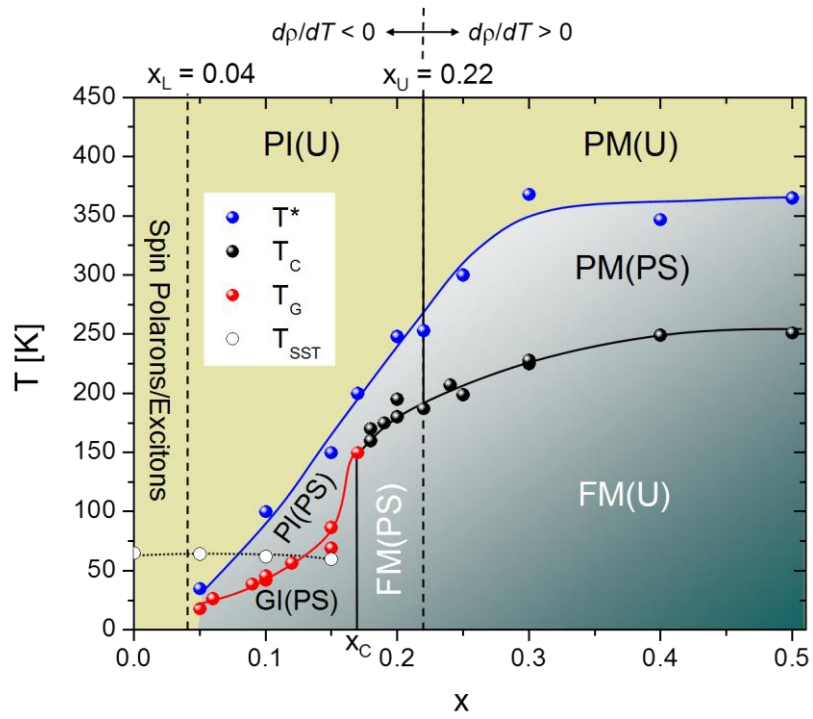

Fig. 1.19: LSCO phase diagram based on magnetometry, transport and SANS. Key: GI – Glassy insulator, PI – Paramagnetic insulator, PM – Paramagnetic metal, FM – Ferromagnetic metal, PS – Phase separated, U – Uniform, T_{SST} – Spin state transition temperature, T_G – Spin-glass transition temperature, T_C – Curie temperature, T* - Cluster formation temperature [88].

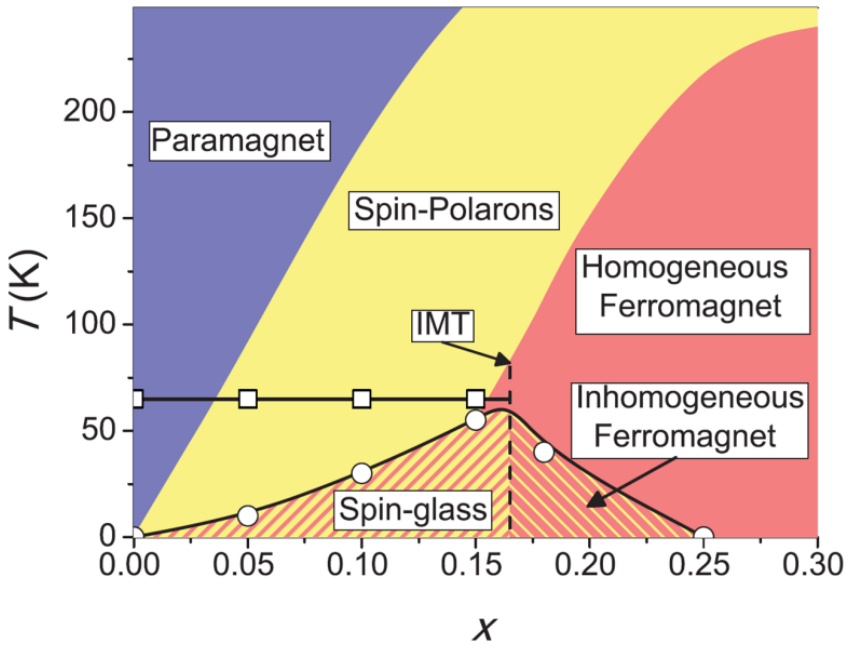

Fig. 1.20: LSCO phase diagram constructed on the basis of ^{139}La NMR measurements [87]

1.5 The brownmillerite structure

A crystal structure that is of particular significance to LSCO, and the cobaltites in general, is the brownmillerite structure, named after the mineral Brownmillerite ($Ca_2(Al,Fe)_2O_5$), a major component of Portland cement. The brownmillerite compounds are essentially oxygen deficient perovskites with the generic formula $A_2B_2O_5$ (or equivalently $ABO_{2.5}$), but are distinguished by the fact that the oxygen vacancies form ordered arrays rather than being randomly distributed. The brownmillerites are not unique in such ordering – they belong to the larger family of ordered oxygen-deficient perovskites having the generic formula $A_nB_nO_{3n-1}$. Oxygen vacancy ordering (OVO) has been seen in compounds with n = 5, 4, 3, 2, 1.5, 1.33 and 1, effectively perovskites with oxygen contents 2.80, 2.75, 2.67, 2.50, 2.33, 2.25 and 2.00 [90] (the stoichiometric perovskite has $n = \infty$). Compounds that are known to crystallize in a brownmillerite structure include $La_2Co_2O_5$ (under special reducing conditions) [91], $LaSrCoFeO_5$ (through partial reduction of the parent perovskite) [92], $Sr_2Co_2O_5$ [93], Sr_2CoFeO_5 [94], and $Sr_2Fe_2O_5$ [95]. LSCO, in the bulk, generally does not form the brownmillerite phase under atmospheric conditions except at very high Sr doping [96]; in thin films, however, the brownmillerite structure is often encountered as an outcome of epitaxial strain, a point that will be discussed in more detail in Section 1.6.

The brownmillerite structure is derived from the parent perovskite lattice by creating rows of oxygen vacancies along the $[110]_P$ direction in every alternate $(001)_P$ plane (the subscript P refers to directions referring to the cubic perovskite cell). With the (001) layering of the perovskite structure being $-AO-BO_2-AO-BO_2-$, the vacancies are created in alternate BO_2 planes, resulting in alternating oxygen-sufficient and oxygen-deficient BO_2 planes, with octahedral (**O**) and tetrahedral (**T**) coordinations respectively. The stacking sequence in a brownmillerite is thus $-AO-BO-AO-BO_2-$. The vacancy lines are staggered along the [001] direction, resulting in two kinds of tetrahedral planes and a tetragonal brownmillerite unit cell with dimensions:

$$a_{BM} = b_{BM} = \sqrt{2}a_P \qquad c_{BM} = 4a_P \tag{1.5.1}$$

The brownmillerite unit cell is rotated by 45° with respect to the perovskite cell, thus $[100]_{BM} \parallel [110]_P$.

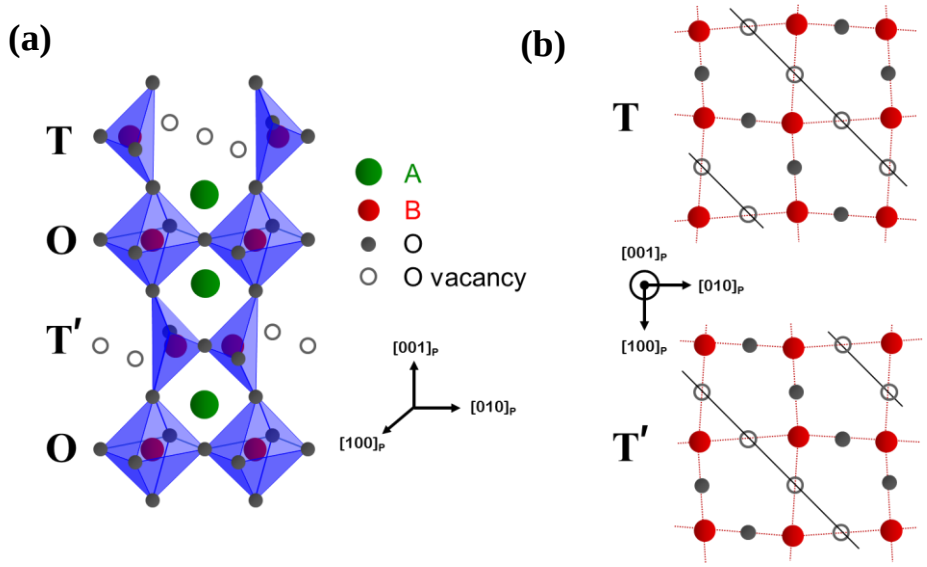

Fig. 1.21: Schematic illustrations of (a) the brownmillerite unit cell, and (b) the two types of oxygen deficient tetrahedral planes. O – octahedral plane, T and T' – tetrahedral planes.

Fig. 1.21 (a) shows the brownmillerite unit cell with the **T** – **O** – **T′** – **O** stacking. The two tetrahedral planes **T** and **T′** are equivalent and simply staggered laterally by one unit cell. Fig. 1.21 (b) shows the atomic layout of the **T** and **T′** planes looking along the $[001]_P$ zone axis, with the oxygen vacancies running along the $(110)_P$ direction. The tetrahedral coordination of the *B* ions results in a loss of their centrosymmetry and their arrangement in a zigzag chain along the $[100]_P$ and $[010]_P$ directions. This has a significant impact on the image created by a brownmillerite in a transmission electron microscope (TEM), since an electron beam fired along either the $[100]_P$ or $[010]_P$ zone axes suffers from a dechanneling effect [97] which, along with the fact that the *A*O planes are displaced away from the **T**, **T′** and towards the **O** planes, results in a significant electron micrograph contrast between the oxygen-sufficient and oxygen-deficient planes, the former appearing far brighter than the latter. As a result, high resolution TEM (HRTEM) has become an invaluable tool in detecting the presence of brownmillerite and other ordered oxygen vacancy phases in perovskite materials. Fig. 1.22 shows an example of the oxygen vacancy ordering in a brownmillerite-like sample of $SrCoO_{3-\delta}$ resulting in alternating bright and dark columns in a high resolution *Z*-contrast TEM [97].

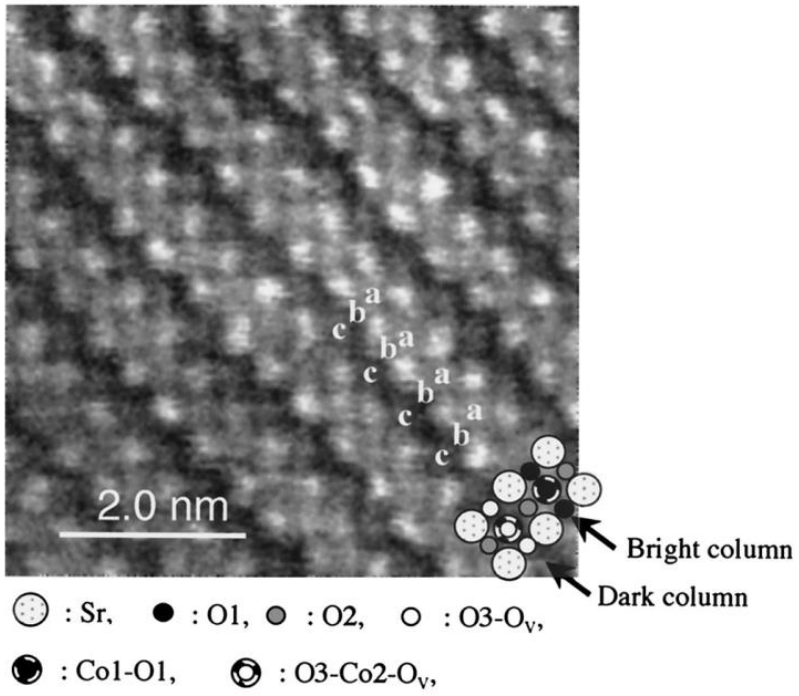

Fig. 1.22: Oxygen vacancy ordering in a brownmillerite-like sample of $SrCoO_{3-\delta}$ seen in high resolution *Z*-contrast TEM. Image is looking along the $[010]_P$ zone axis. [97].

1.6 $La_{1-x}Sr_xCoO_3$ thin films

Thin films are the building blocks of all electronic devices – be they transistors, semiconductor LASERs, CCD sensors or magnetic read/write heads in hard disk drives. Functional thin films range from tens of Angstroms to several microns, and allow utilization of small length scale phenomena, such as tunneling and quantum confinement, as well as manipulation of material properties on similarly short length scales. A high density of interfaces and the proximity of surfaces often results in thin films and heterostructures exhibiting properties not seen in the bulk, a classic example being the GMR effect seen in magnetic multilayers. Furthermore, thin films enable the integration of materials with different functionalities, leading to the potential creation of multifunctional materials such as multiferroics and other transducers. This latter application is of particular significance to the perovskites – the availability of materials with vastly different properties (Fig. 1.3) but nearly identical crystal structures creates an ideal platform for the seamless integration of multiple materials. Thin films are also crucial to the fundamental study of materials, since they offer to physicists, chemists and material scientists

alike a rich playground of conditions not achievable in the bulk, such as dimensional confinement, extreme biaxial stresses, and the proximity of interfaces and surfaces. Thin films are thus of paramount importance for both technological applications as well as fundamental science, and there has thus been a constant endeavor to create thin films of any material that shows interesting and useful properties in the bulk.

The mixed ionic conductivity (charge transport through both electrons and mobile oxygen ions) of LSCO [98] makes it an excellent cathode material for redox reactions and much of the initial work on LSCO thin films was focused on its application as a cathode in solid oxide fuel cells (SOFCs) [99], electrocatalysis [100], gas sensors [101, 102] and oxygen separation membranes [103]. Most of this initial work prepared LSCO films by wet chemical routes, such as the sol-gel process [103, 104], inorganic synthesis [100] or simply drying and sintering of pastes and slurries [101, 102]. These films were all coarse-grained, polycrystalline and several microns thick – they were essentially bulk-like but with smaller dimensions. The discovery of high-T_C superconductors in 1986 spurred the development of epitaxial oxide film deposition techniques such as pulsed laser deposition (PLD) [105] and reactive sputtering [106] and promoted the commercial availability of high quality crystalline substrates such as $SrTiO_3$ and $LaAlO_3$. Although a number of groups have since reported the synthesis of high quality epitaxial oxide films by molecular beam epitaxy (MBE) [107, 108] and even the sol-gel route [109], PLD and sputtering have been the primary epitaxial oxide film deposition techniques over the last 25 years.

The first results on epitaxial LSCO appeared in 1993, with independent reports of LSCO films on $SrTiO_3$ (001) and MgO (100) by Cheung *et al.* [110], on MgO (100) by Cillessen *et al.* [111], and as part of a LSCO/PLZT/LSCO stack on $LaAlO_3$ (001) by Ghonge *et al.* [112]. Subsequent systematic studies by different groups using a variety of deposition techniques all arrived at similar growth windows for LSCO films – a substrate temperature in the range 500 – 700 °C, an oxygen partial pressure in the range 10 – 300 mTorr during deposition, and post deposition cooling in 500 – 760 Torr oxygen [114 – 120]. It was unanimously agreed, and explicitly verified through positron lifetime spectroscopy [121], that LSCO thin films are extremely susceptible to oxygen vacancies, much more so than the bulk; carefully tuned oxygen conditions, both during and post growth, are thus critical to good transport and magnetic behavior. However, despite the best optimization efforts and routine reports of films with

excellent structural quality, the electronic properties never quite reached bulk-like values. The resistivities were consistently higher and Curie temperatures consistently lower. This deviation from the bulk was severely exacerbated in the ultrathin film limit (below ~ 100 Å) – this could not be accounted for simply as a dimensional effect [122, 123]. Through careful magnetometry and magnetotransport measurements, this was instead attributed to strain effects [123] and possible MEPS [119, 122], although the relation between the two was not quite clear. Fig. 1.23 summarizes the transport and magnetic properties of LSCO thin films *vis-à-vis* the bulk.

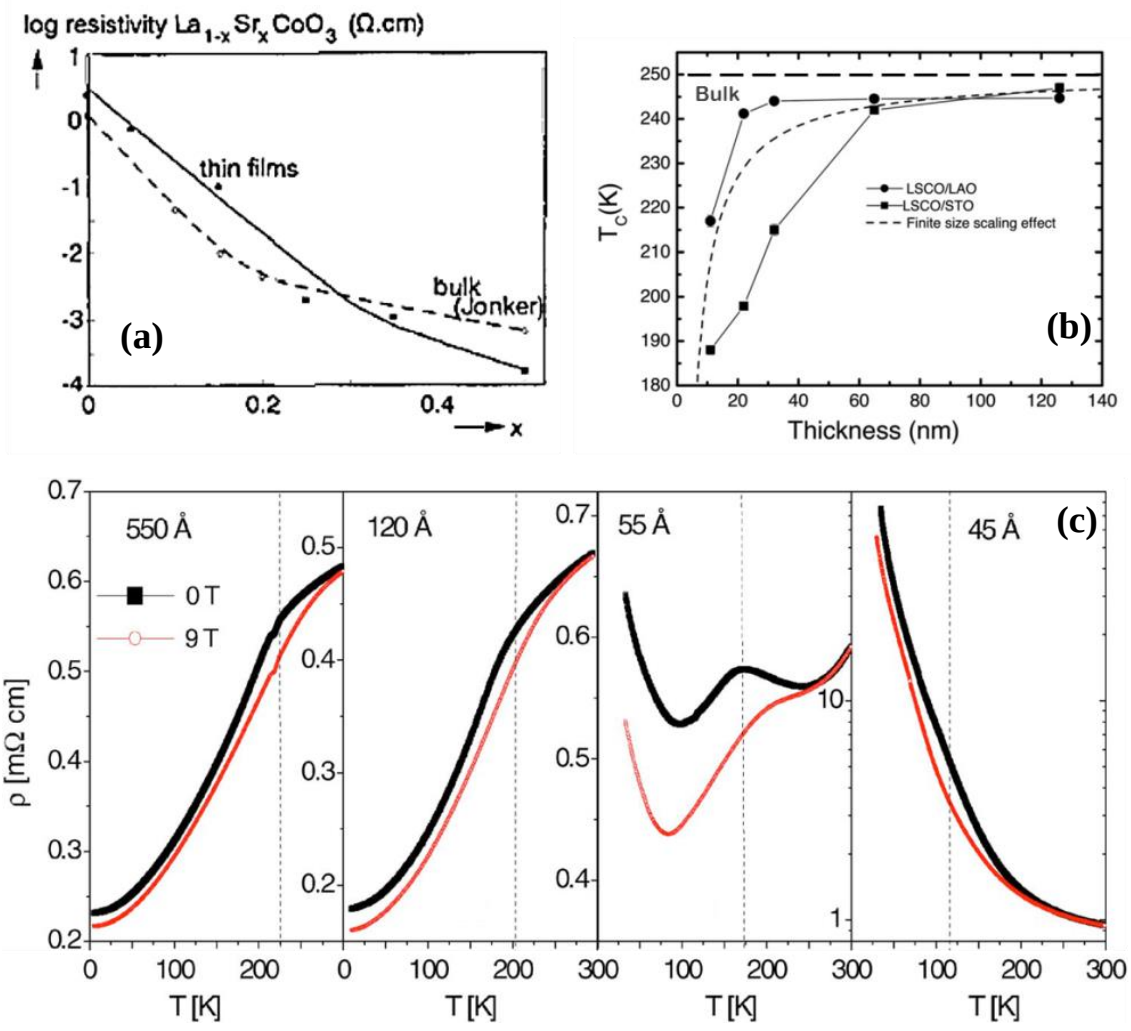

Fig. 1.23: (a) 300 K resistivity of LSCO films on MgO (100) substrates as a function of Sr content compared to bulk resistivities from Ref. 113 [111]. (b) Thickness dependence of the ferromagnetic T_C of $La_{0.5}Sr_{0.5}CoO_3$ films and its deviation from the 250 K bulk value [123]. (c) Thickness evolution of transport of $La_{0.5}Sr_{0.5}CoO_3$ films on $SrTiO_3$ (001) substrates from metallic behavior at 550 Å to insulating behavior at 45 Å [119].

Interestingly, a fascinating phenomenon was observed in epitaxial LSCO films right from the beginning – Cillessen *et al.* [111], Ghonge *et al.* [112], and Wang and Zhang [114] all reported the presence of an ordered superstructure with a doubled unit cell in their films (Fig. 1.24), strikingly similar to the OVO seen many years later in $SrCoO_{3-\delta}$ (Fig. 1.22). None of the groups however suggested an intrinsic OVO in their films, instead attributing their observed superstructure to cation-ordering [111, 114] and to TEM sample preparation induced vacancy diffusion effects [112]. All three groups observed the superstructure with HRTEM, but none could detect it with high-resolution x-ray diffraction. Wang and Zhang reported tetragonal superstructure domains on the order of 30 – 200 nm [114]. Although Wang and Yin, in a later study, did correlate the superstructure to the presence of oxygen vacancies, they attributed the actual structure to anion vacancy induced cation ordering [124].

Stemmer *et al.* were the first to suggest the presence of an ordered oxygen vacancy array in their $La_{0.5}Sr_{0.5}CoO_{3-\delta}$ films on $LaAlO_3$ (001) [125]. They observed three orthogonal domain variants in HRTEM – the modulation vector of these variants pointed along the <001> directions with two of them being visible when imaged along the [100] or [010] zone axes. High temperature annealing suppressed the formation of multiple variants and resulted in a single domain with the modulation vector normal to the substrate surface. This, along with a careful study of Co $L_{2,3}$ electron energy loss spectroscopy (EELS) spectra and multislice HRTEM image simulations,

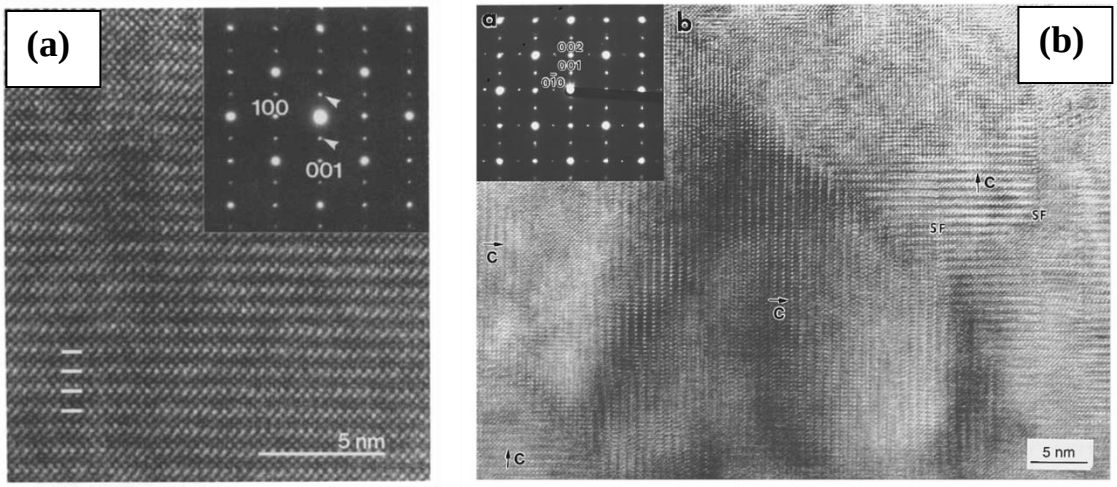

Fig. 1.24: (a) Ordered superstructure with a doubled unit cell observed by high resolution TEM in a $La_{0.5}Sr_{0.5}CoO_3$ film on a MgO (100) substrate [111]. (b) Tetragonal domain structure in a $La_{0.5}Sr_{0.5}CoO_3$ film on a $LaAlO_3$ (001) substrate, looking along the [100] zone axis [114].

led them to conclude the presence of a brownmillerite-like structure over short length scales. A subsequent paper by Klenov *et al.* linked this brownmillerite structure to epitaxial strain [126]. Using $La_{0.5}Sr_{0.5}CoO_{3-\delta}$ films on $SrTiO_3$ (001) and $LaAlO_3$ (001) substrates, they studied the elastic strain energies due to lattice mismatch between the substrate and the film, both with the cubic perovskite and brownmillerite structures, and concluded that lattice expansion through OVO was a favorable means to accommodate epitaxial strain, being considerably less energetically expensive than the formation of misfit dislocations in the cubic lattice. They found the OVO direction to depend on the sign of the strain (tensile *vs.* compressive) and suggested a brownmillerite cell with the long axis parallel to the substrate on $SrTiO_3$ (001) and perpendicular to it on $LaAlO_3$ (001) (Fig. 1.25). Their arguments, though not backed by rigorous theory due to a lack of known material enthalpy values, were in qualitative agreement with experimental observations. Although Choi *et al.* disputed the presence of OVO and suggested a nanoscale monoclinic distortion of the lattice to account for the superstructure in their $LaCoO_3$ films [127], the presence of ordered oxygen vacancies was confirmed by Gazquez *et al.* [128]. They correlated the superstructure of dark and bright stripes to a periodic modulation in the O *K*-edge EELS intensity (dark stripes corresponded to lower intensity, suggesting O vacancies) and a commensurate modulation of the Co spin state – O deficient planes contained HS Co while oxygenated planes contained LS Co, in agreement with the fact that tetrahedrally coordinated Co always favors HS while octahedral Co is subject to strong

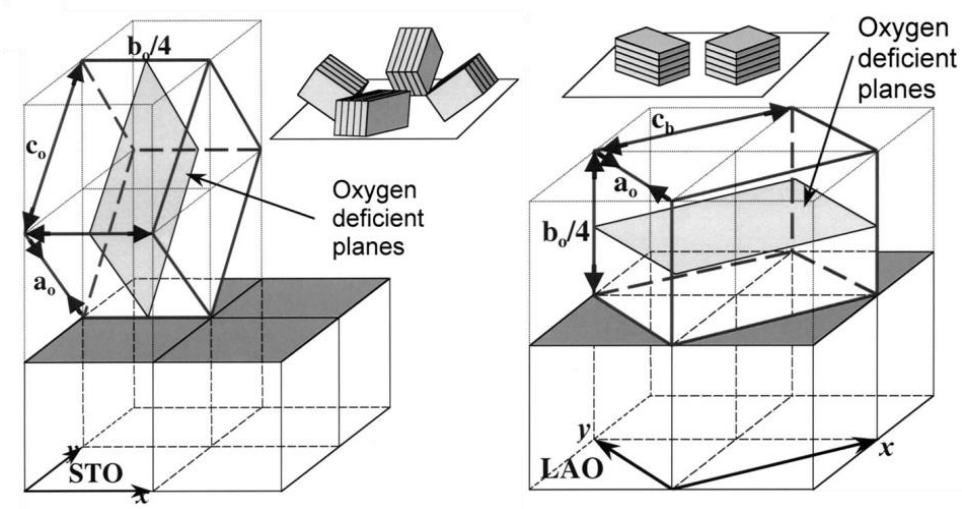

Fig. 1.25: Possible orientations of the brownmillerite unit cell in $La_{0.5}Sr_{0.5}CoO_{3-\delta}$ films on $SrTiO_3$ (001) and $LaAlO_3$ (001) substrates. a_o, b_o, c_o refer to the orthorhombic brownmillerite cell parameters. Note that b_o in this figure is the brownmillerite long axis and is equivalent to c_{BM} defined in Eq. 1.5.1. Adapted from [126].

crystal field splitting and can be stabilized in a LS state. Both facts unequivocally pointed towards a brownmillerite structure.

The crucial link between this OVO superstructure and the electronic properties of the films was provided by Torija *et al.* [129]. A combination of transport, magnetometry, magnetotransport and small-angle neutron scattering (SANS) established the presence of a MEPS region near the interface of $La_{1-x}Sr_xCoO_{3-\delta}$ films with the $SrTiO_3$ (001) substrate. This interfacial MEPS resulted in a magnetic and electronic "dead layer" that exhibited suppressed magnetization and conductivity and extended up to ~ 80 Å in $La_{0.5}Sr_{0.5}CoO_{3-\delta}$ and ~ 600 Å in $La_{0.78}Sr_{0.22}CoO_{3-\delta}$ – the "dead layer" thickness quickly decreased with increasing Sr content. Their key finding however was the origin of this MEPS "dead layer". Using a combination of high resolution *Z*-contrast scanning TEM and EELS, they mapped out a depth profile of the carrier (hole) concentration as well as Sr and O contents in their $La_{0.5}Sr_{0.5}CoO_{3-\delta}$ film (Fig. 1.26). Astoundingly, they found their film to be severely depleted of carriers *and* oxygen near the

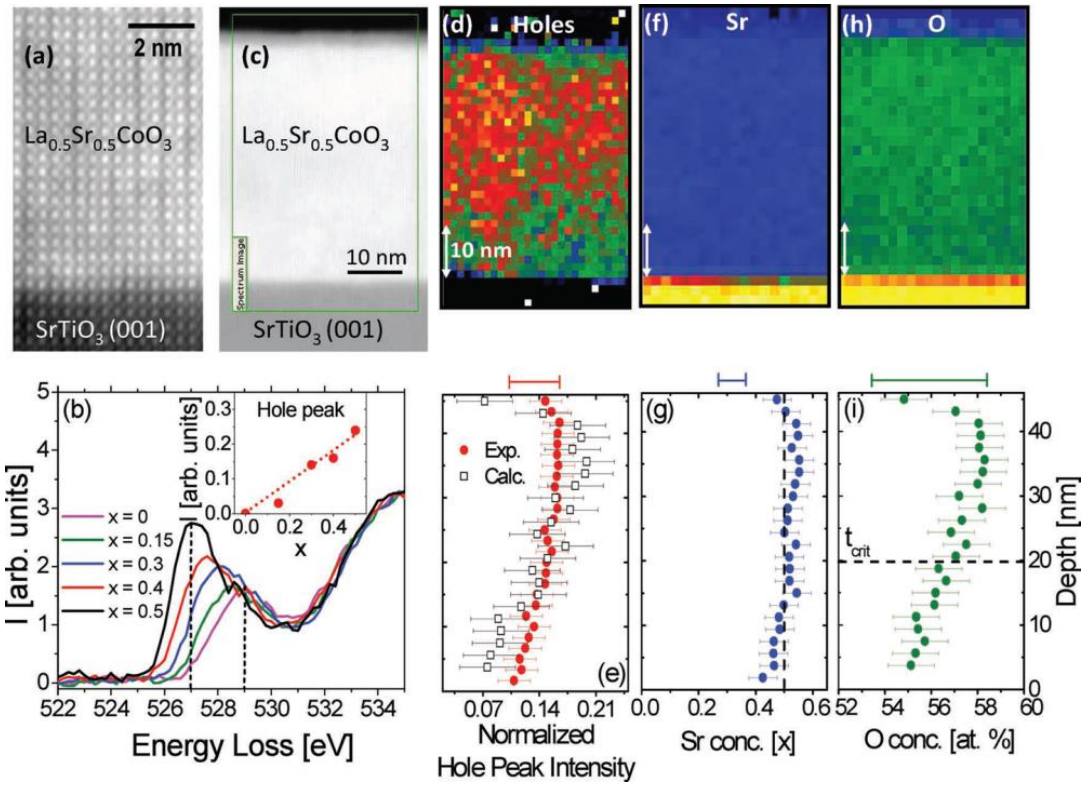

Fig. 1.26: High resolution *Z*-contrast scanning TEM and EELS mapping of a $La_{0.5}Sr_{0.5}CoO_{3-\delta}$ film on $SrTiO_3$ (001) showing the OVO superstructure and the concomitant O and hole depletion near the interface [129].

interface – so much so that their nominally $x = 0.5$ films effectively had a doping of $x = 0.23$ at the interface. This number, being on the cusp of the clustered to long-range transition in the bulk phase diagram (Fig. 1.19), explains the presence of MEPS. Even more fascinating was the fact that this carrier depletion could be explained *solely* by their oxygen deficiency, with the simple assumption that each O vacancy compensated for two holes. This oxygen depletion extended up to their critical strain relaxation thickness – the point at which uniform OVO domain structure gave way to an orthogonal multi-domain pattern and an evolution of the lattice parameter towards the bulk value [119]. They thus proved that the epitaxial strain induced OVO in LSCO films, observed by almost every research group, is inextricably linked to the electronic properties of the film interface and thus would have a profound influence on other properties such as catalytic activity and oxygen exchange.

This dissertation extends the work by Torija *et al.* [129] and further explores the complex relationship between epitaxial strain and oxygen-vacancy ordered superstructures in LSCO thin films, and their manifestation on the magneto-electronic properties of the film – substrate interface.

Chapter 2

Experimental Methods

2.1 High Resolution X-Ray Diffraction and Reciprocal Space Mapping

2.1.1 X-ray diffraction

X-ray diffraction (XRD) is an elastic scattering technique that is an excellent probe of the atomic and molecular structure of crystalline materials. X-rays are a form of electromagnetic radiation having wavelengths between 0.1 Å and 100 Å (approximately corresponding to an energy range of 125 eV to 125 keV). Their wavelength being of the same order of magnitude as interatomic and intermolecular spacings, x-rays can coherently scatter or diffract from a periodic array of atoms and molecules, and their diffraction patterns can be analyzed to yield information about lattice parameters, crystal texture, microstrain and grain size [1, 2]. Although precise quantitative analysis of the diffraction patterns and intensities is based on the dynamic and kinematic theories of x-ray diffraction [3], a simple relationship between the x-rays and the crystal structure of the sample is given by the Bragg condition:

$$n\lambda = 2d_{hkl}\sin\theta_B \tag{2.1.1}$$

where λ is the wavelength of the x-rays, d_{hkl} is the interplanar spacing of the (*hkl*) family of planes, and θ_B is the angle between the incoming x-ray beam and the (*hkl*) planes (also called the Bragg angle).

2.1.2 The scattering vector

Although x-ray diffraction may be analyzed in real space, it is often more intuitive and fruitful to visualize crystals and diffraction in the so called *reciprocal space* (also called *momentum space* or **k**-space). Reciprocal space is simply the three dimensional spatial Fourier transform of real space [4], whereby each family of crystalline planes in real space is represented by a point in reciprocal space. Further, an electromagnetic wave with a wavelength λ is represented in reciprocal space by a vector **k**, called the *wave vector*, that is given by:

$$\mathbf{k} = \frac{2\pi}{\lambda}$$

(2.1.2)

The wave vector points in the direction of propagation of the wave. Consider then an x-ray beam that is incident on a sample at an angle θ with a wave vector $\mathbf{k_{in}}$. After diffraction, the beam exits the sample, again at an angle θ but with a wave vector $\mathbf{k_{out}}$ (Fig. 2.1 (a)). XRD being an elastic scattering event, both $\mathbf{k_{in}}$ and $\mathbf{k_{out}}$ have the same magnitude and differ only in direction. The x-ray beam has therefore been scattered by an angle 2θ (called the *scattering angle)* and can be represented by a scattering vector **q**, which is the *vectorial* difference between $\mathbf{k_{in}}$ and $\mathbf{k_{out}}$. A simple geometrical construct, called the scattering triangle (Fig. 2.1 (b)), then gives **q** to be:

$$\mathbf{q} = \frac{4\pi}{\lambda}\sin\theta$$

(2.1.3)

The scattering vector **q** is always coplanar with the incident ($\mathbf{k_{in}}$) and diffracted ($\mathbf{k_{out}}$) beams and points along their angle bisector. An XRD measurement *only* yields information about the crystalline planes that lie perpendicular to the **q** vector. In the special case where the diffracted beam angle is the same as the incident beam angle θ (as illustrated in Fig. 2.1), the **q** vector is perpendicular to the surface of the sample. Such a measurement, called a *symmetric specular scan*, always maintains the condition $\theta = ½ (2\theta)$ and the measured planes lie parallel to the

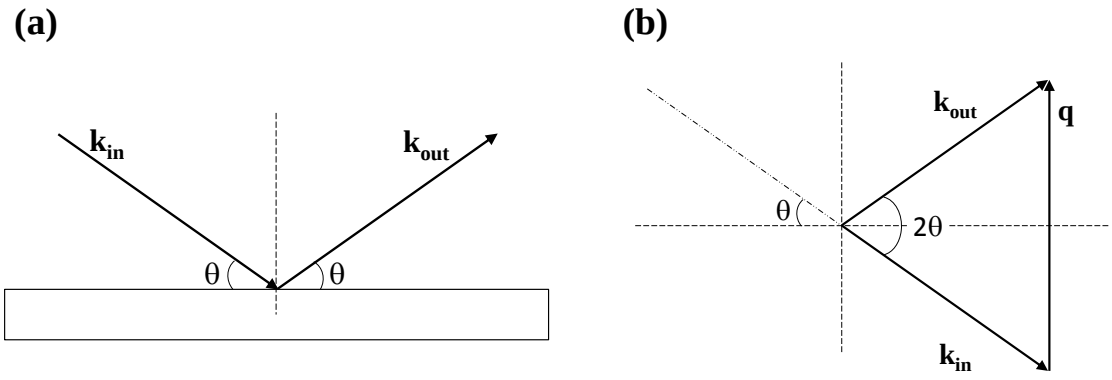

Fig. 2.1: (a) Illustration of an x-ray beam being diffracted at the surface of a crystal. (b) The scattering triangle showing the incident wave vector $\mathbf{k_{in}}$, the diffracted wave vector $\mathbf{k_{out}}$, and the scattering vector **q**.

sample surface. By removing the specular constraint so that $\theta \neq$ ½ (2θ), information can be obtained about crystal planes lying at any angle within the sample – such scans are referred to as *asymmetric* and *skew symmetric* scans.

2.1.3 X-ray diffraction setup

A basic XRD setup requires (1) an x-ray source, (2) a sample stage attached to a goniometer and cradle that can precisely rotate and expose the sample to x-rays at a desired angle, and (3) an x-ray detector. A laboratory scale x-ray source consists of a sealed vacuum tube wherein an electron beam is made to strike a metal target, such as Cu, Fe, Co, etc. The high energy electron beam knocks out core shell electrons from the target and leads to emission lines characteristic of electron transitions in the target material. Monochromation and beam conditioning leads to a tightly focused beam with small angular divergence and wavelength dispersion. Typical lab x-ray sources have power ratings of a few kilowatts and are at a fixed wavelength (characteristic of the target material), although higher intensities and variable wavelengths are achievable in particle accelerator based synchrotron sources. Goniometers typically consist of a set of calibrated motors that can provide translational and rotational motions to the sample. Most goniometer setups have the ability to lock the θ angle to always be half of the 2θ - this is known as a coupled scan and ensures that the specular condition is always satisfied and the **q** vector points in the same direction throughout the scan. The two most commonly used lab scale x-ray detectors are (a) scintillation detectors, that provide transduction between photons and electrons by means of a scintillator crystal and photomultiplier tube, and (b) gas proportional counters, wherein x-ray photons ionize a gas, such as Ar, and the electrons thus generated are accelerated towards an anode wire creating a voltage pulse. In both cases, the detected beam intensity is recorded on a computer.

2.1.4 High resolution x-ray diffraction

In its simplest form, XRD on a powder sample, used for phase identification and structural refinement, is a relatively robust measurement, tolerant to errors and uncertainties in illumination wavelength, beam divergence and sample placement. However, accurate measurements of lattice parameters, strain and mosaic spreads on single crystals and epitaxial thin films require the use of high resolution x-ray diffraction (HRXRD), with an accurately calibrated goniometer cradle for precise sample alignment and multiple beam conditioning optics that provide a high degree of beam monochromation and a narrow beam divergence.

Differentiating Eq. 2.1.1 and rearranging the terms gives the relative uncertainty in determination of d_{hkl} as:

$$\left|\frac{\Delta d_{hkl}}{d_{hkl}}\right| = \left|\frac{\Delta\lambda}{\lambda}\right| + |\cot\theta_B|.|\Delta\theta_B| \tag{2.1.4}$$

Therefore minimization in the uncertainty of the measurement of requires a narrow spread in the wavelength and a small beam divergence.

The HRXRD measurements shown in this thesis have been performed on a PANalytical X'Pert Pro MRD at the University of Minnesota Characterization Facility (CharFac) (Fig. 2.2 (a)). This instrument uses a Cu $K\alpha$ radiation source and a half Eulerian 4-circle goniometer cradle that provides six degrees of freedom for the sample – three translational (x, y, z) and three rotational (ω, ψ, ϕ), along with an independent rotational axis (2θ) for the detector (Fig. 2.2 (b)). X-rays are generated by a high power sealed ceramic tube with a Cu anode and beryllium transmission windows. Primary beam conditioning for diffraction is achieved by a 'Hybrid Monochromator', which is a combination of a parabolic x-ray mirror that collimates the radiation and a 4-bounce 2-crystal Ge (220) monochromator that suppresses the $K\alpha_2$ and $K\beta$ lines.

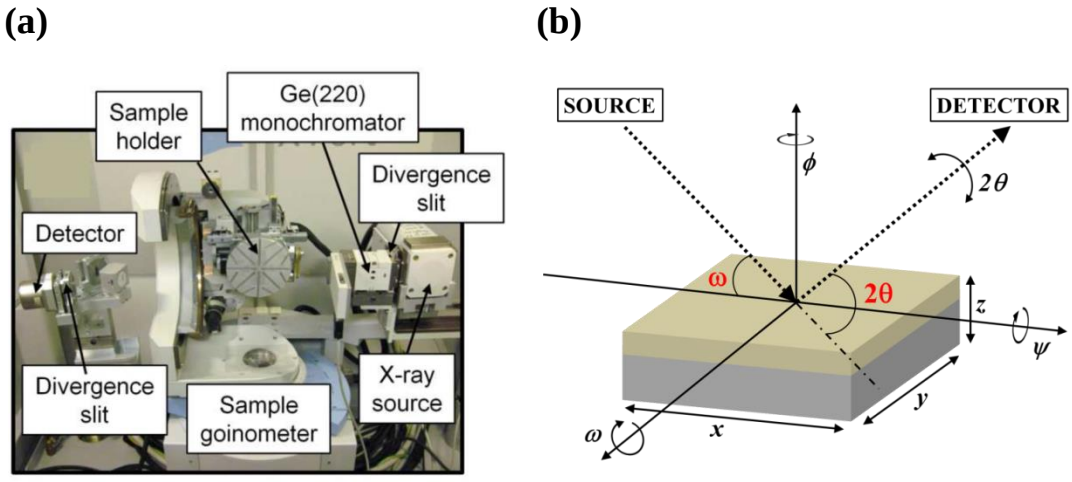

Fig. 2.2: (a) The PANalytical X'Pert Pro MRD used for the HRXRD measurements with the major components labelled (photo taken from Dr. Mike Manno's PhD thesis) (b) Schematic depicting the various angles and degrees of freedom of a sample mounted on the 4-circle goniometer. Red labels indicate the measured angles while the italicized labels mark the axes of motion.

The resulting parallel beam of pure $K\alpha_1$ radiation (λ = 1.54059 Å) has a wavelength dispersion equaling the natural $K\alpha_1$ line width ($\Delta\lambda/\lambda \sim 2.6 \times 10^{-4}$) [5, 6] and an angular divergence $\Delta\theta$ of 0.0068° [7]. A ½° incident beam slit limits the sample illumination length (in mm) to $1.2/\sin\omega$ (ω being the angle between the incident beam and the sample surface) while the illumination width is limited to 5mm by a brass mask. The diffracted beam is passed through a ½° receiving slit and is detected by a sealed gas proportional detector based on a xenon/methane gas mixture. The 4-circle goniometer allows precise alignment of the sample within the x-ray beam to compensate for mounting and positional errors. It further enables the sample to positioned at any desired angle (ω, ψ, ϕ) in the beam, independent of the detector angle 2θ. At any given sample and detector position, the magnitude of the scattering vector **q** is determined solely by the 2θ angle, while the direction of **q** depends on both ω and 2θ, the precise relation being given by:

$$|\mathbf{q}| = \frac{4\pi}{\lambda}\sin\left\{\frac{1}{2}(2\theta)\right\} \tag{2.1.5}$$

$$\Omega = \omega - \frac{1}{2}(2\theta) \tag{2.1.6}$$

Ω being the angle formed by **q** with the normal to the sample surface. In the special case of a symmetric scan, $\Omega = 0$. Since **q** is directly related to the *d* spacing ($d_{hkl} = \frac{2\pi n}{|\mathbf{q}|}$), the Bragg peak being probed is determined by the detector angle. Thus in a diffraction experiment, the 2θ - ω axes are scanned in a coupled fashion (the angular velocity of 2θ is twice that of ω), thereby keeping Ω at a fixed value and effectively monotonically varying the length of the scattering vector while maintaining its direction.

2.1.5 Rocking curves

An ideal single crystal has perfectly ordered lattice planes that are parallel to each other. In such a crystal the Bragg condition is met *only* in one particular direction, when **q** is *exactly* perpendicular to the lattice planes. However, real crystals have a "mosaic structure" on the nanometer length scale, with the perfect lattice broken up into smaller "microcrystallites" that have identical and coherent lattices but have are angularly misaligned with respect to each other (Fig. 2.3 (b)) [1]. The boundaries between these crystallites have high dislocation densities and

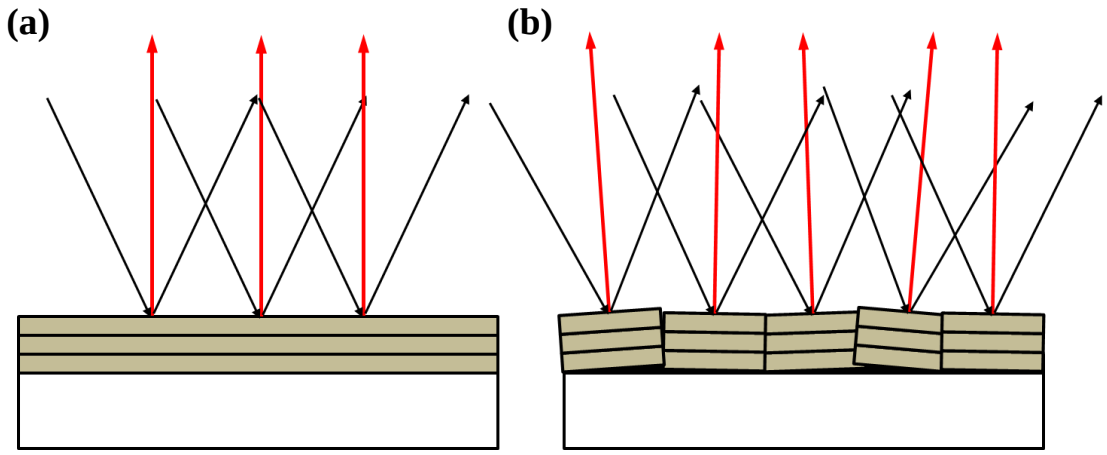

Fig. 2.3: (a) A ideal single crystal thin film on a substrate with perfectly ordered lattice planes. Red arrows mark the **q** vector which satisfies the Bragg condition only when pointing along the normal to the sample surface. (b) A real single crystal thin film with mosaicity. The **q** vector satisfies the Bragg condition along the normal to the surface of *each* microcrystal - it therefore yields non-zero diffraction intensity over a range of tilts away from the sample normal.

disrupt the lattice coherency of the crystal. In such a scenario, the Bragg condition is satisfied over a range of angles for **q** which represent the range of crystallite orientations present in the sample. A scan, therefore, that keeps **|q|** fixed at a particular Bragg peak but rotates the vector **q** over a range of angles (i.e. keeping 2θ fixed while moving ω) could reveal the extent of mosaicity in the sample. Essentially it would be close to a delta function for an ideal crystal but would have a finite peak width for real samples (although dynamical scattering theory predicts a finite sized peak for perfect crystals as well; however the peak in this case, described by the flat topped Darwin curve, would have a width significantly smaller than that of a real crystal with mosaicity [1]). Such a scan is called a rocking curve and is an important probe not only of the mosaicity in single crystals but also strain relaxation in epitaxial thin films. All rocking curve measurements in this thesis were performed on the PANalytical X'Pert PRO at the CharFac using the same optics as the HRXRD scans.

2.1.6 Reciprocal space mapping

A conventional HRXRD scan is a one dimensional measurement that yields information about lattice planes only in one direction. In the case of epitaxial thin films, such a measurement (usually out of plane) quantifies the out-of-plane crystal morphology of both the film and substrate with great precision. However important in-plane information such as in-plane lattice

parameters, lattice mismatch and epitaxial strain relaxation in the film can only be inferred, not directly observed. One way to extract in-plane information would be to run a one dimensional HRXRD scan with an Ω offset and/or a ψ tilt in combination with the out-of-plane measurement. An alternate and more powerful technique to directly and simultaneously visualize the out-of-plane and in-plane relationship between the film and the substrate is a two dimensional scan called *reciprocal space mapping* [3]. As the name suggests, the scan maps out a small region of reciprocal space containing both the film and substrate Bragg peaks. This is done by continuously sweeping the **q** vector to change both its magnitude and its direction (Fig. 2.4 (a)). Essentially the measurement is a set of 2θ - ω coupled scans at different Ω offsets, or equivalently a set of ω scans (rocking curves) at different 2θ values. Each combination of 2θ - ω and Ω can be mapped to a unique point in reciprocal space which can subsequently be resolved into an in-plane ($q_{||}$) and an out-of-plane ($q_{\perp}$) component as follows:

$$q_{||} = \frac{2\pi}{\lambda}\{\cos\omega - \cos(2\theta - \omega)\} \tag{2.1.7}$$

$$q_{\perp} = \frac{2\pi}{\lambda}\{\sin\omega + \sin(2\theta - \omega)\} \tag{2.1.8}$$

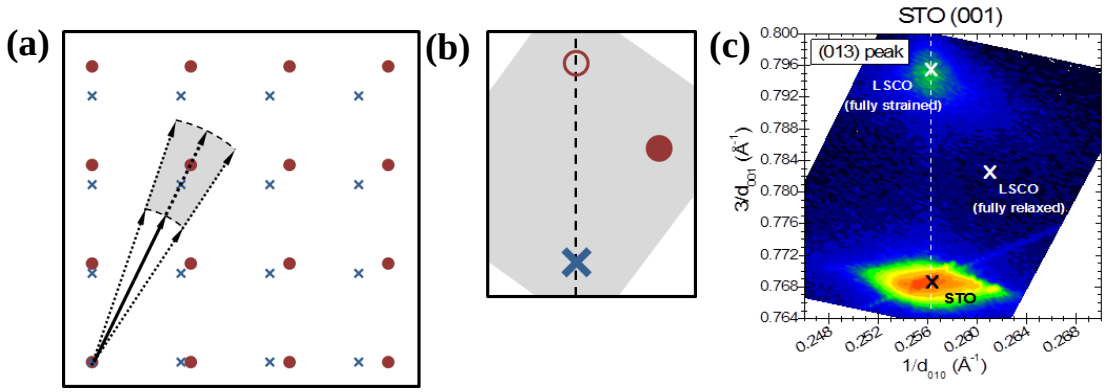

Fig. 2.4: (a) Reciprocal space depictions of two crystals *A* (blue cross) and *B* (red circle) superimposed on each other. The grey shaded area marks the region of reciprocal space mapped out by sweeping the **q** vector. (b) A magnified depiction of the mapped region of reciprocal space. The open red circle marks the hypothetical position of *B* were it to be grown as a fully strained epitaxial film on *A* while the solid red circle marks the bulk position. (c) An RSM showing a fully strained $La_{0.5}Sr_{0.5}CoO_{3-\delta}$ filmon a $SrTiO_3$ (001) substrate.

Often, for the sake of convenience, and ease of conversion into real space lattice units, the 2π factor is dropped and the pre-factor is written simply as $\frac{1}{\lambda}$ in the above equations. The axes of the space map are then labeled in terms of $\frac{1}{d_{h00}}$ and $\frac{1}{d_{00l}}$ (Fig. 2.4 (c)). The reciprocal space maps shown in this thesis were acquired on the PANalytical X'Pert Pro at the CharFac using the same 4-bounce hybrid monochromator as the HRXRD scans, but with ¼° slits on both the source and detector side. No monochromator was used on the detector side which resulted in a decrease in resolution and an increase in the background fluorescence from the cobalt in the films, but a significant enhancement in the signal-to-noise ratio.

2.2 Grazing Incidence X-ray Reflectivity

As with any other form of electromagnetic radiation, x-rays too may be reflected from the surface of materials. While x-ray diffraction works on the principle of collective scattering of x-rays by discrete point scatterers such as atoms and molecules, reflection of x-rays is due to their interaction with the *average* electron density continuum in the material. Grazing incidence x-ray reflectivity (GIXR) is a powerful and sensitive metrology tool that probes surface features such as surface roughness and electron density, and in the case of thin films, thickness and interface roughness. GIXR can be done with or without satisfying the specular condition (**q** is perpendicular to the surface) and, as the name suggests, at shallow incidence angles (usually less than 10° - 12°). X-ray reflectivity can be treated using the classical theory of electromagnetic radiation which gives the complex refractive index of a material as:

$$n = 1 - \delta - i\beta \tag{2.2.1}$$

where δ and β are the dispersion and absorption coefficients respectively and are proportional to the electron density of the material. At x-ray wavelengths, *n* is slightly less than 1, as a result of which x-rays experience *total external reflection* (reflectivity *R* = 1) at a material surface for incident angles less than a critical angle θ_C given by:

$$\theta_C = \cos^{-1}(1 - \delta) \tag{2.2.2a}$$

$$\theta_C \approx \sqrt{2\delta} \tag{2.2.2b}$$

θ_C is thus a material dependent parameter. When the incident angle θ exceeds the critical angle, a part of the x-ray beam penetrates into the material and the reflected intensity follows the laws of Fresnel reflectivity ($R \propto \theta^{-4}$). When there is a thin film at the surface of the material, the x-rays are reflected at both the air-film and film-material interface (assuming the film is thin enough for the x-rays to reach the buried interface). The two reflected beams interfere with each other, their path length difference depending on the exit angle of the beams. They thus give rise to a set of angle dependent constructive and destructive interference fringes, known as *Kiessig fringes*, which are superimposed on top of the Fresnel reflectivity. Using kinematic scattering theory which assumes each x-ray photon is scattered only once by the electrons in the sample, the angular position of the m^{th} interference maximum can be approximated by:

$$\theta_m^2 \approx m^2 \frac{\lambda^2}{4t^2} + \theta_C^2 \tag{2.2.3}$$

where λ is the wavelength of the x-rays and t is the film thickness [8]. The critical angle and Kiessig fringes can thus be used to accurately measure the thickness and density of thin films. However, they are insensitive to the surface and interface roughnesses, both of which have a profound impact on the reflectivity profile. Their effect can be incorporated by modeling the sample as a series of slabs of varying densities and solving the electromagnetic boundary conditions at each interface. GIXR data is analyzed with software such as *GenX Reflectivity* [9] and *ReflPak* [10] which fit the data to a set of mathematical models using refinement algorithms and generate the scattering length density (SLD) profile of the sample from the layer thicknesses, roughness and densities.

GIXR measurements on the X'Pert Pro require a slightly different set of optics than the ones mentioned in section 2.1. The θ^{-4} roll-off of the Fresnel reflectivity implies that the reflected beam intensity quickly falls off to 5 – 6 orders of magnitude lower than the incident beam. In order to get reasonable counting statistics up to 10° - 12° incident beam angles, incident beam intensity is thus given overriding priority over angular resolution and wavelength dispersion. The incident beam is collimated with a parabolic mirror without any monochromator; as a result the radiation contains both *Kα1* and *Kα2* lines, with an average effective wavelength of λ = 1.5419 Å. Since the incident beam impinges on the sample at shallow angles, the beam footprint needs to be limited using a narrow incident beam slit ($^1/_{32}$°). The reflected beam is passed

through a parallel plate collimator set with a 0.1° collimator slit that limits the acceptance angle of the detector to 0.27° [7]. The detector used is the same as HRXRD.

2.3 Polarized Neutron Reflectivity

Neutron reflectivity is a complementary metrology technique to x-ray reflectivity that uses a collimated neutron beam instead of x-rays to investigate thin films and multilayers [11]. Similar to GIXR, neutron reflectivity is a specular and elastic scattering technique that places the **q** vector perpendicular to the sample surface and relies on the interference between beams reflected (scattered) from the top surface and the bottom interface of the film. However, the two probes are fundamentally different in the way they interact with the sample. X-ray photons are massless and characterized by electromagnetic fields – they thus interact with the electronic charge in the material. Neutrons, on the other hand, are massive, chargeless particles that possess a magnetic moment – they therefore interact with the atomic nuclei and the spin of the electrons. As a result, neutron reflectivity is sensitive to the presence of light elements (such as C, O, N) in the material, can distinguish between isotopes of the same element and can detect the presence of ordered magnetic moments, some of which are impossible or extremely difficult with x-rays. As with x-ray reflectivity, neutron reflectivity data is analyzed by fitting to mathematical models in dedicated software. However, unlike x-rays which are treated using classical electromagnetic radiation theory, neutrons are massive and thus need to be treated as particle waves, and their interaction with atomic nuclei calculated using quantum mechanical models of particle scattering [12].

An important application of neutron reflectivity is in the investigation of magnetism in thin films and multilayers. This requires the incident neutron beam to be spin polarized (i.e. the magnetic moments of the majority of incident neutrons point in the same direction), hence the term polarized neutron reflectivity (PNR) [13, 14]. Fig. 2.5 shows the basic schematic of a polarized neutron reflectometer [11]. Neutrons are generated either as a product of a fission reaction in a nuclear reactor or by the impact of a high energy proton cluster with a heavy metal such as mercury in a spallation neutron source. The neutrons thus generated have energies in the MeV range (so called fast neutrons) which is too high for PNR experiments. This high energy beam is passed through an energy-absorbent material (like liquid H_2) called a cold moderator

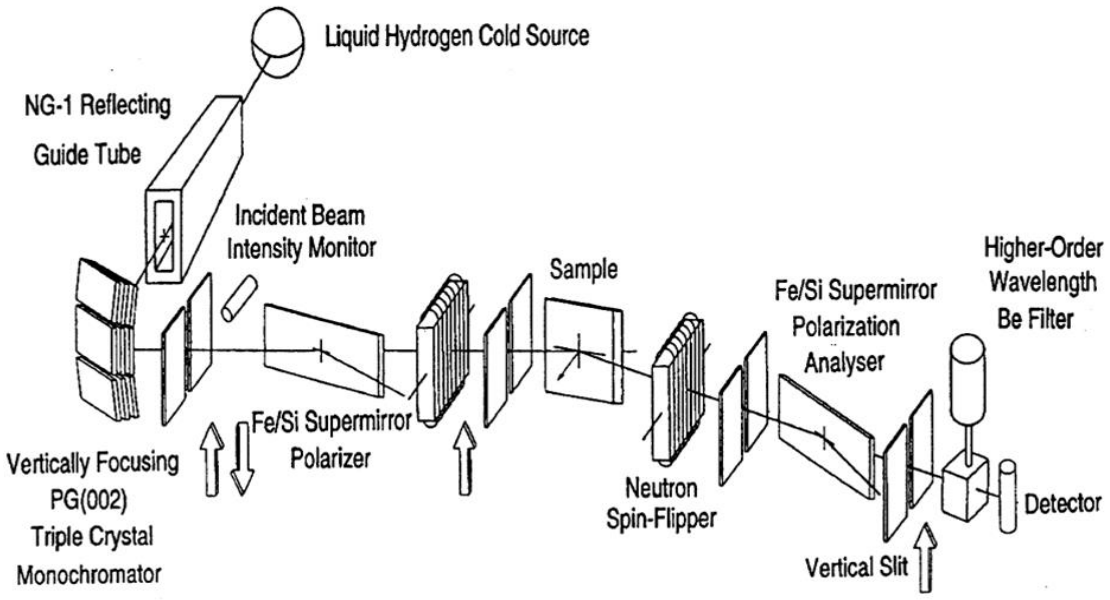

Fig. 2.5: Schematic illustration of a polarized neutron reflectometer [11]

that slows down the neutrons to less than 25 meV (so called cold neutrons, $\lambda \sim 2 - 40$ Å). The cold neutrons are collimated and guided towards the experimental station using a glass pipe (called a neutron guide) whose inner walls are coated with a highly reflective material of neutrons (such as ^{58}Ni and ^{62}Ni). The angular divergence of the beam at the end of the neutron guide is a function of the critical angle of the reflective material, roughly being 1º times the neutron wavelength. The collimated neutron beam is initially unpolarized i.e. it has spin-up and spin-down neutrons in equal proportion. It is passed through a *polarizer* such as a polarizing supermirror to generate a neutron beam with polarization that can exceed 99.5%. Since a PNR experiment requires the analysis of both the spin-up and spin-down reflectivities, the beam is passed through a *spin-flipper* which can control the neutron spins to be either up or down. The beam is then impinged on the sample, which itself is often placed in a saturating magnetic field and is usually mounted on a controlled temperature stage. The reflected beam is passed through a second spin-flipper and an analyzer (similar to a polarizer) before being detected by a 2D position sensitive detector. The angular position and time-of-flight of a detected neutron are then used to compute its *momentum transfer* (scattering) vector **q**, and a plot is thus generated of the reflectivity as a function of **q**.

A neutron scattering event can either be *non-spin-flip* (where the neutron spin is preserved) or *spin-flip* (where the neutron spin is reversed). With two distinct spin possibilities for the incident beam, there are thus *four* distinct possible reflectivity channels – two non-spin-flip channels R^{++} and R^{--}, and two spin-flip channels R^{+-} and R^{-+}. Of these, the non-spin-flip channels are sensitive to the component of sample magnetization that is parallel to the neutron polarization ($M_{\parallel}$) while the spin-flip channels are sensitive to the perpendicular component ($M_{\perp}$). None of the four reflectivity channels are sensitive to any component of the sample magnetization perpendicular to the sample surface i.e. parallel to **q**. It follows, therefore, that if the sample is magnetically saturated and its magnetization is parallel to the neutron spin axis, the R^{++} and R^{--}channels are sufficient to completely characterize the magnetism in the sample. The neutron scattering characteristic of a material is described by two additive quantities – the nuclear SLD ρ_n which characterizes the neutron cross section of the nucleus, and the magnetic SLD ρ_m which describes the interaction between the magnetic moments of the sample and the neutron beam. The two SLDs are given by:

$$\rho_n = \sum_{i=1}^{J} N_i b_{c_i}$$

$$\rho_m = \sum_{i=1}^{J} N_i p_i = C \sum_{i=1}^{J} N_i \mu_i = C' m \qquad (2.3.1)$$

where J is the number of distinct isotopes in the sample, N_i is the number density of the i^{th} isotope, b_{c_i} its bound coherent neutron scattering length, p_i its magnetic scattering length, μ_i its magnetic moment in μ_B per formula unit and m the sample magnetization (in emu/cm^3). C (2.645×10^{-5} Å/μ_B) and C' (2.853×10^{-9} Å^{-2}cm^3/emu) are dimensional physical constants that convert the magnetization to a magnetic scattering length [12]. PNR data is analyzed by *simultaneously* fitting the R^{++} and R^{--} intensities to known scattering models in a refinement software which then generates the resulting chemical (nuclear) and magnetic SLD profiles.

The PNR measurements of the $La_{0.72}Sr_{0.28}CoO_{3-\delta}$ films on $SrTiO_3$ (001) and $LaAlO_3$ (001) samples shown in Chapter 5 were carried out at 10 K and in a 1 T saturating field on the ASTERIX instrument at Los Alamos National Laboratory on 1 in. diameter samples while the

film on $SrTiO_3$ (110) (10mm x 10mm) was measured at 5 K and in a 1 T saturating field at the Spallation Neutron Source at Oak Ridge National Laboratory, using the time-of-flight Magnetism Reflectometer. In all instances, the samples were cooled in a 1 T saturating field and the non-spin flip (R^{++} and R^{--}) scattering channels were measured up to a q of 0.065 – 0.07 $Å^{-1}$. The neutron reflectivity data was analyzed with the *GenX Reflectivity* software [9].

2.4 Electronic transport

Four terminal resistance measurements (van der Pauw method)

The resistivity ρ of a material is a critical parameter in understanding its electrical properties. A widely used technique to accurately measure the resistivity of materials is the van der Pauw method [15, 16]. This is a four terminal technique, meaning the current leads are separated from the voltage leads – this negates the effect of the resistance of the contact leads and wires. The method works for arbitrary shaped samples, the only requirements for the measurement being:

1. The sample should have uniform thickness
2. The sample should be singly connected, i.e. the sample should not have any isolated holes
3. The contacts should be on the circumference of the sample
4. The contacts should be small (total contact area should not exceed 10% of the sample area)

Consider an arbitrary shaped lamellar sample with 4 electrical contacts *A*, *B*, *C*, and *D* (Fig. 2.6 (a)). The sample is assumed to satisfy all the requirements for a van der Pauw measurement. A current is then passed through the sample, entering it at contact *B* and leaving it at *C*, and the potential drop measured between contacts *A* and *D*. A resistance can then be defined as the ratio of this voltage and current, i.e.

$$R_{BC,AD} = \frac{V_{AD}}{I_{BC}} \tag{2.4.1}$$

Similarly, a resistance $R_{AB,DC}$ is measured by switching the direction of current flow. It can then be shown that the two complementary resistances are related by the transcendental equation:

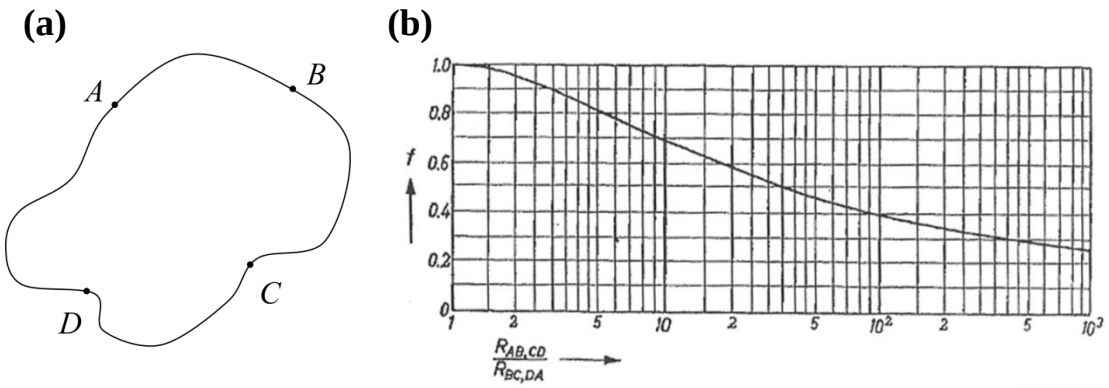

Fig. 2.6: (a) A lamellar sample with four electrical contacts for a van der Pauw resistivity measurement. (b) The transcendental function *f* as a function of the van der Pauw resistance ratio [15]

$$e^{-\left(\frac{\pi d R_{BC,AD}}{\rho}\right)} + e^{-\left(\frac{\pi d R_{AB,DC}}{\rho}\right)} = 1$$

(2.4.2)

where ρ is the resistivity of the material and d is the thickness of the sample. In general, it is not possible to express ρ in terms of explicit analytical functions and eq. 2.4.2 needs to be solved numerically. However, it is possible to write the solution as:

$$\rho = \frac{\pi d}{\ln 2} \frac{R_{BC,AD} + R_{AB,DC}}{2} f\left(\frac{R_{BC,AD}}{R_{AB,DC}}\right)$$

(2.4.3)

where f is function of the resistance ratio $\frac{R_{BC,AD}}{R_{AB,DC}}$ and satisfies the relation:

$$\frac{R_{BC,AD} - R_{AB,DC}}{R_{BC,AD} + R_{AB,DC}} = f \cosh^{-1}\left\{\frac{\exp\left(\frac{\ln 2}{f}\right)}{2}\right\}$$

(2.4.4)

f may be solved for as a function of the resistance ratio numerically or graphically (Fig. 2.6 (b)). When the resistance ratio is close to unity f may be approximated as:

$$f \approx 1 - \left(\frac{R_{BC,AD} - R_{AB,DC}}{R_{BC,AD} + R_{AB,DC}}\right)^2 \frac{\ln 2}{2} - \left(\frac{R_{BC,AD} - R_{AB,DC}}{R_{BC,AD} + R_{AB,DC}}\right)^4 \left\{\frac{(\ln 2)^2}{4} - \frac{(\ln 2)^3}{12}\right\}$$

(2.4.5)

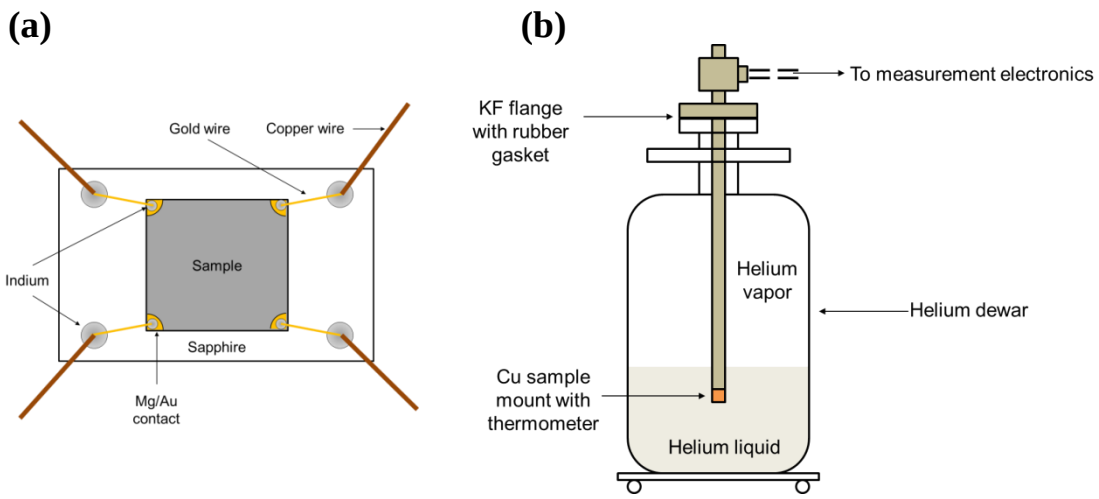

Fig. 2.7: (a) Schematic depiction of a sample mounted on a sapphire substrate and wired for a van der Pauw measurement. (b) Schematic depiction of the home built liquid helium immersion probe.

The van der Pauw technique was used for all resistivity measurements on LSCO thin films shown in this thesis. Sputtered Mg(5nm)/Au(50nm) spots with soldered indium blobs were used as Ohmic contacts and the samples mounted onto a sapphire mounting plate using GE varnish (Fig. 2.7 (a)). Gold wire was used to connect the sample to the sapphire, which was subsequently contacted to the copper wires of the probe. Temperature dependent transport measurements on LSCO thin films were done in a home built liquid helium immersion probe with a Cu sample holder (Fig. 2.7 (b)). The sapphire plate was varnished onto the Cu holder, the underside of which was varnished to a Si diode temperature sensor. The temperature of the sample was varied in the range of 4.2 K – 300 K by varying the depth of immersion of the probe in the dewar, making use of the thermal gradient of the helium vapor inside the dewar. Metallic and conductive samples were measured using AC excitation with a Linear Research LR-700 AC resistance bridge operating at 16 Hz. Insulating samples were measured using DC excitation with the current being sourced from a Keithley 220 current source and the voltage being measured with a Keithley 2002 digital multimeter. Both positive and negative current biases were used to cancel out the effect of thermoelectric voltages. In all cases, the bias current was carefully chosen to minimize Joule heating at the contacts (power dissipation was kept below 1μW) and Ohmic behavior of the contacts was verified down to the lowest temperatures.

2.5 SQUID magnetometry

Magnetometry refers to the investigation and measurement of the magnetic properties of materials. A number of instrumentation techniques are available for such measurements, such as vibrating sample magnetometry, alternating gradient force magnetometry and Superconducting Quantum Interferometry Device (SQUID) magnetometry, of which the latter is the most sensitive, being capable of detecting moments as low as $5x10^{-9}$ emu [17]. This extreme detection capability is made possible by the SQUID sensor – a superconducting circuit that can transduce changes in magnetic flux quanta to an electrical voltage. According to the Bardeen-Cooper-Schrieffer (BCS) theory of superconductivity, charge transport in a superconductor is by means of zero net spin electron pairs called Cooper pairs [4]. These Cooper pairs can be described by a wavefunction:

$$\Psi = \sqrt{n}e^{i\theta} \tag{2.5.1}$$

where n is the local Cooper pair density and θ is the phase of the current. If the superconducting path is broken by the insertion of a sufficiently thin insulating gap, the Cooper pairs are able to tunnel across this gap and the supercurrent continues to flow, even in the absence of an external voltage bias. However the currents on either side of the gap have different phases. The effect is known as the *DC Josephson Effect* [4] and the superconductor-insulator-superconductor combination is known as a *Josephson junction*. The tunneling current, called the Josephson current, is given by:

$$j = j_0 \sin(\varphi) \tag{2.5.2}$$

where j is the supercurrent density, j_0 is the maximum possible Josephson current density and φ is the phase difference across the tunnel barrier. Now, if a DC voltage is applied across the junction or the DC bias current exceeds the critical Josephson current density j_0, an AC current is induced in the circuit and is superimposed on top of the DC current. This is known as the *AC Josephson Effect* [4], and the current density in this case is given by:

$$j = j_0 \sin\left(\varphi - \frac{2eVt}{\hbar}\right) \tag{2.5.3}$$

where V is the applied voltage and t is time. The frequency of oscillation is thus given by $\frac{2eV}{\hbar}$. In the absence of any external magnetic flux threading the junction, the phase difference δ is constant across the junction. However, when a magnetic field is applied, the homogeneity is broken, and the spatial variation of the phase difference is given by [18]:

$$\frac{\partial \varphi}{\partial x} = \frac{2\pi}{\Phi_0}\Phi = \frac{2e}{\hbar}B(t + 2\lambda_l) \tag{2.5.4}$$

where $\Phi_0 = {}^{h}/_{2e} = 2.067 \times 10^{-15}$ is the fundamental flux quantum, Φ is the magnetic flux threading the junction as a result of the external magnetic field B, t is the thickness of the junction and λ_l is the London penetration depth of the superconducting material. Here the junction is assumed to lie in the xy plane with the current flow along z and the B field along y. The total Josephson current I_S is then obtained by integrating Eq. 2.5.4 over the area of the junction, which gives [18]:

$$I_S = I_C \left| \frac{\sin\left(\pi \frac{\Phi}{\Phi_0}\right)}{\pi \frac{\Phi}{\Phi_0}} \right| \tag{2.5.5}$$

The Josephson current thus has an oscillatory dependence on the magnetic flux and has the same mathematical form as a Fraunhofer diffraction pattern.

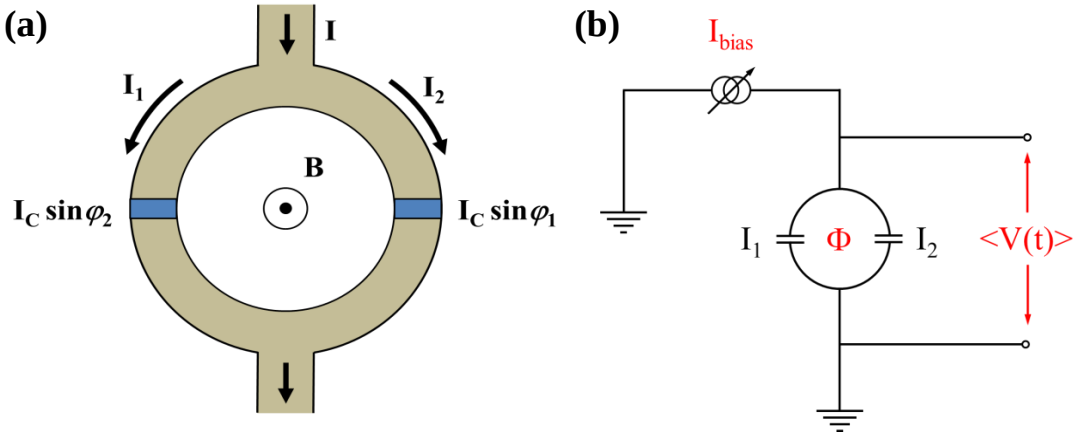

Fig. 2.8: (a) A DC SQUID loop with two Josephson junctions and an external magnetic field B. (b) A DC SQUID biased with an external current source to function as a magnetic field sensor

The transducer at the heart of a SQUID magnetometer is the dc-SQUID – a superconducting loop with two Josephson junctions, one in each branch of the loop (Fig. 2.8 (a)) [17]. The two junctions have identical critical Josephson currents, but have different phase differences across them. The total current flowing through the loop can then be written as the sum of the individual branch currents I_1 and I_2 [19]:

$$I = I_C \sin\varphi_1 + I_C \sin\varphi_2$$

$$= 2I_C \cos\left(\frac{\varphi_1 - \varphi_2}{2}\right) \sin\left(\frac{\varphi_1 + \varphi_2}{2}\right) \tag{2.5.5}$$

In the presence of an external magnetic field, the SQUID loop is threaded by magnetic flux lines. Since the total flux in a superconducting loop must necessarily be quantized, a circulating screening current is induced in the loop such that the total flux is rounded off to the nearest integral multiple of Φ_0. The two branch currents may then be decomposed into an average current $\tilde{I}$ flowing through the SQUID and a circulating current I_{circ} flowing around the loop [19]:

$$\tilde{I} = \frac{I_1 + I_2}{2}$$

$$I_{circ} = \frac{I_1 - I_2}{2} \tag{2.5.6}$$

The phase differences in the two SQUID branches are then related through the flux quantization condition as:

$$\varphi_1 - \varphi_2 = \frac{2\pi\Phi}{\Phi_0} \tag{2.5.7}$$

and Eq. 2.5.5 may be written as:

$$I = 2I_C \cos\left(\pi\frac{\Phi}{\Phi_0}\right) \sin\left(\varphi_1 + \pi\frac{\Phi}{\Phi_0}\right) \tag{2.5.8}$$

SQUID based magnetic sensors are operated under an external current bias that, as a result of the AC Josephson effect, leads to a time varying voltage across it (Fig. 2.8 (b)). The time averaged voltage developed across the loop is given by [19]:

$$\langle V(t)\rangle = I_C R_N \sqrt{\left(\frac{I_{bias}}{2I_C}\right)^2 - \left[\cos\left(\pi \frac{\Phi_{ext}}{\Phi_0}\right)\right]^2}$$

(2.5.9)

where I_C is the critical Josephson current, R_N is the *normal resistance* of the Josephson junctions, I_{bias} is the external bias current, and Φ_{ext} is the total external magnetic flux threading the loop. The SQUID loop thus functions as a direct flux – voltage transducer and the bias current is chosen so as to maximize the sensitivity [19]:

$$S = \left.\frac{\partial V}{\partial \Phi_{ext}}\right|_{I_{bias}}$$

(2.5.10)

Although the DC SQUID offers the highest flux sensitivity, many commercial magnetometers are based on an RF-SQUID sensor, which is less sensitive but has a manufacturing cost and noise rejection (due to lock-in detection) advantage over its DC counterpart. An RF SQUID has single Josephson junction in a superconducting coil and is operated with an RF current bias through inductive coupling with an RF tank circuit [17]. The operational principle of an RF SQUID is similar to that of a DC SQUID, and once again the bias current is chosen so as to maximize the sensitivity of the sensor, which in this case is given by [19]:

$$S = \left.\frac{\partial V}{\partial \Phi_{ext}}\right|_{I_{bias}} = \frac{\omega_{RF}}{\alpha}\sqrt{\frac{L_T}{L_S}}$$

(2.5.11)

where ω_{RF} is the resonance frequency of the RF tank circuit, L_T and L_S are the inductances of the RF tank and the SQUID loop respectively, and α is the coupling coefficient between the RF tank and the SQUID. The effect of the external current bias in an RF SQUID is the appearance of an RF voltage across the tank circuit.

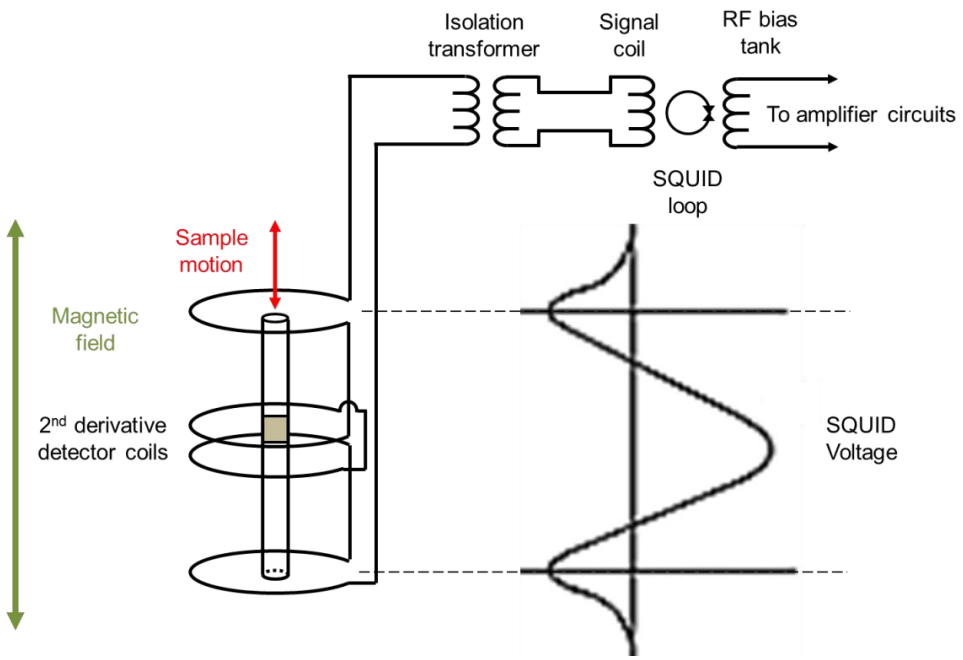

Fig. 2.9: Schematic of the SQUID sensing circuit in the MPMS-*XL* along with the SQUID voltage output

The magnetic properties of the $La_{1-x}Sr_xCoO_{3-\delta}$ thin films shown in this thesis were measured in a Quantum Design MPMS-*XL* SQUID magnetometer. Fig. 2.9 shows the schematic of the SQUID sensing circuit in the MPMS along with the spatial variation of the SQUID voltage response [20]. The samples were mounted in a series of concentric transparent polyethylene drinking straws which were subsequently attached to the sample rod with Kapton® tape. The sample rod suspends the sample inside a set of second derivative gradiometer coils and the sample is made to oscillate along the axis of these coils by the sample transport motor. The gradiometer coils are a set of oppositely wound pickup coils that are sensitive to the emf generated by the sample motion but are unaffected by static magnetic fields from the magnet and the environment. A superconducting magnet applies a magnetic field along the axis of the gradiometer coils – the MPMS-*XL* can generate fields up to 7 Tesla. The output of the gradiometer is inductively coupled to an RF SQUID through an isolation flux transformer. The SQUID loop is biased by an RF tank, the output of which is amplified and logged on a computer. A measurement of magnetic moment is made by moving the sample axially through the gradiometer and recording the SQUID voltage as a function of the sample position. This

voltage – position scan, called the extraction scan (shown in Fig. 2.9), is then fitted to known physical models and the sample moment thereby determined. The MPMS-*XL* is capable of detecting moments as low as 10^{-8} emu. The sample space in the MPMS is part of a helium flow cryostat which is capable of regulating the sample temperature in the range 1.8 K – 400 K.

Each sample was thoroughly cleaned by ultrasonication in acetone, methanol and de-ionized water prior to measurement to remove dust and other sources of ferromagnetic contamination. Measurement statistics were improved by taking each data point to be the average of three measurements, each one of which itself was taken over five extraction scans. Hysteresis loops were recorded with the magnet in persistence mode (to isolate noise from the magnet power supply) while temperature scans were recorded by sweeping the temperature at 2 K/min. The standard measurement protocol also involved degaussing the shield, resetting the magnet and quenching the SQUID coils before starting a measurement.

2.5.1 Quantification of the breadth of the ferromagnetic transition

This section discusses the magnetometry and its analysis used to extract the spread in the ferromagnetic Curie temperatures (T_C's) of $La_{0.5}Sr_{0.5}CoO_{3-\delta}$ films discussed in Chapter 5. Magnetization *vs.* temperature data M (T) were measured using a Quantum Design DC SQUID based vibrating sample magnetometer (MPMS SQUID VSM). Similar to the SQUID magnetometer discussed earlier, a SQUID VSM uses a SQUID sensor to measure magnetic moments. However, instead of traveling the entire length of the gradiometer coils, in this case the sample is placed at the point of maximum SQUID sensitivity and rapidly vibrated about this position through a set of pickup coils. This sinusoidal oscillation by means of a linear motor induces a voltage in the coils through Faraday's law of induction, and the voltage is then used to calculate the magnetic moment of the sample. The SQUID VSM combines the sensitivity of a SQUID magnetometer with the speed of a conventional VSM. Magnetic measurements were made in the temperature range 50 – 330 K and in applied external fields H = 10 Oe – 10 kOe. This temperature span included a sufficient temperature range both above and below the T_C for samples. Magnetization data were recorded in the continuous mode at a temperature sweep rate of 0.03 K/s. Data analysis included a correction to account for the small bias field (~25 Oe) resulting from the trapped flux within the SQUID-VSM's superconducting magnet. The M (T)

data were analyzed following the procedure of Campillo *et al.* and Berger *et al.* [21, 22] to account for the contribution of ferromagnetic inhomogeneity in the sample to the total breadth of the ferromagnetic transition. The method assumes that the *M* (*T*) profile can be modelled as a superposition of power laws centered at different T_C values, the exact form being given by:

$$M(T) = M_0 \int_{T_c} \left(\frac{T_c - T}{T_c}\right)^{\beta} \theta(T_c - T)\rho(T_c)dT_c$$

(2.5.12)

where the pre-factor M_0 is proportional to the saturation magnetization, β is the temperature universal critical exponent quantifying the divergence of magnetization at T_C, θ (x) is the Heaviside function ensuring that the magnetization vanishes for $T > T_C$, and ρ (T_C) is a sample-specific probability distribution of the T_C values. We have assumed the $\rho(T_C)$ to have a Gaussian profile, given by:

$$\rho(T_c, \langle T_c \rangle, \Delta T_c) = \frac{1}{\sqrt{2\pi}\Delta T_c} exp\left(-\frac{(T_c - \langle T_c \rangle)^2}{2\Delta T_c^2}\right)$$

(2.5.13)

where $<T_C>$ is the mean Curie temperature obtained by averaging over the entire sample, and ΔT_C is the standard deviation characterizing the statistical variation around the mean, relating directly to the extent of the disorder within a sample. The Gaussian assumption, though strictly not true, gives sufficiently good fits to capture the essential physics. The parameters $<T_C>$, ΔT_C, and β are extracted at multiple fields *H*. The standard deviation in T_C is then seen to follow with good precision the relation:

$$\Delta T_c(H) = \Delta T_c^0 + cH^{\frac{1}{\eta}}$$

(2.5.14)

where c is a constant, and $\eta = \beta\delta$ with δ being the *H*-related universal critical exponent. Here $\Delta T_c(H)$ is the total broadening of the transition temperature, ΔT_c^0 is the intrinsic broadening due to the T_C distribution and $cH^{1/\eta}$ represents the field induced broadening. The parameter $\Delta T_C{}^0$ is

the width of the sample specific intrinsic T_C distribution independent of the external field value, and is a genuine characteristic quantifying the inhomogeneity of the sample.

2.6 Scanning Probe Microscopy

Scanning probe microscopy (SPM) refers to the general family of techniques that build a two dimensional image of a particular material property by rastering a sharp interactive tip over the material surface. Unlike optical and electron microscopy, which are based on the scattering of particles (photons and electrons) from a material surface, SPM maps the interaction force between the probe tip and the surface at very close range (within a few nanometers). The probe may be suitably modified to respond to different surface properties of the material – as a result a number of imaging techniques have been developed from the basic SPM principle, such as atomic force microscopy (topography) [23], scanning tunneling microscopy (topography and local conductivity) [24], magnetic force microscopy (local magnetic forces) [25], Kelvin force probe microscopy (surface potential) [26] and so on.

2.6.1 Atomic Force Microscopy

Atomic force microscopy (AFM) is the most widely used scanning probe technique and is used to quantitatively measure topography, surface roughness, local friction and elastic response. As the name suggests, the technique is sensitive to the local forces of attraction and repulsion between the atoms of the tip and the surface. The near-field interaction between two atoms is a combination of van der Waals attraction and electron – electron repulsion and can be described by the Lennard – Jones potential [23]:

$$\mathrm{U} = 4\varepsilon\left[\left(\frac{\sigma}{r}\right)^{12} - \left(\frac{\sigma}{r}\right)^{6}\right] \tag{2.6.1}$$

where ε is the depth of the potential well, σ is the atomic diameter and r is the interatomic distance. As shown in Fig. 2.10 (a), this results in a potential that is attractive down to a distance r_m (shaded blue region) and becomes repulsive (shaded red) after that. An AFM uses this

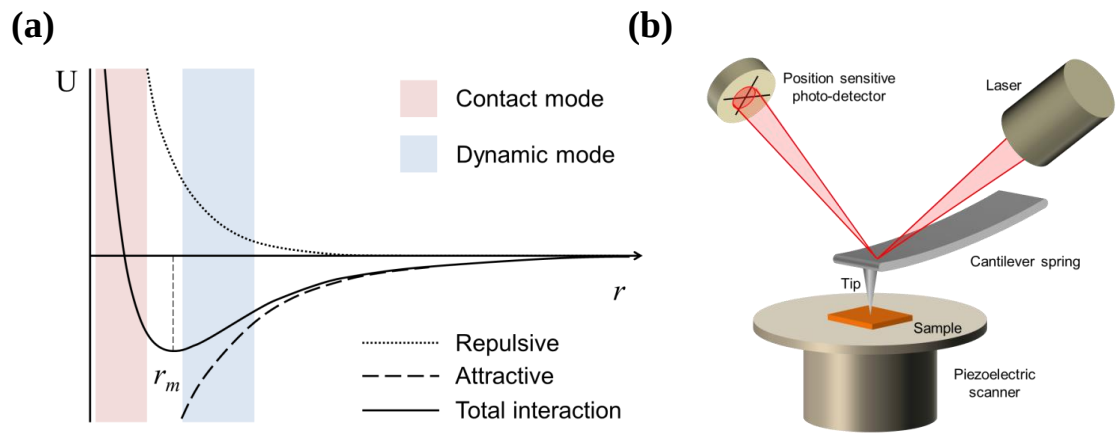

Fig. 2.10: (a) Interactive potential between an AFM tip and the sample surface as a function of distance. In contact mode, the tip is operated in the repulsive (red) region while dynamic mode AFM operates in the attractive (blue) region. (b) Schematic of the basic elements of an AFM system

sensitive dependence of the interactive force to accurately measure the distance between the tip and the sample, or to maintain the tip at a precise distance from the sample. Fig. 2.10 (b) shows the basic schematic of an AFM. The sample is mounted on a piezoelectric scanner that is capable of precise high resolution vertical (*z*) and lateral (*xy*) motion. The sensing probe is a sharp tip (tip radii are typically a few nanometers) machined at the end of a silicon or silicon nitride microcantilever. AFM cantilevers typically have spring constants of tens of N/m. A solid state laser spot is focused on the end of the cantilever and the reflected beam is detected by a four quadrant position sensitive detector (PSD). The laser beam is aligned such that at zero cantilever deflection, the spot is exactly centered on the PSD. To create a topography map, the cantilever is brought close to the sample surface till it enters the repulsive region and the cantilever starts deflecting. The deflection is detected by the position of the laser spot on the PSD. The sample is then rastered by the *xy* piezo stage to scan the tip over the sample surface. The tip's interaction with the topography of the surface results in corresponding deflections of the cantilever which is fed back to the *z* piezo stage through a PID controller. The controller enables the cantilever to be maintained at a constant deflection i.e. at a constant height above the surface by adjusting the z position of the sample stage. A two dimensional map of the *z* positions is thus representative of the sample topography and is called the height image. This is the contact mode operation of an AFM [23]. Another imaging mode is the dynamic mode, where the tip – sample distance is maintained in the attractive regime and the cantilever is driven to oscillate at its resonant frequency. A change in the tip – sample distance (due to

variation in topography) moves the cantilever off resonance and the resulting change in the amplitude and phase of the oscillations is recorded. The resulting maps are called the height and phase images respectively [23].

AFM images of $La_{0.5}Sr_{0.5}CoO_3$ thin films shown in Chapter 3 were acquired with a Digital Instruments NanoScope III at the CharFac. Both contact and dynamic modes were used for imaging. Prior to imaging the samples were ultrasonicated in acetone and methanol and dried with a high velocity stream of dry N_2. Samples were mounted on AFM sample stubs with double sided tape and images were taken over areas between 1 x 1 μm^2 and 5 x 5 μm^2.

2.6.2 Scanning Tunneling Microscopy

Scanning tunneling microscopy (STM) is another widely used imaging technique and was the first SPM method invented. The sensing probe in an STM too is an atomically sharp tip. However, unlike an AFM, the STM senses the tunnel current between the conductive tip and the sample surface, usually under ultrahigh vacuum conditions. STM tips are usually made of W or a Pt/Ir alloy and are sharpened to the point that the very end of the tip contains just one atom. The sample needs to be conductive as well (to provide a return path for the tunnel current) – thus an STM is limited in the type of samples that can be imaged compared to an AFM. The tunnel current between the tip and the sample is well approximated by [24]:

$$I \approx \frac{4\pi e}{\hbar} e^{-\frac{2r}{\hbar}\sqrt{2m\varphi}} \rho_t(0) \int_{-eV}^{0} \rho_s(\varepsilon) d\varepsilon \qquad (2.6.2)$$

where r is the tip – sample distance, m is the mass of the electron, φ is the height of the tunnel barrier and is usually a function of the tip and sample work functions, V is the voltage bias maintained between the tip and sample, $\rho_t(0)$ is the density of states at the Fermi level in the tip, $\rho_s(\varepsilon)$ is the density of filled states in the sample and ε is the energy. The exponential dependence of the tunnel current on the tip – sample distance is the reason for the extreme sensitivity of the STM to sample height changes – a 1 Å change in r results in a 10 fold change

in *I*. A common operating mode of an STM is the constant current mode, whereby the *z* position of the scanner is changed in accordance with the sample topography keeping *I* constant – the topography map thus generated is similar to the height image in an AFM. It is also possible to operate the STM in the constant height mode, where the sample is rastered at a fixed *z*, and the variation in the tunnel current over the scanned area is representative of spatial variations in the local density of states of the sample – the image generated is thus a two dimensional conductance map.

The scanning tunneling microscopy/spectroscopy (STM/STS) measurements shown in Chapter 6 were performed using an STM head built in-house at the Department of Physics, Leiden University (Netherlands) and maintained in ultra-high vacuum (UHV, base pressure 3×10^{-10} Torr). After overnight pumping in a load-lock, samples were introduced into the UHV chamber and scanned using mechanically-cut $Pt_{90}Ir_{10}$ STM tips. STS measurements were made at specific locations by sweeping the bias voltage at a fixed sample-tip separation, producing current-voltage (I-V) curves. Differential conductance maps (scanned simultaneously with topography) were measured with a lock-in amplifier using a 10mV AC modulation at ~1000 Hz. This modulation was superimposed on specified set-point V and I values which serve to fix the sample-tip bias and separation.

2.7 Transmission Electron Microscopy

Transmission electron microscopy (TEM) is a high resolution imaging technique that uses a high energy (~ 60 keV – 300 keV) electron beam transmitted through an ultrathin sample (less than 200 nm) [27]. At these energies, the electrons have a wavelength of a 2 – 5 pm (x-rays used in XRD have wavelengths of ~ 150 pm). This, in conjunction with spherical aberration correction and small chromatic dispersion, allows modern TEMs imaging capabilities with sub-Angstrom resolution. As a result, TEMs have become an invaluable tool in materials characterization and find application in fields as diverse as metallurgy, biology, polymers and materials science.

2.7.1 Scanning TEM and Electron Energy Loss Spectroscopy

Scanning transmission electron microscopy (STEM) is a specialized TEM technique where the high energy electron beam is focused into a narrow spot (typical probe sizes are in the range 0.5 – 2 Å) that is rastered across the sample [28]. Fig. 2.11 shows a representative schematic of the column of a typical STEM. A high energy electron beam generated by a high brightness electron gun is collimated by a set of condenser lenses and apertures and passed through a spherical aberration corrector. Spherical aberration, which refers to the variation in the focal distance of a lens with the radial distance from the lens axis, leads to loss of image resolution and is therefore corrected for by the aberration corrector. The beam is then passed through a set of scan coils which control the position of the beam on the sample and raster the beam in an *xy* Cartesian fashion across the sample. Finally, the beam is passed through a set of objective lenses and apertures that bring it to a tightly focused spot on the sample.

Depending on the detectors used, an STEM is capable of simultaneously detecting a variety of signals from the sample. Three such detectors are shown in Fig. 2.11. A detector placed in the path of the transmitted beam is sensitive to electrons that suffer minimal scattering from the sample and leave the sample within the angular divergence of the incident beam. The image recorded by this detector is called a bright field (BF) image. A complementary image is formed by an annular detector that is placed well outside the angular cone of the transmitted beam. This detector, known as a high angle annular dark field (HAADF) detector is sensitive to electrons that are incoherently scattered by the sample atoms. Since the scattering probability of an electron depends on the *Z* number of the atom, HAADF is an excellent *Z* contrast imaging technique. In addition to detecting the transmitted and scattered electrons, it is also possible to measure the energy of the transmitted electrons. When an impinging electron passes through the sample, there is an inelastic interaction between the electron and the electrons of the sample. The high energy electron loses some of its energy to the sample and this energy transfer is most efficient at the characteristic resonant energies of the atoms of the sample. Since the incoming energy of the electron is known with great accuracy, it is therefore possible to measure the energy loss spectrum of the transmitted beam. This spectrum has peaks at the resonant energies of the atoms in the sample and can therefore be used to identify the atoms in the sample. This technique is known as electron energy loss spectroscopy (EELS) [29]. EELS spectra also present fine structure near the edges of the elemental lines which is sensitive to the

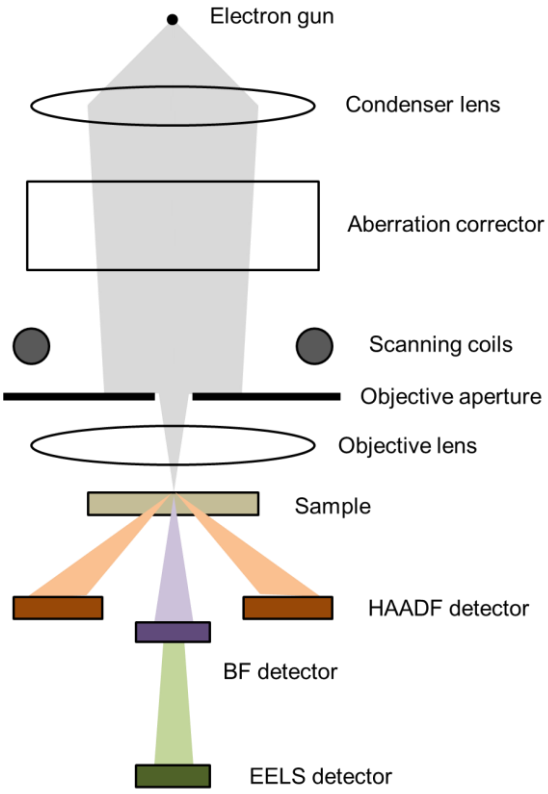

Fig. 2.11: Representative schematic of the electron column in a typical STEM showing beam conditioning lenses, an aberration corrector and three detectors – a high angle annular dark field (HAADF) detector, a bright field (BF) detector, and an electron energy loss spectrometer (EELS)

electron density in the vicinity of the atom. EELS can therefore be used to not only identify the elemental makeup of the material but also electron densities and atomic valences on an atomic scale spatial resolution.

2.7.2 Geometric Phase Analysis

In general, high resolution TEM images are not a simple direct representation of the lattice being imaged. Each lattice fringe imaged is the result of the interference between several electron beams. Image contrast is also extremely sensitive to local variations in sample thickness and lens properties. Although many of these problems are negated due to incoherent scattering in HAADF STEM imaging, which provides sharp images of atomic columns with

sub-Angstrom resolution, the contrast in such images too is affected by lattice tilts, surface relaxation and thickness variations. Therefore, quantitative analysis of the local lattice distortions in the sample is not possible with a simple contrast analysis of the real space image of the sample. A technique commonly used for such analysis is the Geometric Phase Analysis (GPA) which looks at the periodicity of the image in Fourier space and uses the phase angle of the Fourier components to calculate the local displacement fields [30, 31].

The TEM image of a perfect crystal has perfect periodicity in real space, and can therefore be represented as the sum of its Fourier components as [30]:

$$I(\mathbf{r}) = \sum_{g} H_g e^{2\pi i \mathbf{g}.\mathbf{r}} \tag{2.7.1}$$

where **g** is reciprocal lattice vector of a Bragg reflection and H_g are the complex Fourier coefficients. For a perfect crystal, H_g are constant and independent of **r**. Deviations from perfect crystallinity, in other words local lattice distortions, result in a variation of H_g, and the image is then represented as:

$$I(\mathbf{r}) = \sum_{g} H_g(\mathbf{r}) e^{2\pi i \mathbf{g}.\mathbf{r}} \tag{2.7.2}$$

The Fourier coefficients themselves can be written in terms of their amplitude and phase as:

$$H_g(\mathbf{r}) = A_g(\mathbf{r}) e^{iP_g(\mathbf{r})} \tag{2.7.3}$$

where A_g gives the amplitude of the sinusoidal lattice fringe component with vector **g** and the phase P_g describes the deviation of the fringes from their ideal position. The image $B_g(\mathbf{r})$ of the

particular set of lattice fringes can be isolated from the main image by the process of Bragg filtering, whereby a mask is placed around the positions $\pm\mathbf{g}$ of the Fourier transform of the image so that all Bragg spots outside the position are made zero, and subsequently the inverse Fourier transform of the masked image is taken. Ideal masks isolate a Fourier space region corresponding to the Brillouin zone and generate a Bragg filtered image given by:

$$B_g(\mathbf{r}) = 2A_g(\mathbf{r})\cos\{2\pi\mathbf{g}.\mathbf{r} + P_g(\mathbf{r})\} \tag{2.7.4}$$

However, practically used masks often have a Gaussian or Lorentzian shape, with the size of the mask determining the degree of lateral averaging in real space and thus the spatial resolution of the results obtained.

When there are local lattice variations, the reciprocal lattice vector is modified by a small perturbation term as:

$$\mathbf{g} \rightarrow \mathbf{g} + \Delta\mathbf{g} \tag{2.7.5}$$

and the resulting Bragg filtered image would be given by:

$$B_g(\mathbf{r}) = 2A_g(\mathbf{r})\cos\{2\pi\mathbf{g}.\mathbf{r} + 2\pi\Delta\mathbf{g}.\mathbf{r}\} \tag{2.7.6}$$

Comparing equations (2.7.4) and (2.7.6), the phase image is obtained as:

$$P_g(\mathbf{r}) = 2\pi\Delta\mathbf{g}.\mathbf{r} \tag{2.7.7}$$

Thus the local change in the reciprocal lattice vector is given by the gradient of the phase image

$$2\pi\Delta\mathbf{g} = \nabla P_g(\mathbf{r}) \tag{2.7.8}$$

An alternative and equivalent interpretation of lattice distortions is in terms of a displacement field in real space. A displacement field **u** can describe the distorted lattice through the transformation:

$$\mathbf{r} \rightarrow \mathbf{r} - \mathbf{u}$$

(2.7.9)

The Bragg image and phase image are then given by:

$$B_g(\mathbf{r}) = 2A_g(\mathbf{r}) \cos\{2\pi \mathbf{g}.\mathbf{r} - 2\pi \mathbf{g}.\mathbf{u}\}$$

$$P_g(\mathbf{r}) = -2\pi \mathbf{g}.\mathbf{u}$$

(2.7.10)

The phase image centered on **g** thus gives the component of the displacement field $u_g(\mathbf{r})$ in the direction of **g**. The complete displacement field can thus be described by the phase image centered on two non-collinear vectors $\mathbf{g_1}$ and $\mathbf{g_2}$. Any two Bragg spots can be chosen for $\mathbf{g_1}$ and $\mathbf{g_2}$. Usually, however, the two vectors are usually taken to be the highest intensity spots in the power spectrum of the Fourier transform of the TEM image. The relation between the phase image and the displacement field can be written in matrix form as:

$$\begin{pmatrix} u_x \\ u_y \end{pmatrix} = -\frac{1}{2\pi} \begin{pmatrix} g_{1x} & g_{1y} \\ g_{2x} & g_{2y} \end{pmatrix} \begin{pmatrix} P_{g1} \\ P_{g2} \end{pmatrix}$$

(2.7.11)

Finally, the strain field can then be calculated from this displacement field as:

$$\boldsymbol{\varepsilon} = \begin{pmatrix} \varepsilon_{xx} & \varepsilon_{xy} \\ \varepsilon_{yx} & \varepsilon_{yy} \end{pmatrix} = \begin{pmatrix} \frac{\partial u_x}{\partial x} & \frac{\partial u_x}{\partial y} \\ \frac{\partial u_y}{\partial x} & \frac{\partial u_y}{\partial y} \end{pmatrix}$$

(2.7.12)

Fig. 2.12 shows the results of the GPA method applied to a dislocation core in silicon [32]

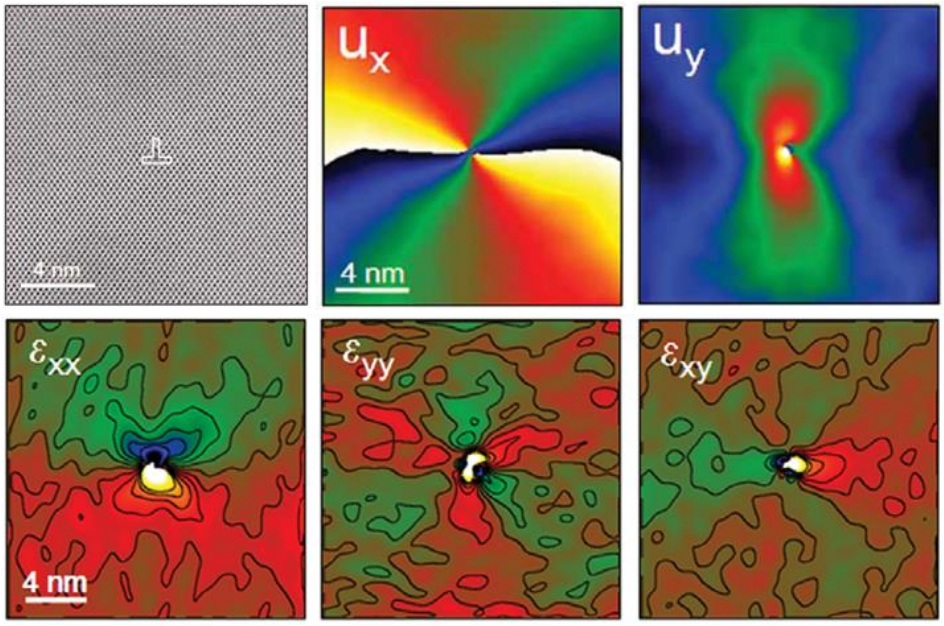

Fig. 2.12: Displacement and strain fields around an edge dislocation core in silicon as calculated by the GPA method. Bragg filtering was done around the (111) and the $(11\overline{1})$ peaks [32].

Aberration corrected annular dark field (ADF) STEM imaging and EELS of the $La_{1-x}Sr_xCoO_3$ reference polycrystals and thin film samples on $SrTiO_3$ (001) substrates shown in Chapters 4 and 5 was done in a VG Microscopes HB501UX operated at 100 kV and equipped with a NION aberration corrector and equipped with a Gatan Enfina EEL spectrometer at the Oak Ridge National Laboratory. ADF-STEM and EELS data of the films on $SrTiO_3$(110) and $LaAlO_3$ substrates were acquired with a Nion UltraSTEM operated at 100 kV with a 5^{th} order NION aberration corrector and equipped with a Gatan Enfina EEL spectrometer. Thin film specimens were prepared by conventional methods – grinding, dimpling and Ar ion milling. Reference polycrystals were crushed and dispersed on a holey carbon film to produce suitable STEM specimens. All samples were tilted to a [001] pseudocubic zone axis for STEM/EELS observation. Care was taken to try to acquire EEL spectra from relatively thin regions, with thickness values (in terms of the inelastic mean free path) being $t/\lambda < 0.5$. EEL spectra and ADF signals were obtained at every pixel of the rastered image and the laterally averaged depth profiles subsequently generated with the Digital Micrograph EELS Quantification tool, with Principal Component Analysis being used to remove random noise in the EEL spectra. GPA analysis of the high resolution *Z*-contrast STEM images shown in Chapter 4 was done using the software package in the Digital Micrograph (Gatan) environment.

Chapter 3

Epitaxial $La_{1-x}Sr_xCoO_{3-\delta}$ ($0.05 \leq x \leq 0.80$) Thin Films by On-Axis High-Pressure Oxygen Reactive DC Sputtering

3.1 Introduction

As mentioned in Chapter 1, epitaxial thin films of $La_{1-x}Sr_xCoO_3$ (LSCO) and other cobaltites are of great interest to the scientific community, both for fundamental physics such as spin state transitions [1], magneto-electronic phase separation [2], spin polarization studies for oxide spintronics [3], strain induced ferromagnetism in $LaCoO_3$ [4] and ferrimagnetism in $PrCoO_3$ [5], coercivity enhancement in $Nd_{0.5}Sr_{0.5}CoO_3$ [6], etc., as well as practical applications as electrodes in solid oxide fuel cells [7] and ferroelectric devices [8,9], electrocatalysis [10], gas sensors [11, 12] and oxygen separation membranes [13]. A number of synthesis routes have thus been developed to deposit high quality epitaxial LSCO films, including reactive sputtering [14, 15], pulsed laser deposition (PLD) [16, 17], sol-gel synthesis [18] and metal-organic chemical vapor deposition (MOCVD) [19]. The propensity of LSCO thin films to form oxygen vacancies [20] and the rather narrow phase stability window of LSCO with respect to the (La+Sr)/Co ratio [21] make the synthesis of phase pure and stoichiometric LSCO thin films extremely challenging – thus each of the aforementioned techniques have been carefully optimized with regards to the deposition temperature, pressure, ambient gas composition and cooling protocol. Amongst them, reactive sputtering is especially attractive from a practical device standpoint, since it is easily scalable to large area targets and substrates for high volume manufacturing. However, conventional reactive sputtering using an Ar/O_2 gas mixture in the 10 – 200 mTorr pressure range suffers from a number of drawbacks. The oxygen atoms in the gas mixture create a large number of negatively charged energetic oxygen ions which are accelerated towards the substrate (anode) and cause re-sputtering of cations from the film [22, 23]. Effectively this etches the film simultaneously with depositing it, and causes severe cation non-stoichiometry and inhomogeneity. This re-sputtering may be somewhat mitigated by reducing the O_2 partial pressure in the sputtering gas mixture; however this typically results in oxygen deficient films which often require post growth annealing at high temperatures to recover stoichiometry.

Alternatively, the substrates may be placed outside the main path of the sputtered beam (in the so called off-axis configuration); however this significantly reduces the deposition rate and is also not as directly scalable to large areas as the on-axis geometry [24]. Another approach is to increase the Ar partial pressure without decreasing the O_2 partial pressure [14], but this severely stresses the heating and pumping components of the deposition system. In order to utilize the process scalability of reactive sputtering, yet overcome the challenges of conventional sputtering, in this chapter we introduce the epitaxial growth of LSCO films by a relatively less commonly used sputtering technique that uses high oxygen pressures, no Ar in the gas mixture and an on-axis sputtering geometry. The high oxygen pressure – on the order of 2 mbar (1 mbar ~ 0.75 Torr) – reduces the mean free path of the oxygen anions in the discharge by more than a factor of 10 (the mean free path of an oxygen atom at 2 mbar is ~ 36 μm *cf.* ~ 530 μm at 100 mTorr). This thermalizes the oxygen anions arriving at the substrate, thereby eliminating re-sputtering of cations in the film and allowing the use of an on-axis sputtering geometry. The use of pure oxygen as the sputtering gas leads to better oxygenation of the films and suppresses the formation of secondary phases often seen at high temperatures in other sputtering techniques [14]. The on-axis geometry also yields growth rates that are more than 10 times higher than off-axis magnetron sputtering. As we shall show in detail, this results in better epitaxy and microstructure of the cobaltite films, which ultimately leads to better electronic and magnetic properties. The high-pressure oxygen sputtering technique was originally developed in 1988 at the Forschungzentrum Jülich by U. Poppe and others [25, 26] to directly deposit epitaxial superconducting films of $YBa_2Cu_3O_7$ without requiring any post growth thermal annealing. The superior microstructure and superconducting T_C's of the films obtained by this technique have since led to its adoption for a wide variety of oxide thin films, including multiferroic $BiMnO_3$ [27], ferromagnetic $La_{2/3}Ca_{1/3}MnO_3$ and $La_{0.8}Sr_{0.2}CoO_3$ [28, 29], ferroelectric $BaTiO_3$ [30] and the high-*k* dielectric HfO_2 [31]. A number of groups have also reported detailed characterizations of the high-pressure oxygen plasma by Langmuir probes and optical emission spectroscopy [32 – 34]. With the increasing adoption of the high pressure sputtering technique, and the great interest in the synthesis of high quality epitaxial cobaltite thin films, our work thus fills an important gap by providing the most comprehensive report to date of the high-pressure sputtered epitaxial growth of LSCO thin films. Using $La_{0.5}Sr_{0.5}CoO_{3-\delta}$ (LSCO50) as our prototypical cobaltite, we systematically examine the effect of each sputtering parameter on the growth morphology and the electronic and magnetic properties of the LSCO50 films.

3.2 The high pressure sputtering system

Fig. 3.1 shows the pumping diagram of the high-pressure oxygen reactive sputtering chamber. The main chamber is essentially a 5.5" spherical cube with no load lock. Samples are loaded and unloaded from the top port with three other ports being used for the turbomolecular pump (TMP), the substrate heater feedthrough and the target movement arm respectively. The remaining two ports serve as quartz viewports. The chamber is pumped by an Agilent V-81M TMP backed by a Vacuubrand MD 4 NT diaphragm pump, with the backing pump doubling up as the roughing pump. The entire pumping system is oil-free and oxygen compatible and the system achieves a base pressure of ~ 1 x 10^{-6} mbar after 3 – 4 hours of pumping. An Oerlikon Leybold IONIVAC ITR-90 gauge is used to measure the base pressure while the TMP backing

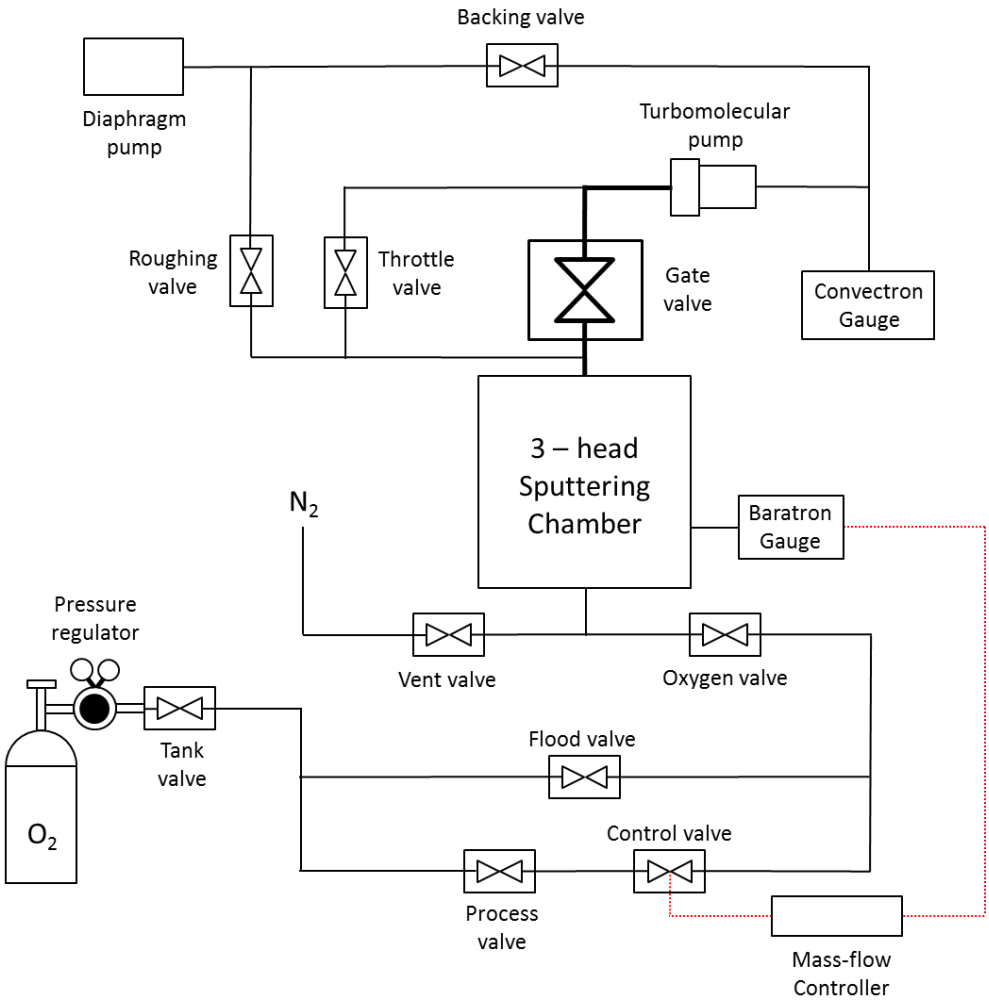

Fig. 3.1: Schematic pumping diagram of the high-pressure oxygen reactive sputtering system.

pressure is monitored by a K. J. Lesker Convectron® equivalent gauge. The process gas used is 99.998% research grade oxygen (Matheson) delivered to the chamber approximately 5" from the plasma. During sputtering, the chamber pressure is maintained at 1.5 – 3 mbar with the main VAT gate valve closed and the TMP pumping through a 1/8" high impedance stainless steel line. The gas pressure during sputtering is measured by an MKS Baratron® Type 626 capacitive manometer and the gas flow is regulated by an MKS 248A flow control valve controlled by an MKS Type 250 pressure/flow controller. At a pressure of 1.75 mbar and with the TMP throttled, the gas flow is approximately 31 sccm. Pure dry nitrogen serves as the vent gas and the chamber is exhausted to a fume hood to prevent oxygen buildup in the laboratory space.

Fig. 3.2 (a) shows the schematic of the DC sputtering gun and the heater assembly. The 1.5" conductive DC target (front-to-back resistance ~ 1 Ω) is bonded to a 2" copper backing plate (details of the target preparation and bonding are given in Section 3.4) which is then screwed onto the water-cooled copper cathode. It must be noted that although the sputter head can accommodate 2" diameter targets, a smaller target diameter was deliberately chosen so as to enhance the plasma current density and thereby the oxygen ion density. A thin lead foil provides conformal electrical and thermal contact between the backing plate and the cathode. The cathode is surrounded by an insulating alumina spacer which isolates it from the outer grounded

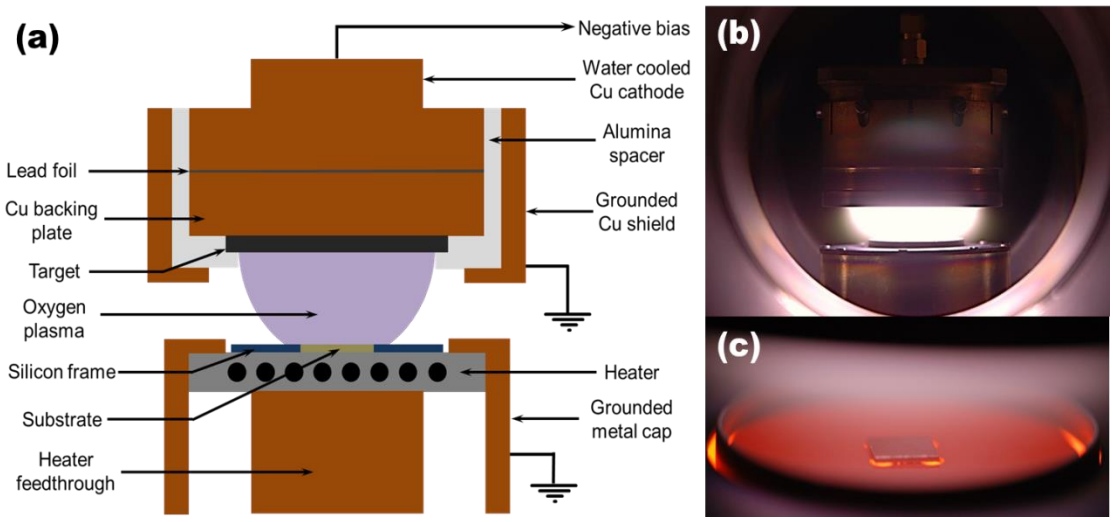

Fig. 3.2: (a) Schematic diagram of the DC sputtering gun and the heater assembly. (b) Photograph showing the DC sputtering gun, the oxygen plasma and the heater assembly. (c) Photograph of the oxygen plasma over a heated substrate placed within a silicon frame.

copper shield. A Heinzinger PNC 600–300 NEG high–precision switched mode power supply (600V, 300mA max) is used to provide negative bias between the cathode and the outer shield.

The heater assembly consists of a cylindrical block with a grounded outer metal cap. The heating element is a meandering strip of Kanthal® (Sandvik Gmbh) FeCrAl resistance heating alloy that is machined from a solid piece and spot welded to terminal leads. The heater assembly is capped by a high temperature stainless steel plate and the temperature measured with a Ni/NiCr thermocouple that is embedded in a small bore inside the assembly. The temperature is read out and controlled with a Eurotherm 2404 temperature controller. The heater assembly is rated up to 920 ºC. Substrates are simply placed on top of the stainless steel top plate; heat transfer between the heater and the substrates is thus through surface conduction. Depending on the temperature and oxygen pressure, the temperature of the top surface of the substrates is therefore 50 – 150 ºC lower than the thermocouple readout. The substrates are surrounded by a silicon frame to reduce radiative heat loss from the heater as well as protect the heater surface from sputtered elements. The heater and gun assembly are cooled by flowing water at 20 – 21 ºC. The substrate – target distance can be adjusted by means of two set screws and is usually maintained in the 15 – 20 mm range. Laterally, the substrates are placed as close to the center of the radially symmetric plasma discharge as possible and are not rotated. Fig. 3.2 (b) shows the DC oxygen plasma and the heater assembly, while Fig. 3.2 (c) shows the oxygen plasma over a heated substrate placed within a silicon frame.

3.3 The high pressure oxygen DC plasma

As mentioned earlier, the high-pressure oxygen DC plasma is controlled by a 300V, 600 mA switched mode power supply that can operate in both constant-voltage and constant-current modes. In the absence of a plasma, the power supply is voltage-controlled. The plasma is struck at a relatively low pressure of 0.6 mbar to minimize the strike voltage and the current limit set to 18 mA. Under these conditions, the voltage is slowly increased until the plasma is struck at a voltage ~ 450 – 490 V. Once the plasma is ignited and a stable glow discharge established, the voltage immediately drops to 275 – 325 V and the power supply automatically switches to a current-controlled mode. Thereafter, the plasma current is the control parameter and the voltage simply a function of both the current and the pressure. The pressure and current are then slowly

and alternately increased to their operational values under growth conditions, always limiting the power ramp rate to ~ 0.3 W/s to minimize target cracking. Although the power supply is capable of sustaining 180W of continuous power, cooling requirements and arcing concerns limit the DC plasma power to 65 – 70 W, the current to 200 mA for a 1.5" target (giving a current density of ~ 17.5 mA/cm^2) and the voltage to ~ 350 V. Fig. 3.3 shows the voltage characteristics of the DC plasma as a function of both pressure and current. It is immediately obvious that the voltage increases with increasing current and decreasing pressure, thereby putting an upper limit on the useable current and a lower limit on the useable pressure. Furthermore, high pressures tend to not only reduce the voltage but also limit the spatial extent of the plasma, thereby severely reducing the growth rate and drastically affecting film properties (details of the pressure dependence of LSCO growth are discussed in Section 3.8). All parametric experiments in this chapter were thus performed at pressures and currents that kept plasma voltage in the 320 – 340 V range. Fig. 3.4 shows the DC plasma at selected currents and pressures, highlighting the effect of both parameters on the spatial extent of the discharge.

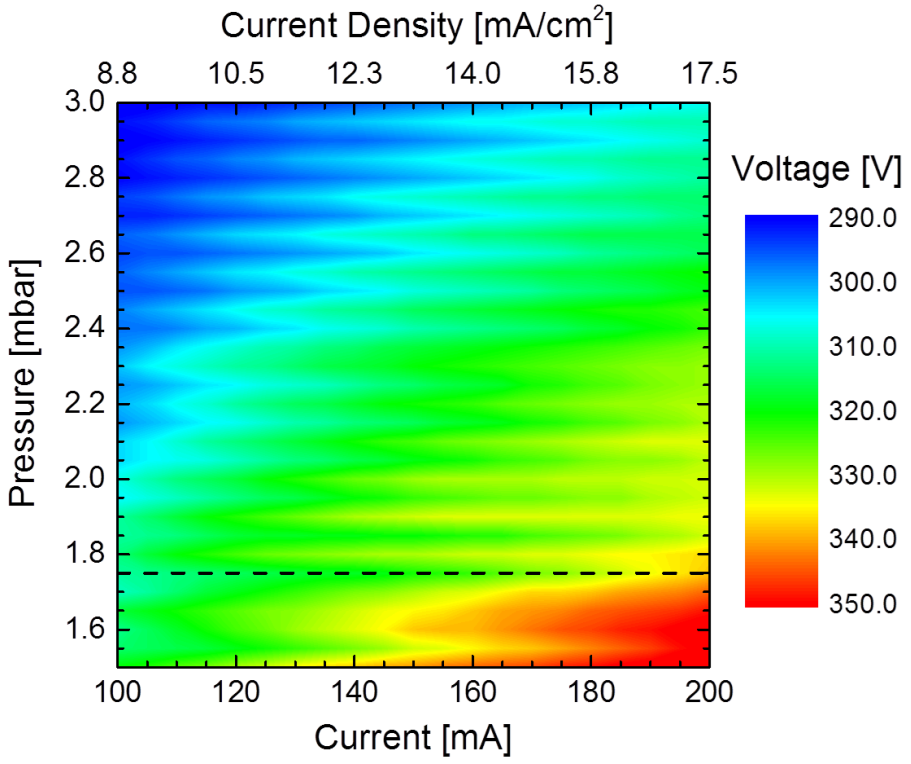

Fig. 3.3: Voltage variation of the DC high-pressure oxygen plasma as a function of the pressure and current. The current density is calculated for a 1.5" diameter target. The black dashed line shows the 1.75 mbar pressure that has been found to be optimal for LSCO growth. Oscillations are rastering artifacts.

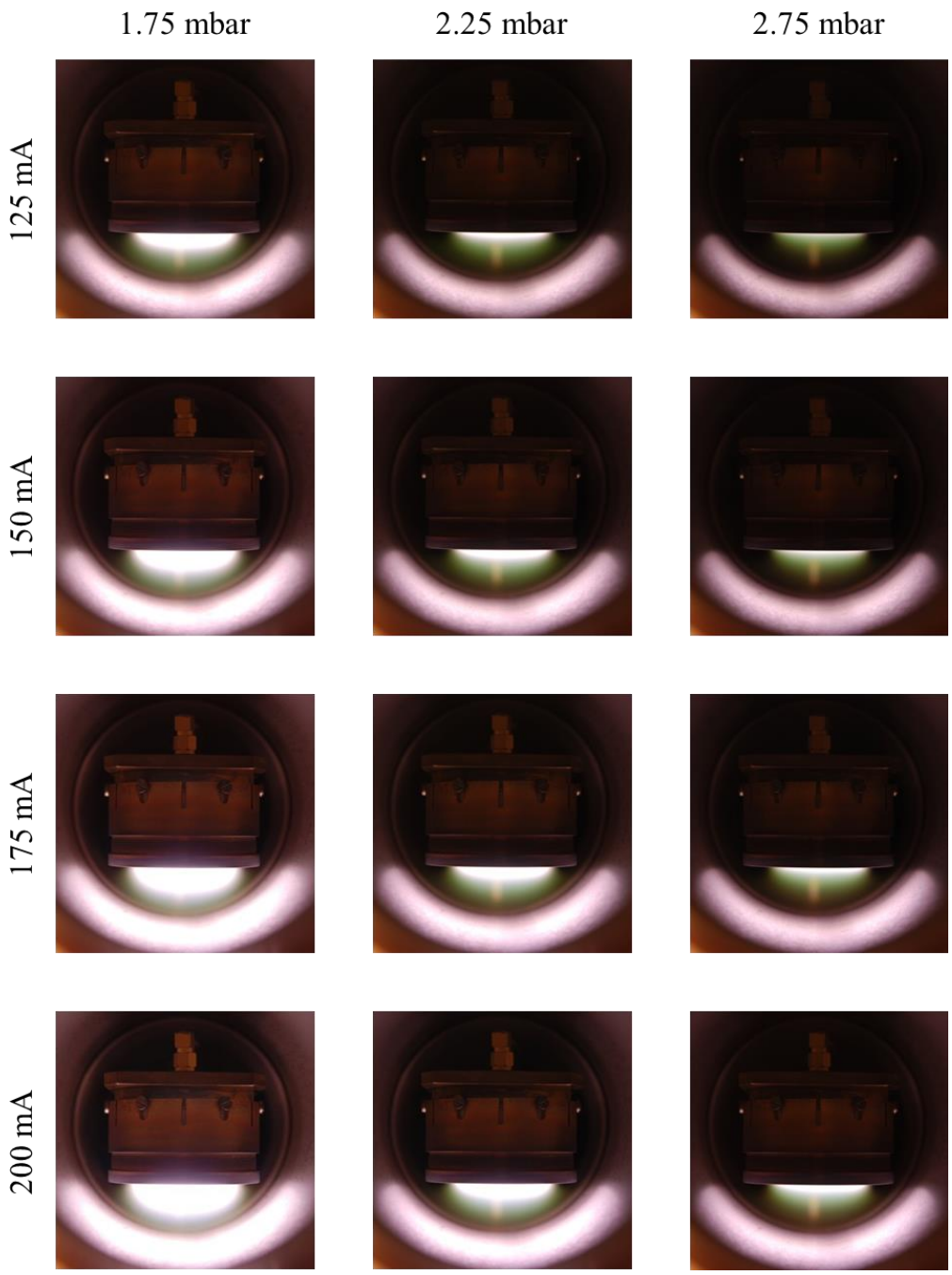

Fig. 3.4: Spatial extent of the DC plasma plume at different pressures and currents. All photographs were taken at identical exposures (ISO 100, f4.5, 5s). The pink arc at the bottom of each photograph is the plasma light reflected off the chamber walls

3.4 $La_{0.5}Sr_{0.5}CoO_3$ target preparation and bonding

LSCO targets were prepared by the solid-state reaction of La_2O_3 (Alfa Aesar, 99.9%), Co_3O_4 (Alfa Aesar, 99.7%) and $SrCO_3$ (Sigma-Aldrich, 99.9%) [35]. Stoichiometric quantities of the reactant powders were weighed and thoroughly ground together for 2 hours. La_2O_3, being hygroscopic, was dried in air at 1000 ºC for 24 hours and weighed while hot. The powders were subsequently calcined in air at 1000 ºC for 7 days, with two intermediate grindings of 30 minutes each. The reacted powders were cold pressed into disks 2" in diameter and ~ 3 mm in thickness at 13,000 psi and sintered in air at 1200 ºC for 24 hours. A liquid binder comprising deionized water (350 ml), glycerine (100 ml, Fisher Scientific, 99.5%) and polyvinyl alcohol (10g, Sigma-Aldrich, 99%, hydrolyzed) was used to provide green strength to the pressed disks. The sintering step used a temperature ramp rate, for both heating and cooling, of 0.5 ºC/minute to minimize thermal stresses and maintain oxygen stoichiometry. The sintered disks were verified to be phase pure by powder XRD and the ferromagnetic T_C verified by SQUID magnetometry. The 2" disks were then sanded down to 1.5" diameter targets. Indium metal was soldered to one side of the targets with a fine tip soldering iron and the targets subsequently bonded to an indium coated copper backing plate on a hotplate at ~ 200 ºC. The bonded assembly was allowed to cool to room temperature and the excess indium sanded off. Precision machined alumina and Macor® washers were then used to mask the uncovered regions of the copper backing plate so as to expose only the LSCO target to the oxygen plasma.

3.5 Substrates

The substrates used for the experiments in this chapter were commercial $SrTiO_3$ (001) (STO (001)) and $LaAlO_3$ (001) (LAO (001)) single crystals, 5 x 5 x 0.5 mm, single side polished (MTI Corporation, Richmond, CA). $SrTiO_3$ (cubic, a = 3.905 Å) and $LaAlO_3$ (orthorhombic, a_{pc} = 3.789 Å, *pc* indicating the pseudocubic lattice parameter) are closely lattice matched with LSCO50 (cubic, a = 3.836 Å) and offer a +1.8% (tensile) and -1.2% (compressive) mismatch respectively. Prior to loading in the chamber, each substrate was thoroughly blown with a high velocity dry nitrogen stream. No solvent cleaning was used as this was found to often leave unwanted residue. Before deposition, the substrates were annealed at 900 ºC in 0.6 mbar oxygen to remove any organic surface contamination. No surface treatments were used to obtain

terraced steps on STO (001) as this was found to have no influence on the structural and electronic properties of the LSCO films at the thicknesses measured.

3.6 Process variables

As already mentioned, the four primary process variables that can be tuned to optimize the sputter deposition are (1) the substrate temperature, (2) the ambient oxygen pressure, (3) the plasma current, and (4) the target to substrate distance. Amongst these, only the substrate temperature is somewhat of an independent variable, with the pressure, current and target to substrate distance being closely coupled with each other. Effectively, the deposition and growth of the film is a sensitive function of the position of the heated substrate within the plasma plume – the greater the spatial extent of the plume, the further away the substrate can be with the same results. Essentially, it is entirely possible to obtain films with identical properties at different pressure-current-distance combinations. For the sake of simplicity, therefore, the target – substrate distance has been kept constant at 18.5 – 19 mm for every experiment, while each of the other parameters was systematically varied. A fifth variable that has also been held constant is the post-growth annealing and cooling protocol. For each experiment, post growth, the chamber was flooded with 800 mbar oxygen while holding the substrates at the growth temperature. The heater was then turned off and the substrates allowed to cool to room temperature at their natural cooling rates, the process taking 20 – 30 minutes. The films were then unloaded after venting the chamber with dry nitrogen. The next three sections in this chapter discuss the effect of each process variable on the structure, transport and magnetic properties of the LSCO50 films. For each sample, the structural characterization was performed on a Panalytical X'Pert high resolution x-ray diffractometer (Section 2.1 and 2.2) while transport measurements were made in a van der Pauw configuration with an AC resistance bridge (Section 2.4) and magnetic measurements made in a Quantum Design MPMS-*XL* SQUID magnetometer (Section 2.5) with the field applied in the plane of the sample. The temperature dependent magnetizations were measured on warming under a 1000 Oe field, with the sample having been cooled in the same 1000 Oe field while hysteresis loops were measured between +/-70 kOe at 5 K.

3.7 Temperature dependence

The substrate temperature is perhaps one of the most important parameters in any form of thin film growth. It controls, in part, the kinetic energy imparted to the film atoms during growth and has a significant impact on the nucleation rate, surface diffusion of adatoms, film crystallization and epitaxy, and thermal stresses generated by differences in the thermal expansion coefficients of the film and the substrate. Along with the adatom flux, it also determines if the film growth is kinetically limited or achieves thermodynamic equilibrium, and thereby often dictates the evolution of the growth from a two-dimensional (2D) layer-by-layer mode to a three-dimensional (3D) Volmer-Weber island mode [36]. Further, in ternary and quaternary oxides such as LSCO, the temperature is also a determining factor of the cation stoichiometry and oxidation kinetics of the film. Therefore, any growth protocol must necessarily optimize the substrate temperature so as to obtain the desired structure – property relationship in the film. Epitaxial thin films of LSCO have been synthesized by a number of research groups who have reported a rather wide temperature window spanning 500 ºC – 850 ºC [14 – 17, 19, 29, 37 – 43]. The primary reason for this is the enormous difference in growth rates between the different techniques, ranging from ~ 2 Å/min. for RF sputtering to more than 200 Å/min. with PLD [15, 37], imposing different kinetic limits on the film growth and morphology. A comprehensive study by Sharma *et al.* of the influence of the growth temperature on the structure, transport and magnetic properties of LSCO50 films (by DC magnetron sputtering) narrowed the temperature window to a much smaller range of 600 ºC – 625 ºC, with lower temperatures resulting in amorphous films and significant cation non-stoichiometry and higher temperatures leading to CoO precipitates, although traces of Co-rich inclusions were detected by STEM/EELS even at 600 ºC [44]. The presence of these secondary phases necessitated a post-growth annealing step at 500 ºC in flowing O_2 to obtain phase-pure LSCO with optimal structural and electronic properties. In this section, we discuss the influence of the substrate temperature on the structure, transport and magnetic properties of high pressure oxygen sputtered LSCO50 on STO (001) and LAO (001) substrates. In all cases, the pressure was held fixed at 1.75 mbar and the current at 200 mA, in keeping with the constraints discussed in Section 3.3 while the temperature was varied in the range of 600 ºC – 800 ºC. The film thicknesses were held approximately constant in the 110 – 160 Å range.

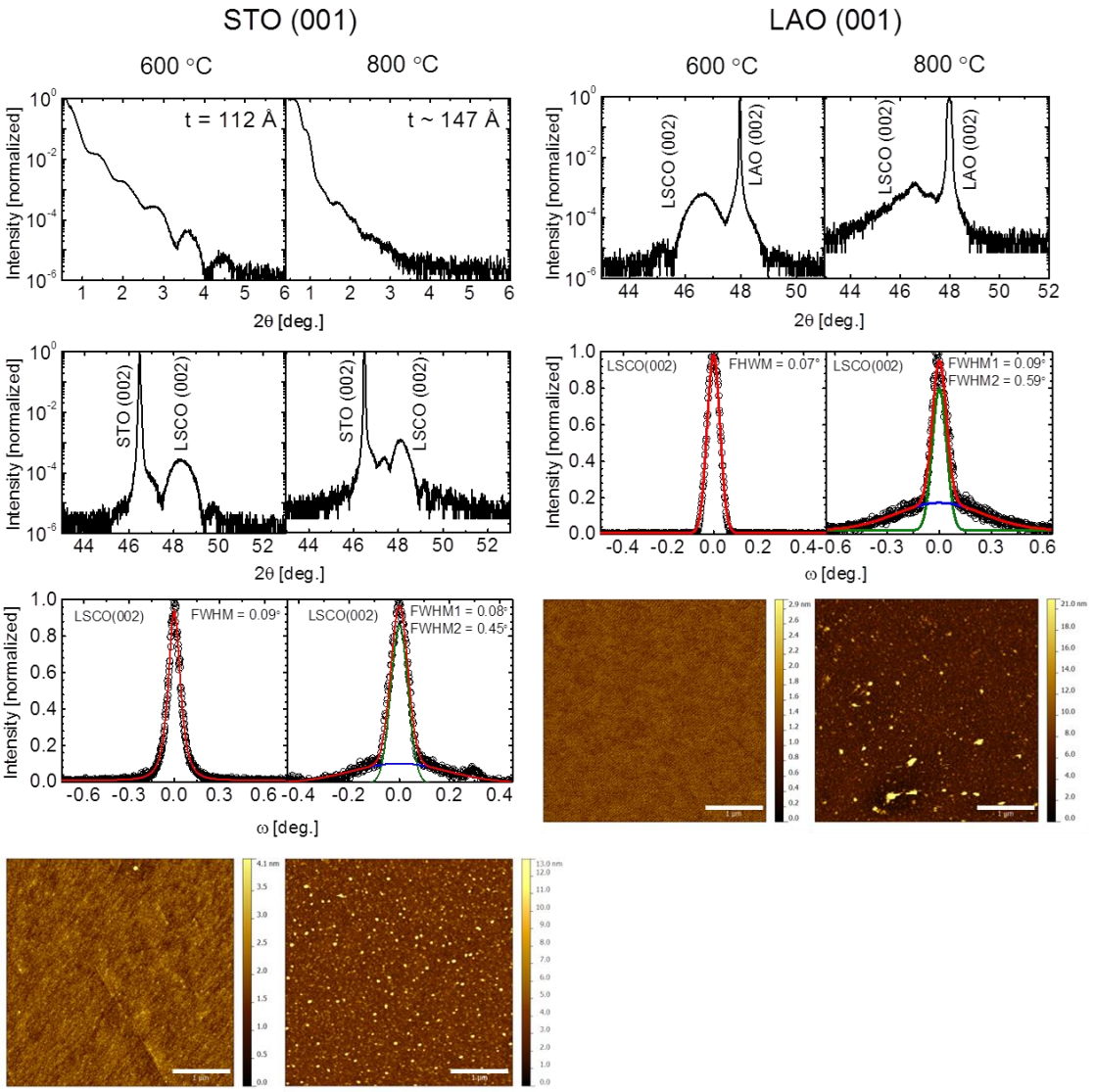

Fig. 3.5: Structural properties of LSCO50 films on STO (001) and LAO (001) at the growth temperature extremes of 600 ºC and 800 ºC, as characterized by GIXR, WAXRD, rocking curves and surface morphology seen with an AFM. The scale bars for the AFM images are 1μm.

Fig. 3.5 shows the structural properties of LSCO50 films on STO (001) and LAO (001) at the growth temperature end points of 600 ºC and 800 ºC, as exemplified by grazing incidence x-ray reflectivity (GIXR), wide angle x-ray diffraction (WAXRD), rocking curve analysis and surface morphology seen with an atomic force microscopy (AFM, Section 2.6.1). GIXR data is only shown for STO (001) since the similar values of x-ray scattering length densities of LSCO and LAO result only in a θ^{-4} Fresnel fall-off with no visible Kiessig fringes. The differences

between the two growth morphologies are striking. At 600 ºC, the film on STO (001) shows both prominent Kiessig fringes in GIXR as well as finite size oscillations in WAXRD, indicating a vanishingly small surface roughness at both long (~ 50 μm) and short (~ 50 nm) length scales respectively. Similar finite size oscillations are observed on LAO (001) as well. These morphologies are in excellent agreement with the AFM images on both STO (001) and LAO (001), which have RMS roughness values of 4.3 Å and 2.5 Å over a 4 μm x 4 μm area respectively. On both substrates, WAXRD scans show only the (00*l*) family of peaks with no secondary phases, indicating phase pure epitaxial films, while narrow rocking curves, which can be fitted to a single Gaussian with an FWHM ~ 0.07º – 0.09º, indicate coherently strained films with low mosaicity. Film roughnesses being on the same order as the substrates indicate a 2D growth mode, although in the absence of any RHEED data, it is not possible to distinguish between layer-by-layer and step-flow modes [36].

Films grown at 800 ºC, on the other hand, are significantly different. On STO (001), GIXR shows weak fringes with a sharp fall-off, although finite-size oscillations are still observed in WAXRD. This is indicative of films that are smooth on the nanometer lateral length scales but have significant roughness on the micron length scales. This is clearly seen in the AFM images which show surface asperities that are 50 – 100 nm laterally but are 130 – 150 Å in height. Observation of metallic transport precludes the possibility of these asperities being isolated LSCO islands; rather, they are postulated to be LSCO clusters coalesced over a continuous LSCO film. This points to a 3D Volmer-Weber or a more likely 2D-3D mixed Stranski-Krastanov growth mode, although a detailed thickness dependent morphological study is required to distinguish between the two. A similar surface morphology is seen on LAO (001) as well. The increase in surface roughness with increasing growth temperature is attributed to the high surface energy of LSCO which results it preferring *not* to wet either the STO or the LAO surface. Given sufficient thermal energy, therefore, LSCO adatoms are able to migrate across the substrate surface and coalesce into clusters to minimize the free surface area. This is in good agreement with the observations of Malavasi *et al.* [45] who reported a significant increase in the roughness of $Nd_{0.8}Sr_{0.2}CoO_3$ films on STO (001) upon a high temperature anneal at 900 ºC, as well as those of Torija *et al.* [14] and Kim *et al.* [46], both of whom reported a growth mode evolution from 2D to 3D with increasing thickness. However, despite the presence of coalesced clusters, both films show epitaxial registration with the substrate as evidenced by the (00*l*) family of peaks seen in the WAXRD scans. Interestingly, rocking curves on both substrates

show a distinct shape that can only be fitted with two Gaussian peaks, with the narrow peak having an FWHM ~ 0.08º - 0.09º and the broad peak ~ 0.5º. Such double Gaussian rocking curves have been observed by Sharma *et al.* and attributed to partially strain relaxed films possessing a coherently strained bottom layer and a partially relaxed top layer [44]. In our case the broad peaks, which are almost an order of magnitude broader than the narrow peaks, are attributed to the clusters with the narrow peak arising from the strained bottom layer. It must be noted that no presence of any secondary phases was observed in the WAXRD even at this high growth temperature, in stark contrast with the CoO peaks observed by Sharma *et al.* at 700 ºC. This almost unequivocally demonstrates the superior oxygenation of high-pressure oxygen sputtered LSCO50 films over those synthesized by conventional O_2/Ar sputtering. Fig. 3.6 summarizes the key structural properties of the LSCO50 films over the investigated deposition temperature range. It can be seen that increasing the temperature from 600 ºC to 800 ºC decreases the growth rate by almost 12%, from ~ 18.5 Å/min. to ~ 16.25 Å/min. This is a well-

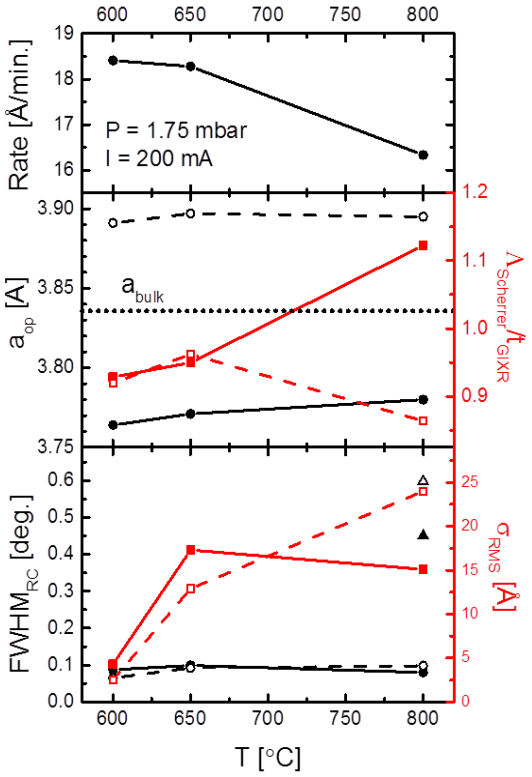

Fig. 3.6: Summary of the structural properties of LSCO50 films on STO (001) and LAO (001) as a function of growth temperature. In all panels, closed symbols with solid lines indicate STO (001) and open symbols with dashed lines indicate LAO (001). Data plotted with circles and triangles belong to the left axes while squares belong to the right axes. Triangles indicate the broad RC component.

known phenomenon and is caused by a reduction in the nucleation rate of the film with increasing substrate temperature [36]. Fig. 3.6 also shows a small monotonic increase in the out-of-plane lattice parameter of the films under tensile strain on STO (001), indicative of partial strain relaxation at higher growth temperatures and consistent with the formation of clusters. Compressively strained films on LAO (001) show a negligible change in lattice parameter. Interestingly, the Scherrer coherence lengths Λ, normalized to the GIXR film thickness, show diverging trends on the two substrates. In each case, the peak width was obtained from a pseudo-Voigt fit to the (002) WAXRD peak with a shape factor of 0.9. On STO (001), the Λ/t_{GIXR} shows a monotonic increase, consistent with formation of clusters at higher temperatures. On LAO (001), on the other hand, the ratio shows a *decreasing* trend, pointing to the dominance of microstrain in the clusters over the increase in the coherence length. The increasing trends in both the rocking curve widths and RMS roughnesses are consistent with the observations of Fig. 3.5.

Fig. 3.7 summarizes the magnetic and transport properties of the LSCO50 films on the two substrates. On both STO (001) and LAO (001), the ferromagnetic T_C as well as the saturation

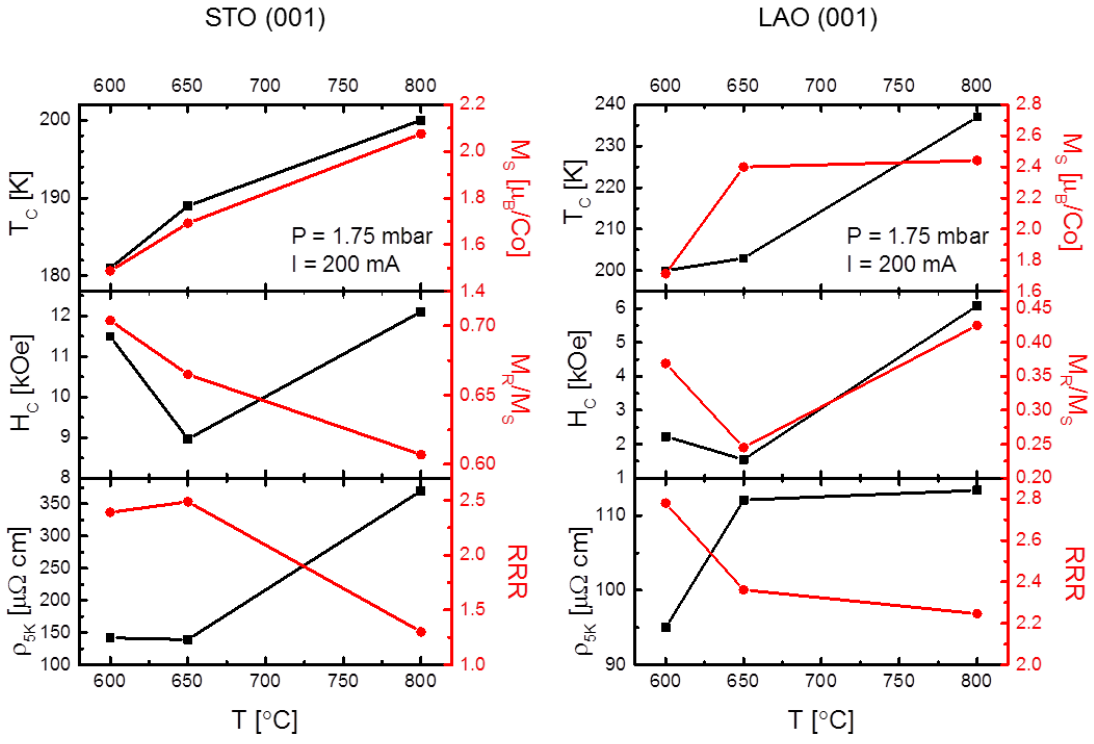

Fig. 3.7: Summary of the magnetic and transport properties of LSCO50 on STO (001) and LAO (001) as a function of growth temperature. In each panel, data plotted with square symbols belong to the left axis while those with circles belong to the right axis.

magnetization M_S show an increasing evolution towards the bulk values of 250 K and 1.92 μ_B/Co. Both trends are consistent with the increase in strain relaxation with increasing temperature. Interestingly, M_S values on both substrates exceed the bulk value at high temperatures. Although such enhanced values of M_S have been reported previously [2] and have been attributed to a possible transition of the Co ions to a higher spin state, a more likely explanation in this case is the overestimation of M_S as a result of neglecting the contribution of the clusters in the normalization process (which simply multiplies the GIXR thickness with the area of the substrate to estimate the number of Co ions). Further, both the coercivity H_C and the remanence M_R show a distinct, though non-monotonic, trend with increasing temperature. Although the exact trend is not understood, it is attributed to a possible change in the magnetic anisotropy and the strain-driven magneto-electronic phase separation (MEPS), which was shown to greatly enhance the coercivity of $Nd_{0.5}Sr_{0.5}CoO_3$ films [6], as a result of temperature induced strain relaxation. Finally, looking at transport, films on both STO (001) and LAO (001) show an increase in the 5 K resistivity as well as a decrease in the residual resistivity ratio (RRR) (which is calculated here as the ratio of the resistivities at 300 K and 5 K) as a result of increasing the growth temperature. Both trends can be attributed to enhanced scattering of the carriers and are consistent with the evolution of the films from coherently strained epitaxial layers to a clustered and "granular" morphology. It must be noted that both ρ_{5K} and the RRR for films grown at 600 ºC are comparable to single crystal values, the numbers being 90 μΩ cm and ~ 4.2 respectively for x = 0.30 crystals [47].

3.8 Pressure dependence

As with any other reactive sputtering process, the high-pressure oxygen sputtering technique is acutely sensitive to the ambient gas pressure during deposition. A major advantage of this process is the simplicity offered by the presence of a single gas species – oxygen, which obviates the need for the rather non-trivial deconvolution of the closely coupled effects of the total gas pressure and the O_2 partial pressure encountered in conventional Ar/O_2 sputtering [14, 15]. The effect of the gas pressure on the plasma characteristics has already been discussed in detail in Section 3.3. In this section we discuss its effect on the structure and electronic properties of the LSCO50 films on STO (001) and LAO (001), once again using GIXR, WAXRD, rocking curves, transport and magnetometry. In all cases, the temperature was held

fixed at 800 ºC and the current at 200 mA while the pressure was varied between 1.75 mbar and 2.75 mbar. The film thicknesses were held approximately constant in the 150 – 170 Å range.

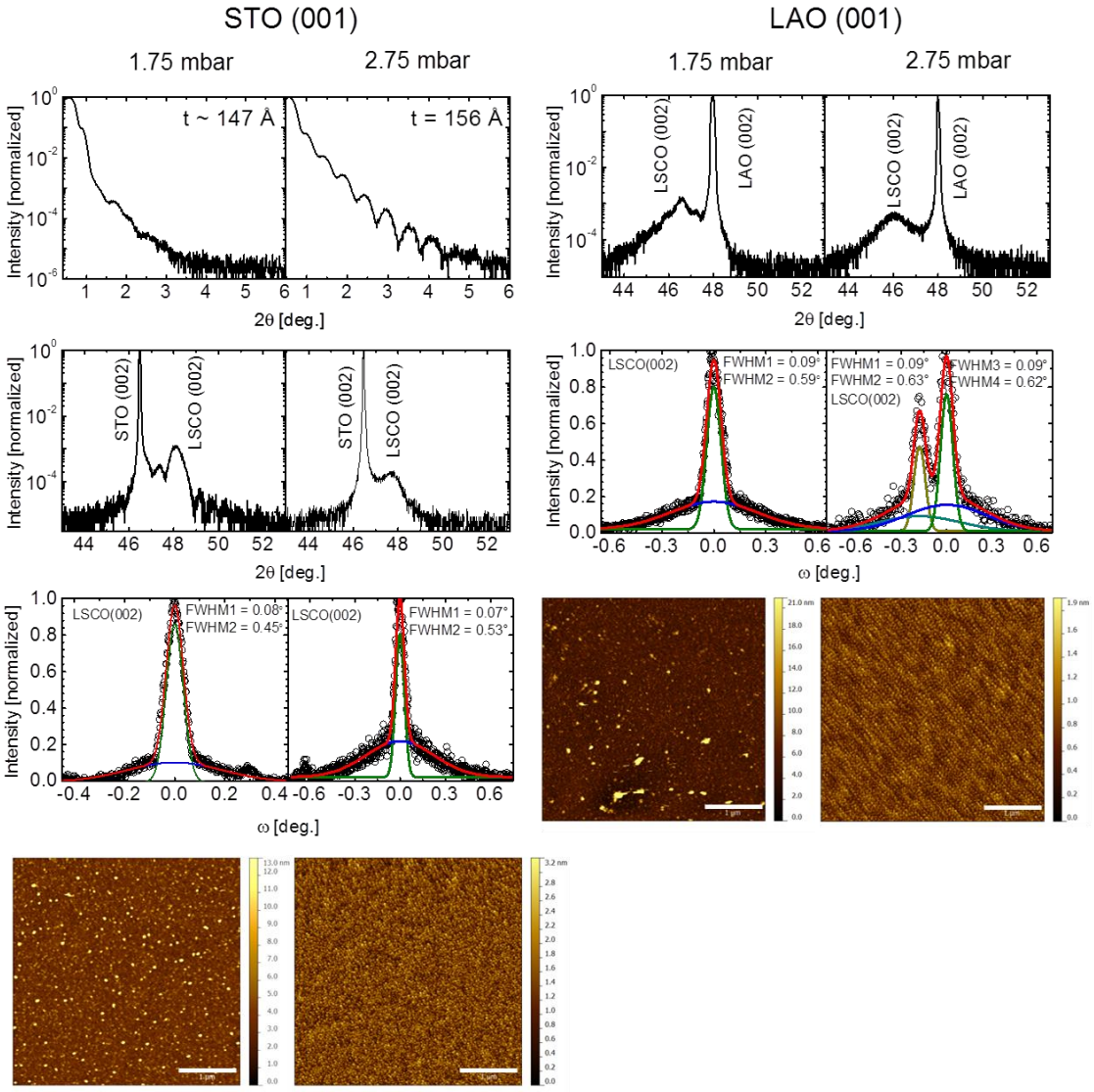

Fig. 3.8: Structural properties of LSCO50 films on STO (001) and LAO (001) at the growth pressure extremes of 1.75 mbar and 2.75 mbar, as characterized by GIXR, WAXRD, rocking curves and surface morphology seen with an AFM. The scale bars for the AFM images are 1μm.

Fig. 3.8 shows the structural properties of LSCO50 films on STO (001) and LAO (001) at 1.75 mbar and 2.75 mbar. It is immediately obvious that the film morphologies at the two pressure extremes are almost complementary. While the films grown at 1.75 mbar are rough on longer

length scales (evidenced by weak Kiessig fringes in GIXR) but smooth at shorter length scales (indicated by the presence of WAXRD finite size oscillations), the complete opposite effect is seen in the films grown at 2.75 mbar. Prominent Kiessig fringes are observed in GIXR on STO (001). However, this apparent long length scale smoothness is somewhat misleading. As clearly seen with an AFM, films on both STO (001) and LAO (001) are still clustered, although in this case the cluster density is much higher and neighboring clusters touch each other, in stark contrast with the sparse cluster distribution seen at 1.75 mbar. The cluster sizes are approximately constant ~ 25 – 30 Å. RMS roughness calculated from the AFM images are 2 – 3 Å on both substrates; these anomalously low numbers are the result of the inability of the finite sized AFM tip to probe the inter-cluster valleys. Although the exact cause of this dramatic change in morphology is unclear, it could possibly be attributed to the effect of the sputtering pressure both on the plasma properties as well the substrate surface. As seen in Section 3.3, increasing the pressure greatly shrinks the spatial extent of the plasma. As a result, at 2.75 mbar, the substrate is well outside the most intense and visible region of the plasma discharge. Furthermore, a reduction in the mean free path of the sputtered radicals places the substrate many more mean paths away from the target as compared to the 1.75 mbar situation. Since the widely different atomic masses of the sputtered radicals results in them having different mobilities within the plasma, it is possible that the compositional ratio of the cation radical flux reaching the substrate is significantly different from that of the target. In the light of the block-by-block growth method proposed by Locquet *et al.* and Varela *et al.* [48, 49], wherein film growth begins with the nucleation of binary oxides on the substrate surface and proceeds with the high temperature conversion of the component binaries to the stoichiometric perovskite phase, this variation of the flux composition would lead to incomplete reactions between the binaries and result in a granular mixture of the perovskite juxtaposed with the binaries. This hypothesis is consistent with the lower LSCO (002) peak intensity (normalized to the substrate) seen in the WAXRD scan on both substrates at 2.75 mbar compared to 1.75 mbar. However, this would also imply a binary phase fraction that is small enough to not be detected as secondary phase peaks in WAXRD. Granularity of the film would be further exacerbated due to a slightly lower temperature of the substrate surface (due to increased thermal coupling with the higher pressure gas) which would limit the lateral migration of the nucleated adatoms. However, more detailed spectroscopic and elemental analysis, both of the plasma as well as the film, is needed to confirm this hypothesis and possibly establish a novel structure-zone diagram for high-pressure reactive sputtering. Finally, rocking curves on both substrates show similar 2-

Gaussian curves indicating similar mosaicity at the two pressure extremes. The multiple peaks seen on LAO (001) are due to the well-known twinning observed in LAO and are often seen in films on this substrate. Fig. 3.9 summarizes the key structural properties of the LSCO50 films over the investigated pressure range. It can be seen that increasing the pressure from 1.75 mbar to 2.75 mbar reduces the growth rate by almost a factor of 2, from ~ 16.25 Å/min. to ~ 8.5 Å/min. This is a well-known effect of sputtering gas pressure and is caused by the reduced gas-phase mobility of sputtered species due to increased scattering from the gas molecules [36]. Increasing the pressure also monotonically increases the out-of-plane lattice parameter and decreases the Scherrer coherence length on both substrates. Both phenomena could be explained by cation and oxygen non-stoichiometry resulting in increased microstrain. In addition to the cation non-stoichiometry proposed earlier, the higher pressure films are also speculated to be oxygen deficient due to a decrease in the positive oxygen ion density in the plasma at higher gas pressures [32, 33]. The rocking curve widths and roughnesses are consistent with the earlier discussion of the evolution of the growth morphology.

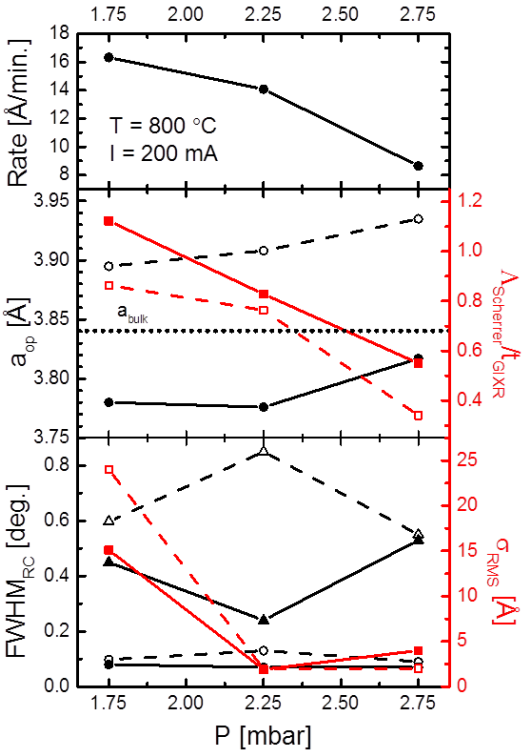

Fig. 3.9: Summary of the structural properties of LSCO50 films on STO (001) and LAO (001) as a function of growth pressure. In all panels, closed symbols with solid lines indicate STO (001) and open symbols with dashed lines indicate LAO (001). Data plotted with circles and triangles belong to the left axes while squares belong to the right axes. Triangles indicate the broad RC component.

Fig. 3.10 summarizes the magnetic and transport properties of the LSCO50 films on the two substrates. On both STO (001) and LAO (001), the T_C as well as the M_S show a significant monotonic decreasing trend with increasing sputtering pressure. In fact, the M_S is almost halved in going from 1.75 mbar to 2.75 mbar while the drop in T_C is more modest, ~ 10% , on both substrates. Both factors suggest a significant degree of oxygen deficiency in the films grown at higher pressures, with perhaps a small degree of cation non-stoichiometry, resulting in a lower effective doping of the higher pressure films; these arguments are consistent with the earlier discussion on the effect of pressure on cation and oxygen non-stoichiometry. Changes in the 5K hysteresis loop shape, as seen by differences in the in-plane coercivity and remanence, is indicative of possible changes in defect density and magnetic anisotropy. Finally, transport on both substrates show similar trends – increasing the gas pressure leads to an increase in the 5 K resistivity as well as a decrease in the RRR. In fact, the 2.75 mbar film on STO (001) is no longer metallic but has an insulator-like transport behavior ($d\rho/dT < 0$). Both trends point to a severe oxygen deficiency and increased granularity as a result of increasing sputtering pressure and are consistent with the structural and magnetic data.

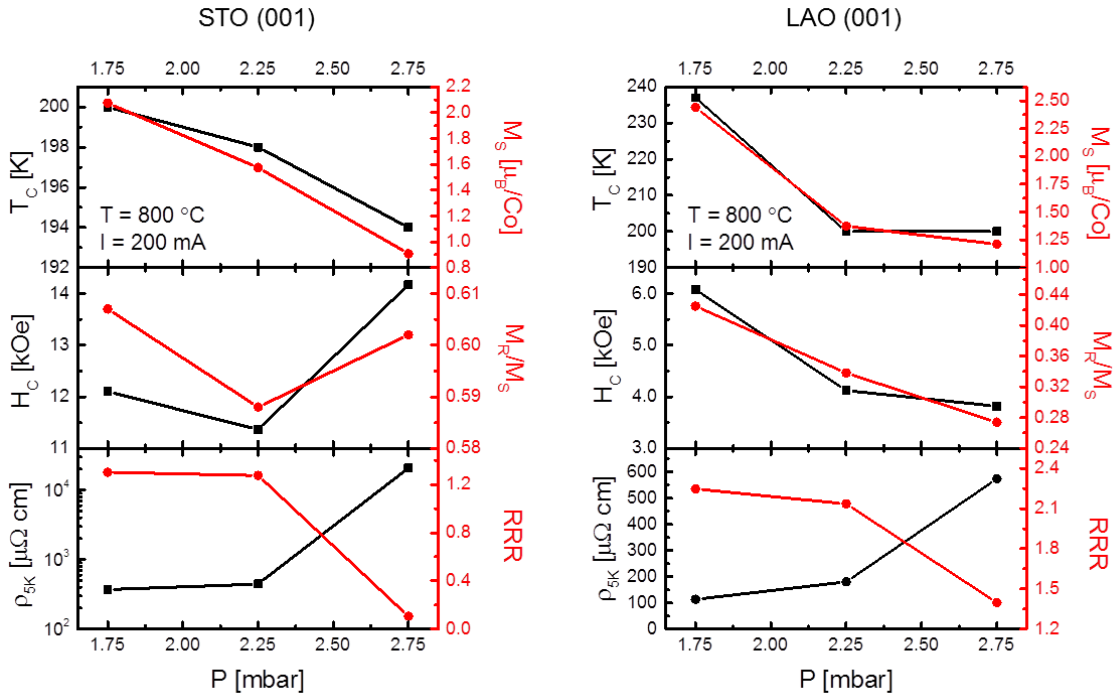

Fig. 3.10: Summary of the magnetic and transport properties of LSCO50 on STO (001) and LAO (001) as a function of growth pressure. In each panel, data plotted with square symbols belong to the left axis while those with circles belong to the right axis.

3.9 Current dependence

The final sputtering parameter that we have investigated is the plasma current. Charge transport in a plasma is through the ambipolar drift – diffusion of both positive ionic species as well as electrons and negative ions. Plasma chemistry is a complex topic and it is well known that the current has a profound and non-trivial influence on the plasma properties, with the resulting voltage being a sensitive function of the ionization energy of the gas, the pressure in the reactor, the spacing between the electrodes and the work function of the electrode materials [50]. A direct effect of the plasma current (or equivalently the power) in sputtering is on the sputtering rate. However, in reactive sputtering processes such as ours, it also has a significant influence on the film stoichiometry. The current flowing in the high-pressure oxygen plasma is directly correlated to the oxygen ion density and is therefore expected to possibly affect oxygen content in our films. We have therefore systematically examined the influence of the plasma current in the range of 125 – 200 mA. For a 1.5" target, this represents a current density range of ~ 11 – 17.5 mA/cm^2 and a plasma power range ~ 40 – 67 W. The temperature and pressure were held constant at 600 ºC and 1.75 mbar respectively.

Fig. 3.11 shows the structural properties of LSCO50 films on STO (001) and LAO (001) at 125 mA and 200 mA. Interestingly, in complete contrast with the temperature and pressure dependences discussed earlier, the sputtering current appears to have no significant influence on the morphology of the sputtered films. At both current extremes, films exhibit well defined Kiessig fringes and finite size oscillations, indicating low roughness at both the nm and μm length scales. Indeed, AFM images of all four films are almost featureless, with RMS roughnesses in the 2 – 4 Å. Rocking curves too are almost identical, showing single Gaussian-like profiles with FWHMs in the 0.07 – 0.09º range, suggesting that all films are coherently strained with the substrate. This apparent lack of correlation between current and morphology is especially significant in the light of the fact that the spatial extent of the visible plasma glow at 200 mA, 1.75 mbar and 125 mA, 2.75 mbar are not very different (Fig. 3.4). Therefore, in both cases the substrates are in a similar spatial position with respect to the plasma discharge. This stark difference in morphology is possibly related to differences in the plasma power and mean free paths leading to different sputter yields and thereby different densities of ions, radicals and sputtered species. Further, the different growth temperatures (600ºC and 800 ºC) used in the pressure and current experiments must surely play a role in determining the film morphology,

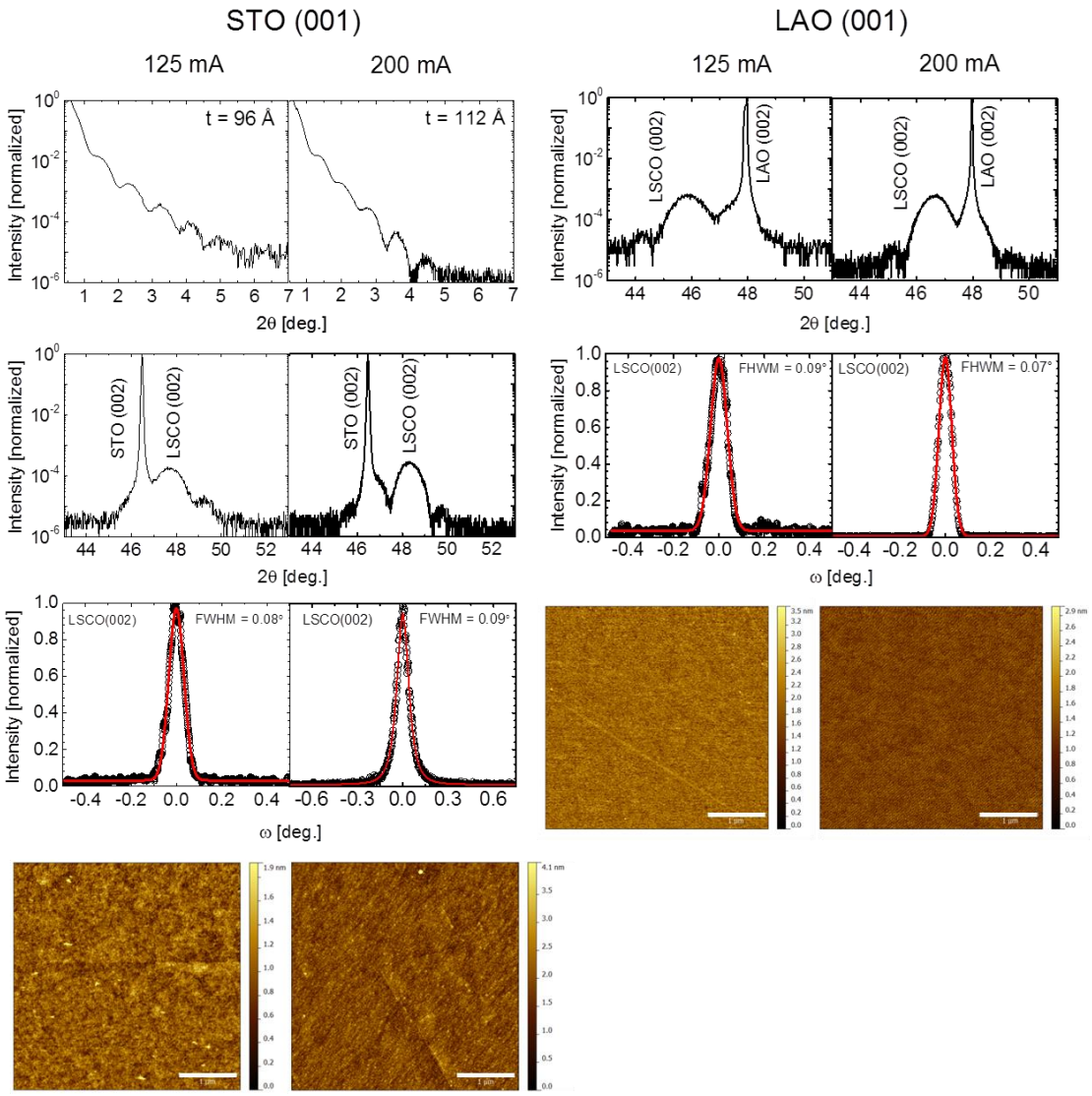

Fig. 3.11: Structural properties of LSCO50 films on STO (001) and LAO (001) at the plasma current extremes of 125 mA and 200 mA, as characterized by GIXR, WAXRD, rocking curves and surface morphology seen with an AFM. The scale bars for the AFM images are 1μm.

since the substrate temperature is known to have a significant influence on the film growth being kinetically or thermodynamically limited, as already seen in the temperature experiments of Section 3.7. A more thorough study of the temperature-pressure-current parametric phase space as well as the plasma is required to fully understand these subtleties of growth kinetics and morphology.

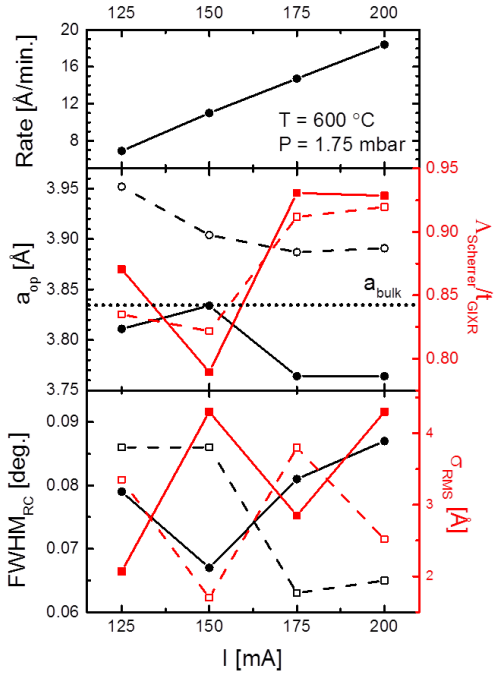

Fig. 3.12: Summary of the structural properties of LSCO50 films on STO (001) and LAO (001) as a function of plasma current. In all panels, closed symbols with solid lines indicate STO (001) and open symbols with dashed lines indicate LAO (001). Data plotted with circles and triangles belong to the left axes while squares belong to the right axes.

Fig. 3.12 summarizes the key structural parameters of the LSCO50 films on both substrates as a function of sputtering current. As expected, the growth rate is strongly and almost linearly correlated to the plasma current since the current directly controls the oxygen ion flux impinging on the target. It can be seen that even with the rate dropping by more than 50% to less than 8 Å/min. at 125 mA, the smooth morphology of the films suggests the persistence of kinetically limited growth at these rates and 600 ºC. However, despite the similarities in morphology, the out-of-plane lattice parameters on both substrates show a significant upward trend with decreasing current, providing the first real clue as to the major impact of lower sputtering current – loss of stoichiometry. The normalized Scherrer lengths too are consistent with this scenario, with lower $\Lambda_{Scherrer}$ at lower currents pointing to an increased contribution of microstrain under these conditions. Although the non-stoichiometry may be ascribed to both cations and oxygen, we speculate it to be dominated by oxygen deficiency. Finally, the rocking curve widths and surface roughnesses measured with an AFM show no trends, being confined to the 0.07º – 0.09º and 2 – 4 Å ranges respectively.

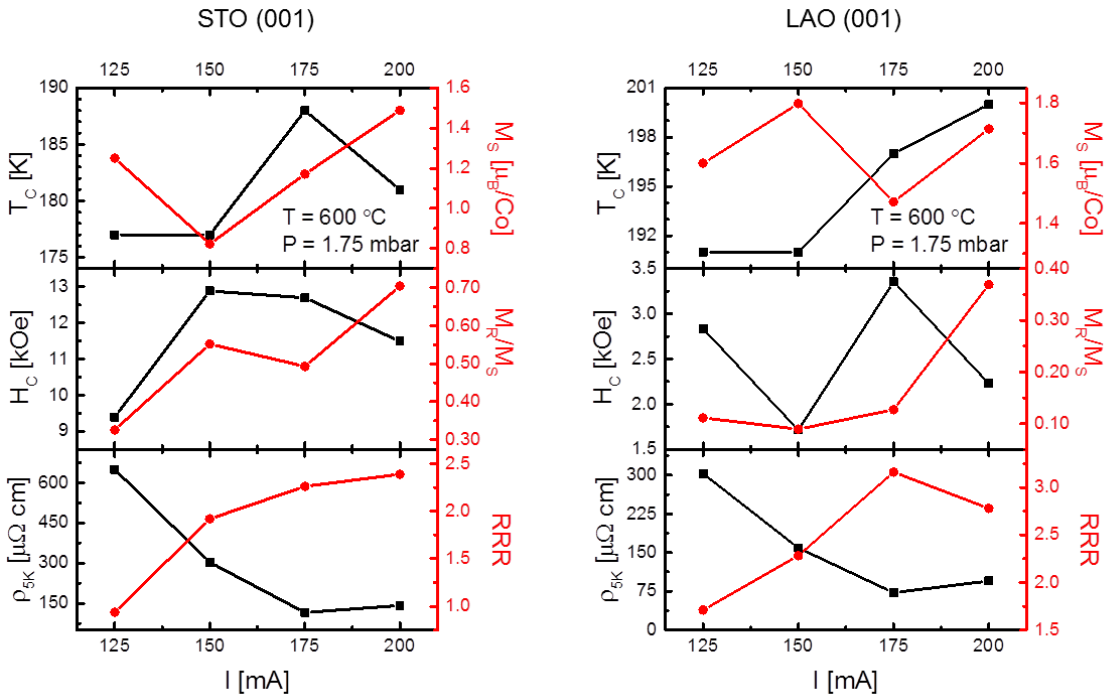

Fig. 3.13: Summary of the magnetic and transport properties of LSCO50 on STO (001) and LAO (001) as a function of sputtering current. In each panel, data plotted with square symbols belong to the left axis while those with circles belong to the right axis.

Fig. 3.13 shows a summary of the magnetic and transport properties of the LSCO50 films on the two substrates as a function of the sputter current. In agreement with the scenario of lower oxygenation, films grown at lower currents have consistently lower ferromagnetic T_C's. Although the magnitude in change in T_C seems slight (~ 5% on both substrates), the breadth of the ferromagnetic transition in the temperature dependent magnetization curves (not shown) increases at lower currents. This manifests itself as an increase in the peak width of the $\partial^2 M/\partial T^2$ curve used to estimate the T_C and indicates a broad distribution of T_C's in the films. This is similar to the T_C distribution seen in LSCO50 on STO (001) at lower thicknesses (~ 50 Å) (see Section 5.4) and points to a similar origin – oxygen deficiency and the onset of magneto-electronic phase separation (MEPS). The 5 K saturation magnetization, M_S, on the other hand does not appear to show any significant trend. We do not quite understand the behavior of M_S at this point, although it must be mentioned that the interpretation of M_S is complicated by the presence of the multiple spin states and valences of the Co ion. Further, the shape of the 5 K hysteresis loop on STO(001), as quantified by the coercivity H_C and the normalized remanence

M_R, points to a possible change in the magnetic easy axis to an out-of-plane direction at lower currents, with both numbers decreasing with the sputter current. Alternately, they could also be indicative of a transition towards a glassy magnetic state, which would be consistent with a MEPS ground state. A more rigorous analysis of the in-plane and out-of-plane magnetizations is needed to differentiate between the two possibilities. The coercivities of the films on LAO (001) do not show any significant trend although the remanences show a decreasing trend in this case as well. Once again, the origin of the trends cannot be confirmed from the present measurements alone. Finally, transport on both substrates show similar behavior – 5K resistivities increase and the RRR decreases with decreasing sputtering current, both trends consistent with the picture of lower oxygenation at lower sputtering currents. It is clear therefore that high sputtering currents, within the power dissipation constraints of the instrument, are desirable to obtain as close to stoichiometric LSCO films as possible.

3.10 Epitaxial $La_{1-x}Sr_xCoO_{3-\delta}$ ($0.05 \leq x \leq 0.80$)

On the basis of the parametric study discussed in the preceding sections, we have thus established the optimal sputtering conditions for LSCO50 thin films to be 600 ºC, 1.75 mbar and 200 mA for a 1.5" target, with a target to substrate distance of ~ 18.5 – 19 mm. Post growth cooling is in 800 mbar of oxygen and takes around 30 minutes after the heater is turned off. Using these optimal deposition conditions, we now demonstrate the extension of the growth protocol to LSCO thin films with other doping values in the range $0.05 \leq x \leq 0.80$. Film thicknesses were held approximately constant in the range 85 – 115 Å and all other target preparation and growth parameters were identical to the ones optimized for LSCO50. The only major change was that the higher room temperature resistivity of LSCO (x = 0.05) and LSCO (x = 0.15) required the target size to be increased to 2" diameter so as to maintain feasible plasma voltages.

Figs. 3.14 (a) and (b) show the specular WAXRD scans around the (002) peak for LSCO films on STO (001) and LAO (001). At all doping values, LSCO films were found to be phase pure perovskite and epitaxial with the substrates (at least in the out of plane direction). Longer range specular WAXRD scans (not shown) showed no evidence of secondary phases. Furthermore, each specular WAXRD scan shows prominent finite size fringes around the (002) LSCO peak,

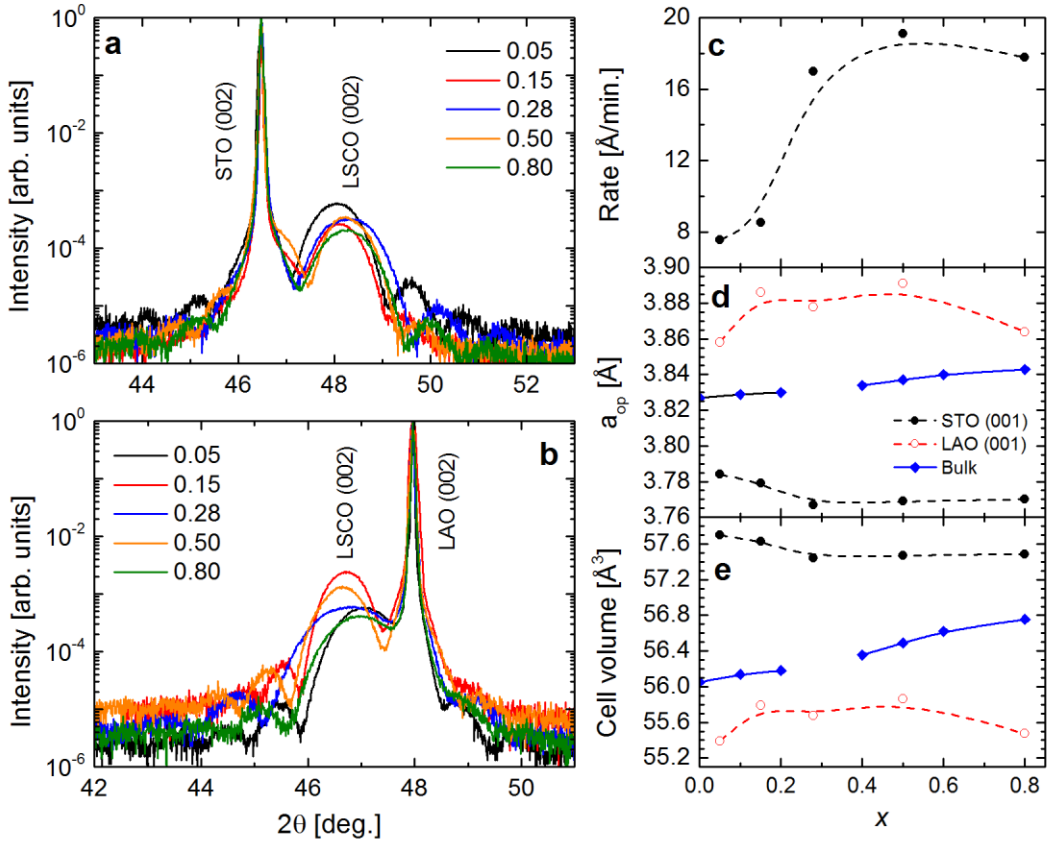

Fig. 3.14: a,b Specular WAXRD scans around the (002) peaks of LSCO films on STO (001) (**a**) and LAO (001) (**b**). **c, d, e** Summary of structural parameters showing the *x* dependence of rate (**c**), out of plane lattice parameter (d) and unit cell volume (**e**) . Bulk polycrystalline data are from [51]. Break in the line is meant to emphasize the well-known abrupt lattice parameter change in LSCO near $x = 0.20$.

suggesting low surface roughness on the short (~ 50 nm) length scale. Combined with prominent GIXR oscillations, this indicates that all films have low roughnesses, both on the short and the long length scales, similar to what is observed on LSCO50 grown under these conditions. The growth rate almost doubled between $x = 0.05$ and $x = 0.80$, with a sharp upturn between $x = 0.15$ and $x = 0.28$. We attribute this increase to the difference in target sizes in this range. Surprisingly, the reduced rate did not appear to affect the film morphology at the lower dopings. Extraction of the true dependence of the rate on the target composition requires more detailed experiments with constant target sizes and more doping values. The out of plane lattice parameters (a_{op}) showed surprising non-monotonic behavior, albeit within a small range, given the generally monotonic increase in LSCO bulk lattice parameter with Sr content [51]. Nonetheless, at all doping values, the a_{op} was smaller than bulk on STO (001) and larger on

LAO (001), consistent with the in-plane tensile and compressive stressed imposed by the two substrates respectively. Unit cell volumes shown in Fig. 3.14(c) were calculated assuming the in-plane lattice parameters of the film were identical to that of the substrates. Naïve first order calculations using these volumes yield nominal Poisson ratios in the range 0.15 – 0.34. Although within a physically reasonable range of values, these numbers must be taken with grain of salt, since the cell volumes are convoluted by the presence of oxygen vacancies, which are almost certainly ordered under these strain conditions (refer to Chapter 4 for more details), thereby breaking down the cubic symmetry of the film. Nonetheless, these numbers give a general idea of the compressibility and expansibility of LSCO films under these stress conditions. Normalized Scherrer widths of all films were in the range of 0.8 – 1, while rocking curves could be fit with a single Gaussian with a width ~ 0.06º. Neither parameter has therefore been plotted.

Fig. 3.15 shows the 5 K in-plane (IP) and out-of-plane (OP) magnetic hysteresis loops of LSCO films at different doping values on STO (001) and LAO (001). It must be noted that in all case, in-plane measurements were made with the field parallel to one of the in-plane (100) axes. A clear *x* dependence is immediately obvious, with different trends on the two substrates. At low doping values (0.05 and 0.15) on STO (001), there is no clear ferromagnetism, with M_S ~ 0.2 – 0.4 μ_B/Co and negligible remanences, both IP and OP. This isotropically small ferromagnetism is suggestive of a glassy magnetic state and is consistent with these doping values being deep in

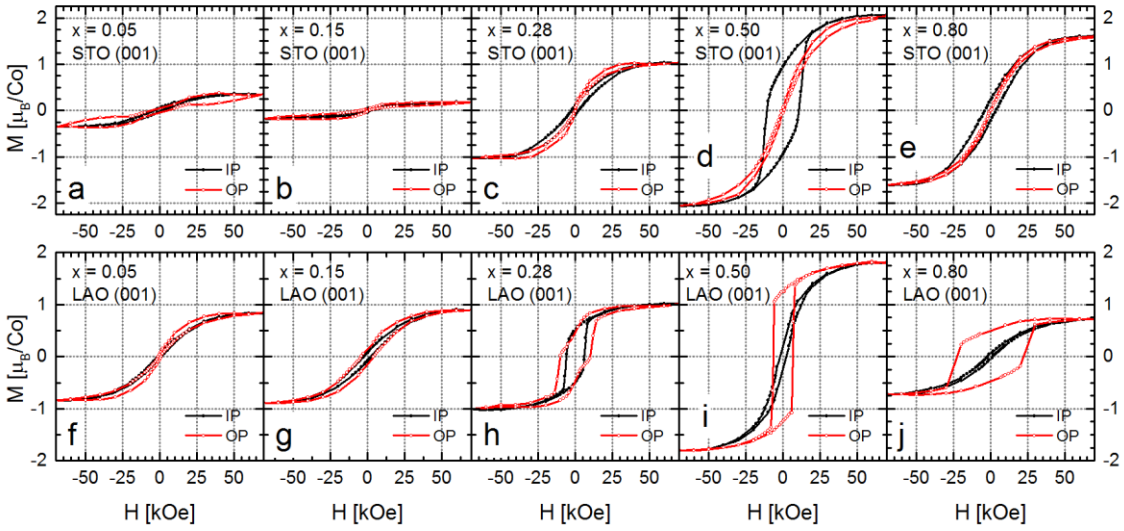

Fig. 3.15: In plane (IP) and out of plane (OP) magnetic hysteresis loops of LSCO films on STO (001) and LAO (001) at 5 K.

the phase-separated region of the phase diagram (Fig. 1.19) [35]. On LAO (001), too, the films exhibit similar behavior, although the saturation magnetizations are almost 1 μ_B/Co. The source of this anomalously large magnetization is unclear and is currently being investigated. As x increases to 0.28, the M_S increases to ~ 1 μ_B/Co on STO (001), with a slightly higher coercivity and remanence in-plane than out-of-plane, although even the in-plane values are not very large. This suggests the weak onset of ferromagnetism with an IP easy axis. On LAO (001), however, the x = 0.28 films exhibits a robust ferromagnetic loop with prominent coercivities and remanences, both IP and OP. Careful examination of the out-of-plane loop shows two switching fields, one of them almost coincident with the in-plane coercivity. This suggests comparable values for IP and OP magnetic anisotropies and multiple easy axes with both IP and OP components. At x = 0.50, films on both STO (001) and LAO (001) are ferromagnetic, with an IP easy axis on STO (001) and an OP easy axis on LAO (001). M_S on both substrates is ~ 2 μ_B/Co, close to the bulk value of 1.98 μ_B/Co [35]. Finally, when x is increased to 0.80, the film on STO (001) reverts back to a magnetic state with no clear easy axis in-plane or out of plane. Qualitatively similar to the x = 0.28 film on STO (001), it nonetheless retains a significant M_S ~ 1.6 μ_B/Co. This apparent loss of magnetism is perhaps suggestive of a higher δ (i.e. lower effective doping) which has been observed in bulk samples with high Sr content, due to the instability of the Co^{4+} valence state. This point will be discussed in more detail later. The x = 0.80 film on LAO (001) is perhaps the most paradoxical of all the samples measured. Like the x = 0.50 film on LAO (001), it too has robust ferromagnetism with a strong OP anisotropy and an OP coercivity of ~ 25 kOe. However, its M_S is about 35% of that of the x = 0.50 film and almost half the M_S of the x = 0.80 film on STO (001). Seemingly suggestive then of higher oxygen deficiency in this sample, it will be shown later how this cannot possibly be the case.

Figs. 3.16 (a) and (b) show the temperature dependent magnetization, normalized to the M_S at 5 K, for the LSCO films on the two substrates. Each measurement was in-plane, along the (100) sample edge. Both x = 0.05 samples and the x = 0.15 film on STO (001) were measured in a 500 Oe field, while all other samples were measured under 1000 Oe. Some of the samples were measured both under zero field cooling (ZFC) and field cooling (FC). In all cases the measuring field was identical to the cooling field (when applicable). It can be seen from the ZFC and FC curves that at x = 0.05 and x = 0.15, LSCO films on both STO (001) and LAO (001) exhibit glassy magnetic behavior, with a prominent ZFC-FC split and a low temperature Curie tail. This

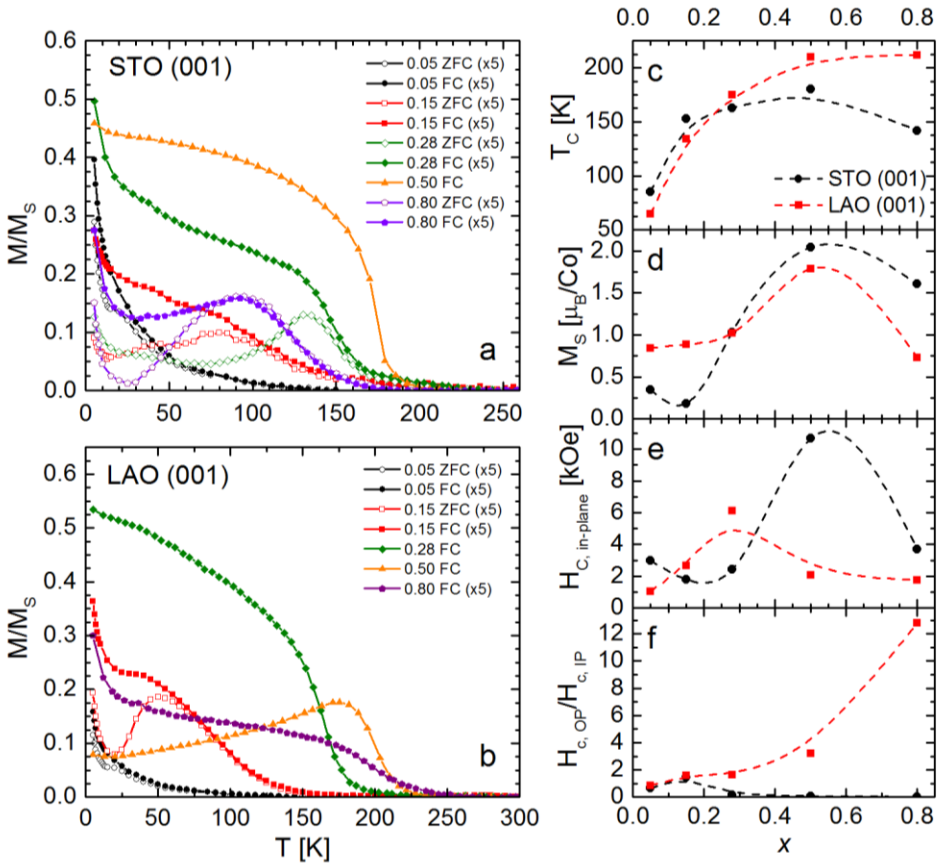

Fig. 3.16: a,b Magnetization, normalized to the saturation magnetization at 5K, as a function of temperature for LSCO films at different doping values on STO (001) (a) and LAO (001) (b). ZFC indicates samples were cooled to 5K under zero field while FC indicates field cooling. Some of the data have been scaled by a factor of 5 (as indicated in the parentheses) for the sake of clarity **c, d, e, f,** summary of the *x* dependence of the Curie temperature (c), 5K saturation magnetization (d), the in-plane coercivity (e), and the ratio of the in-plane and out-of-plane coercivities (f).

is similar to what is observed in the bulk at these doping values [35] and is consistent with the hysteresis loops shown in Fig. 3.15. Interestingly, the x = 0.28 film on STO (001) too shows similar bifurcation of the ZFC and FC curves, although in this case the ZFC curve is non-monotonic below the bifurcation temperature. Given that the measuring field of 1000 Oe is only half the 5 K coercivity (~ 2000 Oe), this ZFC curve cannot be explained by a coercivity argument alone. Rather, it is strongly indicative of contributions from both dominantly glassy and some long range ordered components. The x = 0.50 film exhibits order-parameter like temperature dependent magnetization while the x = 0.80 sample once again looks like a spin glass. Figs. 3.16 (c – f) summarize the magnetic parameters as a function of x. The T_C on both substrates show a monotonically increasing trend up to x = 0.50. This is consistent with the T_C

trend seen in the bulk, although the T_C's seen in the thin films are systematically suppressed compared to the bulk. As the Sr content is increased to x = 0.80, the two T_C lines show significant divergence. The x = 0.80 film on LAO (001) has a T_C not too dissimilar from the x = 0.50 value; however, on STO (001), the T_C drops down significantly to ~ 140 K. This difference in T_C's at x = 0.80 points to a significant difference in oxygen stoichiometries on the two substrates, with the tensile strain on STO (001) favoring the formation of oxygen vacancies and thereby decreasing the Co^{4+}/Co^{3+} ratio [52, 53]. This then is the first apparent contradiction about the x = 0.80 film in LAO (001), which has a 50% higher T_C but less than half the M_S compared to the film on STO (001). Interestingly, the T_C's on the two substrates cross over ~ x = 0.25. The reason for this cross over is unclear at this point.

The x dependence on the M_S is also very different on the two substrates. At the low x end of the series, the M_S on LAO (001) seems to almost level off at ~ 0.8 μ_B/Co. However, it is known that $LaCoO_3$ on LAO (001) is only weakly ferromagnetic, with a T_C ~ 40K and an M_S ~ 0.3 μ_B/Co [54, 55]. A dramatic drop in magnetization is therefore expected on LAO (001) between x = 0 and x = 0.05. The suppression of M_S at x = 0.80 is perhaps due to cancellation from moments due to ferrimagnetically ordered sublattices. It is known that LSCO films under strain exhibit a brownmillerite-like structure, with alternating oxygen-deficient and oxygen-sufficient planes, and commensurately alternating tetrahedral and octahedral Co coordinations (Chapters 4 and 5). Tetrahedrally coordinated Co is always seen to be in the high-spin state whereas octahedral Co could be either the IS or the HS. Coupled with the presence of both Co^{4+} and Co^{3+}, a complex interaction between the different Co ions resulting in ferromagnetic ordering is therefore not impossible. On STO (001), the M_S trend is similar to that on LAO (001) above x = 0.28, with a maximum M_S ~ 2 μ_B/Co occurring around x = 0.50. At low x, however, the films barely show any magnetization. This is especially perplexing given the stable ferromagnetism observed in $LaCoO_3$ on STO (001), which would imply that a small addition of Sr destroys the magnetic ordering in the sample. It could very well be due to an interaction between the Sr induced ferromagnetic clusters and the tetrahedral Co due to the oxygen vacancy ordering. In any case, much is not understood about the magnetic ground state at either doping extremes on the two substrates. More work using high resolution STEM/EELS is needed to fully understand the magnetic ordering in such samples. In terms of coercivity, the films on LAO (001) show a maximum IP coercivity around x = 0.28, after which there is a predominant OP easy axis which gets stronger with increasing Sr doping (Fig. 3.16(f)). On STO (001), the easy axis always lies

in-plane and the coercivity peaks around x = 0.50. The strong contribution from glassy components suppresses the coercivity at other doping values.

Fig. 3.17 shows the temperature dependence of resistivity for the LSCO on both substrates. The figure also shows the resistivity of reference single crystals that most closely resemble the film transport data [47, 56]. It can be seen that at the low doping values of x = 0.05 and 0.15, all samples appear to be bulk like, albeit with a lower doping. At x = 0.28, however, this similarity

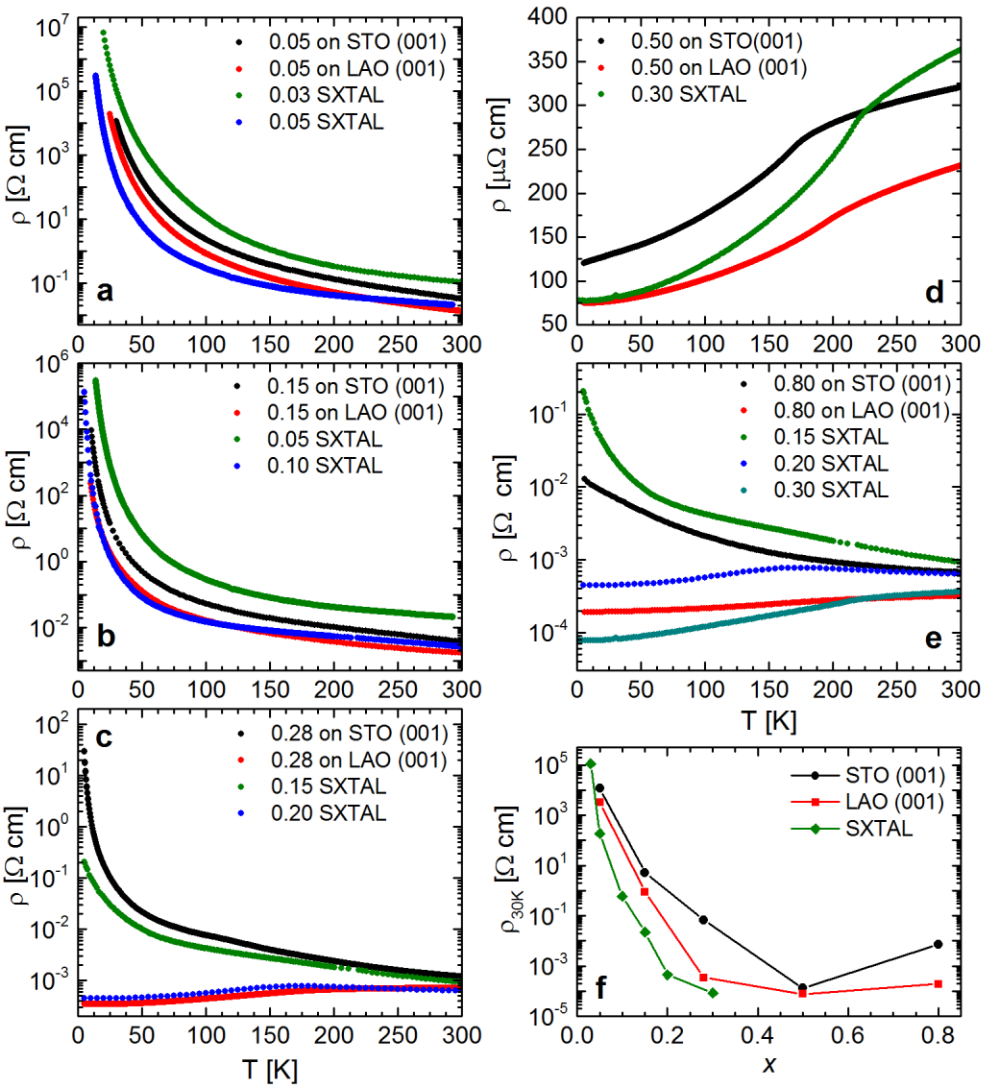

Fig. 3.17: a,b,c,d,e Temperature dependent resistivity of LSCO films on STO (001) and LAO (001) at x = 0.05, 0.15, 0.28, 0.50 and 0.80. Each panel shows the resistivity of the two single crystals that most closely resemble the thin film data. **f** 30K resistivity as a function of x for LSCO films on STO (001) and LAO (001), as well as LSCO single crystals. Some of the single crystal data have been taken from Refs. 47 and 56.

ends. The x = 0.28 film on LAO (001) is metallic (positive dρ/dT) all the way down to 5K and closely resembles an x = 0.20 single crystal. The film on STO (001), on the other hand, has insulator-like transport properties with a small inflection appearing just below the ferromagnetic T_C ~ 150 K. This is due to presence of a magneto-electronically phase separated clustered state at the LSCO interface with STO (001), the thickness extent (t*) of which is x dependent and is ~ 180 Å at x = 0.28 (more details in Chapter 5). As a result, the x = 0.28 film on STO (001) exhibits transport properties similar to an x = 0.14 – 0.15 single crystal. Increasing x to 0.50 decreases t* to ~ 80 Å on STO (001) and less than 30 Å on LAO (001) – as a result x = 0.50 films on both substrates are metallic with transport properties similar to a x = 0.30 single crystal. It must be stressed that transport data on single crystal LSCO is only available as high as 0.30, and therefore it could very well be that the 0.50 films actually resemble higher doped crystals. Finally, at x = 0.80, the film on LAO (001) is again metallic, albeit with slightly higher resistivities resembling crystals closer to ~ 0.25. The film on STO (001), on the other hand, has a negative dρ/dT at all temperatures, but with a finite 0 K intercept, suggesting some form of localized metal. The transport evolution on both substrates between x = 0.50 and x = 0.80 is consistent with a higher oxygen deficiency scenario.

Based on the qualitative comparison of the transport data with single crystals, we can then construct a form of phase diagram showing the evolution of the effective doping in the films as

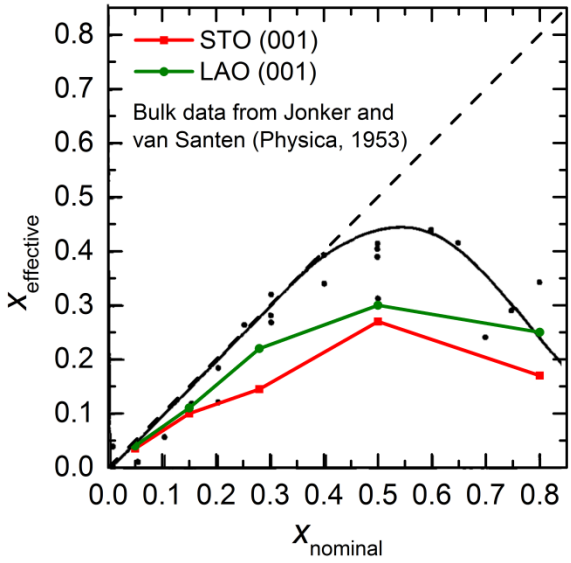

Fig. 3.18: Effective doping in LSCO films on STO (001) and LAO (001) as a function of x as extracted from a qualitative comparison with single crystal transport data. Black curve shows the experimentally measure Co^{4+}/Co^{3+} ratio in bulk polycrystals [57].

a function of x, as shown in Fig. 3.18. For comparison, the phase diagram also shows the ideal $x_{eff} = x_{nominal}$ line as well as the Co^{4+}/Co^{3+} ratio measured in bulk polycrystals by chemical means [57]. It must be stressed that the two datasets are very different. The bulk data are an actual measure of the Co^{4+}/Co^{3+} ratio whereas our thin film data is only a qualitative comparison with single crystal transport. Further, we are hindered by lack of transport data above x = 0.30. Moreover, a simple transport comparison also does not account for the graded x profile seen in thin films on STO (001) (see Chapter 5). Nonetheless, despite the caveats, Fig. 3.18 unequivocally shows the essential doping dependent trend in the thickness range 85 – 115 Å. At low doping values, at x = 0.15 and lower, the films are essentially bulk-like, showing glassy magnetism and insulating behavior. As x increases, the x_{eff} deviates away from the ideal, both due to finite size effects as well as oxygen non-stoichiometry, the latter being more pronounced on STO (001) than on LAO (001). Finally, at x = 0.80, the films are again bulk-like, this time due to the difficulty in maintaining oxygen stoichiometry in high x bulk LSCO. In fact, the curve suggests that it may very well be possible to stabilize oxygen stoichiometries on LAO (001) that are not possible in the bulk. More films need to be grown at different doping ranges to generate a more reliable phase diagram. Furthermore, a better quantitative estimation of x_{eff} is needed from STEM/EELS measurements.

3.11 Concluding remarks

In summary, we have demonstrated the growth of phase pure epitaxial $La_{0.5}Sr_{0.5}CoO_{3-\delta}$ films on $SrTiO_3$ (001) and $LaAlO_3$ (001) using an on-axis high-pressure oxygen reactive DC sputtering technique. We have identified the key tunable deposition parameters to be the substrate temperature, oxygen pressure and plasma current, and have systematically investigated the influence of each on the film properties. We have shown that the temperature plays a significant role in pushing the film growth into the thermodynamic or kinetic limits. The high surface energy of $La_{0.5}Sr_{0.5}CoO_3$ leads a rough, "clumpy" morphology at high growth temperatures; smooth films can only be obtained around 600 ºC. Pressure and current, on the other hand, primarily affect the stoichiometry of the films, and the best films are obtained at pressures below 2 mbar and currents exceeding 175 mA. On the basis of these observations, we have determined the optimal growth conditions to be at 600 ºC, 1.75 mbar oxygen pressure and 200 mA plasma current, with the target – substrate distance maintained ~ 18 – 18.5 mm. Post growth

the films were cooled in 800 mbar oxygen in 20 – 30 minutes. Using these optimal growth conditions, we have been able to synthesize 100 Å films on $LaAlO_3$ (001) that display single crystal like electronic properties, with a T_C ~ 200 K, an M_S ~ 1.7 μ_B/Co, a ρ_{5K} ~ 90 $\mu\Omega$ cm and a RRR ~ 2.7. Finally we have demonstrated an extension of the growth protocol to the large doping window of $0.05 \leq x \leq 0.80$. We have thus demonstrated an avenue to feasibly explore the finite size and strain effects offered by epitaxial thin films without severely degrading the bulk-like properties.

Chapter 4

Lattice Mismatch Accommodation *via* Oxygen Vacancy Ordering in Epitaxial $La_{0.5}Sr_{0.5}CoO_{3-\delta}$ Thin Films

This chapter has been reprinted with permission from J. Gazquez, Shameek Bose, M. Sharma, M. A. Torija, S. J. Pennycook, C. Leighton, and M. Varela, APL Materials **1**, 012105 (2013).

4.1 Introduction

As discussed in Chapter 1, physical phenomena such as magnetic phase separation, spin-state crossovers, and mixed ionic conduction make perovskite cobaltite films of great interest both for basic science, and for applications in solid oxide fuel cells, gas separation membranes, etc. High quality epitaxial films on single crystal substrates are favored for fundamental studies and for proof-of-principle device work (e.g. with oxygen/hole transport in fuel cell cathodes). In such structures the epitaxial strain due to the lattice mismatch with the substrate provides a means to controllably modify structure, thus manipulating properties. $LaCoO_3$ provides a good example as it adopts a low-spin "non-magnetic" ground state in bulk, but exhibits strain-stabilized ferromagnetism in films [1 – 3]. In the doped case, e.g. in bulk $La_{1-x}Sr_xCoO_{3-\delta}$ (LSCO), substitution of Sr^{2+} for La^{3+} changes the Co valence, inducing metallic ferromagnetism [4], but also O vacancies. Without the use of high pressures these vacancies form in high concentrations for $x > 0.5$-0.6 [5], eventually forming ordered superstructures, as exemplified by brownmillerite $SrCoO_{2.5}$ (SCO) [6, 7]. In tensile-strained thin film LSCO on (001) $SrTiO_3$ (STO), recent work has highlighted the complex interplay between strain and these O vacancies (Chapter 1, Section 1.6). For example, interfacial magnetic phase separation occurs in $SrTiO_3$ (001)/LSCO, driven by accumulation of O vacancies near the substrate [8]. These O vacancies undergo long-range ordering [8 – 10], somehow related to epitaxial strain [10]. Recently observed consequences of this vacancy ordering / interfacial accumulation include spin-state superlattice formation [11], induced cation order [12], and a giant coercivity enhancement [13]. Comparisons can be drawn with similar systems such as rare-earth cuprates [14], where interfacial oxygen *dis*order effects impact critical current density. The goal of this chapter is to

more fully elucidate the interplay between strain state and O vacancy formation / ordering in LSCO films.

4.2 Samples: Preparation and characterization

We studied the effects of epitaxial strain on x = 0.50 LSCO films grown on (001) and (110) oriented STO, and on (001) oriented $LaAlO_3$ (LAO), i.e. STO(001)/LSCO, STO(110)/LSCO and LAO(001)/LSCO, respectively. The nominal lattice mismatch between film and substrate is -1.8 % for STO and +1.3 % for LAO (Table 4.1). Films were grown by reactive sputtering [8, 9, 11, 15] at 700 °C, with 100 W of DC power, in O_2 and Ar pressures of 20 and 50 mTorr, and with post-deposition cooling in 500 Torr of O_2. Samples were characterized by high resolution Cu K_α x-ray diffraction (XRD) in wide-angle XRD (WAXRD), rocking curve (RC), and reciprocal space mapping (RSM) modes. They were also observed with scanning transmission electron microscopy (STEM) and analyzed with geometrical phase analysis (GPA) [16, 17]. Measurement and analysis details can be found in Sections 2.1, 2.2 and 2.7.1.

Compound	**a (Å)**	**b (Å)**	**c (Å)**	**ε (a_{pc}/a_s)**	**ε (a_{bm},b_{bm}/a_s)**	**ε (c_{bm}/a_s)**
$La_{0.5}Sr_{0.5}CoO_3$ (pc)	3.836	…	…	…	…	…
$La_{0.5}Sr_{0.5}CoO_{2.5}$ (bm)	5.409	5.556	15.690	…	…	…
$SrTiO_3$	3.905	…	…	-1.8 %	-0.7 %	0.5 %

Table 4.1: Left: Lattice parameters of pseudocubic LSCO (subscript "*pc*"), orthorhombic Brownmillerite-like LSCO (subscript "*bm*"), and cubic STO and pseudocubic LAO substrates (subscript "*s*" for both) [23]. The LSCO pseudocubic and Brownmillerite cells are related by $a_{pc} \approx a_{bm}/\sqrt{2} \approx b_{bm}/\sqrt{2}$, and $a_{pc} \approx c_{bm}/4$. **Right:** Strain values (with respect to the relevant substrate) for pseudocubic LSCO, and Brownmillerite-like LSCO matched to the *a*/*b* or *c* axes.

4.3 Strain relaxation in $La_{0.5}Sr_{0.5}CoO_{3-\delta}$ thin films

A global picture of the thickness (t)-dependent strain relaxation from WAXRD is shown in Fig. 4.1 (a), which plots the strain relaxation percentage [SRP = $|a(t) - a_{strained}|/|a_{relaxed} - a_{strained}|$ x 100 %, where a is the out-of-plane lattice parameter, and $a_{relaxed}$ and $a_{strained}$ are its fully relaxed (bulk) value and fully-strained (pseudomorphic) values]. Note that the $a_{relaxed}$ used here is that of stoichiometric, undistorted cubic LSCO (Table 4.1). The films are strained (SRP < 100 %) at all t, but exhibit a very different t dependence on the three substrates. In STO(001)/LSCO we find a critical thickness for strain relaxation (t_{crit}) around 200 Å [8, 9, 15]. Above this value the SRP increases only slowly, reaching approximately 20 % at $t \approx 400$ Å. On LAO(001) substrates t_{crit} is lower (≈75 Å), the SRP reaching larger values of 60-70 % at 400 Å. Remarkably, and despite the identical mismatch to STO(001), in STO(110)/LSCO the SRP increases almost immediately from $t = 0$, suggesting t_{crit} lies below 30 Å, if in fact it exists at all. As discussed previously [15], strain relaxation in LSCO is also reflected in RCs, through broad and narrow peak components (high and low mosaicity), associated with relaxed and fully strained regions. The t dependence is shown in Fig. 4.1 (b), which plots $I_{broad}/(I_{broad} + I_{narrow})$, where I_{broad} and I_{narrow} are the intensities of the broad and narrow Gaussian components. The trends are similar to Fig. 4.1 (a), the most noteworthy conclusion again being the efficient strain relaxation on STO(110) compared to STO(001). To probe the strain state in more detail, RSMs (Fig. 4.2 (a – c)) were

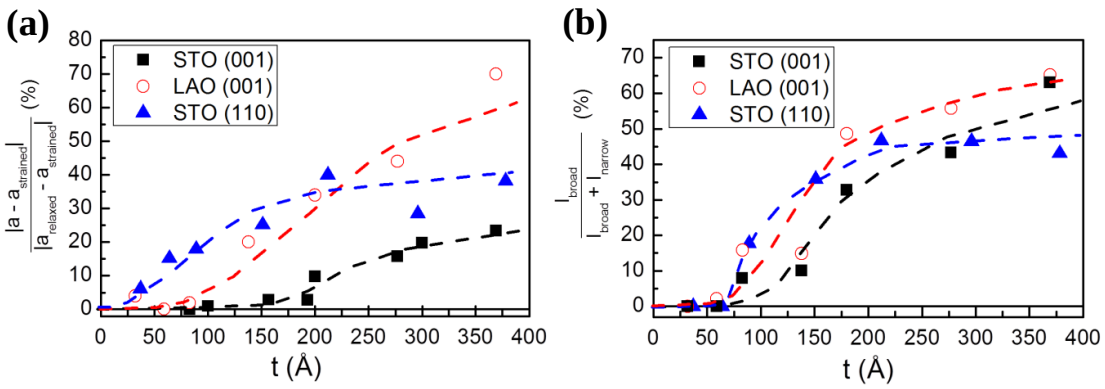

Fig. 4.1: (a) Thickness (t) dependence of the strain relaxation percentage (SRP), as determined from the out-of-plane lattice parameter, for $x = 0.5$ LSCO films on STO(001), STO(110), and LAO(001). The thickness (as determined by x-ray reflectivity) was varied from 30-400 Å in 20 separately grown samples. In the thinnest samples, with broad WAXRD peaks, the out-of-plane lattice parameter was determined by subtracting out a symmetric substrate reflection and fitting the isolated film peak with a Gaussian. (b) Percentage contribution of the broad intensity component from two-Gaussian fitting of rocking curves for the same films. I_{broad} and I_{narrow} are the intensities of the two contributions.

acquired around asymmetric reflections at t = 200 Å. For STO(001)/LSCO and LAO(001)/LSCO the (013) reflection was chosen. For STO(110)/LSCO the 4-fold in-plane symmetry is broken, and we chose the (310) and (222) reflections to probe two orthogonal high symmetry in-plane directions ([1-10] and [001]). In all cases white crosses mark the positionsof the fully strained (pseudomorphic) and fully relaxed (bulk) LSCO reflections. For STO(001)/LSCO (Fig. 4.2 (a)), consistent with Fig. 4.1, we find negligible strain relaxation. The situation is similar for LAO(001)/LSCO (Fig. 4.2 (c)), but with minor relaxation. This is in stark contrast to STO(110) however (Fig. 4.2 (b)), where we find substantial strain relaxation in both in-plane directions. Simple estimates give relaxations ≈ 40 % at this t (200 Å), consistent with Fig. 4.1 (a).

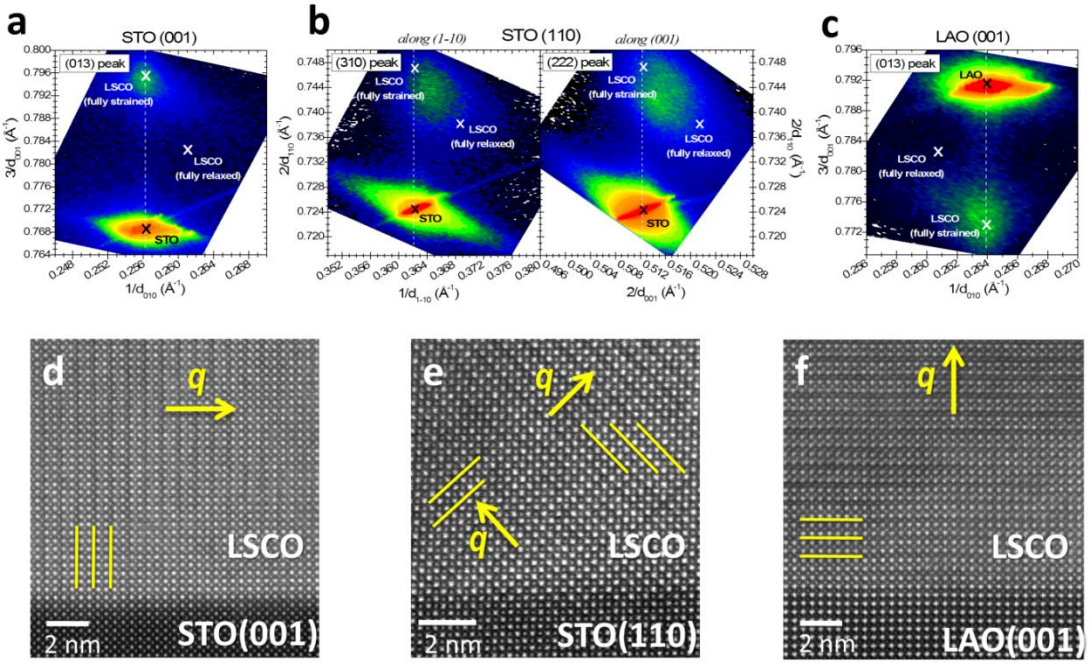

Fig. 4.2: (a), (b) and (c) are asymmetric reciprocal space maps for 200 Å thick x = 0.50 LSCO films on STO(001), STO(110), and LAO(001), respectively. In (a) and (c) the data were collected around the (013) reflection; in (b) around the (310) and (222) reflections. The expected positions of the fully strained and fully relaxed LSCO reflections are marked. (d), (e) and (f) are high resolution *Z*-contrast STEM images of the interface regions in films grown on STO(001), STO(110), and LAO(001), respectively. Yellow lines mark the O deficient Co-O planes. The modulation vector, $\boldsymbol{q}$, is marked.

4.4 Oxygen vacancy ordering: A novel strain accomodation mechanism

The origin of the unusually efficient strain relaxation on STO(110), and indeed the entire strain state / O vacancy interplay, is elucidated by STEM. Fig. 4.2 (d – f) show annular dark field *Z*-contrast STEM images from the interface regions. These images confirm cube-on-cube epitaxy, with the expected epitaxial relationships, in addition to a coherent interface. They also reveal an obvious superstructure, contrast modulation occurring on every other Co-O plane (see yellow lines). This contrast is well known to be due to the structural relaxations that result from the ordering of O vacancies in this system [11] and has been discussed in Chapter 1. O vacancy ordering occurs in the related bulk SCO and high x LSCO compounds [6, 7], and similar superstructures have been found in epitaxial LSCO [8 – 11, 18 – 21]. These superstructures are indicators of O vacancy ordering. In the present set of STO(001)/LSCO samples we have previously reported direct observation of O content modulation by atomic-resolution electron energy loss spectroscopic imaging [11]. Note that in Z-contrast images the dark/bright pattern of Co-O planes arises due to a modulation in cation spacing resulting from the O content modulation [6, 7, 11], or to displaced Co ions [21] (Section 1.5). It does not arise from the variation in O content directly.

Three additional findings suggest that this O vacancy superstructure provides the primary mechanism of lattice mismatch accommodation and strain relief. First, while in bulk such vacancy ordering is well-known in high *x* LSCO and SCO, it has not been reported in $x = 0.50$ bulk compounds to the best of our knowledge, and does not occur in our own bulk samples. There is thus some mechanism promoting O vacancy order in epitaxial films, strain being a likely candidate. Second, we find a remarkable scarcity of misfit dislocations, strongly suggestive of an alternative strain relaxation mechanism involving O vacancy order. A superstructure-related strain relief mechanism has in fact recently been advanced for undoped epitaxial $LaCoO_3$, although the origin of the superstructure is still under debate in that case [22]. Finally, as can be seen from Fig. 4.2 (d – f), the modulation vector of the O vacancy superstructure responds to both strain type (tensile vs. compressive), and crystallographic orientation [(001) vs. (110)], pointing to a fundamental link between strain state and O vacancy order.

A likely candidate for the superstructure in Fig. 4.2 (d – f) is the orthorhombic brownmillerite structure (Sec. 1.5) of bulk SCO. This phase has stoichiometry $SrCoO_{2.5}$, with lines of oxygen vacancies along the [110] direction in alternate (001) Co-O planes, quadrupling the unit cell along the *c*-axis [6, 7, 23] (see Table 4.1). In STO(001)/LSCO (Fig. 4.2 (d)) we propose that the tensile strain is relieved by the formation of a brownmillerite-like superstructure with O vacancy planes perpendicular to the interface, i.e. superlattice modulation vector (***q***) parallel to the interface. The measured (La,Sr)-O interplanar spacings alternate between 3.60 ± 0.20 Å and 4.25 ± 0.30 Å (errors are half-widths of spacing distributions), giving an in-plane lattice parameter of 7.84 Å, very close to twice the $SrTiO_3$ lattice parameter (7.81 Å, see Table 4.1). In essence the mismatch with the substrate is accommodated by formation (at low energy cost [12]) and ordering of O vacancies, thus generating a fundamental link between strain, O vacancy density, and order. In the case of compressive strain on LAO(001) (Fig. 4.2 (f)), the O vacancy planes stack parallel to the interface, with ***q*** out-of-plane, to enable out-of-plane expansion, and thus in-plane compression. A simple analytical model [10] supports this strain-relief scenario. The ***q*** vector can also be controlled by crystallographic orientation. As expected in a brownmillerite-type structure, in the (110) orientation the O vacancy planes make an angle close to 45 ° with the interface (yellow lines in Fig. 4.2 (e)). Lower magnification images of 400 Å thick films are shown in Figs. 3(a-c), illustrating a domain structure. In Fig. 4.3 (a) for example, variants with O vacancy planes running both perpendicular and parallel to the interface are seen [10]. Close to the interface the perpendicular variant dominates, a transition to a multi-domain state occurring ≈ 200 Å from the interface, consistent with t_{crit}.

4.5 Geometric phase analysis: Quantifying the strain evolution

Fourier analysis of these STEM images was performed with GPA (Sec. 2.7.2) to obtain spatially-resolved information on the local lattice relaxation. It must be noted that the GPA extracted strain values are referred to the substrate, as opposed to bulk LSCO, such that fully pseudomorphic growth leads to zero strain. Circular masks with radii producing a lateral resolution ≈ 1 nm in the GPA images were defined around the (001) reflections for STO(001)/LSCO and LAO(001)/LSCO, and the (110) reflections for STO(110)/LSCO. The extracted in-plane (ε_{xx}) and out-of-plane (ε_{yy}) strains (again, with respect to the substrate) are shown in Figs. 4.3 (d – f) and 4.3 (g – i), respectively. Positive and negative values refer to

compressive and tensile strain, respectively. In Fig. 4.4 lateral averages of these strains are plotted *vs.* distance from the interface, *y*, overlaid on sections of the maps from Fig. 4.3 (to scale).

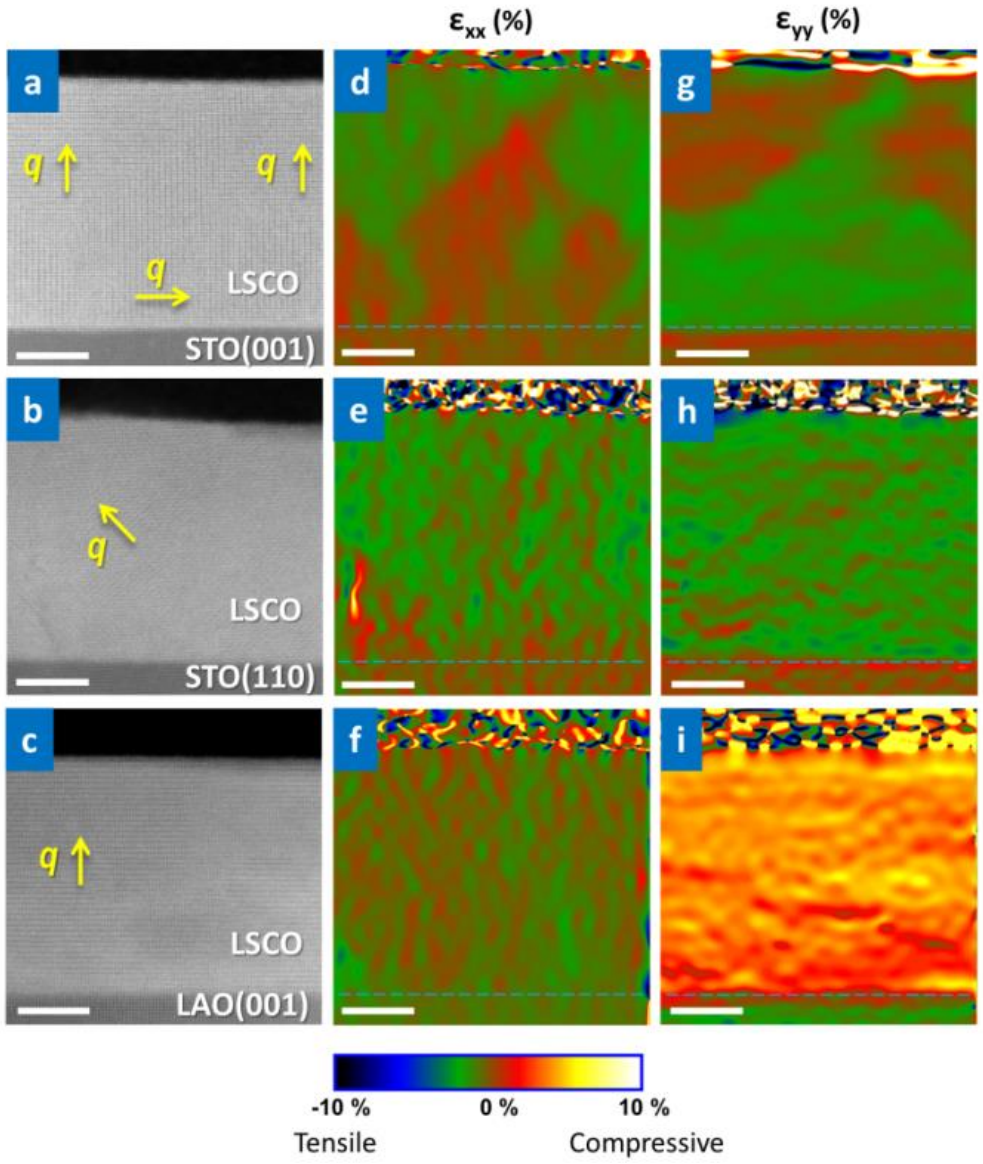

Fig. 4.3: (a), (b) and (c) are *Z*-contrast images of 400 Å thick STO(001)/LSCO, STO(110)/LSCO and LAO(001)/LSCO films. The orientation of the modulation vector, ***q***, is marked. (d) and (g), (e) and (h), and (f) and (j) are in-plane (ε_{xx}) and out-of-plane (ε_{yy}) strain maps of the same three films shown in (a-c), from GPA analysis. Dashed lines mark the substrate/LSCO interface. The *Z*-contrast images do not show the regions in the substrates, as big as 10 x 30 nm, that were used as reference lattices. The scale bar is 10 nm in all panels. The range of the color scale (± 10 %) is the same in all maps.

Considering STO(001)/LSCO first (Fig. 4.3 (d, g) and Fig. 4.4 top panel), the first observation is that the domain structure seen in Fig. 4.3 (a) is clearly reflected in the strain maps (Fig. 4.3 (d, g)), the strain state being remarkably inhomogeneous. As expected, ε_{xx} and ε_{yy} are anti-correlated (Fig. 4.3 (d, g)). Near the interface $\varepsilon_{xx} \approx 0$ (i.e. pseudomorphic growth), and $\varepsilon_{yy} < 0$ (an out-of-plane lattice parameter smaller than the substrate), in agreement with XRD. As can be seen in the top panel of Fig. 4.4, ε_{xx} remains small out to ≈ 150 Å from the interface, in reasonable agreement with t_{crit} from XRD (200 Å). Above this thickness, ε_{xx} increases in magnitude, reaching -0.9 ± 0.1 % at the surface, where the parallel variant of the O vacancy superstructure dominates. Correspondingly, ε_{yy} is relatively constant out to ≈ 150 Å from the interface, beyond which it relaxes gradually, reaching -0.4 ± 0.1 % at the surface. This corresponds to an out-of-plane lattice parameter of 3.889 Å and a strain relaxation percentage of 23 %, in good agreement with XRD (Fig. 4.1 (a)).

In LAO(001)/LSCO (Fig. 4.3 (f, i) and Fig. 4 bottom panel), with compressive strain and smaller mismatch, we find a more uniform strain-state, although anti-phase boundaries occur [20], spaced by about 50 nm. This is smaller than the coherence length in our XRD (several hundred nm in the growth direction, several microns laterally), explaining the absence of superlattice peaks. As anticipated, $\varepsilon_{xx} \approx 0$ near the interface (i.e. pseudomorphic growth),

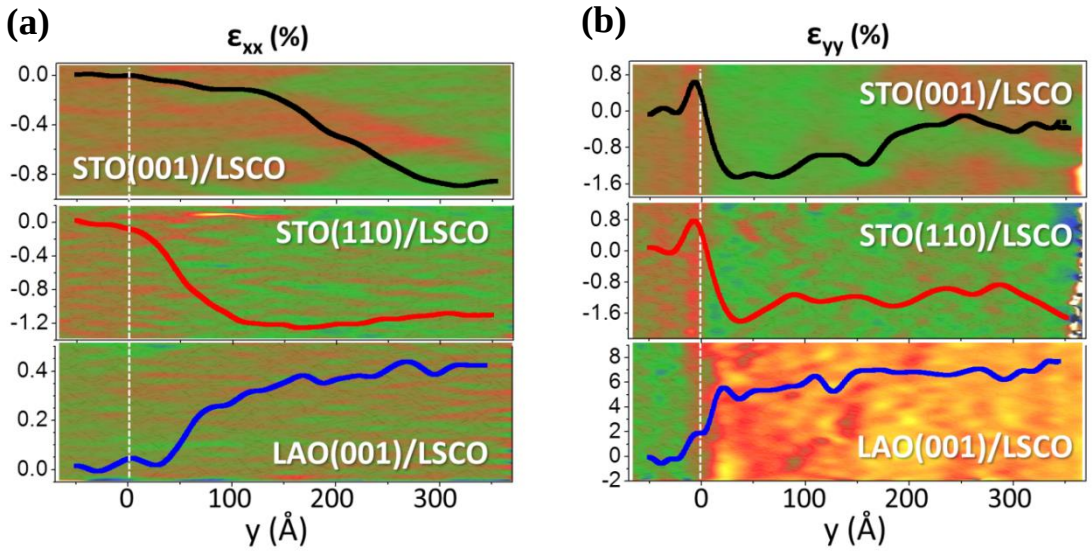

Fig. 4.4: (a) and (b) show averaged profiles of the in-plane (ε_{xx}) and out-of-plane (ε_{yy}) strain maps from Fig. 4.3. *y* is the distance from interface, and vertical dashed lines mark the LSCO/substrate interface. The data are laterally averaged, i.e. in the direction parallel to the interface. These averaged profiles are superimposed (to scale) on their corresponding strain maps from Fig. 4.3.

increasing away from the interface. The data suggest a local t_{crit} of about 50 Å, roughly consistent with XRD (Fig. 4.1 (a)). In the out-of-plane direction (Fig. 4.3 (i)) we find $\varepsilon_{yy} > 0$ (a larger out-of-plane lattice spacing than the substrate), with a laterally-averaged magnitude of 6 ± 0.1 % at the surface. Such large strains are consistent with the > 3.5 % expected from the mismatch between LAO and brownmillerite-like LSCO in this orientation (Table 4.1), although they exceed XRD values. This discrepancy may result from differences between the local and average structures in this case.

Importantly, STO(110)/LSCO is significantly different from STO(001). First, the strain state is relatively uniform in comparison to STO(001) (compare Fig. 4.3 (d, g) and Fig. 4.3 (e, h)). We again find $\varepsilon_{xx} \approx 0$ near the interface, but with a remarkable depth dependence (Fig. 4.4, middle panel). Consistent with spatially-averaged results from XRD, we find essentially no evidence for any well-defined t_{crit}; strain relaxation initiates immediately at the interface, in sharp contrast to STO(001) (compare Fig. 4(a), top and middle panels). Consistent with this, the extent of strain relaxation at the film surface is substantially larger for STO(110) than STO(001). We propose that the surprisingly different strain relaxation behavior in (110) vs. (001) oriented films originates from the differing $\boldsymbol{q}$ orientations. Specifically, in the (110) case all variants can contribute to strain relaxation, due to the 45 ° angles with the growth direction, $\boldsymbol{n}$, (e.g. Fig. 4.2 (e)), which result in a finite value of $\boldsymbol{q}.\boldsymbol{n}$. This is in contrast to the (001) case (e.g. Fig. 4.3 (a)), where for some variants $\boldsymbol{q}.\boldsymbol{n} = 0$. The O vacancy superstructure strain-relief mechanism thus renders crystallographic orientation very useful for controlling strain relaxation.

4.6 Concluding remarks

In summary, by combining high-resolution x-ray diffraction with geometrical phase analysis of scanning transmission electron microscopy images, we have studied the local and global strain relaxation process in $La_{0.5}Sr_{0.5}CoO_{3-\delta}$ films grown on various substrates. The lattice mismatch accommodation / strain relief mechanism is shown to be driven by formation, and ordering, of oxygen vacancies. We have demonstrated that this defect ordering can be manipulated by lattice mismatch and crystallographic orientation. In Chapter 5, I will show how we have used this manipulation capability to tune the electronic ground state of $La_{0.5}Sr_{0.5}CoO_{3-\delta}$ interfaces.

Chapter 5

Engineering Transport and Magnetism at Cobaltite Interfaces *via* Controlled Oxygen Vacancy Ordering

5.1 Introduction

Transition-metal oxides, such as the perovskite cobaltites, have been the focus of intense research due to their fascinating fundamental properties such as colossal magnetoresistance [1], spin-state transitions [2], and mixed-ionic transport [3], and their utilization in potential applications such as solid oxide fuel cells [4], gas sensors [5], catalysis [6], non-volatile memory [7] and multiferroics [8]. Many of these applications are critically reliant on particular electronic ground states, and the structural and electronic complexity of these materials provides a number of tunable "knobs" to stabilize the desired ground state. These knobs include intrinsic parameters such as cation radii and transition-metal valence, as well as external stimuli like temperature, strain and carrier modulation through electric and magnetic fields. Recent advances in high resolution transmission electron microscopy and electron energy loss spectroscopy (EELS) have revealed yet another degree of freedom – oxygen vacancy ordering. Oxygen vacancies are a ubiquitous and unavoidable defect in all transition-metal oxides and their existence as ordered superstructures, rather than randomly distributed point defects, has been observed in a number of perovskite materials [9 – 11]. These superstructures are driven by the interaction between ions and charged defects (vacancies) and lead to a lowering of the overall crystal symmetry along with a transition of the *B*-site coordination from octahedral to tetragonal, square pyramidal or square planar [10]. Being the outcome of the subtle interplay between structural enthalpy and configurational entropy, the presence and form of such oxygen-vacancy ordering (OVO) is acutely sensitive to the nature of the *B*-site cation, the stability of the *B*-site oxidation state, the oxygen chemical potential of the environment, temperature, pressure and strain. This results in myriad different (and often polymorphic) vacancy-ordered structures, with the brownmillerite structure (Section 1.5) being the most common [9, 10]. A number of fascinating properties have been attributed to the presence of ordered oxygen vacancies – epitaxial strain accommodation in $La_{0.5}Sr_{0.5}CoO_{3-\delta}$ (LSCOx50) thin films without

the formation of misfit dislocations [12], the stabilization of a ferromagnetic insulating state in $LaCoO_{3-\delta}$ thin films [13], prominent electrochromism in thin film $Bi_{0.9}Ca_{0.1}FeO_{3-0.05}$ [14], reversible redox reactions in thin film $SrCoO_{3-\delta}$ [15] and the stabilization of a ferroelectric phase in $YMnO_3$ [16]. However, despite a wide variety of systems exhibiting unique OVO induced properties, there have been no reported attempts to tune these properties by engineering the nature of the OVO superstructure. In this chapter, we follow up the modulation of the OVO through crystallographic orientation and epitaxial strain discussed in Chapter 4, and demonstrate the ability to thereby tune the magnetic and electronic ground state at cobaltite thin film interfaces, once again using $La_{1-x}Sr_xCoO_{3-\delta}$ (LSCO) as our prototypical cobaltite.

Bulk LSCOx50 is a robust metallic ferromagnet [17]. However, in thin film form both the magnetism and transport are degraded precipitously with decreasing thickness, the anomalously large degradation being inexplicable through finite size arguments alone [18]. Torija *et al.* revealed the presence of a severely hole-depleted $SrTiO_3$(001)/LSCO interface with a magneto-electronically phase separated (MEPS) ground state, which accounted for both the suppressed magnetization as well as the insulating behavior [19]. Crucially, they provided unequivocal proof that the hole-depletion, which pushes the system into the non-percolated and phase-separated region of the phase diagram, could be explained solely by the strain-induced OVO. The link between epitaxial strain and OVO was already postulated by Klenov *et al.* [12] and discussed in great detail in Chapter 4. Electronically, each oxygen vacancy donates two electrons to the lattice, thereby compensating for holes in LSCO in a simple ionic model. Epitaxial strain and carrier concentration are thus inextricably linked in thin film LSCO. Since heteroepitaxial films are inherently strained, this has profound implications for LSCO devices and functionalities that are reliant on interfacial electronic properties. Our work thus not only opens up new opportunities for interface sensitive applications that are plagued by the presence of interfacial "dead layers", such as oxide magnetic tunnel junctions [20] and spin-injection [21], but also demonstrates a novel tuning parameter for other thin film systems exhibiting oxygen-vacancy ordering.

5.2 Structure

LSCO films were grown on 5x5mm $SrTiO_3$(001) (STO(001)), $SrTiO_3$(110) (STO(110)) and $LaAlO_3$(001) (LAO(001)) substrates (MTI Corp.) by the high pressure oxygen sputtering technique described in Chapter 3. $SrTiO_3$ (a = 3.905 Å) presents a 1.8% tensile mismatch to LSCOx50 (a_{bulk} = 3.835 Å) while $LaAlO_3$ (a_{pc} = 3.789 Å) has a -1.2% compressive mismatch. We are thus able to decouple the two control parameters – crystallographic orientation and epitaxial strain – and independently study their effect on film properties. Film thicknesses were estimated from grazing incidence x-ray reflectivity (GIXR) and the films were verified to be single phase and epitaxial using specular wide angle x-ray diffraction (WAXRD), rocking curves (RC) and grazing incidence ϕ – scans. Specular WAXRD and RC scans of 100 Å

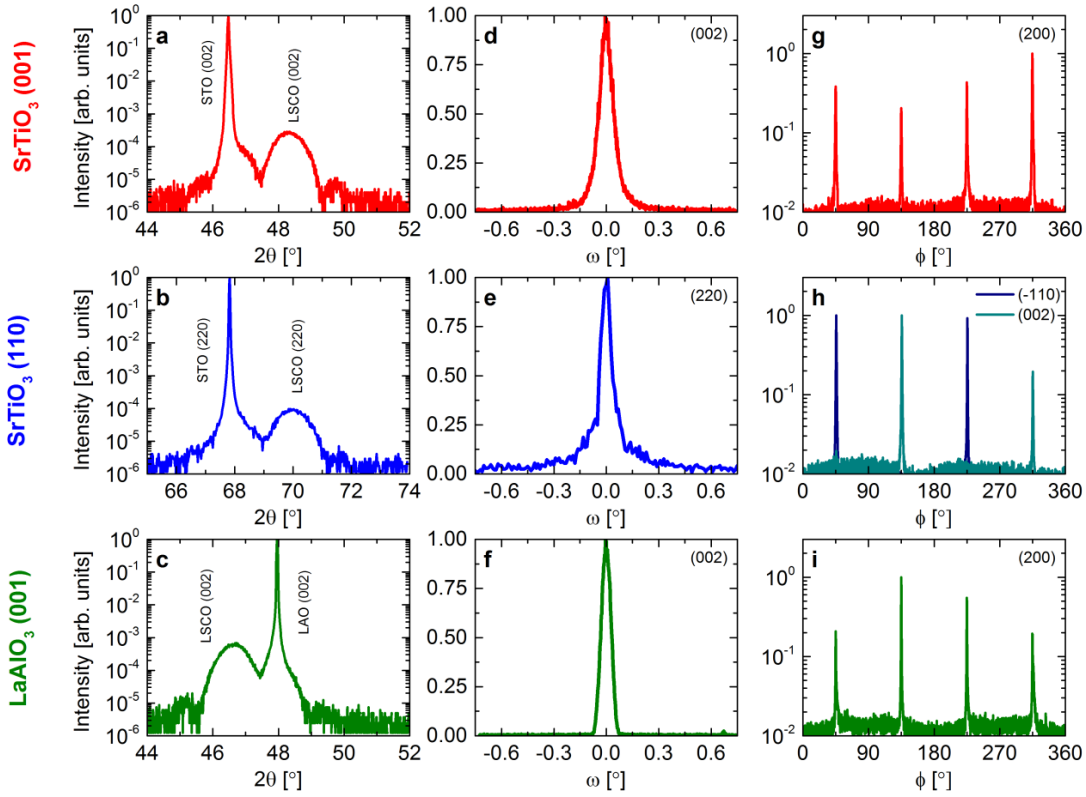

Fig. 5.1: a-c, Specular wide angle x-ray diffraction scans of 100 Å LSCO films showing the (*002*) peaks on STO(001) (**a**) and LAO(001) (**c**) and the (*220*) peak on STO(110) (**b**). **d-f,** Rocking curves through the (002) LSCO peak on STO(001) (**d**) and LAO(001) (**f**) and through the (220) LSCO peak on STO(110) (**e**). **g-i,** Grazing incidence in-plane x-ray diffraction (ϕ-scans) of 370 Å LSCO films from the (200) LSCO peak on STO(001) (**g**) and LAO(001) (**i**), and the (-110) and (002) LSCO peaks on STO(110) (**h**).

LSCOx50 films (Fig. 5.1 (a – f)) exhibit noticeable finite size fringes and narrow rocking curve widths (~ 0.05 – 0.08°), indicating fully strained films with a low surface roughness (on the lateral length scale of a few tens of nanometers) at these thicknesses. Further, ϕ – scans of 370 Å films (Fig. 5.1(g – h)) exhibit the same 4-fold and 2-fold symmetry as the substrates, indicating epitaxy even in partially relaxed films at higher thicknesses.

5.3 STEM/EELS

Chapter 4 discussed the accommodation and subsequent relaxation of epitaxial strain on STO(001), STO(110) and LAO(001) substrates by means of ordered oxygen vacancies. Although contrasting alternate dark and bright stripes (indicating the presence of an OVO superstructure) is clearly observed on all three substrates with *Z*-contrast scanning tunneling electron microscopy (STEM), this contrast is indirectly related to the oxygen vacancies, being caused by vacancy induced cation shifts. Thus direct quantification of vacancy concentration is impossible merely by analyzing the atomic column contrast in STEM images. We therefore make use of electron energy loss spectroscopy (EELS) spectra acquired simultaneously with the STEM images to quantitatively analyze the oxygen and hole concentration at the LSCOx50 interface with the three substrates. Details of the STEM/EELS instrumentation and sample preparation are given in Chapter 2 (Section 2.7.1). Oxygen concentrations were determined from the normalized O *K*-edge intensity while hole concentrations were estimated from the intensity of the 527 eV *K*-edge pre-peak (attributed to O 2p holes) normalized to the 535 eV main peak. A linear calibration, generated with O 2p hole intensities from reference LSCO bulk polycrystals of known composition, was used to convert the thin film hole concentrations to effective doping values. The procedure is identical to the one used by Torija *et al.* and outlined in Ref. 19.

Fig. 5.2 shows cross sectional STEM images and the corresponding EELS maps for oxygen and hole concentrations in representative 35 – 40 nm LSCOx50 films on the three substrates. The STEM images have been adapted from Chapter 4 while the EELS data for the film on STO(001) has been adapted from Ref. 19. It is immediately evident that there is a marked difference in the oxygen and carrier profiles in the three samples. LSCOx50 under tensile strain on STO(001), with oxygen deficient planes running perpendicular to the interface, suffers the most from

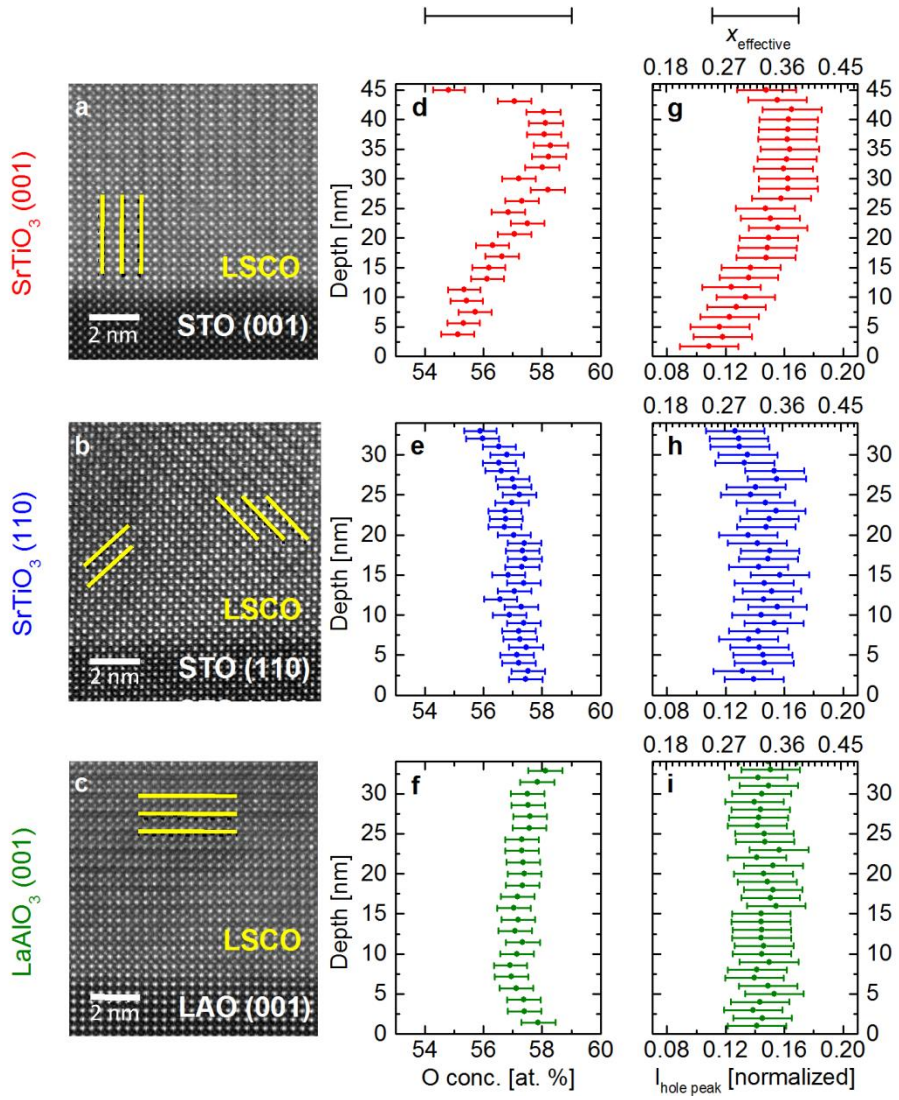

Fig. 5.2: a,b,c, High resolution *Z*-contrast STEM images showing oxygen vacancy ordering in LSCO on STO(001) (**a**), STO(110) (**b**), and LAO(001) (**c**). The image on STO(110) was acquired down the (001) zone axis. Yellow lines illustrate the oxygen deficient planes. **d,e,f,** Depth profiles of the oxygen concentration, as determined from the integrated intensity of the O *K*-edge, in LSCO on STO(001) (**d**), STO(110) (**e**) and LAO(001) (**f**). **g,h,i,** Depth profiles of the effective hole concentration, as determined from the intensity of the pre-peak ascribed to holes in the near-edge O *K* region, in LSCO on STO(001) (**g**), STO(110) (**h**) and LAO(001) (**i**). Data point error bars indicate the random error in each value arising from the uncertainty in the area of the EELS peaks; the black error bars at the top of the figure give the magnitude of the systematic error.

carrier depletion. In fact, conversion of the hole peak intensity to effective doping yields a value of $x \sim 0.23$, a number that is strikingly close to the critical doping for the bulk percolative –

long range metallic transition. This point has been discussed in great detail in Ref. 19. On the other hand, compressively strained LSCOx50 on LAO(001) barely shows any change in its oxygen and hole profile. At first glance, this would seem to suggest that the film has a negligible vacancy concentration. However, clear contrast between alternate lattice planes is seen in the STEM image, similar to the observation on STO(001) but with the OVO direction flipped by 90°. The conclusion then is that LSCOx50 film on both substrates adopts a brownmillerite-like structure, but not every vacancy site is actually vacant – the LAO(001) sample has a lower overall vacancy concentration than the film on STO(001). It must be stressed at this point that the large systematic error (indicated by the black error bars above the top panels) for each measurement make the quantitative determination of the absolute values of the oxygen and carrier concentrations almost impossible. However, the smaller random errors (to be precise, the uncertainty in the Gaussian fits to the EELS peaks and pre-peaks) allow the evaluation of the depth-wise trends in each sample. Qualitatively the differences between the films on STO(001) and LAO(001) can be understood in terms of the effect of strain on lattice volumes. The measured unit cell volumes of LSCOx50 in the bulk, on STO(001) and on LAO(001) are 56.402 $Å^3$, 57.413 $Å^3$ and 55.804 $Å^3$ respectively. The expansion of the unit cell under tensile strain is thus more conducive to the existence of a vacancy (which tends to expand the lattice) than the reduced volume under compressive strain. Our findings are also in agreement with the DFT calculations of Aschauer *et al.* for $CaMnO_3$ [22] and Kushima *et al.* for $LaCoO_3$ [23] as well as the experimental observations of Kubicek *et al.* on strained LSCO [24], all of whom found tensile strain to be more favorable for the formation of oxygen vacancies. Interestingly, the LSCOx50 film on STO(110) too has a negligible change in its oxygen and hole profiles, despite being under the same degree of tensile strain as the film on STO(001). Although we don't yet have a quantitative understanding of this phenomenon, we postulate that it is related to the strain relaxation on STO(110). As discussed in Chapter 4, LSCOx50 films on STO(001) are coherently strained to the substrate up to a thickness ~ 200 Å, at which point strain relaxation sets in with the formation of orthogonal OVO domains. This lattice relaxation coincides with the oxygen content and effective doping assuming stable (albeit less than bulk) values, either due to increased oxygen occupancy of vacancy sites, or oxygen accumulation at domain boundaries. On STO(110), however, this orthogonal OVO domain pattern extends all the way to the interface, resulting in a relatively oxygen-sufficient and hole-rich interface. Thus, by manipulating the OVO modulation vector and the coherency of the domain state of LSCOx50 films, we are able to change the effective hole-doping at the substrate/LSCO

interface. The rest of this chapter discusses the manifestation of these differently oxygenated ground states on the magnetic and transport properties of such films.

5.4 Magnetism

Fig. 5.3(a) shows the thickness evolution of the ferromagnetic Curie temperature (T_C) of LSCOx50 films on STO(001), STO(110) and LAO(001) substrates. All measurements were taken under a 1000 Oe field applied in the plane of the sample, with every sample being cooled in the same 1000 Oe field. The maximum in the 2nd derivative of the temperature dependent

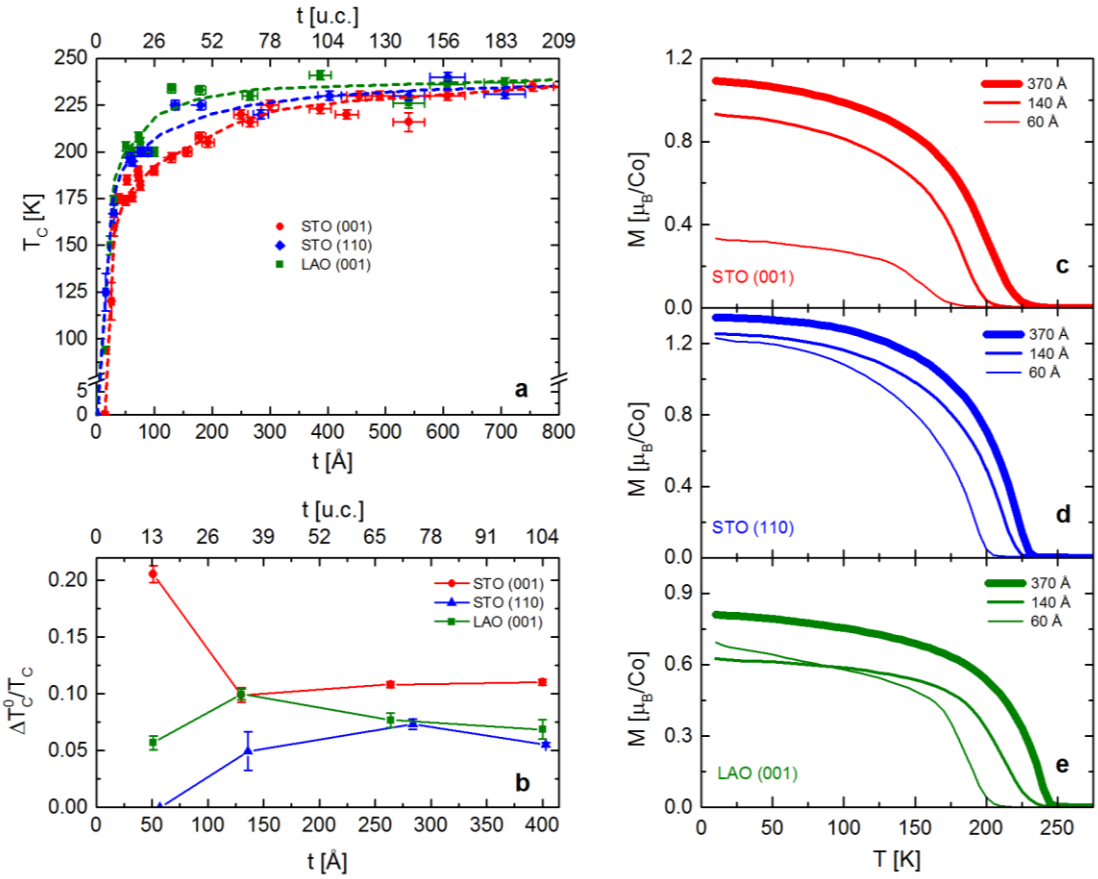

Fig. 5.3: a, Variation of the Curie temperature with thickness for LSCO on STO(001), STO(110) and LAO(001). Dashed lines are guides to the eye. **b,** Spread in the Curie temperature normalized to the average value of the Curie temperature for LSCO films of different thicknesses on STO(001), STO(110) and LAO(001). **c,d,e,** Magnetization as a function of temperature (in an in-plane applied field of 1 kOe) for LSCO of varying thicknesses on STO(001) (**b**), STO(110) (**c**) and LAO(001) (**d**).

magnetization ($\partial^2 M/\partial T^2$) was used to estimate the T_C, except for the thinnest samples for which the zero field extrapolation of the field-cooled/zero-field-cooled magnetization split was taken as the T_C. For each sample the bulk LSCO lattice parameter (3.835 Å) was used to convert the thickness in Angstroms to the approximate number of unit cells. In the bulk, LSCOx50 has a T_C ~ 250 K [17], and it is evident that LSCOx50 films on all three substrates asymptotically approach this value in the thick film limit (≥ 800 Å). In the ultrathin film limit, too, all three substrates exhibit similar behavior, with the T_C on all substrates dropping off sharply below a thickness ~ 30 – 40 Å. However, it is in the intermediate range ~ 50 – 300 Å that the films on the three substrates have strikingly divergent magnetic properties. LSCOx50 on STO(001) shows an almost linear drop in T_C in this range, changing from ~ 175 K at 50 Å to ~ 212 K at 300 Å. In the same thickness interval films on both LAO(001) and STO(110) suffer a far less dramatic T_C suppression, both holding T_C values above 200 K down to ~ 70 – 80 Å, following which there is a sharp downturn with the T_C meeting the STO(001) curve around 50 Å. In fact, the T_C on the LAO(001) a nd STO(110) films exceed the STO(001) sample by almost 35 K at a thickness ~ 140 Å, almost amounting to an 18% modulation in the T_C. This marked difference in T_C, although significant, is however only part of the difference between the STO(001) and the other samples. Figs. 5.3 (c-e) show the temperature dependent magnetization for each substrate at three representative thicknesses of 60 Å, 140 Å, and 370 Å. At each thickness, the STO(001) film not only has a lower T_C but also exhibits a broader ferromagnetic transition *cf.* the STO(110) and LAO(001) films. This broadening cannot be explained as a field induced artifact since each sample was measured in the same 1000 Oe field. Rather, we attribute this broadening to a distribution of T_C's in the STO(001) sample and postulate its origin to lie in the gradient in the oxygen and hole concentrations and the existence of a MEPS clustered state at the STO(001)/LSCOx50 interface [19]. We follow the procedure developed by Berger *et al.* and Campillo *et al.* [25, 26] to quantify this broadening on all three substrates (the detailed procedure is given in Chapter 2, Section 2.5.1). Assuming a Gaussian distribution of T_C's and fitting *M vs. T* curves under different *H* fields to a distribution-modified power law, we are able to extract the standard deviation of the T_C distribution as:

$$\Delta T_c(H) = \Delta T_c^0 + cH^{\frac{1}{\eta}} \tag{5.4.1}$$

where c and η are sample dependent constants. Here $\Delta T_c(H)$ is the total broadening of the transition temperature, ΔT_c^0 is the intrinsic broadening due to the T_C distribution and $cH^{1/\eta}$ represents the field induced broadening. Fig. 5.3(b) plots the thickness evolution of this intrinsic broadening term ΔT_c^0 normalized to the average T_C for each substrate. It is immediately obvious that the LSCOx50 films on STO(001) have a broader T_C *at all thicknesses* – the broadening is especially large at lower thicknesses with ΔT_c^0 increasing up to 20% T_C at 50 Å. On the other hand, ΔT_c^0 for the LAO(001) and STO(110) samples are within 5 – 10% of T_C at all thicknesses. These numbers are in good qualitative agreement with the LSCOx50 film on STO(001) being in a clustered state at 50 Å [19] (magneto-electronic phase separation leading to a distribution of ferromagnetic cluster sizes would certainly result in a broad distribution of T_C's) and suggest that at this thickness the films on LAO(001) and STO(110) still have long range ferromagnetic order. It must be stressed that the assumption of a Gaussian distribution function of T_C's is an oversimplification of the true distribution, which is expected to have a significant skew and depth-wise variation arising from the carrier concentration profile of Fig. 5.2. However, excellent agreement between the Gaussian model and the *M vs. T* data at all fields captures the essential physics and obviates the need for more complex models with additional fit parameters.

Thickness dependent magnetization measurements, such as the ones shown in Fig. 5.3, preclude the deconvolution of interface effects from those arising from the free surface. It is well known that surface reconstructions and changes in symmetry and magnetic anisotropy can result in the magnetic properties of surfaces being significantly different the bulk [27, 28]. In fact, a number of surface sensitive probes have revealed a suppressed surface magnetization in the closely related perovskite manganites [29, 30]. All other parameters being equal, a reduction in the film thickness leads to a greater contribution of the surface magnetization to the total measured moment, and thickness dependent measurements of such films would result in similar trends as Fig. 5.3, even though the substrate interface may possess bulk-like magnetization. To elucidate the true magnetic nature of the substrate/LSCO interface, we employed polarized neutron reflectometry (PNR) – an excellent non-destructive probe of the depth dependence of magnetism in thin films [31, 32]. Measurement details can be found in Chapter 2 (Section 2.3). It must be noted that for this particular experiment we chose a slightly different composition of LSCO, working with $La_{0.72}Sr_{0.28}CoO_{3-\delta}$ (LSCOx28) films on the same three substrates. Bulk LSCOx28, like LSCOx50, is a metallic ferromagnet, albeit with a slightly lower T_C ~ 225 K.

However, as shown by Torija *et al.*, the thickness *t** below which LSCO films exhibit suppressed magneticand electronic properties scales inversely as the doping [19], reaching ~ 150 Å at $x = 0.28$ *cf.* ~ 80 Å in LSCOx50. LSCOx28 would thus makes it significantly simpler to discern a buried magnetic "dead layer" in a PNR measurement while retaining the feasibility of growing a film thick enough to have a "bulk – like" ferromagnetic top layer.

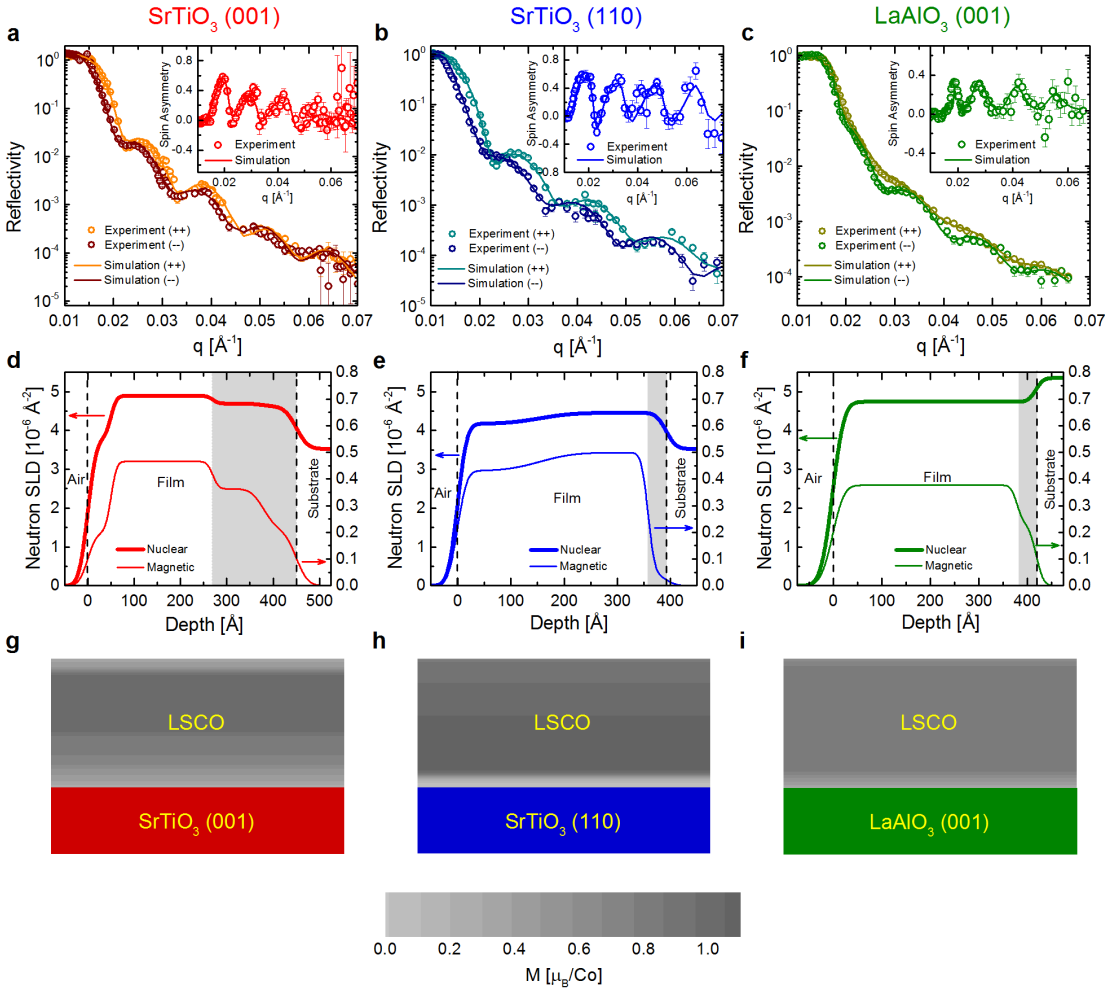

Fig. 5.4: Non spin flip (++ and --) polarized neutron reflectivity *vs.* scattering wavevector and corresponding fits for $t \approx 400$ - 450 Å LSCO on STO(001) (**a**), STO(110) (**b**) and LAO(001) (**c**). The STO(001) and LAO(001) samples were measured at 10 K while the STO(110) was measured at 5 K. All data were taken in an in-plane magnetic field of 1 T. Insets show the spin asymmetry, $(R^{++} - R^{--}) /(R^{++} + R^{--})$ and the corresponding fits. **d,e,f,** Depth profile of the nuclear and magnetic scattering length densities of LSCO on STO(001) (**d**), STO(110) (**e**) and LAO(001) (**f**). The shaded area in each panel indicates the suppressed magnetization interfacial region (the "dead layer"). **g,h,i,** Greyscale maps showing the magnetization depth profile on STO(001) (**g**), STO(110) (**h**) and LAO(001) (**i**).

Figs. 5.4 (a – c) show the low temperature (5 – 10 K) specular PNR data for the two non-spin-flip channels (R^{++} and R^{--}) for ~ 400 – 450 Å LSCOx28 films on STO(001), STO(110) and LAO(001) under a 1 T field applied in the plane of the sample. The solid lines in each panel are mathematical fits obtained using the models shown in Fig. 5.5 with the parameters listed in Table 5.1. The insets in each case show the neutron spin asymmetry (and the associated fits), which is defined as the difference between the intensities of the two spin dependent scattering channels normalized to their sum $((R^{++} - R^{--})/(R^{++} + R^{--}))$ and is proportional to the magnetization in the sample. The scattering length density (SLD) profiles used to obtain the fits are shown in Figs. 5.4 (d – f).

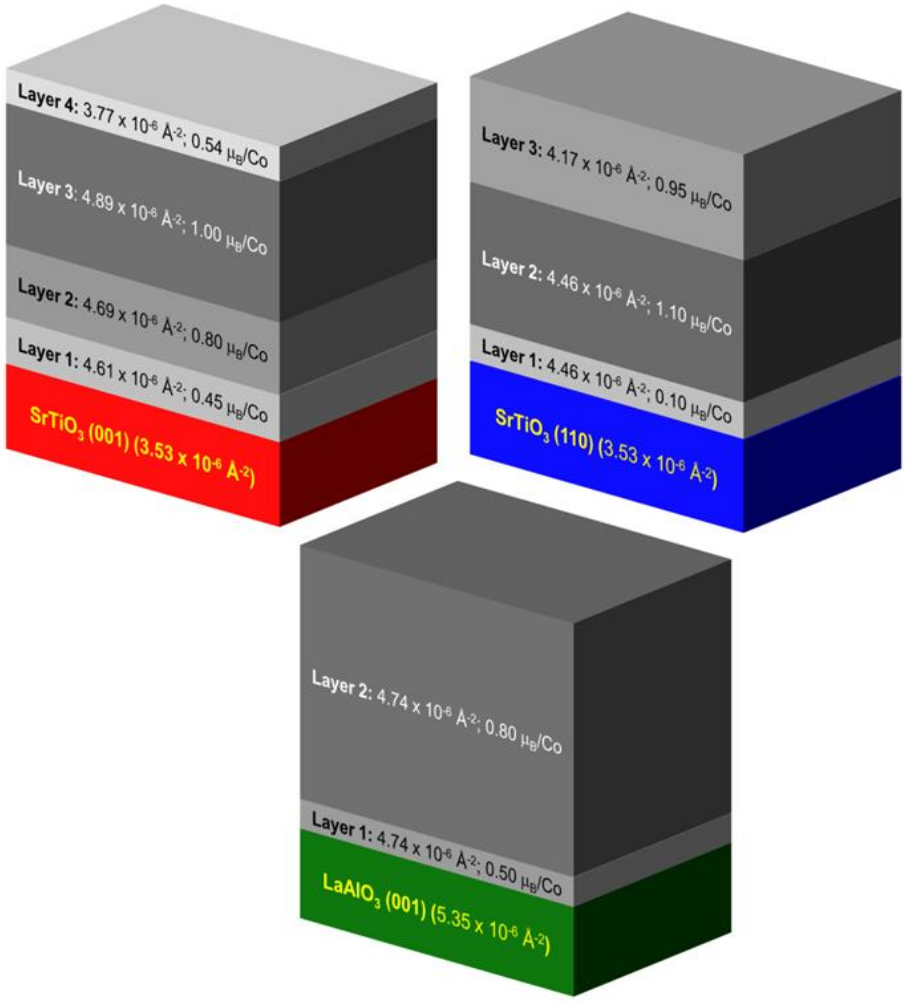

Fig. 5.5: Schematics depicting the layer structures used to model LSCO films on different substrates to obtain the fits shown in Fig. 5.4. The parameters shown for each layer are the nuclear scattering length density (in $Å^{-2}$) and the magnetization (in μ_B/Co).

The total SLD of each layer is the sum of two components – a nuclear SLD which depends on the elemental composition and stoichiometry of each layer, and a magnetic SLD which depends on the magnetization [33]. For each sample, the substrate SLD was fixed at the theoretical bulk value with zero magnetization. It is immediately obvious from the SLD profiles that the LSCOx28 film on STO(001) is significantly different from the ones on STO(110) and LAO(001). On STO(001), it takes the LSCO magnetic SLD ~ 180 Å to reach its maximum value, i.e. almost 40% of the 450 Å film is magnetically suppressed. This is demarcated by the shaded grey region on the SLD profile. Interestingly, the chemical SLD too shows a similarly suppressed profile with concomitant depth variations as the magnetic SLD. This chemical suppression arises from a reduction in oxygen concentration, i.e an increase in oxygen vacancy concentration. Oxygen atoms present a significant neutron scattering cross section (4.232×10^{-24} cm^2) and as a result are a sensitive parameter in PNR refinement models. This 180 Å length scale agrees very well with the *t** seen in the thickness dependent measurements of Torija *et al.* [19] and is a direct proof of the existence of a magnetic "dead layer" at the LSCO/STO(001) interface even in thick films with a ferromagnetic overlayer. Converting the magnetic SLD to a magnetization (in μ_B/Co), Fig. 5.4(g) shows the magnetically suppressed region to have a magnetization ~ 0.45 μ_B/Co up to 70 Å from the interface and increasing to 0.8 μ_B/Co till 180 Å, with the maximum magnetization achieved being 1 μ_B/Co (bulk magnetization for LSCOx28 is ~ 1.1 μ_B/Co). The average integrated moment from the PNR analysis comes out to 0.788 μ_B/Co, which is in good agreement with the 0.812 μ_B/Co obtained from SQUID magnetometry. Contrastingly, LSCOx28 films on both STO(110) and LAO(001) show magnetically suppressed regions that extend to 30 – 40 Å from the substrate interface. Although these regions could certainly be interfacial "dead layers" and would amount to an 80% reduction *cf.* STO(001), it could also be a manifestation of film – substrate interdiffusion, which often occurs at similar length scales. Further, the suppression in the magnetic SLD on these substrates is *not* accompanied by any noticeable change in the nuclear SLD, which could alternatively signify purely electronic origin for this magnetic suppression. Oxygen deficiency at the STO(001) and sufficiency at the STO(110) and LAO(001) interfaces are consistent with our EELS observations. The maximum magnetizations achieved are 1.1 μ_B/Co on STO(110) and 0.8 μ_B/Co on LAO(001), with the average integrated values being 0.954 μ_B/Co and 0.776 μ_B/Co respectively, both numbers once again closely matching magnetometry measurements (0.79 μ_B/Co and 0.747 μ_B/Co for STO(110) and LAO(001) respectively). The lower magnetization on

LAO(001) is due to the magnetic anisotropy on this substrate not being completely in the plane of the sample, a fact that is also manifested in the 1000 Oe *M vs. T* curves.

a $SrTiO_3(001)$ / $La_{0.72}Sr_{0.28}CoO_{3-\delta}$

Parameter	Units	Substrate	Layer 1	Layer 2	Layer 3	Layer 4
Thickness	Å	∞	70	110	220	50
Roughness	Å	20	5	5	10	10
Nuclear SLD	$Å^{-2}$	3.53×10^{-6}	4.61×10^{-6}	4.69×10^{-6}	4.89×10^{-6}	3.77×10^{-6}
Magnetization	μ_B / f.u.	0	0.45	0.8	1	0.54

b $SrTiO_3(110)$ / $La_{0.72}Sr_{0.28}CoO_{3-\delta}$

Parameter	Units	Substrate	Layer 1	Layer 2	Layer 3
Thickness	Å	∞	34	203	155
Roughness	Å	15	10	50	14
Nuclear SLD	$Å^{-2}$	3.53×10^{-6}	4.46×10^{-6}	4.46×10^{-6}	4.17×10^{-6}
Magnetization	μ_B / f.u.	0	0.1	1.1	0.95

c $LaAlO_3(001)$ / $La_{0.72}Sr_{0.28}CoO_{3-\delta}$

Parameter	Units	Substrate	Layer 1	Layer 2
Thickness	Å	∞	39	381
Roughness	Å	12.5	10	19
Nuclear SLD	$Å^{-2}$	5.35×10^{-6}	4.74×10^{-6}	4.74×10^{-6}
Magnetization	μ_B / f.u.	0	0.5	0.8

Table 5.1: Material parameters used in the fits shown in Fig. 3 for LSCO films on STO(001) (**a**), STO(110) (**b**) and LAO(001) (**c**).

5.5 Transport

Although bulk magnetometry and PNR offered useful insights into the nature of the substrate/LSCO interface and hinted at the possibility of MEPS on STO(001), the electronic ground state at the interfaces is perhaps best probed by transport, both in the presence and absence of a magnetic field. Transport in LSCOx50 films on STO(001), STO(110) and LAO(001) substrates was measured in a van der Pauw (vdP) configuration using sputtered 5nm Mg/50nm Au as Ohmic contacts. Excitation currents were carefully chosen to prevent self-heating and ensure Ohmicity at the lowest temperatures.

Fig. 5.6 shows the resistivity of LSCOx50 films on STO(001), STO(110) and LAO(001) as a function of temperature at four representative thicknesses – 130 Å, 55 - 60 Å, 45 Å, and 30 Å. It must be noted that the in-plane crystalline anisotropy of the STO(110) substrate results in the resistances along the two orthogonal in-plane directions [001] and [-110] being significantly different. As a result, application of the vdP method, which was developed for isotropic homogenous materials, is not strictly valid. Indeed, rigorous mathematical treatment has shown the vdP resistivity of an anisotropic sample to be the geometric mean of the principle components of the second rank resistivity tensor and has proved the method to be insufficient to measure the principle components of the tensor from a single sample [34]. Finite element method simulations have also shown the vdP resistivitiy of anisotropic media to have significant deviations from the isotropic values [35]. Although a number of groups have reported modifications to the method with special sample geometries to measure anistropic samples [36 – 38], an accurate determination of the planar resistivity components of LSCO films on STO(110) will require carefully prepared orthogonal Hall bars and is currently being investigated. Here we have simply converted the 4-terminal resistances along the two directions to resistivities using the van der Pauw formulation *only* so that we may compare the values to the other isotropic (001) substrates. Resistance mixing between the two orthogonal channels, which is not only possible but is probable, has been neglected. Bulk LSCOx50 being metallic, it comes as no surprise that thick films at 130 Å (~ 34 unit cells, u.c.) are metallic (possess a negative $\frac{d\rho}{dT}$) down to the lowest temperature on all three substrates. Films thicker than 130 Å show similar metallic behavior, with minor variations attributed to varying surface roughness. Interestingly, on STO(110), while both the [-110] and [001] resistance channels are metallic, the [001] direction has a slightly higher resistance with a small upturn at low temperature,

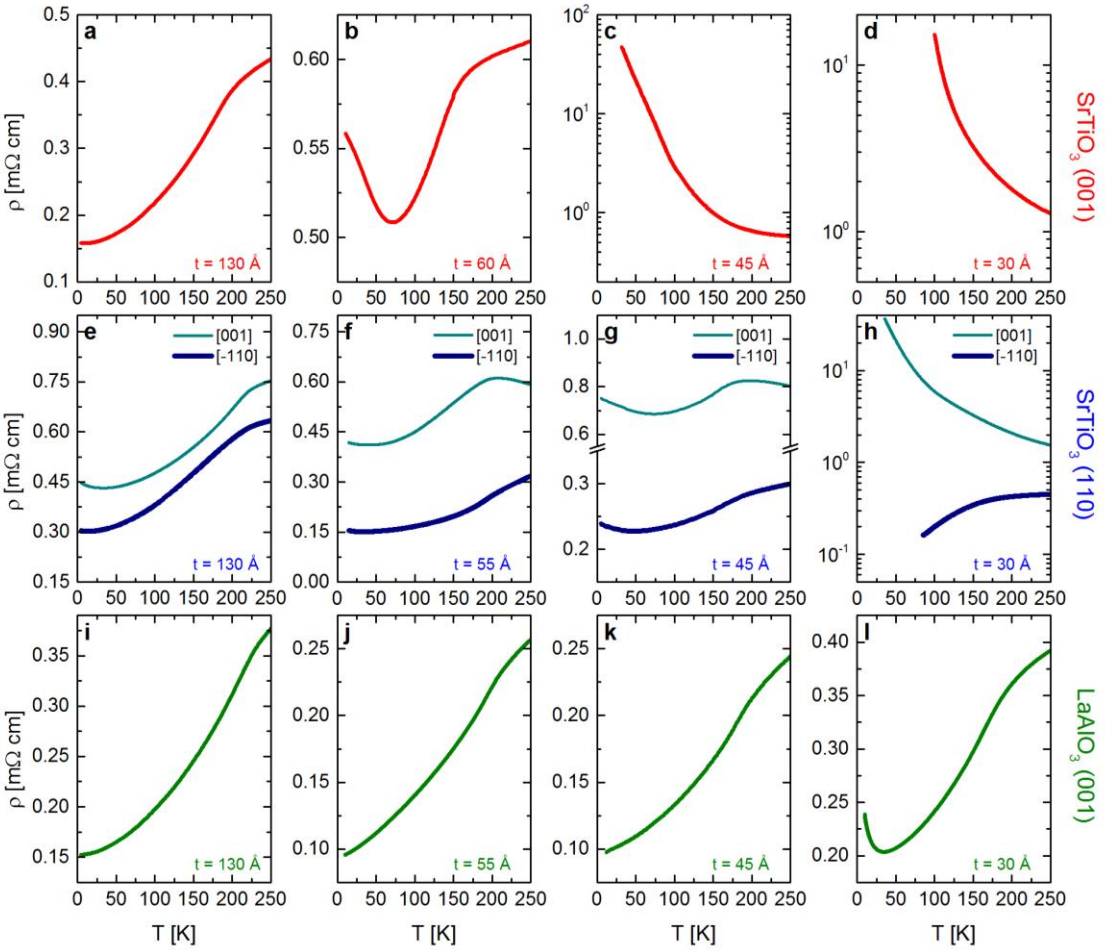

Fig. 5.6: Resistivity in zero magnetic field as a function of temperature for LSCO of varying thicknesses on STO(001) (**a-d**), STO(110) (**e-h**), and LAO(001) (**i-l**). On STO(110) the resistivity is shown along both [-110] and [001].

suggesting the [001] resistance channel to be on the verge of a metal-insulator transition. On both STO(001) and LAO(001), the films have a residual resistivity ratio (RRR, defined as ρ_{300K}/ρ_{0K}) ~ 2.6 – 2.8, which is close to the bulk single crystal value (RRR ~ 4.2 for x = 0.30 single crystals [39]). However the RRR of the STO(110) sample is significantly smaller. Upon reducing the film thickness to 55 – 60 Å (~ 14 – 16 u.c.), the three substrates display very different behavior. The STO(001) sample shows a prominent low temperature upturn, suggesting carrier localization and consistent with this thickness being less than the critical MEPS thickness t^* for LSCOx50 films on STO(001) substrates [19]. On the other hand, the LAO(001) sample shows almost no change from the thicker film. The STO(110) film too is qualitatively similar to the 130 Å sample except that the difference between the two resistance

channels is now larger. Further reduction in thickness to 45 Å (~ 12 u.c.) pushes the STO(001) sample into an insulating state with a positive $\frac{d\rho}{dT}$ at all temperatures while the LAO(001) sample still remains "firmly" metallic. The two resistances on STO(110) are now split even further, with the sample exhibiting a metal – insulator transition along the [001] direction but showing metallic transport along the [-110]. The small low temperature upturn in the [-110] resistance could be a contribution from the [001] resistance. Finally, ultrathin LSCOx50 films ~ 30 Å (~ 8 u.c.) become extremely insulating on STO(001) (being almost impossible to measure below

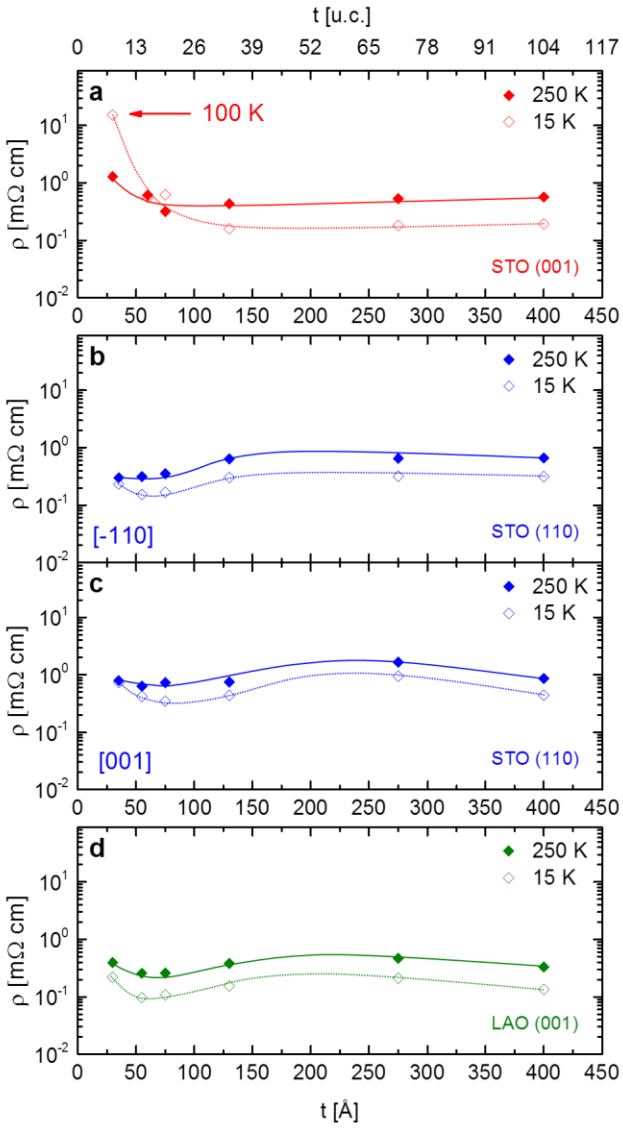

Fig. 5.7: Zero magnetic field resistivity at 250 K and 15 K of LSCO on STO(001) (**a**), STO(110) (**b,c**) and LAO(001) (**d**). On STO(110) the MR is shown along both [-110] and [001]. Lines are guides to the eye.

100K) and develop a low temperature upturn on LAO(001), suggesting a possible onset of MEPS at a slightly lower thickness. On STO(110), the film becomes insulating along [001], almost as much as the STO(001) sample, but remains seemingly metallic along [-110]. It must be noted that the measured van der Pauw resistance along [-110] becomes extremely large at low temperatures, almost equaling the [001] value. However, these numbers cannot be completely trusted due to the likely possibility of resistance mixing between the two channels, and the thus the dataset has been terminated at 75 K. Although the exact origin of the [-110] direction being more conductive than the [001] is unclear, we postulate it to be related to the oxygen vacancy ordering direction along with the crystallographic anisotropy. The thickness evolution of the transport behavior is summarized in Fig. 5.7 which plots the resisitivities at 250 K and 15 K for all three substrates (including the two directions for STO(110)), the lines being mere guides to the eye. The crossing of the two lines around 75 Å marks the existence of a metal – insulator transition and the onset of MEPS on STO(001). The two lines converge ~ 35 Å on STO(110), suggesting similar behavior on this substrate although at a much lower thickness. On LAO(001), on the other hand, the lines never quite converge but would appear to do so (if extrapolated) somewhere below 25 Å. However, the extreme difficulty of maintaining oxygen stoichiometry in such thin films makes the accurate determination of t^* on LAO(001) and STO(110) almost impossible without the use of LSCO/LAO and LSCO/STO superlattices.

5.6 Magnetotransport

Every material shows a change in resistance upon the application of a magnetic field. This resistance change, normalized to its zero field value ($\Delta R/R_0$) is referred to as the magnetoresistance (MR) and has many underlying contributions. Ordinary paramagnetic metals exhibit a positive parabolic MR arising from increased path lengths of the transport electrons due to cyclotron orbits [40]. Long range ordered ferromagnetic metals exhibit what is known as anisotropic magnetoresistance (AMR) [41], where due to spin-orbit coupling and spin dependent scattering, the MR changes sign depending on the whether the magnetic field is applied parallel to the current or perpendicular to it. On the other hand, clustered ferromagnets and granular metals exhibit an isotropic negative MR [42, 43]. Transport in such materials is through inter-cluster electron hopping, the probability of which is maximized when the moments of all clusters are aligned parallel to each other and minimized when they are

completely disordered. The phenomenon is similar to the giant magnetoresistance effect (GMR) seen in metallic ferromagnet-paramagnet multilayers [44] and is referred to by us as intercluster GMR (IGMR). IGMR is a signature of MEPS LSCO and has been used to distinguish between the clustered state and the electronically homogenous state, both in the bulk and in thin films [19, 45].

Fig. 5.8 (a – d) show the MR in 60 Å LSCOx50 films at 10 K on STO(001), STO(110) and LAO(001), both with the current flowing parallel to the magnetic field and perpendicular to it. The MR measurements were carried out in fields up to 9 T with the magnetic field applied in the plane of the sample at all times. This particular thickness was chosen since it is at this point that films on the substrates begin to show diverging electronic and magnetic properties. The STO(001) sample, almost identically to the findings of Torija *et al.* [19], shows negative

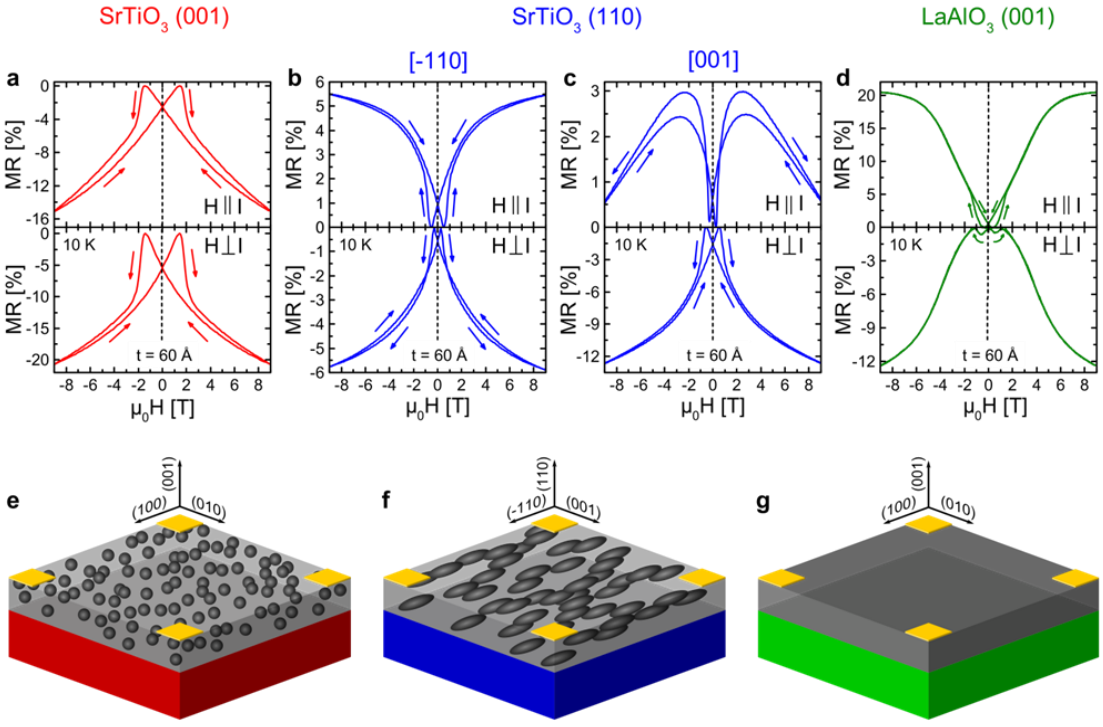

Fig. 5.8: a,b,c,d, Magnetoresistance (((ρ(H)-ρ(0))/ρ(0)) x 100%) at 10 K for 60 Å (≈ 16 u.c.) LSCO films on STO(001) (**a**), STO(110) (**b,c**) and LAO(001) (**d**). The upper half of each panel shows the MR with magnetic field parallel to current, the lower with field perpendicular to current. All measurements were taken with the field in the sample plane. On STO(110) the MR is shown along both [-110] and [001]. **e,f,g** Schematics depicting the magneto-electronic phase separation morphology on the three substrates. Dark regions are hole-rich, metallic and ferromagnetic, while light regions are hole-poor, insulating and non-ferromagnetic. Gold squares represent electrical contacts.

hysteretic MR in both field configurations. The peaks in MR coincide with the coercive field seen in the magnetic hysteresis loop – this makes sense since this is the point at which the sample has maximum spin disorder. The MR, though, is not completely isotropic, reaching ~ -15% at 9 T with the field parallel to the current, and ~ -20% in the perpendicular case. This is consistent with the magnetometry and zero field transport data. AT 60 Å, LSCOx50 has a T_C ~ 175 K (Fig. 5.3(a)) and is in the midst of a metal – insulator transition (Fig. 5.6(b)), implying the presence of small ferromagnetic and metallic percolative pathways that are expected to have an anisotropic MR response to field. However, the MR is certainly dominated by IGMR from the clusters and unequivocally proves the presence of a clustered ground state. It must be noted that the MR never quite saturates even at 9 T, indicating incomplete spin-disorder suppression. In stark contrast, the film on LAO(001) shows extremely large anisotropic MR, reaching ~ 20% and ~ -12% for the parallel and perpendicular configurations respectively. This AMR value of ~ 32% is enormous compared to the bulk value (AMR in ferromagnetic single crystal $SrCoO_3$ is ~ 1.5% [46]) and other traditional ferromagnetic metals (typical AMR in conventional ferromagnets is ~ 5 - 6% [41]) – we believe this huge AMR has its origins in the oxygen vacancy ordering and are cu rrently investigating it in more detail. Further, the MR shows no sign of any high field negative slope, implying IGMR, if at all present, is negligible compared to AMR. This provides definitive proof the LSCOx50 film on LAO(001) has long range ferromagnetic order at 60 Å, with no discernible signs of MEPS. Interestingly, the STO(110) sample seems to lie somewhere between these two extremes. Along the [-110] direction, which is the more conductive of the two orthogonal directions measured, and which appears to be robustly metallic, the sample shows distinct AMR of ~ 11%. On the other hand, along the [001], it exhibits a combination of AMR and IGMR – the MR is still anisotropic, but with the current running parallel to field, it has a large negative high field slope, implying that the IGMR and AMR contributions have comparable magnitudes. This would suggest ferromagnetic clustering, but with some degree of directional bias. Based on these observations, we propose the LSCOx50 ground states at the three interfaces resemble the depictions of Fig. 5.8 (e – g). We postulate that on STO(001), the LSCO interface is isotropically clustered, with a long range ordered ferromagnetic and metallic overlayer appearing at ~ 80 Å. On STO(110), too, the interface exhibits MEPS. However, in this case, the crystalline anisotropy of the substrate biases the clusters to have an almost nematic order – they are either elongated (depicted as ellipsoids in Fig. 5.8 (f) for simplicity), or are more closely spaced and percolative along the [-110] direction compared to the [001]. We are unable to distinguish between the two possibilities with our

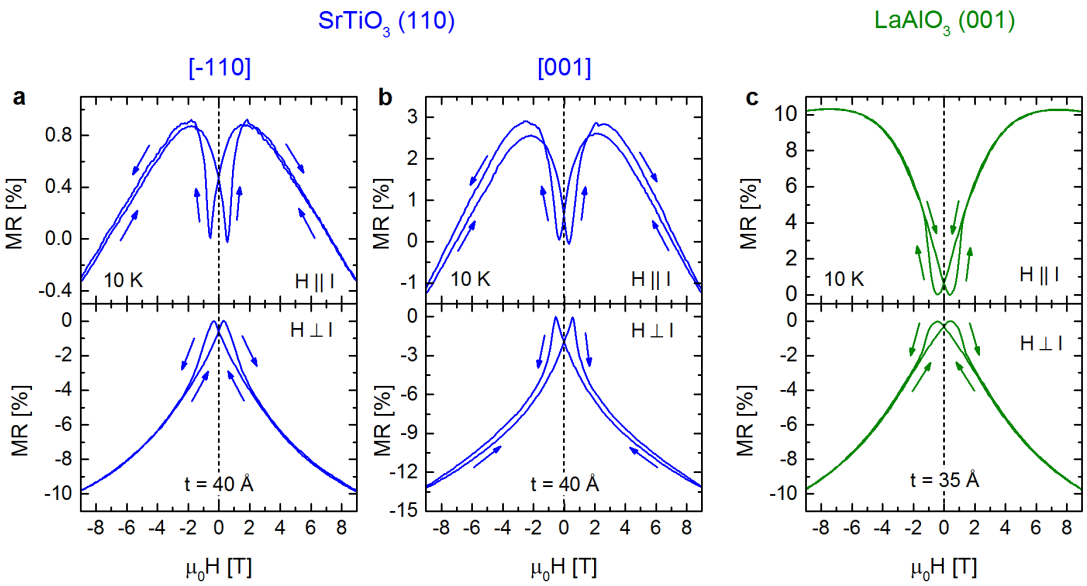

Fig. 5.9: Magnetoresistance data at 10 K for approximately 40 Å (≈ 10 u.c.) LSCO on STO(110) (**a,b**) and LAO(001) (**c**). The upper half of each panel shows the MR ((((ρ(H)-ρ(0))/ρ(0)) x 100%) with magnetic field parallel to current, the lower with field perpendicular to current. All measurements were taken with the field in the sample plane. On STO(110) the MR is shown along both [-110] and [001].

current measurements. On LAO(001), the film appears to be ferromagnetic and metallic. Finally, in ultrathin films ~ 35 – 40 Å (Fig. 5.9), we find that the STO(110) sample shows a combination of AMR and IGMR along both in plane directions, indicating that the clusters are now well separated by an insulating matrix in both directions. The LAO(001) sample, however, *still* shows AMR ~ 20%, which although large is nonetheless lower than the value at 60 Å. The STO(001) sample is too insulating for low temperature MR measurements in this thickness range.

5.7 Concluding remarks

In summary, we have demonstrated that a combination of crystallographic orientation and epitaxial strain can be used rather effectively to modify the magneto-electronic ground states of cobaltite interfaces through manipulation of the oxygen vacancy order found in such systems. Using $La_{0.5}Sr_{0.5}CoO_{3-\delta}$ as our prototypical cobaltite and combining STEM/EELS,

magnetometry, PNR and transport, we have established the presence of a MEPS clustered state at the $SrTiO_3$ (001) interface which changes to a metallic long range ordered ferromagnet on $LaAlO_3$ (001). Interestingly, the $SrTiO_3$ (110) interface shows a directionally biased clustered state, appearing to be ferromagnetic and metallic along [-110] and phase-separated along [001]. We have been able to stabilize ferromagnetism and metallicity in $La_{0.5}Sr_{0.5}CoO_{3-\delta}$ films as thin as 30 Å (~ 8 u.c.) on $LaAlO_3$ (001) substrates, further reduction in thickness leading to oxygen loss and requiring multilayer stacks. Our work thus opens up new avenues to not only tailor interfacial electronic ground states in oxide thin films, but also tune the myriad other unique properties that arise from the presence of oxygen vacancy ordering.

Chapter 6

Direct Real Space Observation of Magneto – Electronic Inhomogeneity in Ultra-thin film $La_{0.5}Sr_{0.5}CoO_{3-\delta}$ on $SrTiO_3$ (001)

Note: This chapter has been reprinted with permission from S. Kelly, F. Galli, J. Aarts, Shameek Bose, M. Sharma, and C. Leighton, Appl. Phys. Lett. **105**, 112909 (2014).

6.1 Introduction

In the preceding chapters, I have discussed how epitaxial $La_{1-x}Sr_xCoO_{3-\delta}$ (LSCO) accommodates lattice mismatch with the substrate through a novel strain relief mechanism *via* oxygen vacancy ordering. Essentially, the perovskite LSCO transforms to a brownmillerite-like orthorhombic structure, with oxygen vacancies ordered along the [110] directions on alternate (001) Co-O planes. This phenomenon inextricably links the substrate induced strain to film stoichiometry, thereby significantly altering the electronic ground state at the interface. The interface with $SrTiO_3$ (001), which imparts a 1.8% tensile strain to the film, exhibits severe degradation of magnetism and transport. The tensile strain favors the formation of oxygen vacancies, each of which donate two electrons to the lattice and compensate for the holes in the system. This pushes the system from deep within the ferromagnetic and metallic region of the phase diagram (Fig. 1.19) across the metal – insulator threshold and into the clustered magneto-electronically phase separated (MEPS) regime. This MEPS region extends to ~ 80 Å from the interface, beyond which the film slowly evolves towards bulk-like ferromagnetism and metallic transport. Torija *et al.* established oxygen vacancies to be the origin of this degradation through careful scanning transmission electron microscopy and electron energy loss spectroscopy (STEM/EELS) and confirmed the MEPS at the interface with small angle neutron scattering (SANS) [1]. Chapters 4 and 5 extended this work and demonstrated how substrate induced strain and crystallographic orientation may be used to tune the interfacial oxygen and hole concentrations and thereby significantly alter the magnetic and transport properties of the interface and ultrathin films. While progress with understanding ultra-thin film structure and property degradation in cobaltites has thus been significant, one missing element is direct, real space proof of the purported magneto-electronic inhomogeneity in $SrTiO_3$ (001)/LSCO. Indeed, despite the considerable work on magneto-electronic phase separation in bulk [2 – 5] and thin

film [1] cobaltites, all studies to date were restricted to reciprocal space or indirect MEPS signatures, due to the dearth of real space methods to probe electronic and/or magnetic inhomogeneity at such short [2] length scales. In this chapter, I shall show how we filled this gap by providing the first direct, real space observation of electronic heterogeneity in $SrTiO_3$ (001)/LSCO. Low temperature scanning tunneling microscopy (STM) and scanning tunneling spectroscopy (STS) have been used to acquire nm spatial resolution conductance maps and current-voltage curves, to probe the local density-of-states (LDOS) at the surface of $SrTiO_3$ (001)/LSCO. Films with thickness 12.4 nm (above t^*) are electronically uniform, while films with thickness 4.7 nm (below t^*) reveal strikingly heterogeneous conductance on nanoscopic scales, with complex correlations with topography and applied magnetic field. These results directly verify nanoscale electronic inhomogeneity in ultra-thin film $SrTiO_3$ (001)/LSCO, in agreement with previous work using less direct techniques.

6.2 Samples: Preparation and characterization

LSCO $x = 0.50$ films with thickness (from x-ray reflectivity) of $t = 4.7$ nm (12 unit cells) and $t = 12.4$ nm (32 unit cells) were deposited on $SrTiO_3$ (001) from ceramic targets by high-pressure reactive DC magnetron sputtering [1, 6, 7]. Depositions were performed at a substrate temperature ~700 °C, total pressure of 140 mTorr, and O_2/Ar pressure ratio of 0.4, followed by cooling in 500 Torr of O_2 and post-annealing in flowing O_2 at 500 °C. This results in single-phase cation-stoichiometric epitaxial LSCO (001) with optimal oxygenation and properties. Films studied here are below the critical thickness for strain relaxation (20 nm). Following high-resolution x-ray characterization, magnetization (M) and resistivity (ρ) were measured at temperature (T) from 5 to 300 K in magnetic fields ($\mu_o H$) to 7 T. STM/STS measurements (T = 2 – 180 K, $\mu_o H \leq 10$ T) were performed using an STM head built in-house at the University of Leiden and maintained in ultra-high vacuum. Details for each measurement may be found in Chapter 2, Sections 2.4, 2.5 and 2.6.2.

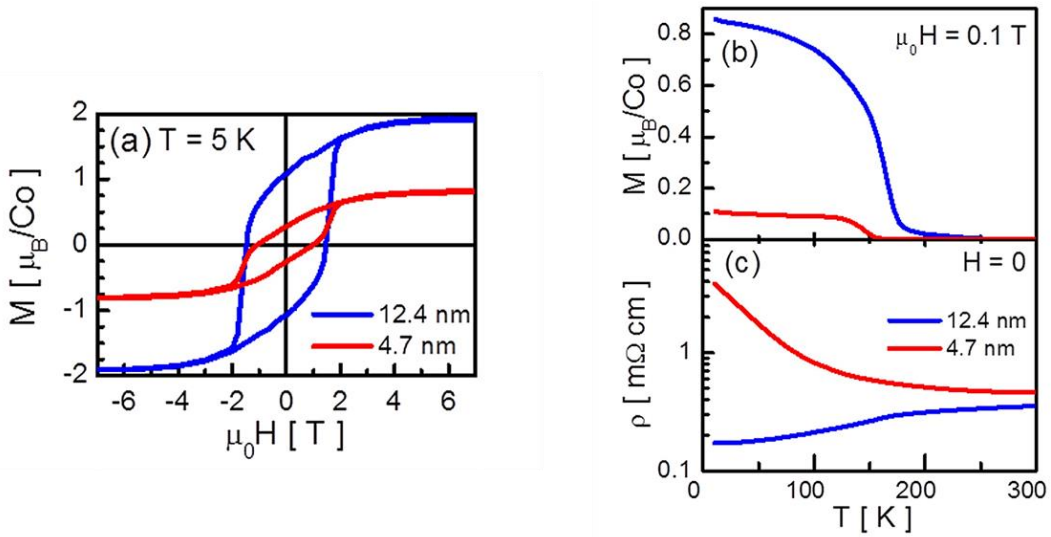

Fig. 6.1: (a) 5 K hysteresis loops of $SrTiO_3(001)/La_{0.5}Sr_{0.5}CoO_{3-\delta}$ films with thickness 4.7 and 12.4 nm. Temperature dependence of (b) the magnetization in a 0.1 T magnetic field, and (c) zero field resistivity of $SrTiO_3(001)/La_{0.5}Sr_{0.5}CoO_{3-\delta}$ films with thickness 4.7 and 12.4 nm.

6.3 Magnetism and transport

As shown in Fig. 6.1 (a), magnetization hysteresis loops at 5 K reveal clear ferromagnetism with substantial coercivity [8], and saturation magnetization that falls from a bulk-like 2 μ_B/Co at t = 12.4 nm to 0.8 μ_B/Co at t = 4.7 nm. As shown in Figs. 6.1 (b, c) this suppression in M is accompanied by a Curie temperature reduction (from ~185 to 150 K), along with a crossover from metallic-like ρ *vs*. T with an inflexion point around the Curie temperature (at t = 12.4 nm), to an insulating - like ρ *vs*. T with much larger low T resistivity (at t = 4.7 nm). This is consistent with prior work [1], confirming that these samples straddle the t* value of 6 – 7 nm marking the crossover to the proposed electronically and magnetically inhomogeneous state.

6.4 Low temperature STM

Beginning with the t = 12.4 nm film, Fig. 6.2 summarizes the typical behavior seen by STM/STS at T = 1.7 K. To acquire the differential conductance map shown in Fig. 6.2 (a), the tip-sample separation was first fixed by the chosen set-point (0.60 V bias, 0.22 nA), and the

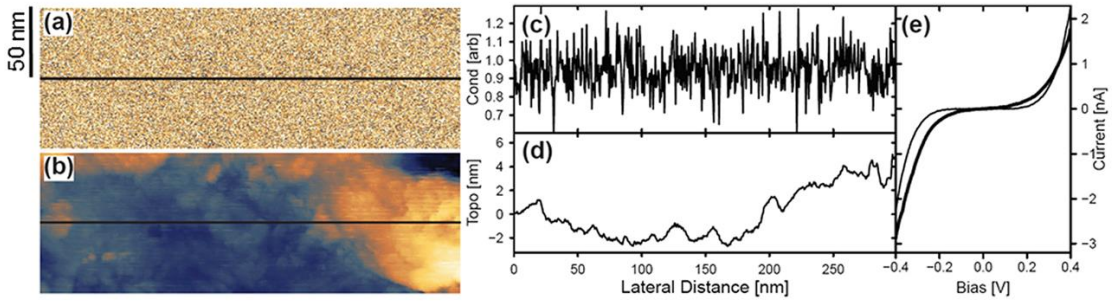

Fig. 6.2: (a) Differential conductance and (b) corresponding topography (where lighter regions are high and darker regions are low) over a 100 × 300 nm region of a 12.4 nm thick $SrTiO_3(001)/La_{0.5}Sr_{0.5}CoO_{3-\delta}$ film. Data were acquired at 1.7 K with a set-point of 0.6 V and 0.219 nA. Horizontal lines denote the positions of the relative differential conductance and topographic line scans shown in (c) and (d). (e) Two example current-voltage scans taken from a set of 16 measured along a diagonal of a 300 × 300 nm region encompassing the one shown in (a) and (b). Data were acquired with a set-point of 0.35 V and 1 nA.

differential conductance about this 0.60 V DC bias probed as a function of position over the 100 × 300 nm area shown. It is essential to note, as clearly illustrated by the representative *I-V* curves shown in Fig. 6.2 (e), that at these relatively high biases the highest differential conductances are actually associated with the most *insulating* local regions, with the *highest* apparent tunneling gaps, and *lowest* zero bias conductance (ZBC). The topographic map acquired simultaneously to this conductance map is shown in Fig. 6.2 (b), while Fig. 6.2 (c, d) show line scans (along the horizontal lines in Fig. 2 (a, b)) of the relative differential conductance and topography.

The most noteworthy feature is clearly the remarkable uniformity in differential conductance and thus LSCO surface LDOS. There are no obvious contiguous nanoscale areas of similar conductance in Fig. 6.2 (a), and no evidence of correlation between conductance (Fig. 6.2 (a)) and topography (Fig. 6.2 (b)), despite the significant root mean square roughness (~ 2 nm). This is borne out by the line scans (Fig. 6.2 (c, d)), which appear uncorrelated, with no systematic changes in conductance where topographical changes occur. Quantifying the conductance fluctuations (Fig. 6.2 (c)) with autocorrelation analysis reveals that correlations are already beneath 95 % confidence at lateral scales as short as 0.6 nm. In contrast, the topographic line scan in Fig. 6.2 (d) results in a lateral correlation length of ~ 50 nm. While the fluctuations in conductance thus must occur on very short length scales, they are indeed present, as confirmed by measurement of *I-V* curves at multiple locations. The curves in Fig. 6.2 (e) are in fact two

examples from 16 such curves taken along a diagonal of a 300 × 300 nm area enclosing the region in Fig. 6.2 (a). 15 of these curves were similar to the fine line in Fig. 6.2 (e), with an average ZBC of 1.4×10^{-2} nA/V and standard deviation 8.4×10^{-3} nA/V. The remaining curve was significantly different (heavy line in Fig. 6.2 (e)), having a ZBC of 3.9×10^{-1} nA/V, *i.e.* 30× larger than the average of the other 15. This behavior was found in multiple cases, in several regions, suggesting very small conductance "hotspots". Somewhat similar effects have been seen in otherwise homogeneous manganite films, and attributed to defects [9], as could be the case here.

As shown in Fig. 6.3 the situation is markedly different in films with thickness 4.7 nm, *i.e.* below t^*. In this figure, panels (a – c) are representative 55 × 55 nm differential conductance maps measured at 3.7 K in $\mu_o H$ = 0, 4, 8 T, while panel (d) depicts topography. Panels (e) and (f) show scans along the horizontal lines marked on panels (a) – (d), while panel (g) shows representative *I*-*V* curves at 7.5 K. Again, it is essential to note that in these conductance maps, which were measured at a set-point of 0.70 V and 0.21 nA (comparable to Fig. 6.2) the highest differential conductances are actually associated with the most *insulating* local regions, with the *highest* apparent tunneling gaps, and *lowest* ZBC, as clearly shown in Fig. 6.3 (g). The dark regions in Figs. 6.3 (a – c) are thus the most metallic, the light areas being more insulating. The heterogeneity visible in Figs. 6.3 (a – c) is striking. As in electronically inhomogeneous manganites [10 – 14], contiguous nanoscale regions of similar differential conductance are evident, conductive clusters forming in an insulating matrix. The extent of this inhomogeneity is reinforced by Fig. 6.3 (g), which shows STS *I* – *V* curves representative of the dark (blue) and light (yellow) regions. The heavy line (representative of the conductive clusters) has a ZBC of 1.6 nA/V, while the fine line (representative of the insulating matrix) yields a ZBC of 1.4×10^{-2} nA/V, the factor of 120 between the two greatly exceeding the factor of 30 between extremal ZBCs on the thicker film. The 4.7 nm LSCO film thus exhibits substantially larger fluctuations in conductance and LDOS than the 12.5 nm film, direct confirmation of the deductions discussed in the introduction.

Interestingly, Fig. 6.3 (a) also reveals that the electronic heterogeneity in these ultra-thin films is not on a single length scale, but instead occurs over a hierarchy of scales from ~ 5 to 50 nm. Numerous additional images confirm this, occasionally even larger showing metallic clusters,

up to 100 nm. As can be seen by comparing Fig. 6.3 (a) and (d), the extent to which this electronic texture is correlated with topography is also non-trivial. There are certainly regions (such as the one labeled "A" in Fig. 6.3), where the conductance and topography are obviously correlated, the more metallic behavior occurring in locally thicker regions, as might be expected. On the other hand, as illustrated by the entire left side of Fig. 6.3 (a) and (d), there are also regions with no clear correlation between conductance and height. Further quantification can be achieved with the line scans shown in Fig. 6.3 (e) and (f). Abrupt topographical features are indeed accompanied by conductance changes in some cases, *e.g.*, at a lateral distance of 22 nm when region A is entered; correlations between conductance and topography are in fact clear across this whole region (from 22 – 50 nm). On the whole however, the fluctuations in conductance in Fig. 6.3 (e) occur over significantly shorter lateral scales than those in the topography, the lateral correlation length of the $H = 0$ conductance fluctuations being only a factor of ~ 2 smaller than the equivalent value for topography.

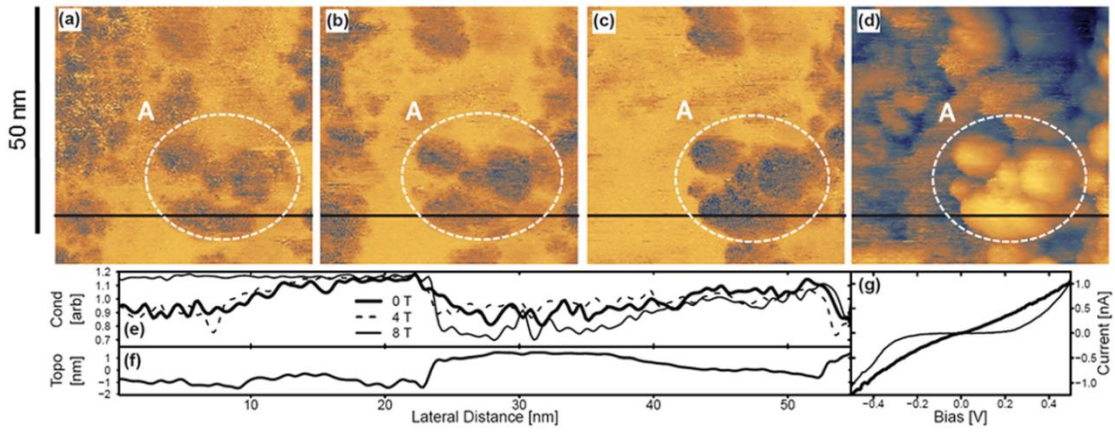

Fig. 6.3: (a) – (c) Differential conductance and (d) topography (where lighter regions are high and darker regions are low) over a 55 × 55 nm representative region of a 4.7 nm thick $SrTiO_3(001)/La_{0.5}Sr_{0.5}CoO_{3-\delta}$ film. Data were acquired at 3.7 K with a set-point of 0.7 V and 210 pA, comparable to the maps in Fig. 6.2. Panels (a)-(c) are differential conductance maps measured in 0, 4, and 8 T magnetic fields, respectively. The horizontal lines denote the positions of the relative differential conductance and topographic line scans shown in (e) and (f). (g) Two example current-voltage scans. Data were taken from a different region to that shown in panels (a)-(d), at 7.5 K, with a setpoint of 0.5 V and 1 nA, comparable to the current-voltage curves in Fig. 6.2. The region marked "A" in (a)-(d) is discussed in the text.

As can also be seen from Fig. 6.3 (a – c), the response to a magnetic field is quite complex, and appears to be opposite in different regions. On the entire left side of Fig. 6.3 (a – c) for instance, where the conductance is uncorrelated with topography, magnetic field appears to favor an insulating state. This can be seen by comparing Fig. 6.3 (a) with Fig. 6.3 (b, c) (where the image gets progressively lighter with increasing *H*), and by examining the line scans in Fig. 6.3 (e) between 0 and 15 nm. The latter reveals a 25% increase in differential conductance in 8 T, meaning a substantial decrease in ZBC and thus a decrease in metallicity, *i.e.*, local positive magnetoresistance. In contrast, in region A (inside the dashed line in Fig. 6.3 (a – d), and from 22 – 50 nm in Fig. 6.3 (e)), where correlations with topography do occur, the situation is opposite. Applied fields decrease the high bias differential conductance, thus increasing the ZBC and metallicity. This corresponds to a local negative magnetoresistance. The line scans in Fig. 6.3 (e) show this to be a 5 – 10% effect in 8 T. The most important point in considering such observations may be that while the magnetoresistance in 4.7 nm films from conventional macroscopic transport is undoubtedly negative (it is about -30% at this *T* and *H*), it arises due to lateral inter-cluster transport, and thus may not be simply reflected in STS. Fig. 6.3 (c) is certainly in qualitative agreement with conventional transport in one important regard however: electronic inhomogeneity is maintained even in large *H*, consistent with the absence of an *H*-induced percolative insulator-metal transition. This is likely due to the essential role played by chemical disorder in electronic/magnetic heterogeneity in LSCO [2, 4].

6.5 Concluding remarks

In summary, STM/STS has been used to probe the surface LDOS in $SrTiO_3$ (001)/LSCO films with thickness 4.7 and 12.4 nm, spanning the 6-7 nm range where electronic and magnetic heterogeneity has been postulated to set in. The data reveal largely homogeneous conductance in the thicker films, but indeed confirm significant nanoscale electronic inhomogeneity below 6-7 nm. This inhomogeneity occurs across a hierarchy of length scales, mostly concentrated from 5 to 50 nm, and is retained even in large applied fields. Direct, real space verification of electronic heterogeneity as the origin of degraded properties in ultrathin $SrTiO_3$ (001)/LSCO is thus obtained.

Chapter 7

Summary and outlook

$La_{1-x}Sr_xCoO_{3-\delta}$ (LSCO) is the prototypical large bandwidth perovskite cobaltite that in its bulk form has for decades interested physicists and material scientists for its unique properties such as spin state transitions, glassy magnetic phases, spin polarons and mixed ionic conductivity. The latter has also rendered it a potential candidate for the cathode material in solid oxide fuel cells. Although epitaxial thin films of LSCO are a more recent development and are in many ways still in the nascent stages of understanding, they have already revealed interesting properties not seen in the bulk, examples being the presence of an ordered oxygen vacancy superstructure, magneto-electronic phase separation in films nominally doped deep in the ferromagnetic region of the phase diagram, and the stabilization of ferromagnetism in $LaCoO_3$ and ferrimagnetism in $PrCoO_3$. Recent advances in high resolution microscopy and spectroscopic elemental analysis have provided crucial insights into the structure-property relationship of strained LSCO films and there is now a general consensus amongst researchers on the intrinsic link between strain and defect concentration in such films. Furthermore, there have recently been an increasing number of reports on the presence of oxygen vacancy ordering in other strained thin film systems, suggesting that LSCO thin films share more in common with other perovskite films than was previously thought. Against this background, this dissertation has attempted to extend the understanding of the fascinating interplay between strain, stoichiometry, magnetism and transport that occurs at cobaltite interfaces, using epitaxial $La_{0.5}Sr_{0.5}CoO_{3-\delta}$ thin films on $SrTiO_3$ and $LaAlO_3$ single crystal substrates as a model system.

We have demonstrated the synthesis of phase pure epitaxial $La_{0.5}Sr_{0.5}coO_{3-\delta}$ films on $SrTiO_3$ (001) and $LaAlO_3$ (001) using a unique on-axis high-pressure oxygen reactive DC sputtering technique. Having identified the key deposition parameters and systematically investigated the influence of each on the film properties, we have been able to synthesize 100 Å films on $LaAlO_3$ (001) that display single crystal like electronic properties, with a T_C ~ 200K, an M_S ~ 1.7 μ_B/Co, a ρ_{5K} ~ 90 μΩ cm and a RRR ~ 2.7. We are currently working on extending the growth technique to other doping values of LSCO and other cobaltites, and as of this writing, have been able to synthesize phase pure LSCO in the range $0.05 \leq x \leq 0.80$ by the DC sputtering

process described in Chapter 2 and are close to honing in on the optimal growth protocol for $LaCoO_3$ by RF sputtering.

Having focused on $La_{0.5}Sr_{0.5}CoO_{3-\delta}$ films, we then used high-resolution x-ray diffraction and reciprocal space mapping in combination with geometrical phase analysis of STEM images to study the strain relaxation process on $SrTiO_3$(001), $SrTiO_3$(110), and $LaAlO_3$(001) single crystal susbtrates. The lattice mismatch accommodation was shown to be driven by the formation, and ordering, of oxygen vacancies, as opposed to misfit dislocations. This unique strain relief mechanism is attributed to the relatively low oxygen vacancy formation enthalpy in highly doped LSCO as a result of the high population of unstable Co^{4+} ions.

We have further demonstrated that this defect ordering can be manipulated by lattice mismatch and crystallographic orientation, and thereby be used rather effectively to modify the magneto-electronic ground states of the substrate/LSCO interface. Using $La_{0.5}Sr_{0.5}CoO_{3-\delta}$ as our prototypical cobaltite and combining STEM/EELS, magnetometry, PNR and transport, we have established the presence of a MEPS clustered state at the $SrTiO_3$ (001) interface which changes to a metallic long range ordered ferromagnet on $LaAlO_3$ (001). Interestingly, the $SrTiO_3$ (110) interface was shown to have a directionally biased clustered state, appearing to be ferromagnetic and metallic along [-110] and phase-separated along [001]. We have been able to stabilize ferromagnetism and metallicity in $La_{0.5}Sr_{0.5}CoO_{3-\delta}$ films as thin as 30 Å (~ 8 u.c.) on $LaAlO_3$ (001) substrates.

Finally, we provided direct, real space verification of electronic heterogeneity as the origin of degraded properties in ultrathin $SrTiO_3$ (001)/LSCO by using scanning tunneling microscopy and spectroscopy to probe the surface local density of states in $SrTiO_3$ (001)/LSCO films with thickness 47 Å and 124 Å, spanning the 60 – 70 Å range where electronic and magnetic heterogeneity has been postulated to set in. The data revealed largely homogeneous conductance in the thicker films, but indeed confirmed significant nanoscale electronic inhomogeneity below 6-7 nm. This inhomogeneity was shown to occur across a hierarchy of length scales, mostly concentrated from 5 to 50 nm, and was retained even in large applied fields.

This dissertation has thus not only shed some light on some of the complexities arising at cobaltite interfaces but has also opened up new opportunities to tailor interfacial electronic ground states in oxide thin films, and especially tune the myriad other unique properties that arise from the presence of oxygen vacancy ordering. However, in the process, it has also thrown open many other questions that would need to be answered before a comprehensive understanding of cobaltite films could be attained. A few such outstanding questions and potential avenues of research are listed below.

1. The exact nature of the oxygen vacancy ordering structure and its evolution with temperature

Although oxygen vacancy ordering has been observed in a number of bulk and thin film systems, the only probe of its existence so far has been high resolution TEM. As a result, there have been many questions of the possible role of the high energy electron beam as well as the sample preparation process in the formation of the ordered superstructure. There have been many attempts to detect the superstructure with other techniques such as x-ray diffraction with synchrotron radiation, but none have succeeded. An alternate probe of the ordering, especially using diffraction, would not only unambiguously prove its intrinsic presence in such samples but would also enable structure factor calculations to precisely determine atomic positions. Furthermore, it would potentially enable temperature dependent measurements that would answer many questions about the formation enthalpy of such structures and their melting temperatures. A thorough thermodynamic understanding of the structure is needed to fully explain its presence (or absence) in certain materials and would enable first principles predictions of many more such materials that have not yet been discovered.

2. The role of the vacancy superstructure in transport and magnetism

We have already seen that the oxygen vacancy superstructures results in giant anistropic magnetoresistance (AMR) values ~ 30% on $LaAlO_3$ (001) and significantly anistropic signatures of magneto-electronic phase separation on $SrTiO_3$ (110). Although qualitative arguments can be made linking these properties to the vacancy ordering, a more quantative understanding would require more temperature, magnetic field, and thickness dependent measurements, in conjunction with theoretical calculations based on first-principles. However, this could prove to be a formidable challenge since many of the required material quantities

might be unknown. Nonetheless, a comprehensive experimental data set showing the dependence of these transport properties as well as magnetic anisotropy would be an invaluable resource in understanding the interaction of the superstructure with transport and magnetism (apart from simple doping arguments), and indeed such measurements are currently underway.

3. The interaction of the oxygen vacancy ordered superstructure with spin polarons

As explained in Chapter 1, the oxygen vacancy ordering results in tetrahedral coordination of the Co ions in alternate lattice planes. Tetrahedral coordination is known to close the crystal field spin gap – as a result all tetrahedrally coordinated Co ions are expected to be in the high spin (HS) state and can possibly drive neighboring Co ions into higher spin states as well. Such a scenario has been postulated to be the origin of ferromagnetism in strained $LaCoO_3$ films which have been shown to possess a robust 85 K T_C. On the other hand, under light doping conditions (less than $x \sim 0.04$), LSCO has been shown to present signatures of isolated magnetic polarons that are distributed over 7 nearest-neighbor Co sites and that possess giant spin values of $S = 10 - 16$. It would really be interesting to investigate the interaction between the two distinctly different magnetic structures in lightly doped LSCO thin films. Such an investigation of would require the synthesis of epitaxial LSCO on $SrTiO_3$ (001) in the range $0 \leq x \leq 0.05$ by RF sputtering and would be taken up once our RF sputtering of $LaCoO_3$ has been optimized.

4. Electrostatic and anion doping of $La_{0,.5}Sr_{0.5}CoO_{3-\delta}$

In the bulk, it is possible to synthesize $La_{0,.5}Sr_{0.5}CoO_{3-\delta}$ without the significant oxygen deficiency seen at thin film interfaces. It can be implied therefore that thermodynamically it is possible to stabilize a Co^{4+}/Co^{3+} ratio close to 0.5 if strain effects are neglected. Thus if electrons donated by the oxygen vacancies could be compensated for by some means that preserves the strain accommodation superstructure, it might be possible to obtain interfacial dopings close to the nominal 0.5. One such way would be to electrostatically dope an ultrathin film with an electrolyte such as an ionic liquid or an ion gel. Alternatively, nitrogen could be introduced onto an oxygen site to act as an anion dopant. Nitrogen, by virtue of having one less valence electron than oxygen, acts as an electron acceptor and a hole donor when introduced on an oxygen site. Such a substitution is indeed possible – there have been a few reports of the

synthesis of perovskite oxynitrides, although they focused on very different materials and applications. Synthesis of such structures using reactive sputtering is non-trivial and would require many experiments exploring the parametric phase space. However, once optimized, it would open up many avenues of research, including the influence of strain on the magnetic ordering of HS Co ions as well as the interaction, if any, of nitrogen ordering (as has been reported for the oxynitrides) with the oxygen vacancy ordering.

Bibliography

Chapter 1

[1] H. Kim, C. M. Gilmore, A. Piqué, J. S. Horwitz, H. Mattoussi, H. Murata, Z. H. Kafafi, and D. B. Chrisey, J. Appl. Phys. **86**, 6451 (1999)

[2] N. Q. Minh, J. Am. Ceram. Soc. **76**, 563 (1993)

[3] G. H. Haertling, J. Am. Ceram. Soc. **82**, 797 (1999)

[4] J. F. Scott, Jap. J. Appl. Phys. **38** (4B), 2272 (1999)

[5] A. M. Glazer, Acta Cryst. A**31**, 756 (1975)

[6] A. Janotti and C. G. Van de Walle, Appl. Phys. Lett. **87**, 122102 (2005)

[7] J. M. D. Coey, M. Viret, and S. von Molnár, Adv. Phys. **58**, 571 (2009)

[8] J. G. Bednorz and K. A. Müller, Angew. Chem. **100**, 757 (1988)

[9] V. V. Kharton, A. P. Viskup, E. N. Naumovich, and N. M. Lapchuk, Solid State Ionics **104**, 67 (1997)

[10] R. E. Cohen, Nature **358**, 136 (1992)

[11] R. Ramesh and N. A. Spaldin, Nat. Mater. **6**, 21 (2007)

[12] L. Pauling, *General Chemistryi* (Dover, 1988)

[13] Y. Tokura and N. Nagaosa, Science **288**, 462 (2000)

[14] M. Gerloch and R. C. Slade, *Ligand-field parameters*, (Cambridge University Press, 1973)

[15] Tapan Chatterji (Ed.), *Colossal Magnetoresistive Manganites*, (Kluwer, 2004)

[16] W. Kutzelnigg and J. D. Morgan III, Z. Phys. D **36**, 197 (1996)

[17] R. Englman, *The Jahn – Teller Effect in Molecules and Crystals*, (Wiley – Interscience, 1972)

[18] C. He, S. El-Khatib, J. Wu, J. W. Lynn, H. Zheng, J. F. Mitchell, and C. Leighton, Eur. Phys. Lett. **87**, 27006 (2009)

[19] P. Sanyal, V. B. Shenoy, H. R. Krishnamurthy, and T. V. Ramakrishnan, Eur. Phys. J. B **81**, 393 (2011)

[20] A. Spinelli, M. A. Torija, C. Liu, C. Jan, and C. Leighton, Phys. Rev. B **81**, 155110 (2010)

[21] C. Zener, Phys. Rev. **82**, 403 (1951)

[22] G. H. Jonker and J. H. van Santen, Physica **16**, 337 (1950)

[23] J. H. van Santen and G. H. Jonker, Physica **16**, 599 (1950)

[24] M. A. Korotin, V. I. Anisimov, D. I. Khomskii, and G. A. Sawatzky, Phys. Rev. Lett. **80**, 4305 (1998)

[25] P. W. Anderson and H. Hasegawa, Phys. Rev. **100**, 675 (1955)

[26] M. Coey, Nature **430**, 155 (2004)

[27] P. W. Anderson, Phys. Rev. **79**, 350 (1950)

[28] M. A. Señarís-Rodríguez and J. B. Goodenough, J. Sol. Stat. Chem. **118**, 323 (1995)

[29] G. Catalan, Phase Transit. **81**, 729 (2008)

[30] X. Leng, J. Garcia-Barriocanal, S. Bose, Y. Lee, and A. M. Goldman, Phys. Rev. Lett. **107**, 027001 (2011)

[31] E. Dagotto, *Nanoscale Phase Separation and Colossal Magnetoresistance: The Physics of Manganites and Related Compounds* (Springer, 2003)

[32] A. N. Pasupathy, A. Pushp, K. K. Gomes, C. V. Parker, J. Wen, Z. Xu, G. Gu, S. Ono, Y. Ando, and A. Yazdani, Science **320**, 196 (2008)

[33] E. Sigmund and K. A. Müller, *Phase Separation in Cuprate Superconductors* (Springer-Verlag, 1994)

[34] J. Wu, *Magneto-Electronic Phase Separation in Strontium Doped Perovskite Cobaltites* (Ph.D. dissertation, University of Minnesota, Twin Cities, 2006)

[35] M. Fäth, S. Freisem, A. A. Menovsky, Y. Tomioka, J. Aarts, and J. A. Mydosh, Science **285**, 1540 (1999)

[36] P. L. Kuhns, M. J. R. Hoch, W. G. Moulton, A. P. Reyes, J. Wu, and C. Leighton, Phys. Rev. Lett. **91**, 127202-1 (2003)

[37] S. –W. Cheong, P. A. Sharma, N. Hur, Y. Horibe, and C. H. Chen, Physica B **318**, 39 (2002)

[38] C. He, S. Eisenberg, C. Jan, H. Zheng, J. F. Mitchell, and C. Leighton, Phys. Rev. B **80**, 214411 (2009)

[39] J. Wu, J. W. Lynn, C. J. Glinka, J. Burley, H. Zheng, J. F. Mitchell, and C. Leighton, Phys. Rev. Lett. **94**, 037201 (2005)

[40] R. C. O'Handley, *Modern Magnetic Materials: Principles and Applications* (John Wiley & Sons, 2000)

[41] Y. Long, Y. Kaneko, S. Ishiwata, Y. Taguchi, and Y. Tokura, J. Phys.: Condens. Mat. **23**, 245601 (2011)

[42] A. Mineshige, M. Inaba, T. Yao, Z. Ogumi, K. Kikuchi, and M. Kawase, J. Sol. Stat. Chem. **121**, 423 (1996)

[43] P. G. Radaelli and S. –W. Cheong, Phys. Rev. B **66**, 094408 (2002)

[44] K. Knížek, J. Hejtmánek, Z. Jirák, P. Tomeš, P. Henry, and G. André, Phys. Rev. B **79**, 134103 (2009)

[45] K. Knížek, Z. Jirák, J. Hejtmánek, M. Veverka, M. Maryško, B. C. Hauback, and H. Fjellvåg, Phys. Rev. B **73**, 214443 (2006)

[46] S. Yamaguchi, Y. Okimoto, and Y. Tokura, Phys. Rev. B **54**, R11022 (1996)

[47] G. Thornton, B. C. Tofield, and A. W. Hewat, J. Sol. Stat. Chem. **61**, 301 (1986)

[48] Y. Kobayashi, T. Mitsunaga, G. Fujinawa, T. Arii, M. Suetake, K. Asai, and J. Harada, J. Phys. Soc. Jpn. **69**, 3468 (2000)

[49] P. Ravindran, P. A. Korzhavyi, H. Fjellvåg, and A. Kjekshus, Phys. Rev. B **60**, 16423 (1999)

[50] T. Arima, Y. Tokura, and J. B. Torrance, Phys. Rev. B **48**, 17006 (1993)

[51] T. Arima and Y. Tokura, J. Phys. Soc. Jpn. **64**, 2488 (1995)

[52] S. Yamaguchi, Y. Okimoto, H. Taniguchi, and Y. Tokura, Phys. Rev. B **53**, R2926 (1996)

[53] M. Itoh, M. Sugahara, I. Natori, and K. Motoya, J. Phys. Soc. Jpn. **64**, 3967 (1995)

[54] J. –Q. Yan, J. –S. Zhou, and J. B. Goodenough, Phys. Rev. B **70**, 014402 (2004)

[55] Y. Tokura, Y. Okimoto, S. Yamaguchi, H. Taniguchi, T. Kimura, and H. Takagi, Phys. Rev. B **58**, R1699 (1998)

[56] S. R. English, J. Wu, and C. Leighton, Phys. Rev. B, **65**, 220407(R) (2002)

[57] K. Asai, A. Yoneda, O. Yokokura, J. M. Tranquada, G. Shirane, and K. Kohn, J. Phys. Soc. Jpn., **67**, 290 (1998)

[58] P. M. Raccah and J. B. Goodenough, Phys. Rev. **155**, 932 (1967)

[59] M. A. Korotin, S. Y. Ezhov, I. V. Solovyev, V. I. Anisimov, D. I. Khomskii, and G. A. Sawatzky, Phys. Rev. B **54**, 5309 (1996)

[60] P. Ravindran, H. Fjellvåg, A. Kjekshus, P. Blaha, K. Schwarz, and J. Luitz, J. Appl. Phys. **91**, 291 (2002)

[61] K. Knížek, Z. Jirák, J. Hejtmánek, and P. Novák, J. Phys.: Condens. Mat. **18**, 3285 (2006)

[62] K. Knížek, Z. Jirák, J. Hejtmánek, P. Novák, and W. Ku, Phys. Rev. B **79**, 014430 (2009)

[63] V. Krápek, P. Novák, J. Kuneš, D. Novoselov, D. M. Korotin, and V. I. Anisimov, Phys. Rev. B **86**, 195104 (2012)

[64] A. Doi, J. Fujioka, T. Fukuda, S. Tsutsui, D. Okuyama, Y. Taguchi, T. Arima, A. Q. R. Baron, and Y. Tokura, Phys. Rev. B **90**, 081109(R) (2014)

[65] J. Mastin, M. –A. Einarsrud, and T. Grande, Chem. Mater. **18**, 6047 (2006)

[66] P. M. Raccah and J. B. Goodenough, J. Appl. Phys. **39**, 1209 (1968)

[67] D. Louca and J. L. Sarrao, Phys. Rev. Lett. **91**, 155501 (2003)

[68] D. Phelan, D. Louca, K. Kamazawa, S. –H. Lee, S. N. Ancona, S. Rosenkranz, Y. Motome, M. F. Hundley, J. F. Mitchell, and Y. Moritomo, Phys. Rev. Lett. **97**, 235501 (2006)

[69] A. Podlesnyak, M. Russina, A. Furrer, A. Alfonsov, E. Vavilova, V. Kataev, B. Büchner, T. Strässle, E. Pomjakushina, K. Conder, and D. I. Khomskii, Phys. Rev. Lett. **101**, 247603 (2008)

[70] A. Podlesnyak, G. Ehlers, M. Frontzek, A. S. Sefat, A. Furrer, T. Strässle, E. Pomjakushina, K. Conder, F. Demmel, and D. I. Khomskii, Phys. Rev. B **83**, 134430 (2011)

[71] E. L. Nagaev and A. I. Podel'shchikov, J. Phys.: Condens. Matter **8**, 5611 (1996)

[72] D. Phelan and C. Leighton, *private communication*

[73] M. J. R. Hoch, P. L. Kuhns, W. G. Moulton, A. P. Reyes, J. Lu, J. Wu, and C. Leighton, Phys. Rev. B **70**, 174443 (2004)

[74] M. J. R. Hoch, P. L. Kuhns, W. G. Moulton, A. P. Reyes, J. Wu, and C. Leighton, Phys. Rev. B **69**, 014425 (2004)

[75] R. X. Smith, M. J. R. Hoch, P. L. Kuhns, W. G. Moulton, A. P. Reyes, G. S. Boebinger, J. Mitchell, and C. Leighton, Phys. Rev. B **78**, 092201 (2008)

[76] D. Phelan, D. Louca, S. Rosenkranz, S. –H. Lee, Y. Qiu, P. J. Chupas, R. Osborn, H. Zheng, J. F. Mitchell, J. R. D. Copley, J. L. Sarrao, and Y. Moritomo, Phys. Rev. Lett. **96**, 027201 (2006)

[77] S. R. Giblin, I. Terry, D. Prabhakaran, A. T. Boothroyd, J. Wu, and C. Leighton, Phys. Rev. B **74**, 104411 (2006)

[78] J. Wu and C. Leighton, Phys. Rev. B **67**, 174408 (2003)

[79] J. Wu, H. Zheng, J. F. Mitchell, and C. Leighton, Phys. Rev. B **73**, 020404(R) (2006)

[80] C. He, S. El-Khatib, S. Eisenberg, M. Manno, J. W. Lynn, H. Zheng, J. F. Mitchell, and C. Leighton, Appl. Phys. Lett. **95**, 222511 (2009)

[81] T. R. McGuire and R. I. Potter, IEEE Trans. Magn. **11**, 1018 (1975)

[82] M. N. Baibich, J. M. Broto, A. Fert, F. N. V. Dau, F. Petroff, P. Eitenne, G. Creuzet, A. Friederich, and J. Chazelas, Phys. Rev. Lett. **61**, 2472 (1988)

[83] W. P. Pratt, Jr., S. –F. Lee, J. M. Slaughter, R. Loloee, P. A. Schroeder, and J. Bass, Phys. Rev. Lett. **66**, 3060 (1991)

[84] J. Q. Xiao, J. S. Jiang, and C. L. Chien, Phys. Rev. Lett. **68**, 3749 (1992)

[85] A. E. Berkowitz, J. R. Mitchell, M. J. Carey, A. P. Young, S. Zhang, F. E. Spada, F. T. Parker, A. Hutten, and G. Thomas, Phys. Rev. Lett. **68**, 3745 (1992)

[86] S. Barzilai, Y. Goldstein, I. Balberg, and J. S. Helman, Phys. Rev. B **23**, 1809 (1991)

[87] R. X. Smith, M. J. R. Hoch, W. G. Moulton, P. L. Kuhns, A. P. Reyes, and G. S. Boebinger, Phys. Rev. B **86**, 054428 (2012)

[88] C. Leighton, *unpublished*

[89] P. Bezdicka, A. Wattiaux, J. C. Grenier, M. Pouchard, and P. Hagenmuller, Z. anorg. Allg. Chem. **619**, 7 (1993)

[90] M. T. Anderson, J. T. Vaughey, and K. R. Poeppelmeier, Chem. Mater. **5**, 151 (1993)

[91] O. H. Hansteen, H. Fjellvåg, and B. C. Hauback, J. Sol. Stat. Chem. **141**, 411 (1998)

[92] H. E. Shinawi, J. F. Marco, F. J. Berry, and C. Greaves, J. Mater. Chem. **20**, 3253 (2010)

[93] T. Takeda, Y. Yamaguchi, and H. Watanabe, J. Phys. Soc. Jpn. **33**, 970 (1972)

[94] P. D. Battle, T. C. Gibb, and P. Lightfoot, J. Sol. Stat. Chem. **76**, 334 (1988)

[95] J. P. Hodges, S. Short, J. D. Jorgensen, X. Xiong, B. Dabrowski, S. M. Mini, and C. W. Kimball, J. Sol. Stat. Chem. **151**, 190 (2000)

[96] J. E. Sunstrom IV, K. V. Ramanujachary, and M. Greenblatt, J. Sol. Stat. Chem. **139**, 388 (1998)

[97] Y. Ito, R. F. Klie, and N. D. Browning, J. Am. Ceram. Soc. **85**, 969 (2002)

[98] Y. Teraoka, H. M. Zhang, K. Okamoto, and N. Yamazoe, Mater. Res. Bull. **23**, 51 (1988)

[99] O. Yamamoto, Y. Takeda, R. Kanno, and M. Noda, Sol. Stat. Ionics **22**, 241 (1987)

[100] S. K. Tiwari, P. Chartier, and R. N. Singh, J. Electrochem. Soc., **142**, 148 (1995)

[101] H. Obayashi, Y. Sakurai, and T. Gejo, J. Sol. Stat. Chem. **17**, 299 (1976)

[102] C. B. Alcock, R. C. Doshi, and Y. Shen, Sol. Stat. Ionics **51**, 281 (1992)

[103] C. Chen, H. J. M. Bouwmeester, H. Kruidhof, J. E. ten Elshof, and A. Burggraaf, J. Mater. Chem. **6**, 815 (1996)

[104] R. N. Singh, S. K. Tiwari, S. P. Singh, N. K. Singh, G. Poillerat, and P. Chartier, J. Chem. Soc., Faraday Trans. **92**, 2593 (1996)

[105] J. T. Cheung, H. Sankur, and T. Chang, Opt. Photonic News **3**, 24 (1992)

[106] R. L. Sandstrom, W. J. Gallagher, T. R. Dinger, R. H. Koch, R. B. Laibowitz, A. W. Kleinsasser, R. J. Gambino, B. Bumble, and M. F. Chisholm, Appl. Phys. Lett. **53**, 444 (1988)

[107] B. Jalan, R. Engel-Herbert, N. J. Wright, and S. Stemmer, J. Vac. Sci. Technol. A **27**, 461 (2009)

[108] W. A. Doolittle, A. G. Carver, and W. Henderson, J. Vac. Sci. Technol. B **23**, 1272 (2005)

[109] K. –S. Hwang, H. –M. Lee, S. –S. Min, and B. –A. Kang, J. Sol-Gel Sci. Tech. **18**, 175 (2000)

[110] J. T. Cheung, P. E. D. Morgan, D. H. Lowndes, X. –Y. Zheng, and J. Breen, Appl. Phys. Lett. **62**, 2045 (1993)

[111] J. F. M. Cillessen, R. M. Wolf, and A. E. M. De Veriman, Appl. Surf. Sci. **69**, 212 (1993)

[112] S. G. Ghonge, E. Goo, R. Ramesh, T. Sands, and V. G. Keramidas, Appl. Phys. Lett. **63**, 1628 (1993)

[113] G. H. Jonker and J. H. van Santen, Physica **19**, 120 (1953)

[114] Z. L. Wang and J. Zhang, Phys. Rev. B **54**, 1153 (1996)

[115] P. W. Chan, W. Wu, K. H. Wong, K. Y. Tong, and J. T. Cheung, J. Phys. D: Appl. Phys. **30**, 957 (1997)

[116] S. Madhukar, S. Aggarwal, A. M. Dhote, R. Ramesh, A. Krishnan, D. Keeble, and E. Poindexter, J. Appl. Phys. **81**, 3543 (1997)

[117] R. A. Gunasekaran, J. D. Pedaring, and M. Dinescu, Appl. Phys. A **69**, 621 (1999)

[118] D. O. Klenov, W. Donner, L. Chen, A. J. Jacobson, and S. Stemmer, J. Mater. Res. **18**, 188 (2003)

[119] M. A. Torija, M. Sharma, M. R. Fitzsimmons, M. Varela, and C. Leighton, J. Appl. Phys. **104**, 023901 (2008)

[120] M. Sharma, J. Gazquez, M. Varela, J. Schmitt, and C. Leighton, J. Vac. Sci. Technol. A **29**, 051511 (2011)

[121] T. Friesnegg, S. Madhukar, B. Nielsen, A. R. Moodenbaugh, S. Aggarwal, D. J. Keeble, E. H. Poindexter, and P. Mascher, Phys. Rev. B **59**, 13365 (1999)

[122] D. Fuchs, T. Schwarz, O. Morán, P. Schweiss, and R. Schneider, Phys. Rev. B **71**, 092406 (2005)

[123] C. Xie, J. I. Budnick, B. O. Wells, J. C. Woicik, Appl. Phys. Lett. **91**, 172509 (2007)

[124] Z. L. Wang and J. S. Yin, Phil. Mag. B **77**, 49 (1998)

[125] S. Stemmer, A. J. Jacobson, X. Chen, and A. Ignatiev, J. Appl. Phys. **90**, 3319 (2001)

[126] D. O. Klenov, W. Donner, B. Foran, and S. Stemmer, App. Phys. Lett. **82**, 3427 (2003)

[127] W. S. Choi, J. –H. Kwon, H. Jeen, J. E. Hamann-Borrero, A. Radi, S. Macke, R. Sutarto, F. He, G. A. Sawatzky, V. Hinkov, M. Kim, and H. N. Lee, Nano Lett. **12**, 4966 (2012)

[128] J. Gazquez, W. Luo, M. P. Oxley, M. Prange, M. A. Torija, M. Sharma, C. Leighton, S. T. Pantelides, S. J. Pennycook, and M. Varela, Nano Lett. **11**, 973 (2011)

[129] M. A. Torija, M. Sharma, J. Gazquez, M. Varela, C. He, J. Schmitt, J. A. Borchers, M. Laver, S. El-Khatib, and C. Leighton, Adv. Mater. **23**, 2711 (2011)

Chapter 2

[1] B. D. Cullity and S. R. Stock, *Elements of X-ray Diffraction* (Prentice Hall, 2001)

[2] G. H. Stout and L. H. Jensen, *X-ray Structure Determination: A Practical Guide* (Wiley – Interscience, 1989)

[3] D. K. Bowen and B. K. Tanner, *High Resolution X-ray Diffractometry and Topography* (Taylor & Francis, 1998)

[4] C. Kittel, *Introduction to Solid State Physics* (John Wiley & Sons, Inc, 2005)

[5] J. A. Bearden, Rev. Mod. Phys. **39**, 78 (1967)

[6] M. O. Krause and J. H. Oliver, J. Phys. Chem. Ref. Data **8**, 329 (1979)

[7] PANalytical, *X'Pert PRO User's Guide* (2002)

[8] U. Pietsch, V. Holý and T. Baumbach, *High Resolution X-ray Scattering: From Thin Films to Lateral Nanostructures* (Springer, 2004)

[9] M. Björck and G. Andersson, J. Appl. Cryst. **40** (2007)

[10] http://www.ncnr.nist.gov/reflpak/

[11] C. F. Majkrzak, Acta Physica Polonica A **96**, 81 (1999)

[12] M. R. Fitzsimmons and C. F. Majkrzak, *Modern Techniques for Characterizing Magnetic Materials* (Ch. 3, pp. 107 – 155) (Springer, 2005)

[13] J. F. Ankner and G. P. Felcher, J. Magn. Magn. Mater. **200**, 741 (1999)

[14] C. F. Majkrzak, Physica B **173**, 75 (1991)

[15] L. J. van der Pauw, Philips Res. Rep. **13**, 1 (1958)

[16] L. J. van der Pauw, Philips Tech. Rev. **20**, 220 (1958)

[17] R. L. Fagaly, Rev. Sci. Instrum. **77**, 101101 (2006)

[18] M. Tinkham, *Introduction to Superconductivity* (Dover, 2004)

[19] R. Gross and A. Marx, *Applied Superconductivity: Josephson Effect and Superconducting Electronics* (Walther-Meissner-Institut, 2005)

[20] Quantum Design MPMS-*XL* Hardware Manual

[21] G. Campillo, A. Berger, J. Osorio, J. E. Pearson, S. D. Bader, E. Baca, and P. Prieto, J. Magn. Magn. Mater. **237**, 61 (2001)

[22] A. Berger, G. Campillo, P. Vivas, J. E. Pearson, S. D. Bader, E. Baca, and P. Prieto, J. Appl. Phys. **91**, 8393 (2002)

[23] F. J. Giessibl, Rev. Mod. Phys. **75**, 949 (2003)

[24] C. J. Chen, *Introduction to Scanning Tunneling Microscopy* (Oxford University Press, 1993)

[25] A. Hendrych, R. Kubinek, and A. V. Zhukov, *Modern Research and Educational Topics in Microscopy* (pp. 805 – 811) (Formatex, 2007)

[26] M. Nonnenmacher, M. P. O'Boyle, and H. K. Wickramasinghe, Appl. Phys. Lett. **58**, 2921 (1991)

[27] D. B. Williams and C. B. Carter, *Transmission Electron Microscopy: A Textbook for Materials Science* (Springer, 2009)

[28] S. J. Pennycook and P. D. Nellist, *Scanning Transmission Electron Microscopy: Imaging and Analysis* (Springer, 2011)

[29] M. Bosman, M. Watanabe, D. T. L. Alexander, and V. J. Keast, Ultramicroscopy **106**, 1024 (2006)

[30] M. J. Hÿtch, Microsc. Microanal. Microstruct. **8**, 41 (1997)

[31] M. J. Hÿtch, E. Snoeck, and R. Kilaas, Ultramicroscopy **74**, 131 (1998)

[32] M. J. Hÿtch, J. –L. Putaux, and J. Thibault, Phil. Mag. **86**, 4641 (2006)

Chapter 3

[1] P. M. Raccah and J. B. Goodenough, J. Appl. Phys. **39**, 1209 (1968)

[2] M. A. Torija, M. Sharma, J. Gazquez, M. Varela, C. He, J. Schmitt, J. A. Borchers, M. Laver, S. El-Khatib, and C. Leighton, Adv. Mater. **23**, 2711 (2011)

[3] Y. Ishii, H. Yamada, H. Sato, H. Akoh, M. Kawasaki, and Y. Tokura, Appl. Phys. Lett. **91**, 192504 (2007)

[4] D. Fuchs, C. Pinta, T. Schwarz, P. Schweiss, P. Nagel, S. Schuppler, R. Schneider, M. Merz, G. Roth, and H. v. Löhneysen, Phys. Rev. B **75**, 144402 (2007)

[5] Virat V. Mehta, Shameek Bose, Jodi M. Iwata-Harms, Elke Arenholz, C. Leighton, and Y. Suzuki, Phys. Rev. B **87**, 020405(R) (2013)

[6] M. Sharma, J. Gazquez, M. Varela, J. Schmitt, and C. Leighton, Phys. Rev. B **84**, 024417 (2011)

[7] O. Yamamoto, Y. Takeda, R. Kanno, and M. Noda, Sol. Stat. Ionics **22**, 241 (1987)

[8] Jeffrey T. Cheung, Peter E. D. Morgan, R. Neugaonkar, and Mark Goorsk, Integr. Ferroelectr. **3**, 147 (1993)

[9] J. F. M. Cillessen, M. W. J. Prins, and R. M. Wolf, J. Appl. Phys. **81**, 2777 (1997)

[10] S. K. Tiwari, P. Chartier, and R. N. Singh, J. Electrochem. Soc., **142**, 148 (1995)

[11] H. Obayashi, Y. Sakurai, and T. Gejo, J. Sol. Stat. Chem. **17**, 299 (1976)

[12] C. B. Alcock, R. C. Doshi, and Y. Shen, Sol. Stat. Ionics **51**, 281 (1992)

[13] C. Chen, H. J. M. Bouwmeester, H. Kruidhof, J. E. ten Elshof, and A. Burggraaf, J. Mater. Chem. **6**, 815 (1996)

[14] M. A. Torija, M. Sharma, M. R. Fitzsimmons, M. Varela, and C. Leighton, J. Appl. Phys. **104**, 023901 (2008)

[15] D. O. Klenov, W. Donner, L. Chen, A. J. Jacobson, and S. Stemmer, J. Mater. Res. **18**, 188 (2003)

[16] J. T. Cheung, P. E. D. Morgan, D. H. Lowndes, X. –Y. Zheng, and J. Breen, Appl. Phys. Lett. **62**, 2045 (1993)

[17] R. A. Gunasekaran, J. D. Pedaring, and M. Dinescu, Appl. Phys. A **69**, 621 (1999)

[18] K. –S. Hwang, H. –M. Lee, S. –S. Min, and B. –A. Kang, J. Sol-Gel Sci. Tech. **18**, 175 (2000)

[19] Z. L. Wang and J. S. Yin, Philos. Mag. B **77**, 49 (1998)

[20] T. Friesnegg, S. Madhukar, B. Nielsen, A. R. Moodenbaugh, S. Aggarwal, D. J. Keeble, E. H. Poindexter, and P. Mascher, Phys. Rev. B **59**, 13365 (1999)

[21] F. Morin, G. Trudel, and Y. Denos, Solid State Ionics **96**, 129 (1997)

[22] T. I. Selinder, G. Larsson, U. Helmersson, and S. Rudner, J. Appl. Phys. **69**, 390 (1991)

[23] Daniel J. Kester and Russell Messier, J. Mater. Res. **8**, 1928 (1993)

[24] E. Yin, M. Rubin, and C. B. Hopper, Mater. Lett. **13**, 89 (1992)

[25] U. Poppe, J. Schubert, R. R. Arons, W. Evers, C. H. Freiburg, W. Reichert, K. Schmidt, W. Sybertz, and K. Urban, Solid State Commun. **66**, 661 (1988)

[26] U. Poppe, N. Klein, U. Dähne, H. Soltner, C. L. Jia, B. Kabius, K. Urban, A. Lubig, and K. Schmidt, J. Appl. Phys. **71**, 5572 (1992)

[27] M. Grizalez, E. Delgado, M. E. Gómez, and P. Prieto, Phys. Stat. C **11**, 4203 (2007)

[28] O. Morán, R. Hott, K. Grube, D. Fuchs, R. Schneider, E. Baca, W. Saldarriaga, and P. Prieto, J. Appl. Phys. **95**, 6240 (2004)

[29] F. Y. Bruno, J. Garcia-Barriocanal, M. Torija, A. Rivera, Z. Sefrioui, C. Leighton, C. Leon, and J. Santamaria, Appl. Phys. Lett. **92**, 082106 (2008)

[30] N. A. Pertsev, A. Petraru, H. Kohlstedt, R. Waser, I. K. Bdikin, D. Kiselev, and A. L. Kholkin, Nanotechnology **19**, 375703 (2008)

[31] M. Toledano-Luque, E. San Andrés, A. del Prado, I. Mártil, M. L. Lucía, G. González-Díaz, F. L. Martínez, W. Bohne, J. Röhrich, and E. Strub, J. Appl. Phys. **102**, 044106 (2007)

[32] G. K. Muralidhar, G. Mohan Rao, A. G. Menon, and S. Mohan, Thin Solid Films **224**, 137 (1993)

[33] D. Giratá, Y. Rojas, E. Bacca, M. Chacón, W. Lopera, P. Prieto, and J. Heiras, Solid State Commun. **90**, 539 (1994)

[34] S. Senthil Nathan, G. K. Muralidhar, G. Mohan Rao, and S. Mohan, Vacuum **49**, 221 (1998)

[35] J. Wu and C. Leighton, Phys. Rev. B **67**, 174408 (2003)

[36] M. Ohring, *Materials Science of Thin Films: Deposition & Structure* (Academic Press, 2002)

[37] Z. Feng, Y. Yacoby, W. T. Hong, H. Zhou, M. D. Biegalski, H. M. Christen, and Y. Shao-Horn, Energy Environ. Sci. **7**, 1166 (2014)

[38] H. Tanaka and T. Kawai, Phys. Rev. B **60**, 14163 (1999)

[39] S. Madhukar, S. Aggarwal, A. M. Dhote, R. Ramesh, A. Krishnan, D. Keeble, and E. Poindexter, J. Appl. Phys. **81**, 3543 (1997)

[40] D. Fuchs, T. Schwarz, O. Morán, P. Schweiss, and R. Schneider, Phys. Rev. B **71**, 092406 (2005)

[41] N-C Yeh, R. P. Vasquez, D. A. Beam, C-C Fu, J. Huynh, and G. Beach, J. Phys.: Condens. Matter **9**, 3713 (1997)

[42] C. Xie, J. I. Budnick, B. O. Wells, J. C. Woicik, Appl. Phys. Lett. **91**, 172509 (2007)

[43] V. G. Prokhorov, Y. P. Lee, K. W. Kim, V. M. Ishchuk, and I. n. Chukanova, Phys. Rev. B **66**, 132410 (2002)

[44] M. Sharma, J. Gazquez, M. Varela, J. Schmitt, and C. Leighton, J. Vac. Sci. Technol. A **29**, 051511 (2011)

[45] L. Malavasi, E. Quartarone, C. Sanna, N. Lampis, A. G. Lehmann, C. Tealdi, M. C. Mozzati, and G. Flor, Chem. Mater. **18**, 5230 (2006)

[46] J. Kim, P. B. Thang, T. Choi, C. Jung, and J. Lee, J. Kor. Phys. Soc. **49**, S604 (2006)

[47] H. M. Aarbogh, J. Wu, L. Wang, H. Zheng, J. F. Mitchell, and C. Leighton, Phys. Rev. B **74**, 134408 (2006)

[48] J. –P. Locquet, A. Catana, E. Mächler, C. Gerber, and J. G. Bednorz, Appl. Phys. Lett. **64**, 372 (1994)

[49] M. Varela, W. Grogger, D. Arias, Z. Sefrioui, C. León, C. Ballesteros, K. M. Krishnan, and J. Santamaría, Phys. Rev. Lett. **86**, 5156 (2001)

[50] M. A. Lieberman and A. J. Lichtenberg, *Principles of Plasma Discharges and Materials Processing* (Wiley-Interscience, 2005)

Chapter 4

[1] D. Fuchs, C. Pinta, T. Schwarz, P. Schweiss, P. Nagel, S. Schuppler, R. Schneider, M. Merz, G. Roth, and H. v. Löhhneysen, Phys. Rev. B **75**, 144402 (2007)

[2] D. Fuchs, E. Arac, C. Pinta, S. Schuppler, R. Schneider, and H. v. Löhneysen, Phys. Rev. B **77**, 014434 (2008)

[3] H. Seo, A. Posadas, and A. A. Demkov, Phys. Rev. B **86**, 014430 (2012)

[4] J. Wu and C. Leighton, Phys. Rev. B **67**, 174408 (2003)

[5] G. H. Jonker and J. H. van Santen, Physica **19**, 120 (1953)

[6] R. F. Klie, Y. Ito, S. Stemmer, and N. D. Browning, Ultramicroscopy, **86**, 289 (2001)

[7] Y. Ito, R. F. Klie, N. D. Browning,and T. J. Mazanec, J. Am. Ceram. Soc. **85**, 969 (2002)

[8] M. A. Torija, M. Sharma, J. Gazquez, M. Varela, C. He, J. Schmitt, J.A. Borchers, M. Laver, S. El-Khatib, and C. Leighton, Adv. Mater. **23,** 2711 (2011)

[9] M. A. Torija, M. Sharma, M. R. Fitzsimmons, M. Varela, and C. Leighton, J. Appl. Phys.**104**, 023901 (2008)

[10] D. O. Klenov, W. Donner, B. Foran, and S. Stemmer, Appl. Phys. Lett. **82**, 3427 (2003)

[11] J. Gazquez, W. Luo, M. P. Oxley, M. Prange, M. A. Torija, M. Sharma, C. Leighton, S. T. Pantelides, S. J. Pennycook, and M. Varela, Nano Lett., **11** 973 (2011)

[12] W. Donner, C. Chen, M. Liu, A. J. Jacobson, Y. –L. Lee, M. Gadre, and D. Morgan, Chem. Mater. **23**, 984 (2011)

[13] M. Sharma, J. Gazquez, M. Varela, J. Schmitt and C. Leighton, Phys. Rev. B **84**, 024417 (2011)

[14] S. C. Wimbush, M. Li, M. E. Vickers, B. Maiorov, D. M. Feldmann, Q. Jia, and J. L. MacManus-Driscoll, Adv. Funct. Mater. **19**, 835 (2009)

[15] M. Sharma, J. Gazquez, M. Varela, J. Schmitt, and C. Leighton, J. Vac. Sci. Technol. **29**, 051511 (2011)

[16] HREM Research, Available from: http://www.hremresearch.com

[17] M.J. Hytch, E. Snoeck, and R. Kilaas, Ultramicroscopy **74**, 131 (1998)

[18] D.O. Klenov, W. Donner, L. Chen, A.J. Jacobson, and S. Stemmer, J. Mater. Res. **18**, 188 **(**2003)

[19] Y.M. Kim, J. He, M. D. Biegalski, H. Ambaye, V. Lauter, H. M. Christen, S. T. Pantelides, S. J. Pennycook, S. V. Kalinin, and A. Y. Borisevich, Nat. Mater. **11**, 1 (2012)

[20] A. Y. Borisevich,, A. N. Morozovska, Young-Min Kim, D. Leonard, M. P. Oxley, M. D. Biegalski, E. A. Eliseev, and S. V. Kalinin, Phys. Rev. Lett. **109**, 065702 (2012)

[21] S. Stemmer, A.J. Jacobson, X. Chen, and A. Ignatiev, J. Appl. Phys. **90**, 3319 (2001)

[22] W. S. Choi, J.-H. Kwon, H. Jeen, J.E. Hamann-Borrero, A. Radi, S. Macke, R. Sutarto, F. He, G.A. Sawatzky, V. Hinkov, M. Kim, and H. N. Lee, Nano Lett. **12**, 4966 (2012)

[23] S. Ramesh, S.S. Manoharan, and M. S. Hedge, J. Mater. Chem. **5**, 1053 (1995)

Chapter 5

[1] A. P. Ramirez, J. Phys.: Condens. Mat. **9**, 8171 (1997)

[2] S. Yamaguchi, Y. Okimoto, H. Taniguchi, and Y. Tokura, Phys. Rev. B **53**, R2926 (1996)

[3] V. V. Kharton, A. P. Viskup, E. N. Naumovich, and N. M. Lapchuk, Solid State Ionics **104**, 67 (1997)

[4] O. Yamamoto, Y. Takeda, R. Kanno, and M. Noda, Sol. Stat. Ionics **22**, 241 (1987)

[5] C. B. Alcock, R. C. Doshi, and Y. Shen, Sol. Stat. Ionics **51**, 281 (1992)

[6] R. J. H. Voorhoeve, D. W. Johnson, Jr., J. P. Remeika, and P. K. Gallagher, Science **195**, 827 (1977)

[7] J. F. Scott and C. Dearaujo, Science **246**, 1400 (1989)

[8] R. Ramesh and N. A. Spaldin, Nat. Mater. **6**, 21 (2007)

[9] M. T. Anderson, J. T. Vaughey, and K. R. Poeppelmeier, Chem. Mater. **5**, 151 (1993)

[10] S. Stølen, E. Bakken, and C. E. Mohn, Phys. Chem. Chem. Phys. **8**, 429 (2006)

[11] R. F. Klie, Y. Ito, S. Stemmer, and N. D. Browning, Ultramicroscopy **86**, 289 (2001)

[12] D. O. Klenov, W. Donner, B. Foran, and S. Stemmer, App. Phys. Lett. **82**, 3427 (2003)

[13] N. Biškup, J. Salafranca, V. Mehta, M. P. Oxley, Y. Suzuki, S. J. Pennycook, S. T. Pantelides, and M. Varela, Phys. Rev. Lett. **112**, 087202 (2014)

[14] J. Seidel, W. Luo, S. J. Suresha, P. –K. Nguyen, A. S. Lee, S. –Y. Kim, C. –H. Yang, S. J. Pennycook, S. T. Pantelides, J. F. Scott, and R. Ramesh, Nat. Comm. **3**, 799 (2012)

[15] H. Jeen, W. S. Choi, M. D. Biegalski, C. M. Folkman, I. –C. Tung, D. D. Fong, J. W. Freeland, D. Shin, H. Ohta, M. F. Chisholm, and H. N. Lee, Nat. Mater. **12**, 1057 (2013)

[16] Q. Zhang, S. Guo, B. Ge, P. Chen, Y. Yao, L. Wang, L. Gu, Y. Wang, X. Duan, C. Jin, B. Liu, and R. Yu, J. Am. Ceram. Soc. **97**, 1264 (2014)

[17] J. Wu and C. Leighton, Phys. Rev. B **67**, 174408 (2003)

[18] D. Fuchs, T. Schwarz, O. Morán, P. Schweiss, and R. Schneider, Phys. Rev. B **71**, 092406 (2005)

[19] M. A. Torija, M. Sharma, J. Gazquez, M. Varela, C. He, J. Schmitt, J. A. Borchers, M. Laver, S. El-Khatib, and C. Leighton, Adv. Mater. **23**, 2711 (2011)

[20] M. Bowen, M. Bibes, A. Barthélémy, J. –P. Contour, A. Anane, Y. Lemaître, and A. Fert, Appl. Phys. Lett. **82**, 233 (2003)

[21] V. Dediu, M. Murgia, F. C. Matacotta, C. Taliani, and S. Barbanera, Sol. Stat. Comm. **122**, 181 (2002)

[22] U. Aschauer, R. Pfenninger, S. M. Selbach, T. Grande, and N. A. Spaldin, Phys. Rev. B **88**, 054111 (2013)

[23] A. Kushima, S. Yip, and B. Yildiz, Phys. Rev. B **82**, 115435 (2010)

[24] M. Kubicek, Z. Cai, W. Ma, B. Yildiz, H. Hutter, and J. Fleig, ACS Nano **7**, 3276 (2013)

[25] G. Campillo, A. Berger, J. Osorio, J. E. Pearson, S. D. Bader, E. Baca, and P. Prieto, J. Magn. Magn. Mater. **237**, 61 (2001)

[26] A. Berger, G. Campillo, P. Vivas, J. E. Pearson, S. D. Bader, E. Baca, and P. Prieto, J. Appl. Phys. **91**, 8393 (2002)

[27] L. M. Falicov, D. T. Pierce, S. D. Bader, R. Gronsky, K. B. Hathaway, H. J. Hopster, D. N. Lambeth, S. S. P. Parkin, G. Pinz, M. Salamon, I. K. Schuller, and R. H. Victora, J. Mater. Res. **5**, 1299 (1990)

[28] T. Kaneyoshi, J. Phys.: Condens. Mat. **3**, 4497 (1991)

[29] J. –H. Park, E. Vescovo, H. –J. Kim, C. Kwon, R. Ramesh, and T. Venkatesan, Phys. Rev. Lett. **81**, 1953 (1998)

[30] J. W. Freeland, J. J. Kavich, K. E. Gray, L. Ozyuzer, H. Zheng, J. F. Mitchell, M. P. Warusawithana, P. Ryan, X. Zhai, R. H. Kodama, and J. N. Eckstein, J. Phys.: Condens. Mat. **19**, 315210 (2007)

[31] C. F. Majkrzak, Physica B **173**, 75 (1991)

[32] J. F. Ankner and G. P. Felcher, J. Magn. Magn. Mater. **200**, 741 (1999)

[33] M. R. Fitzsimmons and C. F. Majkrzak, *Modern Techniques for Characterizing Magnetic Materials* (Ch. 3, pp. 107 – 155) (Springer, 2005)

[34] W. L. V. Price, J. Phys. D: Appl. Phys. **5**, 1127 (1972)

[35] Y. Sato and S. Sato, Jpn. J. Appl. Phys. **40**, 4256 (2001)

[36] O. Bierwagen, R. Pomraenke, S. Eilers, and W. T. Masselink, Phys. Rev. B **70**, 165307 (2004)

[37] J. Kleiza, M. Sapagovas, and V. Kleiza, Informatica **18**, 253 (2007)

[38] N. Martin, J. Sauget, and T. Nyberg, Mater. Lett. **105**, 20 (2013)

[39] H. M. Aarbogh, J. Wu, L. Wang, H. Zheng, J. F. Mitchell, and C. Leighton, Phys. Rev. B **74**, 134408 (2006)

[40] R. C. O'Handley, *Modern Magnetic Materials: Principles and Applications* (John Wiley & Sons, 2000)

[41] T. R. McGuire and R. I. Potter, IEEE Trans. Magn. **11**, 1018 (1975)

[42] S. Barzilai, Y. Goldstein, I. Balberg, and J. S. Helman, Phys. Rev. B **23**, 1809 (1991)

[43] J. Q. Xiao, J. S. Jiang, and C. L. Chien, Phys. Rev. Lett. **68**, 3749 (1992)

[44] W. P. Pratt, Jr., S. –F. Lee, J. M. Slaughter, R. Loloee, P. A. Schroeder, and J. Bass, Phys. Rev. Lett. **66**, 3060 (1991)

[45] J. Wu, J. W. Lynn, C. J. Glinka, J. Burley, H. Zheng, J. F. Mitchell, and C. Leighton, Phys. Rev. Lett. **94**, 037201 (2005)

[46] Y. Long, Y. Kaneko, S. Ishiwata, Y. Taguchi, and Y. Tokura, J. Phys.: Condens. Mat. **23**, 245601 (2011)

Chapter 6

[1] M.A. Torija, M. Sharma, J. Gazquez, M. Varela, C. He, J. Schmitt, J.A. Borchers, M. Laver, S. El-Khatib and C. Leighton, Adv. Mater. **23**, 2711 (2011)

[2] C. He, S. El-Khatib, J. Wu, J.W. Lynn, H. Zheng, J.F. Mitchell and C. Leighton, EPL **87**, 27006 (2009)

[3] C. He, S. El-Khatib, S. Eisenberg, M. Manno, J.W. Lynn, H. Zheng, J.F. Mitchell and C. Leighton, Appl. Phys. Lett. **95**, 222511 (2009)

[4] C. He, S. Eisenberg, C. Jan, H. Zheng, J.F. Mitchell and C. Leighton, Phys. Rev. B., **80**, 214411 (2009)

[5] J. Wu, J.W. Lynn, C. Glinka, J. Burley, H. Zheng, J.F. Mitchell and C. Leighton, Phys. Rev. Lett. **94**, 037201 (2005).

[6] M. A. Torija, M. Sharma, M. R. Fitzsimmons, M. Varela, and C. Leighton, J. Appl. Phys. **104**, 023901 (2008)

[7] M. Sharma, J. Gazquez, M. Varela, J. Schmitt and C. Leighton, J. Vac. Sci. Technol. **29**, 051511 (2011)

[8] M. Sharma, J. Gazquez, M. Varela, J. Schmitt and C. Leighton, Phys. Rev. B. **84**, 024417 (2011)

[9] U.R. Singh, S. Chaudhuri, R.C. Budhani and A.K. Gupta, J. Phys. Cond. Mat. **21**, 355001 (2009)

[10] M. Fath, S. Freisem, A.A. Menovsky, Y. Tomioka, J. Aarts and J.A. Mydosh, Science **285**, 1540 (1999)

[11] T. Becker, C. Streng, Y. Luo, V. Moshnyaga, B. Damaschke, N. Shannon and K. Samwer, Phys. Rev. Lett. **89**, 237203 (2002)

[12] J.X. Ma, D.T. Gillespie, E.W. Plummer and J. Shen, Phys. Rev. Lett. **95**, 237210 (2005)

[13] Ch. Renner, G. Aeppli, B.-G. Kim, Y.-A. Soh and S.W. Cheong, Nature **416**, 518 (2002).

[14] S. Seiro, Y. Fasano, I. Maggio-Aprile, E. Koller, O. Kuffer and O. Fischer, Phys. Rev. B. **77**, 020407R (2008)